

**STUDY OF INDIVIDUAL InAs NANOWIRES USING RAMAN  
SPECTROSCOPY**

*By*

**VANDNA KUMARI GUPTA**

**Enrolment No: PHYS03201204018**

**Raja Ramanna Centre for Advanced Technology, Indore**

*A thesis submitted to the*

*Board of Studies in Physical Sciences*

*In partial fulfilment of requirements for the Degree of*

**DOCTOR OF PHILOSOPHY**

*of*

**HOMI BHABHA NATIONAL INSTITUTE**



**August 2018**

## STATEMENT BY AUTHOR

This dissertation has been submitted in partial fulfilment of requirements for an advanced degree at Homi Bhabha National Institute (HBNI) and is deposited in the Library to be made available to borrowers under rules of the HBNI.

Brief quotations from this dissertation are allowable without special permission, provided that accurate acknowledgement of the source is made. Requests for permission for extended quotation from or reproduction of this manuscript in whole or in part may be granted by the Competent Authority of HBNI when in his or her judgment the proposed use of the material is in the interests of scholarship. In all other instances, however, permission must be obtained from the author.

*Vandana Gupta*

Vandna Kumari Gupta

## DECLARATION

I, hereby declare that the investigation presented in the thesis has been carried out by me. The work is original and has not been submitted earlier as a whole or in part for a degree / diploma at this or any other Institution / University.

*Vandana Kumari Gupta*  
Vandna Kumari Gupta

---

### **List of Publications arising from the thesis Journal**

1. “Time evolution studies of laser induced chemical changes in InAs nanowire using Raman spectroscopy”,

Suparna Pal, R. Aggarwal, **Vandna K Gupta**, Alka A Ingale; **Appl. Phys. Lett.** **105**, 012110 (2014).

2. “Spatially resolved Raman spectroscopy study of uniform and tapered InAs micro-nano wires: correlation of strain and polytypism”

**Vandna K Gupta**, Alka A Ingale, Suparna Pal, R. Aggarwal and, V. Sathe; **J. Raman Spectroscopy** **48**, 855 (2017).

3. “Predicting surface modification of InAs nanowires on laser irradiation using transient thermal simulation and time evolution of Raman spectra”

**Vandna K Gupta**, Alka A Ingale, Vikas Jain, R. Aggarwal and S. Pal; **J. Alloys and Compounds** **735**, 1331 (2018).

4. “Understanding effect of nanowire orientation on time evolution of Raman spectra from laser irradiated InAs nanowire surface.

**Vandna K Gupta**, Alka A Ingale, Arnab Bhattacharya, Mahesh Gokhale, R. Aggarwal and Suparna Pal; **Nanotechnology** **42**, 29 (2018).

### **Conference proceedings:**

1. “Study of InAs nanowire structure using spatially resolved Raman spectroscopy”

**Vandna K Gupta**, Alka A Ingale, R. Aggarwal and Arnab Bhattacharya;

*62<sup>nd</sup> DAE-Solid state physics symposium (SSPS-2017)*

**AIP conference proc. 1832**, 050121 (2018).

2. “Study of Polytypism in InAs Nanowires using Resonance Raman Spectroscopy”

**Vandna K Gupta**, Alka A Ingale and Mahesh Ghokale;

*International conference on Nanotechnology: Ideas, Innovations & Initiatives- 2017*

**Material Today proc. 1069** 132 (2017).

**I DEDICATED THIS THESIS TO**  
**MY FAMILY AND HUSBAND**

# Acknowledgment

First of all, I would like to thank God for the blessings showered on me, which has enabled me to acknowledge all the people who helped me in one way or the other during of my research work. When I look back, I realize that there are many people who deserve special mention for making the time spent during my Ph.D. in the institute a period, I will cherish all my life.

It is my great honor and privilege to express my deep sense of gratitude towards my Ph.D. guide Dr. Alka A. Ingale, at the successful completion of this thesis work. I cannot find words to express my feelings. At every step of my research she encouraged me to be a better physicist as well as a better person. She has always inspired me with her enthusiastic attitude towards science and life. She has helped me to develop my experimental skills and gave me the direction of thinking at a very basic level. She has given me a lot of her invaluable time for discussion. Each meeting with her added invaluable aspects to the implementation of ideas, which has broadened my perspective. I thank her for guiding my thesis work and the willingness to share her knowledge and experience. Her profound practical skills, immense knowledge and critical but valuable remarks led me to do a good research. I am greatly indebted to her for her support, trust, guidance and encouragement throughout these years. She pushed me to work on my weaknesses and exploit my strengths. She owns a great quality to sort out the experimental difficulties with many excellent ideas that eventually helped me in reaching the targets. There were times, when I was not happy about my research life, she helped me to come out of those situations. She has taught me the way to deal with problems, whether it is professional or personal. She has a great ability to keep the person motivated. She has also been very helpful to me during my sickness, which I cannot forget in lifetime. I will always remember her and thank her at every step of my career.

I would like to thank to Dr. Suparna Pal for helping me in the initial stages of my research work. She has introduced me to literature survey and preparing presentations. I greatly appreciate the encouragement provided by her in the initial stage of my Ph.D. work.

I am very grateful to Mr. Rahul Aggarwal for the support provided while working in the Raman labs from time to time. He has always given me time from his busy schedule while working for his own Ph.D. and looking after the labs. I greatly appreciate his selflessness, which created a positive working atmosphere in the group. This encouraged me in performing my research work successfully. He has generously shared his understanding of Raman spectroscopy with me on various occasions i.e. whenever, I was stuck in either doing the measurements or in understanding of theory. I am very thankful to him for his generosity.

I will specially like to mention how lucky, I am to have a senior like Dr. Ekta Rani. I am very thankful to her for teaching me how to perform Raman spectroscopy and atomic force microscopy measurements on SPM-integrated Raman system. Discussion with her has always increased my self-confidence and I am indebted to her for encouraging me to continue my research work. Her help in reading of my first drafts of manuscripts, while she was working in the lab and patiently teaching me fitting of Raman data, are greatly appreciated. I am eternally grateful for her support, love and care bestowed on me at all stages of my Ph.D.

I am thankful to Mr. Chandrasekhar for experimental help in using triple stage Raman system. He is always ready to help in the experimental work and thus makes our life easier. His support in performing Resonance Raman experiments are greatly appreciated. He has been a great support system during my Ph.D. and I am very grateful to him for that.

I am extremely thankful to Dr. Vikas Jain in the help provided in understanding of FEM analysis using ANSYS for temperature simulation in 3D geometry. I greatly appreciate and is thankful for the valuable time he has given me, while he was here (RRCAT) and also while he was abroad for his postdoc. Every discussion with him has not only helped me in

simulation experiment, but also gave me encouragement for my work. His positive approach is greatly appreciated and I am thankful to him for checking discussion on simulation in the manuscript and thesis.

I am also thankful to Dr. Suparna Pal and Dr. Arnab Bhattacharya (T.I.F.R., Mumbai) for providing InAs nanowire samples. I am thankful to Dr. V. K. Dixit, Dr. T. K. Sharma and Dr. S. D. Singh for the growth of InAs NWs using MOCVD at RRCAT and Mr. Mahesh Ghokhale at T.I.F.R., Mumbai. I am grateful to Dr. T. K. Sharma and Dr. V. K. Dixit for their constant encouragement and support during my Ph.D.

I thank Dr. V. Sathe, UGC-DAE CSR Indore for allowing temperature dependent Raman measurements. I am also thankful to Mr. Ajay Kumar Rathore, UGC-DAE CSR, Indore for performing the temperature dependent Raman measurements.

I thank to Mr. Vijay Bhardwaj for introducing me to the simulation in 2D geometry using ANSYS. I would like to thank Mr. M. K. Singh, Smt. Rashmi Singh and Dr. D. M. Phase for SEM measurements at RRCAT and UGC-DAE CSR, Indore, respectively. Thanks are due to Mrs. Sushmita Bhartiya for teaching me sample preparation for SEM measurements. The support of the scientific computing group, Computer Centre, RRCAT, is acknowledged. I thank Smt. Sapana Rege for the help provided in the LPAS office during the Ph.D. I thank to Dr. A. K. Srivastava and Dr. Himanshu Srivastava for TEM measurements. I specially thank Dr. Himanshu Srivastava for painstakingly performing HRTEM and SAED with in situ thermal annealing of nanowires and teaching me analysis of this data.

I am thankful to Dr. H. S. Rawat, Dr. P. K. Gupta, Dr. S. K. Deb, Dr. P. A. Naik, Dr. G. S. Lodha, and Dr. Tapas Ganguli for their support during my Ph.D. I wish to thank Dr. P. D. Gupta, Director RRCAT for his continual support provided to me during my Ph.D.

I am very grateful to Dr. D. K. Aswal and Dr. G. Ravi Kumar (External members) for their encouragement and positive feedback during my yearly, pre-synopsis and viva-voce

presentations. I greatly appreciate all the members of doctoral committees, who have given their valuable time and feedback.

\*I am thankful to Prof. Ravikant Soni, IIT Delhi, India and Prof. O. Pages, University of Lorraine, France for careful and patient reading and evaluation of the Ph.D. thesis.

My time at RRCAT was made enjoyable in large part due to my batch-mates and friends who had become a part of my life. We had valuable research discussions and together enjoyed small picnics, sports and parties. I thank Dr. Aparna Chakraborty for inviting us for dinner on several occasions at her home, which helped us come together.

Above all, it would have not been possible for me to achieve this milestone in my career without encouragement and support from my parental family members as well as my in laws. Last and most important, I must mention that I greatly value the support and encouragement provided by my husband to complete my Ph.D. after the marriage.

\*: I am thankful to Dr. S R Mishra for his continual support during my Ph.D. His encouraging words and his moral support in times of need are greatly appreciated.

# CONTENTS

<b>CONTENTS</b> .....	<b>i</b>
<b>SYNOPSIS</b> .....	<b>vi</b>
<b>LIST OF FIGURES</b> .....	<b>xvii</b>
<b>LIST OF TABLES</b> .....	<b>xxx</b>
<b>CHAPTER -1: INTRODUCTION</b> .....	<b>1</b>
1.1 History of semiconductors.....	2
1.1.1. Application of semiconductors and recent trends.....	4
1.1.2. History of nanostructures.....	5
1.2 Nanostructures.....	7
1.2.1. Classification of nanostructures (2D, 1D, 0D) .....	7
1.2.2. Properties and applications of semiconductor nanostructures.....	8
1.3 Properties and applications of 1D semiconductor nanostructures.....	10
1.3.1 Physical properties.....	10
1.3.2 Chemical properties.....	10
1.3.3 Optoelectronic properties.....	10
1.3.4 Magnetic properties .....	11
1.3.5 Thermal properties.....	12
1.3.6 Electrical properties.....	13
1.3.7 Mechanical properties.....	13
1.4. III-V semiconductor nanowires.....	14
1.5. Raman spectroscopy.....	15
1.5.1. Spatially resolved Raman spectroscopy.....	15
1.6. Aim of the thesis.....	15

**CHAPTER – 2: EXPERIMENTAL TECHNIQUES.....18**

2.1. Introduction..... 19

2.2 Raman spectroscopy..... 19

    2.2.1 Quantum theory of Raman scattering.....20

    2.2.2 Stokes and anti-Stoke Raman scattering.....25

    2.2.3 Raman selection rules.....26

2.3. Instrumentation.....27

    2.3.1 Light source: laser.....27

    2.3.2. Filter: Spectrometer/spectrograph.....28

    2.3.1 Detector: Charged-coupled device (CCD).....29

2.4. Micro-Raman spectroscopy.....30

    2.4.1 Resolution.....33

    2.4.2 Polarized Raman spectroscopy.....34

    2.4.3 Temperature dependent Raman Spectroscopy.....34

    2.4.4 Wavelength dependent Raman Spectroscopy.....35

2.5 Atomic force microscopy (AFM).....35

2.6 Electron microscopy.....38

    2.6.1 Scanning electron microscopy (SEM).....38

    2.6.2 Transmission electron microscopy (TEM).....39

**CHAPTER-3: TIME EVOLUTION STUDIES OF LASER INDUCED  
CHEMICAL CHANGES IN InAs NANOWIRE .....43**

3.1. Introduction.....44

3.2. Systematic study of Time evolution of Raman spectra on laser irradiation of InAs NWs.....	49
3.2.1. Experimental.....	49
3.2.2 Systematic laser power dependence study of surface modification on laser irradiation .....	50
3.2.3. Time evolution of Raman spectra under different ambient conditions.....	62
3.3. Conclusion.....	66

## **CHAPTER-4: CORRLATION OF STRAIN AND POLYTYPISM IN InAs**

<b>NANOWIRE.....</b>	<b>69</b>
4.1. Introduction.....	70
4.2 Spatially resolved Raman spectroscopy study of InAs MNWs and spheres/Si (001).....	71
4.2.1 Uniform diameter NW.....	72
4.2.2 Bent NWs.....	74
4.2.3 Tapered micro-nanowires (MNWs).....	76
4.2.4 Sphere.....	77
4.3 Understanding red and blue shift in SRR of InAs MNWs.....	78
4.3.1 Growth mapping studies of InAs NWs reported in literature.....	79
4.3.2 Understanding correlation of strain and polytypism in InAs NWs.....	81
4.3.2.1 Understanding polytypism in InAs MNWs.....	81
4.3.2.2 Confirmation of polytypism using Polarized Raman spectroscopy.....	84
4.3.2.3 Diameter dependence of polytypism in InAs NWs.....	90
4.3.2.4 Wavelength dependent Raman spectroscopy.....	94
4.3.2.5 Correlation of strain and polytypism in InAs MNWs.....	95
4.4 Effect of strain on temperature dependent properties of InAs NWs.....	98

4.4.1 Spatially resolved Temperature dependent Raman study: Effect of polytypism.....	98
4.4.2 Calculation of effective Thermal expansion for WZ structure.....	105
4.5. Revisiting Raman spectra of bent MNWs.....	107
4.6. Conclusions.....	109

**CHAPTER – 5: UNDERSTANDING THERMAL OXIDATION OF InAs MICRO-NANOWIRES ON LASER IRRADIATION, USING SIMULATED TEMPERATURE.....111**

5.1 Introduction.....	112
5.2 Theory of temperature simulation.....	115
5.2.1 Convergence check for meshing sizes and choice of other parameters for temperature simulation.....	116
5.2.1.1 2D geometry.....	118
5.2.1.2 3D geometry.....	119
5.3 Corroboration of time evolution Raman spectra with simulated temperature.....	126
5.4 General applicability of this methodology.....	137
5.4.1 Application to different diameter NWs and same aspect ratio.....	137
5.4.2 Application to NWs with very different diameter and aspect ratio.....	138
5.5 Conclusion.....	142

**CHAPTER-6: UNDERSTANDING EFFECT OF NW ORIENTATION ON TIME EVOLUTION OF RAMAN SPECTRA FROM LASER IRRADIATED InAs NWs.....145**

6.1 Introduction.....	146
6.2 Raman spectra of differently oriented InAs NWs.....	147
6.2.1 Differences in time evolution of unpoalrized Raman spectra from in-plane horizontally and vertically oriented NWs.....	148
6.2.2 Polarized Raman spectroscopy.....	155
6.2.3 Two-step polarized Raman spectroscopy.....	159
6.2.4 Heating–cooling experiment: monitored by Raman spectroscopy.....	163
6.3 Application of Resonance Raman spectroscopy to study polytypism.....	168
6.3.1 Resonance Raman spectroscopy for investigation of InAs NWs with diameter <600 nm.....	172
6.3.2 Investigation of conversion of wurtzite to zinblende phase on laser irradiation using Resonance Raman spectroscopy .....	174
6.3.3 Investigation of conversion of wurtzite to zinblende phase using transmission electron microscopy on thermal annealing.....	176
6.4 Conclusion.....	182
<b>CHAPTER -7: CONCLUSION.....</b>	<b>185</b>
<b>ANNEXURE.....</b>	<b>193</b>
<b>BIBLIOGRAPHY.....</b>	<b>196</b>

# **SYNOPSIS**

Nanoscience and nanotechnology has been the frontline research area for last two decades. Nanoscience has shown intensive growth in both new methods of synthesis along with advancement of characterization methods for the nanostructures [1-2]. It is now a well-established field owing to uniqueness of chemistry and physics (energetics and dynamics) of these nanomaterials [3]. One dimensional nanostructures, nanowires (NWs) show remarkable properties like large mechanical strength, large electrical conductivity, lower thermal conductivity, high fractural damage threshold, large functional surface area etc., which are useful in variety of applications ranging from optoelectronics, thermo-electrics to chemical sensors [4-5]. InAs, a III-V semiconductor material has high electron mobility and is considered a potential candidate for high-speed electronics in addition to infrared detectors [6-7]. Residual strain free, NW geometry has several advantages and is expected to lead to higher speed electronics [3]. For realizing new devices and technologies from these NWs, fundamental understanding of these nanostructures and thereby suitable control of the properties is required and this is the motivation of this thesis work.

*Thus, the motivation of this thesis work is to study individual InAs nanowires using Raman spectroscopy.* The damage and time evolution of Raman spectra was observed during Raman mapping of a long InAs NW (dia  $\sim 1 \mu\text{m}$ ,  $L \sim 40 \mu\text{m}$ ). To understand time evolution of Raman spectra, systematic investigation of this effect is performed using various laser power densities (LPDs: 30-800 kW/cm<sup>2</sup>). Three different LPD regions were identified on the basis of observed Raman spectra, wherein i) No oxidation ii) low, intermediate and higher level of oxidation occurred and iii) At highest power, oscillatory behavior of the presence of Arsenic on evaporation and generation of Arsenic is observed. In the next chapter the observed redshift of transverse optical (TO) phonon frequency from that of bulk InAs value is investigated using spatially resolved Raman spectroscopy of various types of NWs

observed in the sample. The redshift in TO phonon frequency is found to be due to the presence of polytypism i.e. presence of both Zincblende (ZB) and Wurtzite (WZ) phases in InAs NW. With the above understanding, different types of thermal oxidation processes of InAs NW on laser irradiation are identified corresponding to simulated temperature. Predictability of oxidation processes is further checked with different set of NWs to confirm general applicability of the methodology for its use in predicting and or controlling surface modification of InAs NWs using laser irradiation. During this work, it was noted that differently oriented NWs gives rise to different time evolution of Raman spectra with similar LPD's i.e. at similar simulated temperatures. Investigation of the effect of orientation on unpolarized Raman spectra revealed that the difference in the spectra is due to formation of oriented crystalline oxides.

In summary, Raman spectroscopy study of individual InAs NWs grown on Si (001) and (111) using metal organic chemical vapor deposition (MOCVD) is presented in this thesis. The systematic laser irradiation studies showed formation of metastable oxide states which decomposes at high temperatures to form elemental As allotropes. Simulated temperature is successfully used to predict and obtain desired oxidation processes for randomly chosen NWs. The strain observed in these NWs is attributed to the presence of polytypism. One dimensional nanostructures show very different Raman spectra for same simulated temperature, when oriented differently, owing to the formation of oriented crystalline oxides.

In the following, study presented in each chapter is discussed in brief.

## **Chapter 1: Introduction**

In this chapter, the brief history of semiconductors is described with emphasis on III-V semiconductors used in many applications like, optoelectronic devices, MOSFET, photovoltaics and detectors. Further, recent trends in semiconductor nanotechnologies are described along with classification of nanostructures into 0D, 1D and 2D. Importance of one dimensional InAs nanostructures and use of Raman spectroscopy for study of InAs NWs is also discussed. The aim of the thesis work is presented as a natural conclusion of this chapter.

## **Chapter 2: Experimental techniques**

This chapter describes experimental techniques used for the study. Raman spectroscopy is the main research technique used for the thesis work and atomic force microscopy (AFM), Scanning electron microscopy (SEM) are used for morphology study of NWs. Various Raman spectroscopy set ups used for different types of work are described along with basic theory of Raman spectroscopy. The AFM and SEM used for study of morphology of NWs are also described in brief. Use of transmission electron spectroscopy (TEM) to support the understanding developed by Raman spectroscopy is also briefly discussed.

## **Chapter 3: Study of time evolution of Raman spectra of InAs nanowires on laser irradiation**

While Raman mapping of MOCVD grown InAs MNW (SPDL, RRCAT), it was found that it was getting easily damaged for very low power densities and further that time evolution of Raman spectra was observed during the experiment. To investigate this effect, systematic power dependent laser irradiation study using time evolution of Raman spectra is performed on InAs nanowire (dia:800 nm, length ~36  $\mu$ m). Time evolution over 8 to 16

minutes were studied for laser power densities (LPDs) in the range 30-800 kW/cm<sup>2</sup>. The three types of Raman spectra is observed in which, 1) LPD: 30- 90 kW/cm<sup>2</sup>: only TO and longitudinal optical (LO) phonons of InAs are observed 2) LPD: 100-500 kW/cm<sup>2</sup>: Additional modes in the range 180-200 and 240-260 cm<sup>-1</sup> are observed and 3) LPD: 600-800 kW/cm<sup>2</sup>: The intensity of elemental As mode ~ 257 cm<sup>-1</sup> shows oscillatory behavior in time, suggesting removal of As by evaporation and regeneration of As by oxidation of the next InAs layer. A mixture of three compounds i.e. crystalline InAsO<sub>4</sub>, As<sub>2</sub>O<sub>3</sub> and As is observed, where the concentration of each compound varies with time. First redshift and then blueshift of a peak in the range 240-250 cm<sup>-1</sup> (InAsO<sub>4</sub>) is attributed to formation of hydrous and anhydrous InAsO<sub>4</sub>, respectively from Raman spectroscopy experiments performed under different environment like water (wet) and Silica gel (dry).

The knowledge gained from this study can be used for position controlled laser induced chemical modification of a NW without affecting the core. To make this knowledge useful for NW based device fabrication, it is important to know the temperature at the surface of NW on laser irradiation and it's corroboration with Raman spectroscopy data. This is attempted in chapter 5.

It is important to note here that TO phonon frequency of studied NW (~214 cm<sup>-1</sup>) is redshifted with respect to that of bulk value (~ 217 cm<sup>-1</sup>) [9]. This redshift is the topic of investigation of the next chapter.

#### **Chapter 4: Spatially resolved Raman spectroscopy study of uniform and tapered InAs micro-nanowires: Correlation of strain and polytypism**

To understand origin of the redshift observed in TO phonon of a studied InAs NW, several NWs of different morphologies observed in the same sample of InAs/Si(001) are studied along the length using spatially resolved Raman spectroscopy (SRRS). The

asymmetric TO phonon peak in the range 212 - 218  $\text{cm}^{-1}$  is observed on uniform, bent and long tapered micro-nanowires (MNWs: diameter: 2  $\mu\text{m}$  – 400 nm) using SRRS. Considering various possibilities of this redshift, it is attributed to superposition of  $E_{2h}$  phonon (Wurtzite: WZ) and TO phonon (Zincblende: ZB) of InAs. Polarized and wavelength dependent SRRS establishes the presence of WZ and ZB phases in these MNWs. However, formation of WZ phase for larger diameter InAs MNWs studied is not commensurate with existing growth mapping studies [10]. Growth mapping studies of MOCVD grown InAs NWs reported in literature suggest MNWs of large diameter (500 nm - 2  $\mu\text{m}$ ) to have pure ZB structure. Further, study of these MNWs suggests that the fraction of WZ to ZB content in a MNW depends not only on the diameter, but also seems to be governed by local growth seeding/conditions. This in turn leads to either tapered or uniform MNW growth under the same growth conditions. The variation of these frequencies than that of bulk value is correlated to the residual strain in ZB and WZ phases due to the presence of the other (WZ/ZB) phase.

The strain was further investigated using spatially resolved temperature dependent Raman spectroscopy. Consistently, temperature dependent Raman data shows that there is a measurable contribution of stress to  $d\omega/dT$ , a positive for ZB and negative for WZ phonons, due to differences in their thermal expansions. Considering the hetero structure and knowing thermal expansion of ZB phase, effective thermal expansion of WZ is calculated to be in the range 10 - 19  $\times 10^{-6}$  / K from base to tip of a MNW at  $\sim 80$  K. Effective thermal expansion of WZ increases from base to tip consistent with increase in lattice constant of WZ i.e. relaxation of compressive stress from base to tip. The AFM, polarization and temperature dependent Raman spectroscopy is performed on the same wire.

In summary, presence of polytypism is attributed to be the reason of residual strain in these tapered and uniform MNWs. It is also observed that diameter alone does not

decide the residual strain/content ratio of WZ/ZB, but it may be related to local seeding conditions. Raman study of bent NWs show that sudden large change in diameter and thereby content ratio of WZ/ZB phase or vice-versa, generates further strain leading to sharp bends. Further, temperature dependent Raman spectroscopy is used, to evaluate the effect of strain on WZ and ZB phases of InAs.

## **Chapter 5: Simulation of temperature to understand thermal oxidation of InAs nanowires on laser irradiation using time evolution of Raman spectra**

For fine tuning of semiconductor nanowire properties, modification of surface and dimensions using laser irradiation is being suggested as one of the fast and easy to use methods. In this chapter, role of temperature simulation is investigated for understanding and thereby predicting surface modification of InAs nanowire (NW) using laser irradiation. The surface modification is monitored by Raman spectroscopy. We first establish correlation between simulated temperatures at the surface of a InAs nanowire (NW) with time evolution of Raman spectra, on laser irradiation. Transient thermal simulations are performed with ANSYS software using finite element method, considering 3D geometry of the irradiation setup. The oxidation processes are identified as weak reactions WP1, WP2, WP3, intermediate temperature reactions IP1, IP2 and higher temperature strong reactions as SP1, SP2, SP3 & SP4, using time evolution of Raman spectra at various LPDs. The predictability of the methodology was then investigated by applying it to random conditions of NW like diameter, aspect ratio and laser power density etc. for i) NWs found in the same sample and ii) InAs NWs grown elsewhere (DCMP&MS, T.I.F.R., Mumbai) \* and transferred on other Si substrate. One of the important result of this study is that reaching of steady state temperature and stabilization of Raman spectra (oxidation), both occurs in ~8 minutes. This further confirms the success of the methodology in predicting oxidation processes.

The study thus establishes predictability of various oxidation processes for given NW dimensions, laser power density and irradiation time, thereby ascertaining importance and applicability of the temperature simulation in controlling surface modification of randomly chosen InAs NWs using laser irradiation. This methodology can be used to control the oxidation process as desired for using NWs in device technology, where oxidation is used for creating an insulating layer.

The Raman data presented in this chapter is of the same geometry/orientation of NWs to avoid complications related to Raman scattering configuration. It is to be noted that very different Raman spectra are observed for orthogonally oriented NWs for similar LPDs, which is investigated further and makes the content of chapter-6.

## **Chapter 6: Understanding the effect of InAs nanowire orientations on time evolution of Raman spectra**

In this chapter, difference in Raman spectra of NWs oriented perpendicular/at  $45^\circ$  angle to each other for similar LPDs are investigated using polarized Raman spectroscopy. The distinctive differences are observed in Raman spectra taken on differently oriented NWs at same/similar LPDs with NWs of same/similar dimensions. Due to unavailability of old set of InAs NWs, new set of InAs NWs\* is used for following experiments to elucidate the difference observed in Raman spectra on NW orientation. Few NWs from this set are first tested for similar effect on laser irradiation before further investigation. The simulated temperature is considered to be better parameter for comparison of data and hence temperature is simulated for all the laser irradiation experiments performed. Various polarized Raman spectroscopy experiments were designed to understand origin of these differences. Raman selection rules for generated oxides is found to be the reason for the differences observed, which suggests that laser irradiation allows us to generate oriented

crystalline oxide film on InAs NW surface. Further, the blue shift of TO\*(combination mode of  $E_{2h}$  and TO phonons) phonon and reappearance of sharper TO\* and LO phonons at higher simulated temperature ( $> 1200$  K) are investigated using specially designed polarization and heating cooling experiments. The blueshift and reappearance of TO\* mode are attributed to i) The formation of specific allotrope of elemental As i.e. gray-As (rhombohedral) and black-As (orthorhombic), which are formed while cooling initiated on As evaporation from low and high temperatures, respectively, and ii) possibility of metamorphic growth of InAs/conversion from WZ to ZB phase. Resonance Raman spectroscopy is developed as an alternative method to study polytypism and is used to investigate the metamorphic growth/conversion to ZB phase at higher simulated temperatures. This effect is further investigated using TEM. Selected area electron diffraction (SAED) confirmed the ZB phase after thermal annealing of mixed and pure WZ phase InAs NWs.

To conclude, this study reveals that oriented crystalline oxides are formed on laser irradiation and chemical processes continue even after laser irradiation is stopped i.e. while cooling and further, heating history decides which allotrope of elemental As is formed as a byproduct.

## **Chapter 7: Conclusion**

The aim was to study individual InAs nanowires, which had very low density and hence could not be studied by conventional techniques. Raman spectroscopy is chosen as an experimental technique to study individual micro-nanowires for its specificity and possibility of good signal to noise ratio (Resonance enhancement) from InAs MNWs.

While Raman mapping of InAs MNW, it was found that it was getting easily damaged for very low laser power densities and further, time evolution of Raman spectra was observed during this study. Using systematic Laser power dependence, three different regions

were identified, i) oxides are not formed, ii)  $\text{InAsO}_4$ ,  $\text{As}_2\text{O}_3$  and As are formed and the composition of oxides vary with time and iii) oscillatory behavior of As peak with time due to evaporation and generation of As i.e. layer by layer removal of InAs.

The residual strain in InAs NWs is attributed to polytypism (WZ and ZB phase) using spatially resolved polarization, temperature and wavelength (resonance) dependent Raman spectroscopy. The study on several nanowires with different morphology further suggests that although, growth condition is same, difference in local growth conditions (seeding/nucleating sites) decides, if grown wire would be of uniform diameter/tapered and with what phase content i.e. WZ/ZB ratio.

For the controlled surface modification of NWs, it is essential to envisage the rise in the local temperature due to laser irradiation. Therefore, the local temperature is simulated by solving heat transfer equation numerically using finite element method using ANSYS software. Simulated temperature is corroborated with time evolution of Raman spectra for several NWs for several LPDs. The study establishes predictability of complicated oxidation processes for randomly chosen NW and LPDs and thus has potential to be extended for controlling surface modifications in other semiconductor NWs.

The difference in Raman spectra (unpolarized) between two nearly perpendicular orientations of InAs NWs for similar LPDs and NW dimensions is investigated using specially designed polarized Raman spectroscopy and heating cooling experiment. The study reveals that oxides formed are oriented and crystalline in nature. Further, at higher simulated temperatures elemental As is formed in Grey(stable) and black (Metastable) phase for simulated temperature  $> 900$  K and  $>1300$  K respectively. At higher simulated temperatures, Raman data is indicative of metamorphic growth of ZB InAs/conversion of WZ phase to ZB phase. This is confirmed using Resonance Raman spectroscopy and TEM.

Future plan of work includes, study of the WZ to ZB conversion process with thermal annealing using Raman spectroscopy. Further, it is planned to extend simulation of temperature for different geometry of NWs and spheres on laser irradiation and while cooling.

### References:

- [1] J. Jortner and C. N. R. Rao, *Pure Appl. Chem.* **74**, 1491 (2002).
- [2] Y. Gogotsi, “Nanomaterial handbook” Taylor & Francis group (2006).
- [3] C. K. Chan, H. Peng, G. Liu, K. Mcilwrath, X. F. Zhang, R. A. Huggins and Y. Cui, *Nat nanotechnol.* **3**, 37 (2011).
- [4] S. A. Dayeh, D. P. R. Aplin, X. Zhou, P. K. L. Yu, E. T. Yu, and D. Wang, *Small* **3**, 326 (2007).
- [5] Y. Tian, M. R. Sakr, J. M. Kinder, D. Liang, M. J. MacDonald, R. L. J. Qiu, H.-J. Gao, Xuan, P. A. Gao, *Nano Lett.* **12**, 6492 (2012).
- [6] E. Comini, and G. Sberveglieri, *Materials Today* **13**, 37 (2010).
- [7] S. A. Dayeh, *Semicond. Sci. Technol.* **25**, 024004 (2010).
- [8] W. Wei, X-Y. Bao, C. Soci, Y. Ding, Z- L. Wang, and D. Wang, *Nano Lett.* **9**, 2926 (2009).
- [9] R. Caries, N. Saint-Cricq, J. B. Renucci, M. A. Renucci, and A. Zwick, *Phys. Rev. B* **22** 4804 (1980).
- [10] K. A. Dick, J. Bolinsson, M. E. Messing, S. Lehmann, J. Johansson, and P. Caroff, *J. Vac. Sci. Technol. B* **29**, 04D103 (2011).

**List of Figures:**

**Figure 2.4.1:** Alpha 300 S\_SPM integrated Raman system (Acton 2500i (single), WiTec) set up showing different parts .....30

**Figure 2.4.2:** Enlarged view of (a), (b) microscope, and spectrometer shows different components, respectively as noted in the figure, TW LCU: two way light coupling unit and (c) Enlarged view of lasers.....31

**Figure 2.4.3:** (a) Front view of microscope with different components i.e. SLB: scattered laser blocker, TW LCU: two way light coupling unit, (b) enlarge view of triple stage spectrometer and CCD, BP: beam path: TS: triple stage and SS: single stage (c) Enlarged view laser.....31

**Fig. 2.4.4:** (a) “Trivista 557”(S & I spectroscopy and imaging) Raman system set up showing different parts as noted in the figure i.e. MC: monochromator, OP1: optical assemble 1 (line filter, half wave plate, mirrors etc.), I/P to MS: input to microscope, OP2: optical assembly 2 (45° mirror, ND filter and beam splitter etc.) and O/P: output. \*: pre-monochromator and coupling lenses are not in beam path.....32

**Figure 2.5.1:** Graph between force experience by tip v/s its distance from the sample surface .....36

**Figure 2.5.2:** Schematic diagram of AFM.....36

**Figure 2.5.3:** (a), (b) and (c) Showing AFM image of uniform, tapered and bent NW, respectively at 50 nm resolution.....37

**Figure 2.6.1:** (a) Showing SEM image of InAs NWs (b), (c) and (d) with uniform, bent and tapered InAs NW, respectively at 18 A<sup>0</sup> resolution.....39

**Figure 2.6.2:** (a) and (b) TEM image of uniform and tapered NWs at 2A<sup>0</sup> resolution.....40

**Figure 3.1.1.1:** (a) Optical image of InAs sphere b) Raman mapping generated by taking intensity from 215-220  $\text{cm}^{-1}$  and c) Raman spectra at position 1, 2 and 3 which are marked in the Raman image. ....46

**Figure 3.1.1.2:** (a) Generated Raman image of InAs MNW to take the intensity from 210-220  $\text{cm}^{-1}$  inset Fig show optical image of InAs NW before Raman imaging and b) Raman spectra for marked positions on the Raman image.....46

**Figure 3.1.1.3:** (a) Optical image of InAs MNW after Raman mapping and (b) Raman spectra which are taken at position marked in optical image. ....47

**Figure 3.1.1.4:** (a) Raman image generated using intensity of phonon in the range of 150-300  $\text{cm}^{-1}$ , inset shows the optical images of InAs MNW before and after Raman mapping b) Raman spectra for marked positions 1-9 in MNW image. ....48

**Figure 3.1.1.5:** a) Optical image of InAs MNW after Raman mapping b) Corresponding time dependent Raman spectra.....48

**Figure 3.2.2.1:** (a) Time evolution of Raman spectra of the InAs NW (image shown in the inset) from T1 (10s) to T6 (500s), showing top and bottom 6 spectra at LPD  $\sim$  30 and 100  $\text{kW}/\text{cm}^2$ , respectively and b) Time evolution of Raman spectra from T1 (10s) to T12 (500s) at LPD  $\sim$  140  $\text{kW}/\text{cm}^2$ .....51

**Figure 3.2.2.2:** Time evolution of Raman spectra of the InAs NW from T1 (10s) to T12 (500s) at LPD  $\sim$  200  $\text{kW}/\text{cm}^2$  .....52

**Figure 3.2.2.3.** (a) and (b) time evolution of Raman spectra of the InAs NW(image shown in the inset) from T1 (10s) to T12 (500s) at LPD  $\sim$  200 and 250  $\text{kW}/\text{cm}^2$ , respectively .....53

**Figure 3.2.2.4:** (a) and (b) Time evolution of Raman spectra of the InAs NW (image shown in the inset) from T1 (10s) to T12 (500s) at LPD  $\sim$  300 and 350  $\text{kW}/\text{cm}^2$ , respectively .....54

**Figure 3.2.2.5:** (a) Raman spectra of the time series from T1 (10s)-T12 (500s) At LPD  $\sim$  450  $\text{kW}/\text{cm}^2$  and (b) Deconvoluted Raman spectra showing the time evolution of the peaks in the

range of 180-200, 240-258  $\text{cm}^{-1}$  from T1(10s) to T5(500s). Cumulative fit (red solid line) to the raw data (+) and separate Lorentzian fits are shown with blue solid line.....55

**Figure 3.2.2.6:** Time evolution of Raman spectra of InAs NW at the incident laser (488 nm) power density of 900  $\text{kW}/\text{cm}^2$ . (b) Optical image after laser irradiation and (c) variation of intensity of As mode with time. ....61

**Figure 3.2.3.1:** (a) Raman spectra at whole time series from T1(10s)-T16(500s) at LPD  $\sim$  254  $\text{kW}/\text{cm}^2$ , (b) Optical image of InAs NW and (c) Raman spectra from range  $\sim$  150-500  $\text{cm}^{-1}$  at T1(10s).....63

**Figure 3.2.3.2:** Raman spectra from T1 (10s) to T9 (500s) at ambient condition with 488 nm excitation at 200  $\text{kW}/\text{cm}^2$  and inset show the optical image of NW (d  $\sim$  1  $\mu\text{m}$  and l $\sim$  20  $\mu\text{m}$ )..... 65

**Figure 3.2.3.3:** (a) and (b) Raman spectra from T1 to T12 and T7 in water and in silica gel environment with 442 and 488 nm excitation at 450 and 400  $\text{kW}/\text{cm}^2$ , respectively.....66

**Figure 4.2.1.1:** (a) Optical image of uniform InAs MNW (dia  $\sim$  1.2  $\mu\text{m}$ ) and (b) Spatially resolved Raman spectra (SRRS) at positions (1-5) as marked in the optical image.....73

**Figure 4.2.1.2:** SRR spectra at positions (1-3) as marked in the optical image, which is shown inset (InAs NW: dia  $\sim$  0.8  $\mu\text{m}$ ).....73

**Figure 4.2.2.1:** (a) Optical image of sharp bent tapered MNW (base dia  $\sim$  1.3  $\mu\text{m}$  and tip  $\sim$  400 nm, b) SRR spectra at positions (1-7) as marked in the optical image.....74

**Figure 4.2.2.2:** (a) Optical image of smooth bent tapered MNW (base dia  $\sim$  800 nm and tip  $\sim$  400 nm) and (b) SRRS at positions (1-8) as marked in the optical image. ....75

**Figure 4.2.3:** (a) Optical image of straight tapered MNW, wherein objective is focused near the base (dia  $\sim$  2  $\mu\text{m}$ ), (b) Optical image of same wire, wherein objective is focused at the tip ( $\sim$ 400 nm) and (c) SRRS at positions (1-8) as marked in both optical images.....76

**Figure 4.2.4:** a) Optical image of sphere, b) SRRS at position 1-4 and c) Cumulative fit (red solid line) to the raw data ( + ) and separate Lorentzian fits are shown with blue solid line.....78

**Figure 4.3.2.1.1:** (a) and (b) SRR spectra at positions (2-5) as marked in the optical image (Fig.4.2.1.1a). Inset of Fig.4.3.1.1a shows Raman spectrum for position 1 marked in the optical image (Fig.4.2.1.1a). Cumulative fit (red solid line) to the raw data ( + ) and separate Lorentzian fits are shown with blue solid line.....82

**Figure 4.3.2.1.2:** SRRS at positions (1-6) as marked in both optical images (4.2.3.1a and b). Cumulative fit (red solid line) to the raw data ( + ) and separate Lorentzian fits are shown with blue solid line.....83

**Figure 4.3.2.2.1:** Schematic diagram of the Raman scattering configuration w.r.t. NW axis taken to be in Z direction for back scattering geometry. x and x axes are the incident and scattering polarization. Z-axis is taken to be [111] and [0001] for ZB and WZ phases, respectively.....84

**Figure 4.3.2.2.2:** (a) Optical image of uniform wire (dia ~ 600 nm) a) in horizontal direction, (b) in vertical direction and c) Polarized Raman data in  $x(z,z)\bar{x}$  and  $x(y,y)\bar{x}$  configuration at positions as marked in optical image (a) and (b), respectively. Cumulative fit (red solid line) to the raw data ( + ) and separate Lorentzian compartments are shown with blue solid line...87

**Figure 4.3.2.2.3:** (a) Optical image shows tapered MNW (base dia ~ 2  $\mu\text{m}$  and center dia ~ 1.6  $\mu\text{m}$  and tip ~ 800 nm), (b) unpolarized Raman data at position marked for base, center and tip, (c), (d) and (e) Polarized Raman data for base center and tip position, respectively in  $x(z,z)\bar{x}$  and  $x(y,y)\bar{x}$  configuration. Cumulative fit (red solid line) to the raw data ( + ) and separate Lorentzian fits are shown with blue solid line.....89

**Figure 4.3.2.3.1:** Shows diameter v/s frequency for 6 Tapered MNWs (TW1-6: Table-II). Here cross (X) and Plus (+) represent TO and  $E_{2h}$  phonon for TW 1-6, respectively.....90

**Figure 4.3.2.3.2:** (a) and (b) Cumulative fit (red solid line) to the raw data (+) and separate Lorentzian fits are shown with blue solid line for TW 1,5,2,6 at base and center and 1,3,5,6. For center and tip position, respectively. ....92

**Figure 4.3.2.3.3:** (a) Cumulative fit (red solid line) to the raw data (+) and separate Lorentzian fits are shown with blue solid line for TW 1,2 and b) Shows diameter v/s frequency for 3 uniform wires. Symbols (X) and (+) show  $E_{2h}$  and TO, respectively.....93

**Figure 4.3.2.4:** (a) and (b) Polarized Raman data performed with 488 nm and 442 nm excitation, respectively at same wire and at similar position in  $x(z,z)\bar{x}$  and  $x(y,y)\bar{x}$  configuration for uniform wire (dia  $\sim 1.2 \mu\text{m}$ ). Cumulative fit (red solid line) to the raw data (+) and separate Lorentzian compartments are shown with blue solid line.....95

**Figure 4.4.1.1:** (a) Optical image of InAs MNW. Frequency v/s temperature plot showing linear fit for TO and LO frequency for (b) sphere and (c) base position. The Error bar corresponds to the standard error to  $\omega$  as obtained from nonlinear least square fir to the spectra. The solid line are the best fit to the data points, from which slope are calculated in Fig. (b) and (c).....99

**Figure 4.4.1.2:** a) The AFM image of InAs MNW. b), c) and d) The temperature dependent Raman spectra in the temperature range 300K to 80K for base ( $\sim 2 \mu\text{m}$ ), center ( $\sim 1.6 \mu\text{m}$ ) and tip ( $\sim 800 \text{ nm}$ ) position, respectively. Cumulative fit (red solid line) to the raw data (+) and separate Lorentzian fits are shown with blue solid line.....99

**Figure 4.4.1.3:** Frequency v/s temperature plot showing linear fit for TO, LO and  $E_{2h}$  frequency s for d) base, e) center and f) tip position. The Error bar corresponds to the standard error to  $\omega$  as obtained from nonlinear least square fir to the spectra. The solid line are the best fit to the data points, from which slope are calculated in fig. d)-f).....101

**Fig. 4.4.1.4:** (a) The temperature dependent Raman spectra in the temperature range 300K to 80K for uniform wire (dia  $\sim 500 \text{ nm}$ ). Cumulative fit (red solid line) to the raw data (+) and

separate Lorentzian fits are shown with blue solid line and b) Frequency  $\nu$ /s temperature plot showing linear fit for TO, LO and  $E_{2h}$  frequencies for uniform wire. The solid line are the best fit to the data points.....102

**Figure 4.4.2:** Schematic diagram showing effect of difference in thermal expansion on generation of strain when, a) the ZB is taken as a substrate and WZ is taken as a layer and b) the WZ is taken as a substrate and ZB is taken as a layer.....107

**Figure 4.5:** a) SRR spectra at positions (1-7) as marked in the optical image (Fig. 4.2.2.1a), b) SRRS at positions (1-8) as marked in the optical image (Fig. 4.2.2.1a). Cumulative fit (red solid line) to the raw data ( + ) and separate Lorentzian fits are shown with blue solid line.....108

**Figure 5.2.1:** Raman spectra at 200s at laser power density (LPD)  $\sim 200$  kW/cm<sup>2</sup>. Cumulative fit (red solid line) to the raw data ( + ) and separate Lorentzian fits are shown with blue solid line.....117

**Figure 5.2.1.1:** (a) The blue color is showing temperature profile of Si substrate, (b) Cyne color is showing temperature profile of InAs NW and (c) Zoom image of temperature profile of InAs NW.....118

**Figure 5.2.1.2.1:** 3D Schematic of InAs nanowire with Gaussian laser spot with penetration depth  $\sim 22$  nm on Si substrate with 5 nm SiO<sub>2</sub> layer. All dimensions are in  $\mu$ m.....119

**Figure 5.2.1.2.2:** Meshing size convergence graph for a) laser spot b) Si Substrate (SiS) and c) InAs NW.....121

**Figure 5.2.1.2.3:** (a) Graph between temperature and laser irradiation time and b) temperature and meshing size of NW.....121

**Figure 5.2.1.2.4:** (a) 3D temperature profile view for InAs nanowire (NW:  $d \sim 800$  nm,  $L \sim 36\mu$ m) on Si substrate, (b) and (c) The front and side tilted view of temperature profile, respectively.....122

**Figure 5.2.1.2.5:** (a) Graph between temperature and laser irradiation time.....123

**Figure 5.2.1.2.6:** Graph between temperature and (a) laser irradiation time and (b) number of step, respectively.....125

**Figure 5.2.2.2:** (a) and (b) Simulated temperature at the surface of InAs (center of laser spot) as a function of irradiation time for laser power density  $\sim 200 \text{ kW/cm}^2$  and  $636 \text{ kW/cm}^2$  for 12 % elemental contact area, respectively. Right inset shows simulated temperature under same conditions with perfect contact.....125

**Figure 5.3.1:** a) Raman spectra along with simulated temperature (a) Time evolution using 488nm laser irradiation of D1 with laser power density (LPD)  $\sim 100 \text{ kW/cm}^2$ , b) for LPD  $\sim 200 \text{ kW/cm}^2$ , c) for LPD  $\sim 254 \text{ kW/cm}^2$  and d) for LPD  $\sim 445 \text{ kW/cm}^2$ . Cumulative fit (red solid line) to the raw data ( + ) and separate Lorentzian fits are shown with blue solid line.....129

**Figure 5.3.2:** Raman spectra along with simulated temperature (a), (b), (c) and (d) For irradiation time of 10s, 200s, 300s and 500s, respectively at all discrete LPDs from  $100 \text{ kW/cm}^2$  to  $636 \text{ kW/cm}^2$ . Cumulative fit (red solid line) to the raw data ( + ) and separate Lorentzian fits are shown with blue solid line.....131

**Figure 5.3.3:** Consolidation of time evolution of simulated temperature and various oxidation processes as a function of LPDs for a NW (D1)..... 133

**Figure 5.3.4:** Raman spectra along with simulated temperature (a) Time evolution using 488nm laser irradiation of D1 with laser power density (LPD)  $\sim 573 \text{ kW/cm}^2$  and (b) for LPD  $\sim 636 \text{ kW/cm}^2$ . Cumulative fit (red solid line) to the raw data ( + ) and separate Lorentzian fits are shown with blue solid line. ....134

**Figure 5.3.5:** Raman spectra along with simulated temperature (a) top and down three time evolution using 488nm laser irradiation of D1 with laser power density (LPD)  $\sim 573$  and  $300$

kW/cm<sup>2</sup>, respectively. Cumulative fit (red solid line) to the raw data ( + ) and separate Lorentzian fits are shown with blue solid line.....136

**Figure 5.4.1:** Raman spectra along with simulated temperature (a) and (b) Time evolution for 488nm laser irradiation with laser power density (LPD) ~200 and 254 kW/cm<sup>2</sup>, respectively for irradiation time of 10s, 100s, 300s and 500s. Cumulative fit (red solid line) to the raw data ( + ) and separate Lorentzian fits are shown with blue solid line.....138

**Figure 5.4.2.1:** Raman spectra along with simulated temperature for D3 InAs NW (optical image: inset, d ~ 900 nm and l ~ 8 μm) (a) and (b)Time evolution for 488nm laser irradiation with laser power density (LPD) ~764 and 900 kW/cm<sup>2</sup>, respectively. Cumulative fit (red solid line) to the raw data ( + ) and separate Lorentzian fits are shown with blue solid line.....139

**Figure 5.4.2.2:** Consolidation of simulated temperature for different NWs at 10s as a function of LPDs.....140

**Figure 5.4.2.3:** For two different nanowires with dia ~200 nm and length ~5 μm, grown elsewhere and transferred on the Other Si substrate for different LPDs at 90s. Cumulative fit (red solid line) to the raw data ( + ) and separate Lorentzian fits are shown with blue solid line.....141

**Figure 6.2.1.1:** (a) and (b) show optical images of InAs NWs D1 and D2 oriented in-plane horizontally (H) and nearly vertically (V) on Si substrate, respectively. (c), (d) and (e) show time evolution of Raman spectra for 20s, 210s and 480s in which top three Raman spectra are for D1 and bottom three Raman spectra for D2. Cumulative fit (red solid line) to the raw data ( + ) and separate Lorentzian fits are shown with blue solid line.....150

**Figure 6.2.1.2:** (a) show optical images of InAs NW for D3 (inset) and D4 oriented in-plane horizontally (H) and nearly vertically (V) on Si substrate. (b) Show time evolution of Raman spectra for 200s and 500s for D4. (c) and (d) show time evolution of Raman spectra for 10s, 200s and 500s in which top three Raman spectra are for D3 and bottom three Raman spectra

for D4. Cumulative fit (red solid line) to the raw data (+) and separate Lorentzian fits are shown with blue solid line.....152

**Figure 6.2.1.3:** Fitting of Raman spectra of figure 2c and 2d at simulated temperature at 1360 and 1460 K on D4 NW in near vertical geometry. Cumulative fit (red solid line) to the raw data (+) and separate Lorentzian fits are shown with blue solid line.....153

**Figure 6.2.2.1:** (a) Optical image of InAs NW D5 on Si substrate and the inset shows schematic used for Raman scatterings configuration. (b) Polarized and unpolarized Raman spectra with incident polarization parallel and perpendicular to NW axis. Cumulative fit (red solid line) to the raw data (+) and separate Lorentzian fits are shown with blue solid line.....156

**Figure 6.2.2.2:** (a) Shows optical image of for InAs NW D6 on Si substrate. (b) Polarized Raman spectra for various LPDs showing oxide modes observable only in  $x(z,z)\bar{x}$  configuration. Cumulative fit (red solid line) to the raw data (+) and separate Lorentzian fits are shown with blue solid line.....157

**Figure 6.2.3.1:** (a) and (b) shows polarized Raman spectra at lower LPD followed by Raman spectra and laser irradiation with higher LPD and later Raman spectra at lower LPD to check the effect of polarization configuration v/s polarized irradiation for D7 NW. Cumulative fit (red solid line) to the raw data (+) and separate Lorentzian fits are shown with blue solid line.....159

**Figure 6.2.3.2:** (a) and (b) Show unpolarized Raman spectra for higher LPD ( $\sim 2900 \text{ kW/cm}^2$ ) with incident polarization perpendicular and parallel to NW axis, respectively, followed by Lower LPD ( $\sim 800 \text{ kW/cm}^2$ ) Raman spectra in 4 different polarization configuration for D8 NW. Cumulative fit (red solid line) to the raw data (+) and separate Lorentzian fits are shown with blue solid line.....161

**Figure 6.2.3.3:** (a) Simulated 3D temperature profile view for InAs nanowire (D8: NW:  $d \sim 350$  nm,  $L \sim 4$   $\mu$ m) on Si substrate (complete NW and part of the NW with different tilts) for LPD  $\sim 2900$  kW/cm<sup>2</sup>, b) Simulated transient temperature as a function of laser irradiation time (c) Fitting of Raman spectra of figure 6.2.3.2b in  $x(y,z)\bar{x}$  configuration range from 200-250 cm<sup>-1</sup>. Cumulative fit (red solid line) to the raw data (+) and separate Lorentzian fits are shown with blue solid line.....162

**Figure 6.2.4.1:** (a) and (b) Optical image of InAs NW (D8) before and after Raman experiment, respectively. (c) Show the zoomed image of position A and B. (d) and (e) unpolarized Raman spectra during heating cooling experiments showing formation of Grey and Black allotropes of elemental As on cooling of low and high LPD irradiated InAs NW, respectively. Cumulative fit (red solid line) to the raw data (+) and separate Lorentzian fits are shown with blue solid line.....164

**Figure 6.2.4.2:** (a) Raman spectra elucidating apparent large blueshift in TO\* phonon as due to formation of black As at higher simulated temperature through fitting of mode  $\sim 220$  cm<sup>-1</sup>, (b) Raman spectra at  $T > 1600$  K showing decrease and then increase in intensity of TO\* mode as temperature increases. Cumulative fit (red solid line) to the raw data (+) and separate Lorentzian fits are shown with blue solid line.....167

**Figure 6.3.1:** Top is the unpolarized Raman spectrum for InAs NW (D9:  $d \sim 650$  nm) and bottom two are the polarized Raman spectra for  $x(y,y)\bar{x}$  and  $x(z,z)\bar{x}$  configuration using 488 nm excitation. Raman configuration are described using Porto's notations. Cumulative fit (red solid line) to the raw data (+) and separate Lorentzian fits are shown with blue solid line.....169

**Figure 6.3.2:** a) Wavelength dependent unpolarized Raman spectra, b) and c) wavelength dependent polarized Raman spectra for  $x(y,y)\bar{x}$  and  $x(z,z)\bar{x}$  configuration, respectively using

514, 488, 476 and 458 nm excitation. Cumulative fit (red solid line) to the raw data (+) and separate Lorentzian fits are shown with blue solid line.....171

**Figure 6.3.1.1:** Show the Raman spectra by taking incident Y and Z and polarized Raman spectra for  $x(y,y)\bar{x}$  and  $x(z,z)\bar{x}$  configuration using 514 excitation. Cumulative fit (red solid line) to the raw data (+) and separate Lorentzian fits are shown with blue solid line.....172

**Figure 6.3.1.2:**a) and b) wavelength dependent unpolarized Raman spectra by taking incident Y and Z for each wavelength 514, 458 nm excitation for diameter 300, 270 nm,, respectively. Cumulative fit (red solid line) to the raw data (+) and separate Lorentzian fits are shown with blue solid line.....173

**Figure 6.3.2:** a) Fig. 6.3.2.a) Before heating, wavelength dependent unpolarized Raman spectra by taking incident Y and Z polarization for each wavelength 514, 488 and 458 nm excitation at LPD  $\sim 800$  kW/cm<sup>2</sup>, b) top two Raman spectra are for LPD  $\sim 6500$  kW/cm<sup>2</sup> at 150s and 300s for incident Y and bottom Raman spectra is for LPD  $\sim 800$  kW/cm<sup>2</sup> after heating, for incident Z using 488 nm excitation. The top and bottom of (b) are optical and AFM images, before and after heating, respectively. c) After heating, wavelength dependent unpolarized Raman spectra spectra by taking incident Y and Z polarization for each wavelength 514, 488 and 458 nm excitation at LPD  $\sim 800$  kW/cm<sup>2</sup>. Cumulative fit (red solid line) to the raw data (+) and separate Lorentzian fits are shown with blue solid line.....175

**Figure 6.3.3.1:** (a) TEM image of NW1 and HRTEM was performed on position marked by (red) square, (b) HRTEM image, c)Filtered image of the region marked in b, inter planer d is calculated over region marked by the rectangle(magenta), and (d) The SAED pattern in center position of the NW.....177

**Figure 6.3.3.2:** (a), (c) and (d) TEM image of NW2- NW4, respectively. (b), (e) and (f) The SAED pattern in center position of the NW 2-4 respectively. (g) TEM image of NW2 after heating.....178

**Figure 6.3.3.3:** (a) and (b) TEM image of NW1 before and after heating, respectively. (c) The SAED pattern after hating in center position.....180

**Figure 6.3.3.4:** (a) and (b) TEM image of NW5 before and after heating, respectively. HRTEM was performed on position marked by (red) square (b), (c) HRTEM image, d)Filtered image of the region marked in b, inter planer d is calculated over region marked by the rectangle (magenta).....181



**List of Tables:**

**Table 2.2.3.** Raman selection rule for zinc blende structure.  $x$ ,  $y$  and  $z$  denote the set of three mutually perpendicular  $[1T0]$ ,  $[11\bar{2}]$  and  $[111]$  axes .....27

**Table 4.3.1** Consolidation of results of growth mapping studies .....81

**Table 4.3.2.2:** Raman selection for different Raman scattering configurations.....86

**Table 4.3.2.3.2:** Diameter of base, center and tip positions for tapered wires (TW) designated as 1, 2, 3, 4, 5 and 6 for which phonon wavenumbers are plotted in Fig. 4.3.2.3.1.....91

**Table 4.4.1.1.** Frequencies of  $E_{2h}$  ( $\omega_l$ ) and TO ( $\omega_h$ ), intensity ratio of TO to  $E_{2h}$  phonons at 300K and 80K and  $d\omega_{E_{2h}}/dT$ ,  $d\omega_{TO}/dT$ ,  $d\omega_{LO}/dT$  for different positions on a tapered MNWs and for a uniform wire are summarized.....103

**Table 4.4.1.2:** Strain component of  $(d\omega_{E_{2h}}/dT)_S$ ,  $(d\omega_{TO}/dT)_S$  and  $(d\omega_{LO}/dT)_S$  for different positions on a tapered MNWs and for a uniform wire are summarized.....104

**Table 5.2.1.2** Parameters of bulk InAs, Si, used in the temperature simulations .....120

**Table 5.3.1.** Consolidation of various oxides formed in weak, intermediate and strong interaction regimes, corresponding Raman peak frequencies and temperature for these oxidation processes .....128

**Table 6.3.4:** Consolidation of Raman peaks frequencies for gray and black As from the literature.....166

**Table 6.3.3.1:** Consolidation results of SAED and HRTEM for NW1-4.....179

**Table 6.3.3.2:** Consolidation result of SAED for NW1 before and after heating.....181





# **Chapter 1**

## **Introduction**

*“Equipped with his five senses, man explores the universe around him and calls the adventure, Science” \_\_\_\_\_ Edwin Powell Hubble*

Nanoscience and nanotechnology has been the frontline research area for last few decades. Nanoscience has shown intensive growth in both new methods of synthesis along with advancement of characterization methods for the nanostructures [1]. It is now a well-established field owing to uniqueness of chemistry and physics (energetics and dynamics) of these nanomaterials. One dimensional nanostructures, i.e. nanowires (NWs) show remarkable properties like large mechanical strength [2-7], large electrical conductivity [8], lower thermal conductivity [9-12] high fractural damage threshold [5-6], large functional surface area etc., which are useful in variety of applications ranging from optoelectronics [13], thermo-electrics to chemical sensors [13-15]. For realizing new devices and technologies from these NWs, fundamental understanding of these nanostructures and thereby suitable control of the properties is required and that is the motivation of this thesis work. We start with brief history of semiconductors and then discuss nanostructures in general and in particular one dimensional semiconductor NWs. Their properties and applications are briefly discussed. Further, importance of using Raman spectroscopy to study one dimensional semiconductor NWs is described. Chapter is concluded by outlining the aim of thesis work.

## **1.1 History of semiconductors**

The term “semiconducting” was used for the first time by Alessandro Volta in 1782 [16]. The semiconductor were being studied in laboratories as early as in 1830’s. The Michael Faraday was the first person who observed a semiconducting effect in 1833 and also noticed that the dependence of resistance with temperature of AgS is different than that of metal [17]. The research in semiconductors has started by Faraday et al. in 1839 in which they have reported

the negative temperature coefficient of resistance of silver sulfide [18]. The Johann Hittorf et al. have published about how to change electrical conductivity with temperature for  $\text{Cu}_2\text{S}$  and  $\text{Ag}_2\text{S}$  in 1851 [19]. In 1874 Karl Ferdinand Braun have observed conduction and rectification in metal sulfides probed with a metal point (whisker) [19]. Arthur Schuster observed the rectification and made the circuit by copper wire and after some time, he has noticed the circuit was not working due to copper oxide was formed at end of the wire [20]. After this, he discovered the copper oxide is a semiconductor [21]. Braun et al. [20] have played an important role to develop the radio and microwave radiation detector in World War II radar system and he got Nobel prize in physics with Marconi, in 1909. Walter Schottky have experimentally confirmed the presence of barrier in a metal semiconductor junction, in 1909 [21]. The photovoltaic effect at a junction between semiconductor and electrolyte is discovered by Alexander Edmund Becquerel in 1839 [22]. In 1883, Charles Fritts constructed the first solar cell which consist a metal plate and a thin layer of selenium covered with thin layer of gold and efficiency of cell is below 1% [23]. The  $\text{ZnS}$  is first semiconductor discovered which has novel fundamental properties and diverse application [24].

Under the influence of temperature, few insulators may possess the property of variable/changing conductivity. This remarkable property is of vital importance for the world of electronics and communications. Materials possessing this property are commonly known as semiconductors. The most common semiconductors include Silicon, Germanium (IV). However, the most widely used semiconductors is Silicon. It's vast presence, simple processing, reasonable speed and useful temperature range makes it a versatile semiconductor. This semiconductor has huge technological importance in the field of microelectronics, semiconductor devices and material science. Before beginning of the era of semiconductors, the field of technology was predominated by vacuum tubes whose size was quite large.

However with the advent of semiconductors, transistors (consisting of semiconductor material) replaced vacuum tubes. The size of the transistor is far smaller than that of vacuum tubes; moreover they were lighter, durable and consumed less power. In accordance to the Moore's law, the size of the transistors used in the electronic components is continuously decreasing [25].

### 1.1.1 Application of semiconductors and recent trends

Semiconductor (SC) has conductivity between conductor and insulator at finite temperature with band gap in visible-UV region of solar spectra. Thus they are very useful materials for photovoltaic application [26]. Transportation of charges in semiconductors materials can be enhanced via injection of charges by doping, which can change the scattering process in semiconductor. Thus, semiconductor can be tailored for specific applications. Semiconductor materials are widely used in optoelectronic devices, electronics, transistors, solar cells, metal oxide semiconductor field effect transistors (MOSFET) and detectors. The first successful solar cell on single crystalline silicon was fabricated Chapin et al. [27], which had an energy conversion efficiency of  $\sim 6\%$ . On the other hand, higher mobility of electron/holes in Ge w.r.t. Si can be used in high speed MOSFETs, and solar cells [28]. Compound SCs of the type III-V, II-VI are well known for high mobility of charges and greater radiative recombination of electron-hole pairs. Therefore, Compound SCs have attracted attention. CdS is a significant II-VI SC which has, high reflectance in the infrared range, high transmittance in the visible region, low resistivity, electron affinity and high optical band gap as well as its ability to form good ohmic contacts [29]. According to theoretical studies, higher efficiency of solar cell can be achieved from III-V SC [30]. In addition, III -V materials such as InAs, GaSb, InSb can be useful as far infrared detectors, Hall sensors, high frequency and thermos-voltaic devices [31] etc. Wide bandgap II-VI compounds have

applications in laser diodes (LDs) and light-emitting diodes (LEDs) in the high frequency like blue - UV region of spectra [32]. Polycrystalline ZnSe is a preferred window material for high power lasers in near IR region. Further, HgCdTe/CdTe are useful materials for far-infrared detectors [31].

It was found that the properties of materials can be changed by changing the size and or by increasing surface to volume ratio by reducing the dimensions [33] With change in size of materials, optical, chemical, mechanical, magnetic and thermal properties can be changed, which is due to the quantum confinement of electrons, holes and phonons. Large surface to volume ratio of nano-structures gives rise to larger number of dangling bonds thus leading larger number of reaction centers. This increases optical-sensitivity as well as catalytic activity of nanostructures and can be suitably used for appropriate applications. As an example, gold is non-reactive material however, gold nanoparticles (NPs) is often used in many reactions, which is due to the presence of large number of dangling bonds in gold NPs [34].

### **1.1.2 History of nanostructures**

Nanostructure science and technology is a field, which has capacity to solve some of the most pressing problems of the world. Its interdisciplinary nature has contributed to its rapid growth. Nanostructures exist in nature on earth since its beginning, however, the aim of intense research in the field of nanoscience is to gain control over growth of nanostructure of various dimensions ( 1D: nanowire, 2D, quantum well, 3D: quantum dot) and size and study them for specific applications. Major application areas include optoelectronics, electronics, medicine, storage devices and space etc. In electronics applications include improving speed of current processors, faster RAMs and ROMs along etc. with miniaturization. In medicine, it is mainly used for marking agents for drug delivery, better efficacy drugs, imaging and diagnosis.

Some of the items of daily use have already benefited from nanoscience. These are stain-resistant clothing, cosmetic products safety gears and sports goods [35].

The history of carbon is quite interesting. It took time to realize that carbon existed in many forms. The fact that diamonds are nothing but carbon, was first proved by Antoine Lavoisier, in 1772 [36]. Another scientist name Carl Wilhelm Scheele in 1779 proved that graphite is also a form of carbon which was hitherto thought to be a form of lead. Fullerenes, a form of carbon was discovered by Kroto and Smalley while synthesizing carbon clusters [36]. They analyzed the distribution of gas-phase carbon clusters using mass spectrometry, and found that cluster containing 60 carbon atoms were generated in large numbers. Nanotubes, yet another different form of carbon were discovered by Iijima in 1991 [37]. These Nanotubes had more than one graphitic layer. This was slightly problematic because it was thought that ideal nanotubes must be single-walled tubes. In further experiments, single-walled nanotubes were synthesized [38]. Following these researchers worldwide focus was shifted to producing carbon nanotubes and their study [37-38]. Monolayer layer of graphite i.e. 2 dimensional graphitic layer sheet is described as graphene for the first time in 1987[39]. Graphene is thus the basic building block for different graphitic C materials like fullerene, carbon nano tubes, and graphite. It consists of a single layer of carbon atoms arranged in a honeycomb-like structure. Graphene is good heat conductor and have high thermal conductivity which is used in electronic circuits as a heat sink [40]. Graphene sheets show high flexibility. A novel electronic property of graphene is that it can sustained high electric currents. Graphene exhibit the excellent carrier motilities of  $\sim 500,000 \text{ cm}^2 \text{ V}^{-1} \text{ s}^{-1}$  [40].

## 1.2 Nanostructures

The spatial confinement of electrons and phonons in nanostructures leads to a phenomena known quantum confinement [41]. Electron quantum confinement occurs when the De Broglie wavelength of electron i.e. Bohr radius of an exciton is in the order or larger than the spatial dimension of the nanocrystal. Bohr radius for semiconductors lies in the range ~2 to ~50 nm for different materials [42]. In bulk material, the electrons are moving freely at infinite distance but in nanomaterial, the electron are confined within a potential barrier, as a consequence energy levels of electron become discrete and thus band gap can be tuned as a function of dimension. Band gap is inversely proportional to size of material [43]. This effect can be observed in optical experiment like absorption, reflection, photoluminescence spectroscopy. Nanostructure is defined formally as the structure with at least one-dimension  $d$  is less or equal to typically few hundred nm.

In bulk material, the surface may not alter material properties significantly as it's volume is much larger than surface area. However, surface gains significance in the nano material, as surface/volume ratio increases as size decreases. This has important consequence for all those process, which occur at a material surface like detection, catalysis etc. [1].

### 1.2.1 Classification of nanostructures (2D, 1D, 0D)

Confining the particle in particular direction/s will change it's physical, chemical, electrical, optical properties. If the electron is confined in one dimension, then electron potential is called quantum well and these are 2D nanostructures (NS). There involves thin films on a substrate because this film has one dimension confined (size in nm range) and other two dimensions are bulk like. Thin film materials have been used in multifunctional emerging coating, solar cells, wireless and telecommunication, integrated circuits, lithography etc. If the electron is confined in two dimensions, then i.e. Nanowire (NW), nanorods, nanotubes,

nanobelts and nanoribbons then they are 1D nanostructures [44]. In these 1D nanostructures, when NW diameter have very small size (5-100 nm) and very large aspect ratio then nanowire behaves like a waveguide and this effect is called antenna effect [45]. Coupling of incident electric field is different in parallel or perpendicular of NW axis as a result of this antenna effect. NWs are thus used as a wave guide because of high contrast of the refractive index between nanowire ( $n \sim 3.5$ ) and air ( $n \sim 1$ ) [46]. They have important role to play in electronics, optoelectronics and electrochemical energy devices in nano dimensions. NWs also have potential to be used as nano-laser, as light can be well confined in cavity [47]. If the system confined in three dimensions i.e. quantum dots (QD) and it is called 0D nanostructures. Energy spectrum is completely quantized and band gap tuning can be achieved due to 3D confinement [48].

### **1.2.2 Properties and applications of semiconductor nanostructures**

In thin films, confinement starts influencing electrical properties of materials at lower dimensions. Recently, Eslamian et al. [49] have shown the high conversion efficiency with low fabrication cost for CdS thin film photovoltaic (PV) devices. Single or multilayer optical coatings are being used as an antireflecting, reflecting and transmitting coating for different regions of spectra [50]. Efficiency of electrochemical energy devices (EED) [51] is increased by the large surface area and novel size effects of nanostructured materials. Thin film transistor (TFT) is responsible for driving current in memory cell, digital circuits and light emitting diode [52,53]. Mechanical properties of thin films are different from those of bulk materials because of their increased surface-to-volume ratio and confinement in one dimension [54]. Thin films are remarkably stable at room temperature and has higher mechanical strength compared to bulk [47].

Band gap of the material can be easily tuned using 0-dimensional (0D) nanostructures. A 20 nm platinum (Pt), gold (Au), palladium (Pd) and silver (Ag), NPs have the characteristic/typical, yellowish gray, wine red color dark black colors and black, respectively [55]. Khan et al. [55] have shown the color changes as size and shape change of the gold NPs. These gold NPs is used in bio imaging applications [56]. The NPs can be used for drug delivery [57], CO<sub>2</sub> capturing [58] gas sensing [59-61], chemical and biological sensing [62] and other related applications [63]. Au NPs, Cu and Ag have a wide absorption band in the visible range of the electromagnetic spectrum. Gold NPs coating is routinely used for conducting away the charge from the sample in SEM measurement. Due to thin layer/film of Gold NPs on the sample, high quality SEM images of sample can be obtained. Ceramic NPs have also attracted to researchers because of their use/utility in many applications like catalysis, imaging applications, photo catalysis and photo degradation of dyes [64]. Semiconductor NPs is known for the broad ranging bandgap and therefore can be significantly modified in their properties with adjustment in bandgap. Hence, for many device i.e. photo catalysis, photo optics and electronic devices, semiconductor materials are becoming important [65] and people are also investigating day by day. For example, efficiency of water splitting applications is obtained exceptionally/extraordinary by using various semiconductor NPs due to their suitable bandgap and band edge positions [66]. Size dependent optical properties of noble metals NPs show a strong UV-visible extinction band but in bulk metal, extinction band is absent. Furthermore, 0D NS, such as quantum dots has been studied in single-electron transistors, lasers light emitting diodes (LEDs) and solar cells, [44].

### 1.3 Properties and applications of semiconductors 1D nanostructures

In the last decade, 1D NSs i.e. nanowires, nanotubes, nanobelts etc. have attracted lot of researcher's attention due to their significance in various potential applications [67]. They are believed to play major role at the nanoscale as both interconnects and basic building blocks in manufacturing electronic, optoelectronic, and EEDs. The field of 1D NS such as nanotubes has also attracted attention after the pioneering work done by Iijima et al. [68]. 1D NSs have a profoundly influenced field of nanoelectronics, nanodevices, alternative energy resources [69].

Semiconductor nanowires can be integrated to fabricate novel functional structures. For example, nanowires may give enhanced catalytic performance (e.g. for water splitting), improved batteries, solar to electric energy conversion devices and LEDs with improve efficiency [70-71]. The properties and application of 1D NSs are described in the following,

***1.3.1 Physical properties:*** As the diameter of a nanowire becomes comparable to de Broglie wavelength of electron, it leads to increase in the DOS, which is useful in lasers. In the nanowire lasers, the main advantage can be obtained i.e. subwavelength lasers with improved efficiency, directional due to shape of nanowire and the low threshold emission due to larger DOS. In NW lasers, optical gain medium and optical cavity is same due to the shape of nanowire [72].

***1.3.2 Chemical properties:*** In nanowire, significant increase in surface to volume ratio is obtained by reducing the size, which give rise to larger number of dangling bond leading to increased sensitivity for sensors and chemical reactivity. Nanowires also show interesting optical and chemical properties because of high aspect ratio (dia/length), enhancement in

surface to volume ratio, and large curvature at the nanowire tips. Hence they are very attractive/agreeable for sensor devices applications [13-15].

**1.3.3 Optoelectronics properties:** Application of nanowires have also shown improvement in optoelectronic devices, including infrared (IR) camera and photodetector technology [13].

**Optical properties:** Due to electronic confinement in 2 dimensions, the band gap of 1D NS can be varied. III–V compound semiconductors are among the most promising photodetector materials due to their high absorption coefficient, high carrier mobility, and widely tunable bandgap. However, photodetectors based on Group III–V materials (e.g. InGaAs, InAs, or InSb) are also expensive to manufacture and restricted to small areas [72]. The use of p – n junction nanowires has been studied for laser applications. The lower threshold energy for lasing of ZnO NWs as compared to ZnO bulk, has been attributed to the exciton confinement effect in the laser action, which decreases the threshold lasing energy in nanowires [73-75].

**Electronic properties:** 1D NS have 2 dimensional confinement which leads to decrease in scattering in the system. Large aspect ratio of 1D NS is greatly useful in applications like FET [76]. Transportation of electron is channelized which leads to increases in efficiency as well as speed of electronics device like MOSFET [77-79]. Good rectifying characteristics/features is exhibited when made by junctions of GaAs and GaP semiconductor NWs [80]. 1D NS junctions have been fabricated for number of semiconductor devices like junction diodes [81-82], memory cells and switches [83], transistors, FETs [83-84], LEDs [85, 80] and inverter [86] etc.

**1.3.4 Magnetic properties:** Coercivity is the measure of the field required to switch magnetization in a given direction. Decrease in NW diameter increases the coercivity because

low dimension act as a single domain. For low dimensions, after removal of the external magnetic field, magnetization is remains. To remove this remaining magnetization, large magnetic field needs to be applied on the material in the negative direction. Ferromagnetic materials can be converted to super paramagnetic materials when their size is compared to the domain size. The magnetic nano particles are extensively used in drug delivery technique. NWs show/establish unique properties as compared to bulk counterparts because of confinement in radial direction. It is apparent/evident/clear/obvious that by changing the NWs diameter, the magnetic properties of the nanowires can be tuned, which lead to change the coercivity, remanence, magnetization, and squareness of the hysteresis loop [87] Strong enhancement/increment/amplification/improvement in magnetic coercivity as compared to bulk material is shown/reported by Nilelsch et al. for Fe, Co, Ni magnetic nanowires. Recently, in research field, researchers are interested on growth of ferromagnetic NWs for the potential application to future ultra-high-density magnetic recording media [88-89]. The demagnetization depends on the materials shape. For nanowires, the demagnetization is different along the parallel and perpendicular direction due to have easy and hard axes. The nanowires have uniaxial anisotropy, with their easy axes aligned along the wire axes and perpendicular to the film plane. The strong perpendicular anisotropy has been attributed to magnetic shape anisotropy [90]. Because of their potential applications in spintronic devices they are used in such as magnetic optic switches, magnetic sensors, spin valve transistors, and spin LEDs.

***1.3.5 Thermal properties:*** In last decades, researcher have been interested in thermoelectric materials due to their applications. They are trying to increases the conversion efficiency ( $S\sigma^2T/k$ ) which depends on thermo power (S) thermal conductivity (k) and electrical conductivity ( $\sigma$ ) [8]. In low dimensional system, decreases in size increases phonon scattering,

which leads to reduction in thermal conductivity ( $k$ ) [9-12]. Reduction in size leads to increase in DOS due to quantum confinement, which further leads to increase in  $S$  and  $\sigma$ . It is observed that the nanowire have diameter dependent variation in DOS as well as unique electronic band structure, which is used in various thermo-electric applications [91-92]. Metal nanowires exhibit/show many fold increase in Seebeck coefficient due to enhancement in their DOS at the one-dimensional sub-band edges, aspect ratio and NW diameter.

**1.3.6 Electrical properties:** In nanowire, the transportation mechanism of electron is decided by three parameters i. e. diameter of wire, mean free path and de-Broglie wavelength of electron [93]. When the wire diameter is in the range of mean free path and de-Broglie wavelength then quantum confinement effect comes and DOS of electron will be increased. Electron transport properties of nanowires are very important for electrical measurements. It has been observed that the wire diameter, crystal structure wire surface condition, and its quality, crystallographic orientation along the NW axis and chemical composition etc are important parameters, which influence the electron transport mechanism of nanowires [14]. By the variation/tuning of the surface scattering phenomena of charge carriers in NWs, in terms of the diameter of the NWs are varied then electrical conductivity can be modified. Presently, some investigators are exploring the variation in resistivity ( $\rho$ ) of copper nanowire by variation in surface due to surface scattering or grain boundary scattering [94-99].

**1.3.7. Mechanical properties:** As size decrease, the grain size is decreased leading to restriction in movement of dislocation in a grain which further leads to increase in yield strength. The fabrication of NW with improved mechanical properties as compared to their bulk materials are a challenge even though the technical equipment are improving. The many aspects i.e. the intrinsic material properties, crystal structures, surface geometry, applied

stress state, axial and surface orientation etc. can be changed the deformation mechanism. Nanostructures such as nanowires [2], carbon nanotubes (CNT) [3], and/or graphene [4] have interested mechanical properties due to have unique mechanical response of such structures as a building block. Some nanostructures as compared to their bulk materials show the superior mechanical properties for example elastic modulus and/or fracture stress [5-6]. Desai, et al. [7] have reported that significant increase in Young's modulus by reducing diameter from ~ 120 to 17 nm for ZnO NW.

#### 1.4 III-V Semiconductor Nanowires

III-V semiconductors, have attracted considerable attention for their optoelectronic applications [100]. Among various NWs, III-V NWs are of particularly interest due to it's high electron mobility and better optical properties. III-V NWs are potential candidates for advanced technologies like sensors, thermo electric devices and high performance field effect transistors etc. [100,101] A wide range of nanowire-based electronic and photonic devices are already developed like photodetectors [102-103], chemical sensors [104-106], light emitting diodes [107-108], memory devices integrated photonic circuits [109-111], solar cells [112-116], lasers [117-123], resonant tunneling diodes [124] single photon sources [125], single-electron transistors and memory devices [126-130] waveguides [131], field emission electron sources [132], field-effect transistors for ultrahigh density logic and and highly sensitive biological [133-135] and

InAs is an important material in high speed electronics due to its high electron mobility ( $30000 \text{ cm}^2/\text{V s}$ ) [136], semimetallic nature (0.35 eV) and strong orbit-spin coupling [137,138]. InAs NWs has applications in spintronic and sensors too. In combination of unique features of NWS and InAs properties, InAs NWs is considered to be a promising

candidate for applications in ballistic transistors, single-electron transistors, resonant tunneling diodes etc. [139,140].

## **1.5 Raman spectroscopy**

Raman spectroscopy can give information of chemical composition, structure, crystalline quality, electronic band structure, stress etc. in the material under study. Added advantage to being nondestructive technique is that it does not require any sample preparation. Raman spectroscopy of a single nanowire can give information about its chemical composition, residual strain if any, crystalline quality and structure. Raman mapping/imaging has emerged as a potential technique for structural and compositional identification of nanostructures.

### **1.5.1 Spatially resolved Raman spectroscopy**

The study of spatial variation along the length of a NW is very important for NWs and can be achieved using Raman mapping/imaging or spatially resolved Raman spectroscopy. Spatially resolved Raman spectroscopy allows us to study local variation chemical composition, structure, crystalline quality, electronic band structure, stress etc. along the length of the nanowires.

## **1.6 Aim of the thesis**

The aim of research work was to study the individual InAs nanowires (NW) using Raman spectroscopy, which was not feasible to do by conventional technique like XRD, TEM due to low density and large diameter of NWs. It may be appropriate to note here that although, the diameter of NWs studied in this thesis is on the higher side  $\sim 200$ - $1000$  nm, they show interesting surface effects due to high aspect ratio and one dimensional nature of

wire. However, no confinement effects are observed as expected for studied dimensions. Further, these weakly confined NWs show many other interesting properties which can be probed by spatially resolved Raman spectroscopy along the length of the NW.

The morphology of InAs NWs in the sample studied is found to be very different under same external growth conditions. Raman spectroscopy is used as a local probe for these NWs. Further, Raman spectroscopy for InAs has resonance enhancement in visible (E1 ~2.5 eV) [141], thus specificity of Raman spectroscopy and possibility of good signal to noise ratio on InAs MNWs, makes it an ideal technique to study these individual InAs NWs.

The InAs is a semi metal and hence, it can be easily affected at small laser power by visible irradiation due to large absorption. It was noted while mapping the InAs micro-nanowire (MNW:  $d \sim 1 \mu\text{m}$  ,  $L \sim 35 \mu\text{m}$ ) , that it is getting damaged and there was time evolution of Raman spectra. This was systematically investigated using time evolution of Raman spectra for 8-16 minutes in laser power density regimes from 30 to 800 kW/cm<sup>2</sup>. The complicated oxidation processes involved were studied using Raman spectroscopy. It's thermal nature was further investigated using simulated temperature. The temperature rise on laser irradiation is simulated by 'ANSYS' software using finite element method (FEM) and was corroborated with time evolution of Raman spectra. The predictability of this methodology was confirmed using random NWs and random LPD's. This is described in Chapter 3 and 5.

The redshift in TO phonons of InAs in these NWs was studied using spatially resolved Raman spectroscopy (SRRS) at very low LPD  $\sim 30 \text{ kW/cm}^2$  on different types of MNWs, i.e. uniform, bent and long tapered MNWs with diameter in the range of 2  $\mu\text{m}$  – 400 nm. This study revealed the presence of polytypism in InAs MNW even for these large diameter MNWs, which was not reported in earlier studies. Effect of residual stress was

studied using temperature (300 K- 80 K) dependent Raman spectroscopy. This is discussed in Chapter 4.

In later chapter (6) we discuss the effect of orientation of laser irradiated InAs NWs on time evolution of unpolarized Raman spectra. Specially designed two step polarized Raman spectroscopy revealed that gray- As and black-As are generated as byproducts of oxidation processes at high simulated temperatures in the range  $\sim 700$  -900 K and  $>1400$  K, respectively. Further it confirmed formation of oriented crystalline oxides by laser irradiation.

Resonance Raman spectroscopy is shown to be an efficient alternative method to study polytypism in InAs NWs, which can be applied to much lower dimensional NWs compared to conventional polarized Raman spectroscopy. Conversion of WZ to ZB phase of InAs NW at higher simulated temperatures is studied using Resonance Raman spectroscopy.

The understanding developed of InAs MNWs and oxidation processes on laser irradiation are summarized in chapter 7.

## **Chapter 2**

# **Experimental techniques**

*“Nothing in life is to be feared, it is only to be understood. Now is the time to understand more, so that we may fear less” — Marie Curie*

## 2.1 Introduction

In this chapter, experimental techniques used for study of metal organic chemical vapor deposition (MOCVD) grown InAs micro-nanowires (MNWs) is described. Raman spectroscopy is used as the main research technique and its theory and instrumentation is discussed in brief details. Polarized, temperature dependent and wavelength dependent Raman spectroscopy used for the investigation are also separately discussed to understand their specific use. Electron microscopies like scanning electron microscopy (SEM), transmission electron microscopy (TEM) and their variants, which are used to support understanding developed by Raman spectroscopy are also briefly outlined. Growth of InAs NWs used in the above mentioned study are performed at two different labs using MOVPE by collaborators and is described briefly in the annexure. InAs NWs grown at RRCAT, Indore are in the range diameter  $\sim 600$  nm to  $2.5 \mu\text{m}$  and length  $\sim 20 \mu\text{m}$  to  $80 \mu\text{m}$  [142] and NWs grown at TIFR, Mumbai are of dimensions in the range diameter  $\sim 50$  nm to  $600$  nm and length  $\sim 1 \mu\text{m}$  to  $10 \mu\text{m}$  [143].

## 2.2 Raman spectroscopy

When the incident light falls on matter, different interactions take place like absorption, reflection, transmission and scattering. There are two types of scattering processes, 1) Elastic scattering: Incident frequency of photon matches with the scattered photon and 2) Inelastic scattering: Scattered photon frequency is different from incident photon. Raman scattering is an inelastic scattering of photon from low level excitation of the material under study [144]. Here, scattering of light (2-3 eV) from optical phonons (2-3 meV)

is studied. In the following, quantum theory of Raman scattering is described.

### 2.2.1 Quantum theory of Raman scattering

When a monochromatic light of frequency  $\omega$  falls on a system, most of the light passes as such but in addition, scattering of light occurs [144, 145]. It was found that scattered light consists of a very strong line in the spectrum at the frequency  $\omega$  (elastic scattering- Rayleigh scattering) as well as series of weaker lines at frequency  $\omega \pm \omega(\mathbf{q})$ , which is due to inelastic scattering and is called Raman scattering. Here,  $\omega(\mathbf{q})$  is the frequency of optical phonon. Frequencies  $\omega - \omega(\mathbf{q})$  corresponds to Stokes lines and  $\omega + \omega(\mathbf{q})$  corresponds to anti-Stokes lines. The interaction of radiation with matter is treated as a problem of time dependent perturbation in quantum mechanics. When a photon is incident on a crystal, it sets up a perturbation of its electronic wave function, as only electron can follow the fast changing electric field of incident light. Thus, wave function of perturbed crystal acquires a mixed character and becomes linear combination of all possible wave function of unperturbed crystal with time dependent coefficient. Hamiltonian of this system is given by,

$$\hat{H}_s = \hat{H}_R + \hat{H}_m + \hat{H}_{sR} \quad (2.1)$$

Where  $\hat{H}_R$  = Hamiltonian of radiation in absence of medium,  $\hat{H}_{sR}$  = Interaction Hamiltonian of radiation and medium,  $\hat{H}_m$  = Hamiltonian of medium in absence of radiation and is given by

$$\hat{H}_m = \hat{H}_0 + \hat{H}_1 \quad (2.2)$$

Here,  $\hat{H}_0$  = Total Hamiltonian of electronic level of medium before interaction between electronic and vibration level,  $\hat{H}_1$  = interaction Hamiltonian between electronic and vibration level. Thus,  $\hat{H}_{sR}$  and  $\hat{H}_1$  are treated as perturbation Hamiltonian and  $\hat{H}_0$  and  $\hat{H}_R$  are treated as unperturbed Hamiltonian. Each scattering event in the quantum mechanical theory

corresponds to transition between initial states  $|i\rangle$  and final states  $|f\rangle$  of the scattering medium, these being Eigen states of  $\hat{H}_0$ .

$$\hat{H}_0|i\rangle = \hbar\omega_i |i\rangle \quad (2.3)$$

$$\hat{H}_0|f\rangle = \hbar\omega_f |f\rangle \quad (2.4)$$

The radiation field simultaneously undergoes from transition an initial state with  $n_i$  and  $n_s$  to final state with  $n_i-1$  and  $n_s+1$ .

$$\hat{H}_R|n_i, n_s\rangle = (n_i\hbar\omega_i + n_s\hbar\omega_s)|n_i, n_s\rangle \quad (2.5)$$

$$\hat{H}_R|n_i-1, n_s+1\rangle = [(n_i-1)\hbar\omega_i + (n_s+1)\hbar\omega_s]|n_i-1, n_s+1\rangle \quad (2.6)$$

These transitions in the system are due to perturbation  $\hat{H}_{eR}$ . The energy lost/gained by the scattering medium in the process  $|\hbar\omega_f - \hbar\omega_i|$  and the conservation of energy of the system requirement that this is equal to energy gained/lost by photon  $|\hbar\omega_i - \hbar\omega_s|$ .

In this scattering experiment, scattering cross-section is defined that the rate of removal energy from incident beam to scattering medium by the scattering process into solid angle  $d\Omega$ , in volume  $V$  for scattering frequency between incident medium.

$$\frac{d^2\sigma}{d\omega_s d\Omega} = \frac{1}{r} \frac{\hbar\omega_i}{I_i} \quad (2.7)$$

$\frac{1}{r}$  is the transition rate between initial and final state of medium in event of scattering.  $\bar{I}_i$  is mean intensity of incident beam. The transition rate is given by Fermi golden rule [quantum theory book 5] from time dependent perturbation theory

$$\frac{1}{r} = \frac{8\pi^3}{\hbar^2} \frac{n_i}{\eta_i^3 \eta_s^3} \sum_{i', j'} [\hat{\mathbf{e}}_s \cdot \Delta\chi_R \cdot \hat{\mathbf{e}}_i]^2 \delta(\omega_{i'} - \omega_{j'}) \cdot P(i') \quad (2.8)$$

For Raman scattering by phonons in crystal one has to appeal electron-phonon interaction in first order adding to 2<sup>nd</sup> order in electron-radiation interaction  $\hat{H}_{eR}(\hat{\mathbf{A}}, \mathbf{p})$ . Such that scattering of light is third order process. In this involve (1) annihilation of incident photon (2) creation

or annihilation of phonon corresponding to stoke/anti-stoke processes (3) creation of scattered photon. There are six terms in Raman susceptibility for stoke scattering by phonons due to there are being process simultaneously.

$$\Delta\chi_R = (2.9)$$

$$\begin{aligned} & \frac{e^2}{m^2 V w_s^2 \hbar^2} \left( \sum_u \frac{\langle 0 | p(-\vec{k}_s) | u_2 \rangle \langle u_2, n+1 | \hat{H}_{eL} | u_1, n \rangle \langle u_1 | p(\vec{k}_l) | 0 \rangle}{(\omega_{u_2} - \omega_s)(\omega_{u_1} - \omega_l)} + \right. \\ & \frac{\langle 0 | p(\vec{k}_l) | u_2 \rangle \langle u_2, n+1 | \hat{H}_{eL} | u_1, n \rangle \langle u_1 | p(-\vec{k}_s) | 0 \rangle}{(\omega_l + \omega_{u_2})(\omega_s + \omega_{u_1})} + \\ & \frac{\langle 0, n+1 | \hat{H}_{eL} | u_2, n \rangle \langle u_2 | p(-\vec{k}_s) | u_1 \rangle \langle u_1 | p(\vec{k}_l) | 0 \rangle}{(\omega_{u_2} - \omega_{ph})(\omega_{u_1} - \omega_l)} + \\ & \frac{\langle 0, n+1 | \hat{H}_{eL} | u_2, n \rangle \langle u_2 | p(\vec{k}_l) | u_1 \rangle \langle u_1 | p(-\vec{k}_s) | 0 \rangle}{(\omega_{u_1} + \omega_s)(\omega_{u_2} - \omega_{ph})} + \\ & \frac{\langle 0 | p(-\vec{k}_s) | u_2 \rangle \langle u_2 | p(\vec{k}_l) | u_1 \rangle \langle u_1, n+1 | \hat{H}_{eL} | 0, n \rangle}{(\omega_{u_2} - \omega_s)(\omega_{u_1} + \omega_{ph})} + \\ & \left. \frac{\langle 0 | p(\vec{k}_l) | u_2 \rangle \langle u_2 | p(-\vec{k}_s) | u_1 \rangle \langle u_1, n+1 | \hat{H}_{eL} | 0, n \rangle}{(\omega_l + \omega_{u_2})(\omega_{u_1} - \omega_{ph})} \right) \end{aligned}$$

It is possible to obtain information of electronic band structure and e-phonon interaction where the incident laser resonates with an electronic transition. When this happens there is large enhancement of the Raman cross section as relevant denominator term in equation 2.9 tends to zero. This is known as **resonant Raman scattering**. Under resonance conditions, the contributions of the non-resonant terms of the scattering probability can be regarded as constant.

Considering, initial electronic state is the ground state  $|0\rangle$  of the semiconductor with no electron-hole pairs excited, and its energy is taken to be zero. We shall denote the resonant intermediate state as  $|u_1\rangle = |u_2\rangle = u$  with energy  $\hbar\omega_u$ . The Raman scattering probability for a given phonon mode in the vicinity of  $\hbar\omega_u$  (after summing over  $\hat{s}$  to remove the delta function) can be approximated by [146]

$$\Delta\chi_R = \frac{e^2}{m^2 v_w \hbar^2} \sum_u \frac{\langle 0 | p(-\vec{k}_s) | u \rangle \langle u, n+1 | \hat{H}_{eL} | u, n \rangle \langle u | p(\vec{k}_I) | 0 \rangle}{(\omega_u - \omega_s)(\omega_u - \omega_I)} + C \quad (2.10)$$

Where  $C$  is a constant background. Other terms, where the difference between  $\hbar\omega_i$  and  $\hbar\omega_s$  is equal to the phonon energy are also resonant, as generally phonon energies are much smaller than electronic energies. Whenever  $(\hbar\omega_u - \hbar\omega_i)$  is small  $(\hbar\omega_u - \hbar\omega_s)$  will also be small. Thus the term we include in equation 2.10 has “almost” two resonant denominators, while the other terms contain at most one. The case  $(\hbar\omega_u - \hbar\omega_i)$  is referred to as an **incoming resonance**, when incident photon energy matches that of an electronic transition of the material and  $(\hbar\omega_u - \hbar\omega_s)$  is referred to an **outgoing resonance**, when scattered photon energy matches that of an electronic transition of the material. The less resonant and non-resonant contributions are denoted by the constant  $C$ . Scattering probability is obtained by first adding the constant term  $C$  to the resonant term and then taking square of the sum. Thus depending on the relative sign, resonant term can interfere with  $C$ . Within this approximation the constant term can be put outside the absolute square sign for calculating scattering probability. When, either the incident  $\hbar\omega_i$  or the scattering photon energy  $\hbar\omega_s$  is resonant with  $\hbar\omega_u$  (2.10) diverges (the energy denominator vanishes). In reality, this is not the case, when finite lifetime  $\tau_u$  of the intermediate state  $|u\rangle$  due to radiative and non-radiative decay processes is taken into account.

The Hamiltonian of electron and radiation is written by

$$\hat{H}_{eR} = \left( \frac{\partial V}{\partial Q} \right) Q \quad (2.11)$$

Electron-phonon interaction for short range interaction

$$Q |n\rangle = \frac{\hbar(n+1)}{(2M_r w_p \hbar N)^{1/2}} |n+1\rangle \quad (2.12)$$

$N$  is Bose Einstein occupation factor of phonons

$$\frac{\partial V}{\partial Q} = \frac{d_{LD}(eV)}{a_0}, \quad a_0 = \text{lattice constant} \quad (2.13)$$

From eq. (2.7)

$$\frac{d^2\sigma}{d\omega_s d\Omega} = \frac{1}{\tau} \frac{\hbar\omega_I}{I_I} = \frac{1}{\tau} \frac{\eta_I v}{n_I c} \quad (2.14)$$

Where  $v$  is scattering volume,  $\eta_I$  is refractive index and  $n_I$  is number of incident photon. The transition rate is given by eq. (2.14)

$$\frac{1}{\tau} = \frac{8\pi^3 \omega_s^3 n_I}{\eta_I^2 \eta_s^2 \omega_I} \sum_{i', f'} [\hat{\mathbf{e}}_s \cdot \Delta\chi_R \cdot \hat{\mathbf{e}}_I]^2 \delta(\omega_{i'} - \omega_{f'}) \cdot P(i') \quad (2.15)$$

$$\sum_{\omega_s} \delta(\omega_{i'} - \omega_{f'}) = \frac{V}{(2\pi)^3} \int \omega_s^2 d\omega_s \cdot \delta(\omega_{i'} - \omega_{f'}) p(i') \text{ for scattering frequency}$$

$$\omega_s = \frac{V}{8\pi^3} \frac{\omega_s^3 \eta_s^3}{c^3} \quad (2.16)$$

From eq. (2.12), (2.13), (2.14) and (2.15)

$$\frac{d\sigma}{d\Omega} = v * \frac{V}{N} * \frac{\eta_s}{\eta_I} * \frac{1}{c^4} * \frac{\omega_s^3}{\omega_I} \frac{\hbar(n+1)}{2M_r \omega_p \hbar} [\hat{\mathbf{e}}_s \cdot \Delta\chi_R \cdot \hat{\mathbf{e}}_I]^2 \quad (2.17)$$

$$\frac{V}{N} = \text{volume of primitive cell} = \frac{1}{a_0^3}$$

$$\frac{d\sigma}{d\Omega} = v \frac{\eta_s}{\eta_I} * \frac{1}{c^4} * \frac{\omega_s^3}{\omega_I} \frac{\hbar(n+1)}{2M_r \omega_p \hbar a_0^3} [\hat{\mathbf{e}}_s \cdot \Delta\chi_R \cdot \hat{\mathbf{e}}_I]^2 \quad (2.18)$$

We define  $S$  in angle by dropping  $v$ .  $n_I$  is number of incident photon per second on the sample.  $S$  is ratio between the scattered and incident power for a path length in solid. From (2.18)

$$S = n_I \frac{\eta_s}{\eta_I} * \frac{1}{c^4} * \frac{\omega_s^3}{\omega_I} \frac{\hbar(n+1)}{2M_r \omega_p \hbar a_0^3} [\hat{\mathbf{e}}_s \cdot \Delta\chi_R \cdot \hat{\mathbf{e}}_I]^2 \quad (2.19)$$

In eq. (2.19),  $\Delta\chi_R$  is material dependent quantity. It gives information about the dipole selection rule.  $\eta_s$  and  $\eta_I$  depend on scattered and incident frequency, respectively.  $[\hat{\mathbf{e}}_s \cdot \Delta\chi_R \cdot \hat{\mathbf{e}}_I]^2$  term gives the microscopic cross section. Here,  $S$  is macroscopic cross section.

This depend on the number of incident photon, forth power of scattered frequency

( $\omega_s \approx \omega_i$ ; equation 2.19). Raman cross section is proportional to number of incident photon and scattering volume. Raman cross-section is very weak. If we do not change the number of incident photon and increase the scattering volume, we can amplify the Raman signal. We want to amplify the Raman signal.

If the incident energy is close to the band gap of the material (energy of electronic transition), scattering enhancement up to  $10^6$  have been observed [147] and they are quite often of the order of  $10^3$  or  $10^4$ . Raman susceptibility will go to infinite. This process is called Resonance Raman. In  $\Delta\chi_R$ , first term is incoming and outgoing resonance, third term is incoming and fifth term is outgoing resonance. In our case, InAs has very low band gap material and highly reflective material but due to E1 transition which is close to resonance so we are getting good signal.

### 2.2.2 Stokes and anti-Stokes Raman scattering

when the electron excites from ground state and comes on the upper level of ground state, it is called stoke scattering and when electron excite from excited state of electron and comes on ground state, it is called anti-stoke scattering. Annihilation operator annihilate one phonon and the creation operator create one phonon in anti-stoke and stoke process, respectively. The scattering cross section is shown in above eq. (2.19) for stoke scattering, similarly we can write the scattering cross section for anti-stoke scattering.

$$S = n_I \frac{\eta_s}{\eta_I} * \frac{1}{c^4} * \frac{\omega_s^5}{\omega_I} \frac{\hbar(n)}{2M_r \omega_{ph} \alpha_0^3} [\hat{e}_s \cdot \Delta\chi_R \cdot \hat{e}_I]^2$$

The relative intensity of stoke is greater than anti-stoke due to population inversion. The population is worked out Boltzmann distribution below:

$$n_{ph}(\omega) = \frac{1}{\exp\left(\frac{\hbar\omega}{kT}\right) - 1} \quad (2.20)$$

(2.21)

$$\frac{I_{Stokes}}{I_{anti-Stokes}} = \frac{(\omega_I - \omega_S)^4 n + 1}{(\omega_I + \omega_S)^4 n}$$

$$\frac{I_{Stokes}}{I_{anti-Stokes}} = \frac{(\omega_I - \omega_S)^4}{(\omega_I + \omega_S)^4} \exp\left(\frac{\hbar\omega}{kT}\right) \quad (2.22)$$

The local temperature of system is measured from ratio of stoke to anti-Stoke's intensity and frequency of phonon. In present whole work, this is not feasible due to resonance enhancement. The E1 band gap of InAs is  $\sim 2.5$  eV and we are using wavelength from 458 nm to 514 nm which energy is close to band gap. The intensity of stoke and anti-stoke will not give the real value and calculated temperature is not correct using eq. 2.22.

### 2.2.3 Raman Selection rules

The microscopic cross-section is given by,

$$I_s = [\hat{\mathbf{e}}_s \cdot \Delta\chi_R \cdot \hat{\mathbf{e}}_i]^2 \quad (2.23)$$

The  $\hat{\mathbf{e}}_i$  and  $\hat{\mathbf{e}}_s$  are polarization of incident and scattered light, respectively and  $\Delta\chi_R$  is the Raman tensor, which depends on the symmetry of the structure and phonon vibration under consideration [146]. Calculated Raman cross section under different scattering configurations for (1T0) face are consolidated in the table 2.2.3.

*Table 2.2.3. Raman selection rule for zinc blende structure. x, y and z denote the set of three mutually perpendicular [110], [112] and [111] axes.*

Scattering configuration	TO	LO
x(z,z) $\bar{x}$	4/3 [d <sub>TO</sub> ] <sup>2</sup>	0
x(y,y) $\bar{x}$	2/3 [d <sub>TO</sub> ] <sup>2</sup>	0
x(y,z) $\bar{x}$ , x(z,y) $\bar{x}$	1/3 [d <sub>TO</sub> ] <sup>2</sup>	0

## 2.3 Instrumentation

Raman scattering is much weaker ( $\sim 10^{-8}$ ) than Rayleigh scattering (in which there is no frequency shift of excitation laser) [144] and detection of Raman signal in presence of Rayleigh thus require,

- 1) A laser light source: Raman scattering is a weak process and thus intense laser light source is required to obtain good signal. Further, property of laser such it's monochromatic nature to achieve spectral resolution is required.
- 2) Spectrometer: The main aim of a spectrometer is to separate and transmit a narrow portion of the optical signal required. Thus, it helps filter Rayleigh from Raman signal and measurement of Raman signal as a function of Raman shift in wavenumber( $\text{cm}^{-1}$ ).
- 3) Detector: It is used to detect the scattered photons i.e. intensity of output signal.
- 4) External optics is required to focus the laser beam on sample and collect and transfer the optical signal to the monochromator to achieve maximum output.

### 2.3.1 Light source: Laser

Raman scattering is a second order scattering process and thus, intense laser light source is required to excite the Raman spectra. Gas lasers are preferred for the excitation of Raman spectra. This is because, the line width of gas lasers (Ar ion laser  $\sim 0.01 \text{ cm}^{-1}$ ) is quite less, which is much smaller than operational spectral resolutions ( $\geq 1 \text{ cm}^{-1}$ ) of Raman systems used. Further, tightly focused ( $\sim 1 \mu\text{m}$ ) laser beam can achieve better spatial resolution in the case of micro Raman spectroscopy/mapping. We have used the 5 laser excitations of Ar ion laser 458, 476, 488 and 514 nm and 441.6 nm of He-Cd laser for Raman spectroscopy experiments reported in this thesis.

### 2.3.2 Filter: Spectrometer/spectrograph

A spectrometer consists of entrance and exit slit, focusing mirrors and a dispersive element (grating). The spectrometer system can be used in two configurations, i) monochromator and ii) spectrograph. A monochromator has entrance slit, exit slit, focusing mirrors, dispersive element and photomultiplier tube as detector, whereas, spectrograph has charge coupled device as a detector, which also works as an exit slit. When using monochromator one has to scan whole wavelength range in chosen steps, in line with spectral resolution. Thus, it takes large time depending upon the wavelength range and the steps in which one is taking the measurements. For example step size is  $0.5 \text{ cm}^{-1}$ , wavelength range to be scanned is  $250 \text{ cm}^{-1}$  and time taken for one step size is 20s, then total time taken to obtain Raman spectra is 1000s, whereas, when using spectrograph, total time consumed will be only 20s, if all other parameters are kept same. This is called multichannel detection, as range of wavelengths are simultaneously detected. Spectrograph are available in single and triple stages. Three factor that decide whether to use single, double or triple stage spectrometer/spectrograph are, i) Stray light rejection, ii) Resolution and iii) Throughput.

Single spectrograph uses one dispersive element. This type of spectrometer is good choice, when high throughput is more important than resolution and stray light rejection. Edge/notch filters are used with single spectrograph to attain required stray light rejection. The single stage spectrograph used for thesis work is Acton 2500i (single) monochromator with air cooled CCD detector, a part of SPM\_integrated Raman system set up, WiTec (Germany) and will be described later in section.

The double stage is preferably used as double monochromator, which has two dispersing elements i.e. as a spectrometer. It has high resolution, good stray light rejection and lesser throughput as compared to single stage.

Triple stage spectrograph can be used as spectrometer (triple additive) or as spectrograph when first two stages are used in subtractive configuration and dispersion of last stage determines spectral resolution of the system.

In both cases, throughput will be less. Triple stage Raman with double subtractive and third stage as a spectrograph with multichannel detection is used for most present studies, wherein double subtractive stage acts as a tunable notch filter. The model no. Trivista 557 with cooled CCD detector (S & I spectroscopy and imaging, Germany) is used for Raman spectroscopy and will be described later in section.

### **2.3.3 Detector: Charged-coupled device (CCD)**

CCD is an array of cells which captures light image via photoelectric effect. These photosensitive elements are called pixels. Each cell generates photoelectrons and stores them as electrons (charge). The number of photons detected depends on quantum efficiency and sensitivity of the pixel/CCD. Noise, dynamic range and gain determines measurability of signal against noise. Primary sources of noise in CCD are 1) Photon noise, 2) Dark noise and 3) Readout noise. Both LN<sub>2</sub> (~ 193°C) cooled CCD and thermoelectrically cooled (~ - 70°C) CCD's are commonly used in Raman systems to reduce thermal/dark noise as per requirement. Quantum efficiency for CCD in visible region is ~ 10 % (front illuminated) and 45% (back illuminated). Photon noise is the number of photoelectrons collected by CCD pixel shows a Poisson distribution and has a square root relationship between signal and noise, thus photon noise is  $\sim \sqrt{n}$  where n is number of incident photons. Readout noise is produced by CCD when conversion of analog signal to digital signal. This noise depends on the deviation associated with analog to digital convertor. It is typically ~ 3 electrons (rms) for 30 frames/sec reading speed.

## 2.4 Micro-Raman spectroscopy:

Single stage spectrograph with microscope attachment is used for micro Raman spectroscopy is shown in Fig. 2.4.1 and 2.4.2. The sample stage, vibration table, objective, beam splitter, laser coupler, edge/notch filter, video camera and output optical fiber are the major parts of the system as marked in the Fig. 2.4.2a. The incident laser light is carried via single mode optical fiber to laser coupler (it has dichroic mirror at  $45^\circ$  angle, which transmits wavelength of incident beam and reflected other wave length). Different objectives (20, 50,100x) are used to focus the laser beam on the sample. Further, the back scattered light passes through the laser coupler which contains edge/notch filter which filter laser line and transmits Raman signal. The scattered signal is carried through the multi-mode fiber to the spectrometer with thermoelectrically cooled CCD detector (Fig. 2.4.2b). The spectrometer has provision for 600/ mm, 1200/ mm and 2400/ mm grating which covers spectral range  $\sim 3600, 1500$  and  $600 \text{ cm}^{-1}$ , respectively at 488 nm. Back illuminated CCD model # DV401-BV with pixel size of  $26 * 26 \mu\text{m}^2$  is used for multichannel detection.

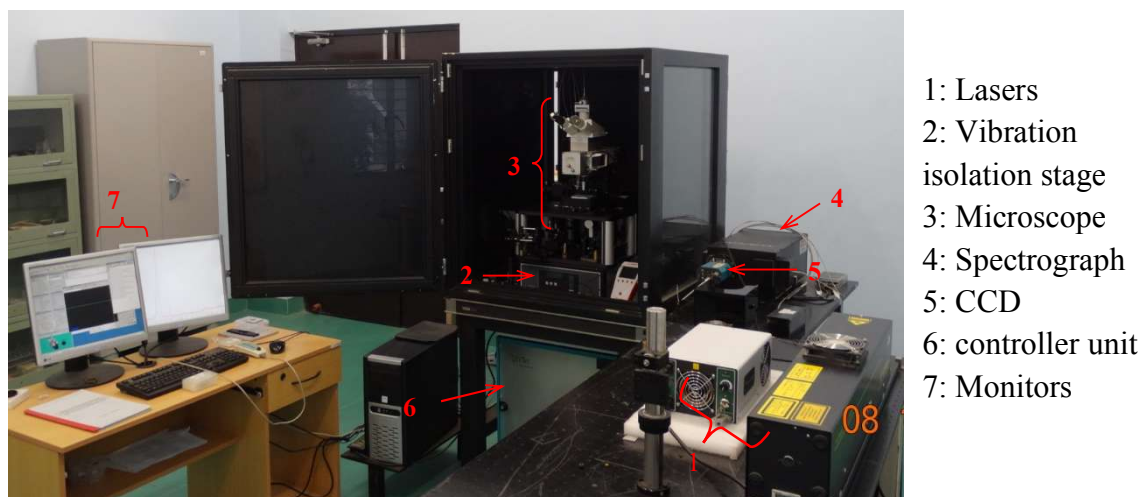


*Fig. 2.4.1 Alpha 300 S\_SPM integrated Raman system (Acton 2500i (single monochromator), WiTec) set up showing different parts as noted in the figure.*

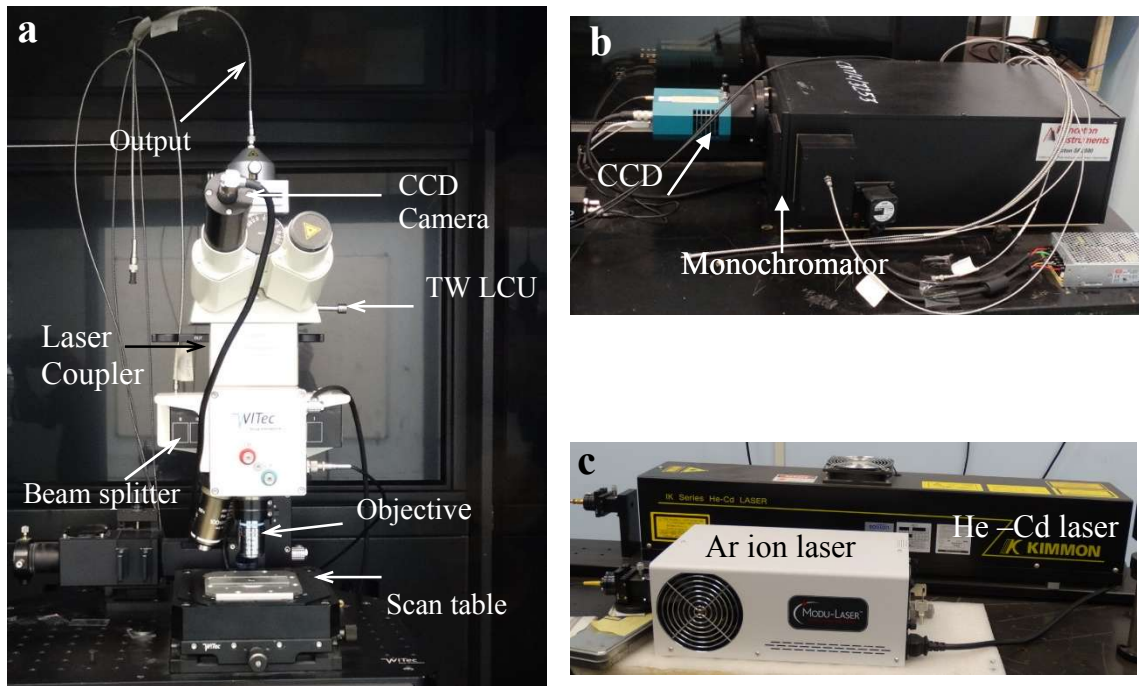


Fig. 2.4.2. (a) and (b) Enlarged view of microscope, and spectrometer shows different components, respectively, TW LCU: two way light coupling unit and (c) Enlarged view of lasers.

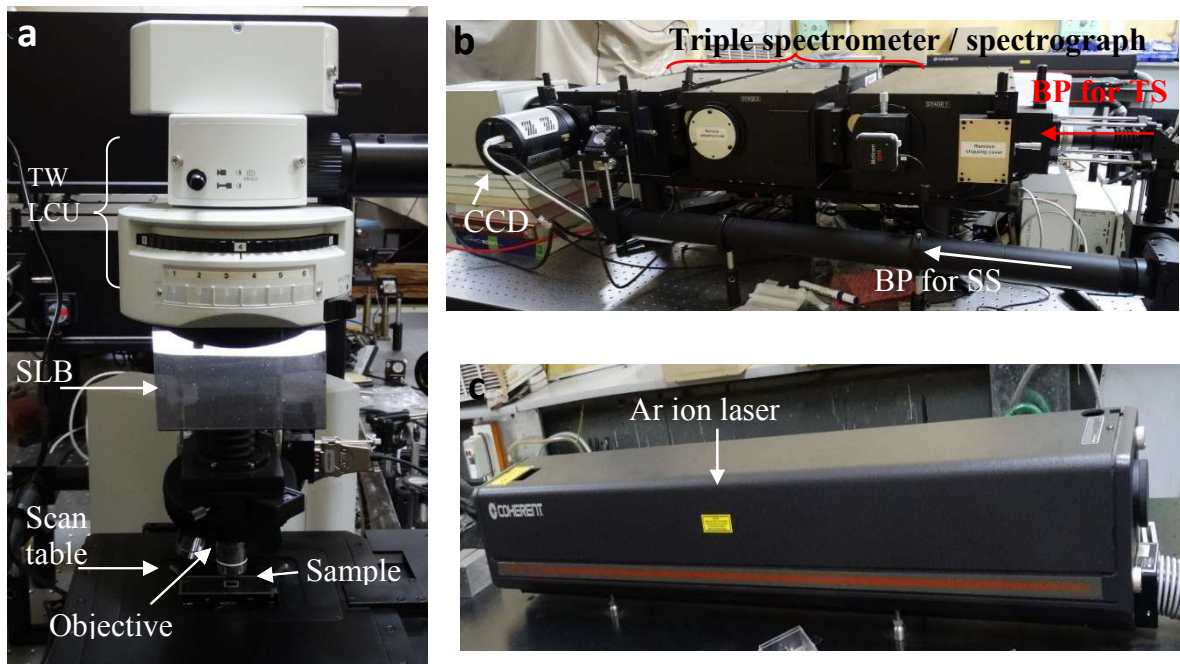


Fig. 2.4.3. (a) Front view of microscope with different components, SLB: scattered laser blocker TW LCU: two way light coupling unit, (b) Enlarged view of triple stage spectrometer and CCD, BP: beam path: TS: triple stage and SS: single stage (c) Enlarged view of laser.

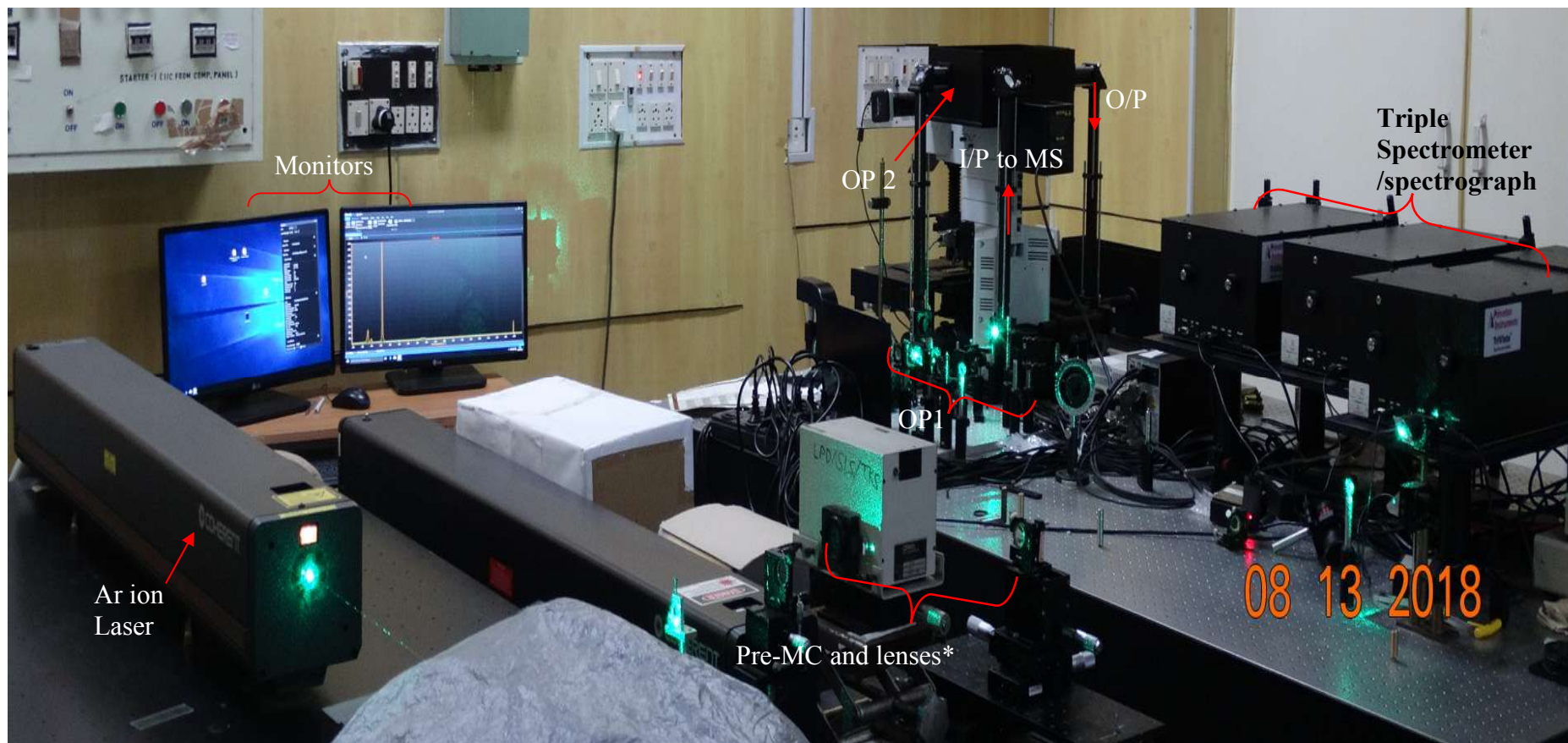


Fig. 2.4.3. (a) “Trivista 557”(S & I spectroscopy and imaging) Raman system set up showing different parts, MC: monochromator, OP1: optical asseble 1 (line filter, half wave plate, mirrors etc.), I/P to MS: input to microscope, OP2: optical asseble 2 (45<sup>o</sup> mirror, ND filter and beam splitter etc.) and O/P: output. \*: pre-monochromator and coupling lenses are not in beam path.

Triple stage Raman spectrograph model # Trivista 557” (S & I spectroscopy and imaging, Germany) of Spectroscopy and imaging system triple stage monochromator with air cooled CCD detector used for this work is shown in Fig (2.4.3 and 2.4.4). The dispersive stage has focal length of 700 mm. Thermoelectric cooled CCD model # PIXIS-256 OE, USA is used for multichannel detection (Fig. 2.4.3b). The 900, 900 and 1800 l/mm grating set is used for work presented in this thesis with first two stages (500 mm) in subtractive mode (Fig. 2.4.3b). Further, while using Raman spectroscopy as a local probe, it is important to consider i) Spatial resolution, ii) Depth of focus and iii) Spectral resolution as described below.

### 2.4.1 Resolution

**Spectral resolution**: Spectral resolution is ability to resolve two peaks separately when maxima of these peaks are very close to each other in frequency and intensity. The spectral resolution of the system is given by:

$$R_{\text{Spectral}} = d\lambda / \lambda^2 \quad (2.24)$$

$$d\lambda = 4d (dx)/f \quad (2.25)$$

$dx$  is the entrance slit width. The resolution can be improved by increasing i) the focal length, ii) grating grooves density and iii) reducing input slit width. In our case, CCD coverage per pixel is in the range of  $\sim 0.5\text{-}1.2 \text{ cm}^{-1}$ .

**Spatial resolution**: Spatial resolution is separation of positions in space which can be resolved as separate spatial points from corresponding Raman data and is given by diffraction limit below:

$$R_{\text{Spatial}} = 1.22 * \lambda / \text{N.A.} \quad (2.26)$$

$\text{N.A.} = n \sin \theta$ , where  $n$  is refractive index of medium and  $\theta$  is collection angle from objective to sample. For 100X and 50X objectives used for taking data, Numerical aperture (N.A.) = 0.9 and 0.5, which gives spatial resolution  $\sim 0.6$  and  $1 \mu\text{m}$  at 488nm, respectively.

**Depth of focus**: When the incident light is focused using objective, then the measure of the tolerance of the placement of the image plane in relation to the lens is called depth of focus, which decides depth resolution of the Raman spectra. The depth resolution (DR) is given by [148]. For DR for 100X and 50X are  $\sim 0.4$  and  $1.3 \mu\text{m}$  for 488nm, respectively.

$$\text{DR} = \lambda / (\text{N.A.})^2 \quad (2.27)$$

### 2.4.2 Polarized Raman spectroscopy

Polarized Raman spectroscopy using SPM integrated Raman system is performed using polarizer is placed in beam path, where both incident and scattered beams pass through it. In this way we could choose only two parallel polarization configurations i.e.  $x(z,z)\bar{x}$ ,  $x(y,y)\bar{x}$ . For  $x(y,z)\bar{x}$ ,  $x(z,y)\bar{x}$  polarizations, since it was not feasible to use polarization rotator in input beam path i.e. NW was instead rotated using  $360^\circ$  manually operated rotational stage, which was a involved experiment. The polarization data using Trivista 557 (S & I spectroscopy and imaging, Germany), was straightforward by putting polarizer (OP1) and analyzer with scrambler in the input and output beam paths, respectively. Spatially resolved polarized Raman spectroscopy is extensively used in the study presented in the thesis.

### 2.4.3 Temperature dependent Raman Spectroscopy

The temperature dependent Raman measurements are performed using LINKAM THMS 600 stage coupled with Jobin-Yvon Horibra LABRAM-HR at IUAC-UGC, Indore (Dr. V. Sathe). Ar ion laser line at 488nm is used for the excitation of Raman spectra. Spatial resolution of the Raman system is  $\sim 1 \mu\text{m}$  and one pixel coverage  $\sim 0.5 \text{ cm}^{-1}$  is used for temperature dependent Raman spectroscopy measurements. Low temperature Raman spectra for temperature from 300 K to  $\sim 70$  K on a InAs NW, which was already studied using AFM and polarized Raman spectroscopy. For this purpose, its location was identified using various optical images saved and noted for their relative positions from all sides. During low

temperature measurement on isolated NW, first the optical image of InAs NW, as well as surrounded sphere is noted in a notebook, then distances are noted for position of NW, where we are taking data and a sphere. By doing this, we ensured that at all temperature data is taken on same position on a NW for all temperatures. Raman spectra were taken at different temperatures as set after it's stabilization in the set value.

#### 2.4.4 Wavelength dependent Raman Spectroscopy

Wavelength dependent Raman spectroscopy is performed mainly to investigate it's use to study polytypism in InAs NWs with small diameter (< 600nm), where, polarized Raman data is difficult to obtain. Ar ion laser excitations 514.5, 488, 476.5 and 458nm are used for this purpose. Since, line filter of 476.5 and 458nm are not available, arrangement to put a small monochromator (Fig. 2.4.3: 18.5 cm) in the input beam path is made and the whole set up is needed to align for the purpose for each wavelength. Position on NW is optically marked with software position marking to take data on same position for each wavelength.

#### 2.5 Atomic force microscopy (AFM)

Two forces work, when two atoms are brought close to each other i) long range attractive force and ii) short range repulsive force. Combined force is given by the equation

$$F = \frac{A}{R^{12}} - \frac{B}{R^6} \quad (2.29)$$

F is resultant force between atoms, A, B is constant and R is distance between two atoms. The variation of resultant force with AFM tip-sample distance is shown in Fig. (2.5.1). Different shaded region corresponds to different force regions for different operating modes of AFM. In AFM, the probe tip is brought very close to the sample surface. AFM tip experience a repulsive force, when it is in close vicinity of the sample surface. This results into bending of the cantilever.

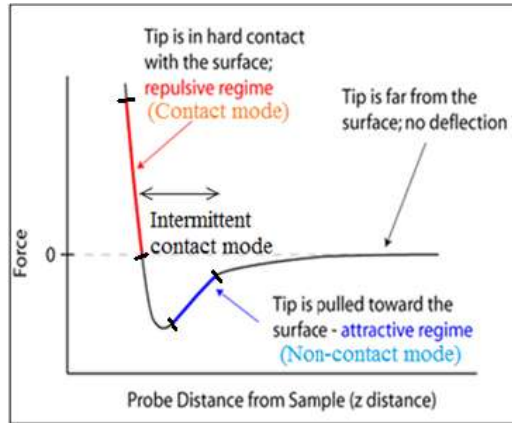


*Fig.2.5.1: Graph between force experiences by tip v/s its distance from the sample surface and distance*

A laser beam is directed on back of the cantilever in Fig. (2.5.2) which, after reflection passes to a position sensitive detector. Small deflection caused by the tip- sample interaction is recorded by a position sensitive photodiodes.

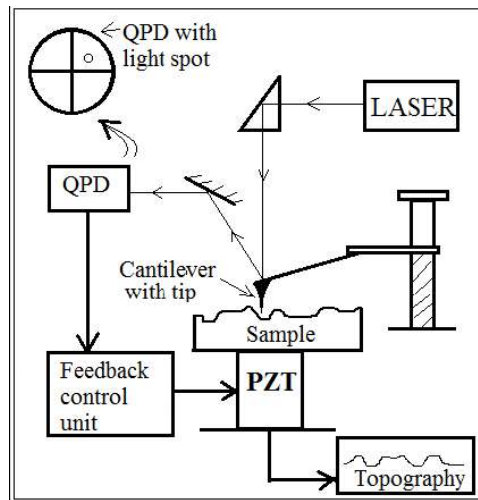


*Fig. 2.5.2: Schematic diagram*

Three modes of operation are described in brief in the following.

**Contact mode:** In this case the tip is in contact with the sample surface, however due to repulsive interaction between electron charge cloud of the tip atom and that of the surface atom, the tip is repelled back, which bends the cantilever and deviate the direction of the laser

beam. The main disadvantage is that the tip or sample can be damaged due to forcing of the tip into sample.

**Non-contact mode:** In this the tip is kept at small distance away from the sample surface. Therefore, in this method the sample damage can be avoided. In this mode the attractive force dominates and it arises due to polarization of the interacting atoms and is due to dipole-dipole interaction of tip and surface atoms.

**Tapping mode:** This mode is combined of contact and non-contact mode. The resolution is in contact mode higher than that due to non-contact mode, because in contact mode the interaction between tip and surface atoms is much more sensitive to the distance as compared to that in non-contact mode. In tapping mode, we get two advantages first is that the high resolution due to contact mode and second is that the no damage of tip or surface due to non-contact mode. The tip is oscillated in the vicinity of the surface at a distance  $\sim 5 \text{ \AA}$  to  $50 \text{ \AA}$  such a way that it nearly touches the sample during its cycle of oscillation.

**Resolution:** Resolution of AFM is determined by the minimum radius of the tip as the interaction area between the tip and sample depends upon the tip radius. Tip radius varies from  $\sim 20 \text{ nm}$ .

AFM is useful to obtain surface morphology of the nanostructures under investigation.

The AFM images of uniform, tapered and bent InAs NWs, performed in non-contact mode are shown in Fig. 2.5.3a b and c, respectively. Long tapered MNW image is also shown in Fig. 2.5.3d.

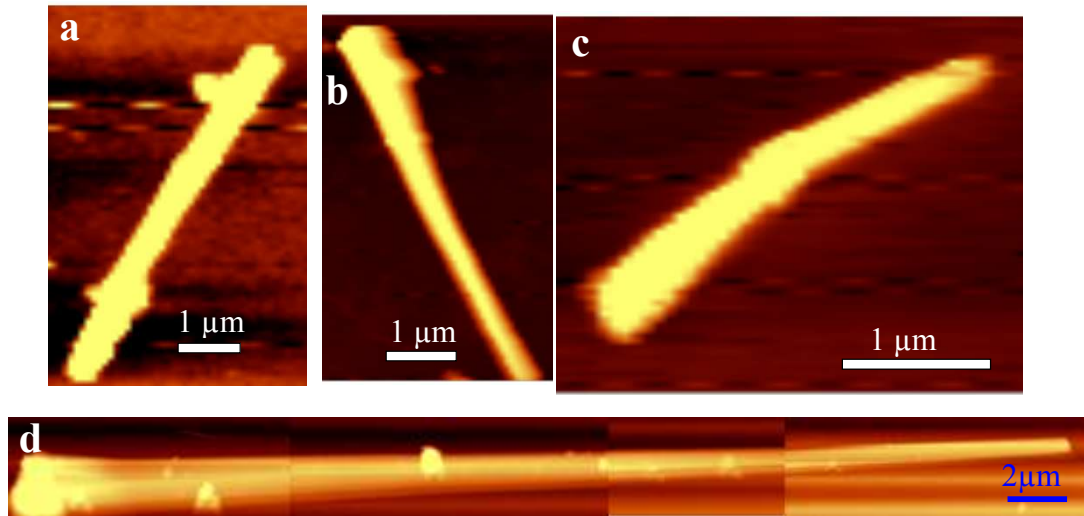


*Fig. 2.5.3. (a), (b), (c) and (d) AFM image of uniform, tapered and bent NW and long tapered MNW, respectively at 50 nm resolution.*

## 2.6 Electron microscopy

In electron microscopes, electrons are used in place of electromagnetic radiation and electrostatic or magnetic lenses are used instead of glass lenses. According to wave-particle duality electrons have both particle and wave nature [149].

Advantage of using electrons is that their wavelength can be tuned to a very small value, just by changing their energies/momentum so that the resolution can be increased because resolution is wavelength dependent. Electron microscopes are classified in two categories – scanning electron microscopy (SEM) and transmission electron microscopy (TEM).

### 2.6.1 Scanning electron microscopy

The SEM uses the focused beam of high energy electron to generate a variety of signals at the surface of sample. Secondary electrons have low energy but high yield. The secondary electron generated inside the bulk gets absorbed within the sample. Only the electrons generated in the surface of the sample can escape from the sample. The secondary electrons

are collected in faraday cage which are detected by scintillation material to image the sample surface. The scintillation material produces photon when struck by an electron. SEM images also gives surface morphology.

**Resolution:** Resolution depends on the beam size. Beam with smaller diameter resolves more detailed structure of the sample as compared to beam with larger diameter. Beam diameter can be decreased by increasing the current in the condenser lens. Using 15 kV, resolution  $\sim 18 \text{ \AA}$  can be obtained [149]. SEM images on InAs NWs were taken using XL30CP (30 kV) (Philips, Holland) and CARLZEISS SIGMA field emission (FE)-SEM (Jena) (Rashmi Singh, LMS, RRCAT) images are shown in Fig 2.6.1.

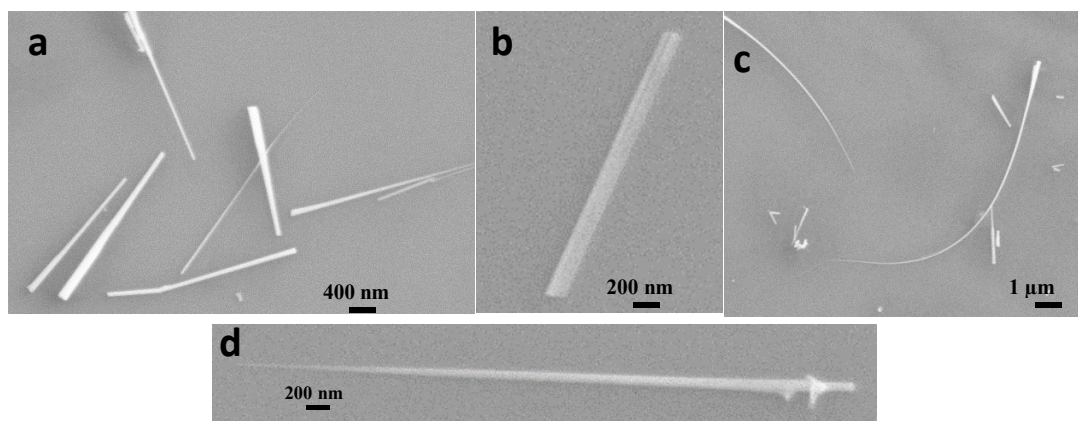


*Fig. 2.6.1: (a) Show the SEM image of InAs NWs (b), (c) and (d) with uniform, bent and tapered InAs NW, respectively at  $18 \text{ \AA}$  resolution.*

## 2.6.2 Transmission electron microscopy (TEM)

Electron of very high energy (typically  $\approx 200 \text{ keV}$ ) compared to that used in SEM, are used in TEM, which pass through a series of magnetic lenses. The various component of TEM are electron source, condenser lens, specimen, objective lens etc. there are some additional lenses in different microscopes in order to improve the image quality and resolution. In TEM, where an electron beam interact with a thin specimen and passes through a specimen. Due to

interaction with sample some of the electrons go through coherent elastic scattering, incoherent elastic scattering, and rest goes through incoherent inelastic scattering.

The inelastically scattered electrons produce noise in the image. Acceleration voltage decides the velocity of electron, wavelength, and the resolution of the microscope. Since the electron has a very high velocity so wavelength of the electron using relativistic correction is given by [149],

$$\lambda = \frac{h}{\sqrt{2m_0 eV \left(1 + \frac{eV}{2m_0 c^2}\right)}} \quad (2.30)$$

Using  $\lambda$  with acceleration voltage 200 kV resolution achieved in TEM is  $2.4 \text{ \AA}$ . The electron beam gets collimated and passes the condenser aperture and fall the sample surface. Samples should be very thin ( $\sim 100 \text{ nm}$ ) to obtain the information about transmitted electrons. Here electron has enough energy to travel through the specimen and these electrons get scattered in the specimen. The transmitted beam is focused by an intermediate lens. Selected area diaphragm is used to choose of the elastically scattering electrons to form the image of microscope.

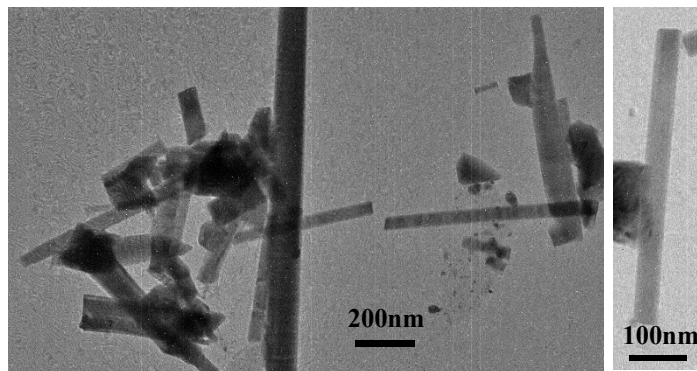


*Fig.2.6.2. Show the TEM image of NWs at  $2.4 \text{ \AA}$*

The beam focused the fluorescent screen and strikes the screen and light is generated. The darker area of the image represents those areas of the sample, where electron is more. The lighter areas of the image represent those areas of the sample that more electrons are

transmitted through it. For scattered electrons have to be transmitted through the sample should be thin. TEM also in diffraction mode. By the Bragg's law, transmission beam get diffracted from the atoms of the sample. So we get diffraction pattern and by this, we can get information about crystallographic such as crystalline phases, amorphous regions, crystal orientation and defects of the sample. For TEM measurements Phillips CM 200 was used (Dr. Himanshu Srivastava, SUS, RRCAT).

**High resolution transmission electron microscope (HRTEM):** The high-resolution transmission electron microscopy uses both the transmitted and the scattered beams to create an interference image. It image can be as small as the unit cell of crystal. In this case, the outgoing modulated electron waves at very low angles interfere with itself during propagation through the objective lens. All electrons emerging from the specimen are combined at a point in the image plane. HRTEM has been extensively and successfully used for analyzing crystal structures and lattice imperfections on an atomic resolution scale [150].

**Selective area diffraction method (SAED):** SAED is an experimental technique, which can be performed using TEM. It is basically called diffraction method, where, we let electron beam fall on selected area and the resulting diffraction pattern is produced by transmitted electrons through the sample. This gives information about local structure/s of an area selected on a nanostructure [151].

**Resolution:** Using 200 kV the resolution achieved is 2.4 Å.



## **Chapter 3**

# **Time evolution studies of laser induced chemical changes in InAs nanowire**

*“Scientific discovery and scientific knowledge have been achieved only by those who have gone in pursuit of it without any practical purpose whatsoever in view” — Max Planck*

### 3.1 Introduction

III-V nanowires (NWs) are realized to play a potential role in the advanced devices like, high performance field effect transistors, photodetectors [107-108], chemical/biosensors and thermo electric devices [100-101]. InAs nanowires, in particular, find an application in high speed circuits, other devices like superconductor Josephson junction devices [152] dilute magnetic semiconductor devices [153]. InAs has very low band gap material  $\sim 0.36$  eV which is used in IR detector. Promising thermoelectric power generation has also been proposed for low band gap InAs NW material [154]. It has intrinsic charge carrier concentration  $\sim 10^{15}\text{cm}^{-3}$  [155]. InAs nanowire is very interesting material because of their small electron effective mass, high electron mobility [136], a larger energy level separation strong quantum confinement effect, a higher efficiency lower threshold at room temperature as compare to other semiconductor nanowires [157]. They can applied as a device point of view in electronics and optoelectronics devices based on NW.

Earlier, Raman spectroscopy was performed at single InAs micro-wires (MW) along the length of MW as Raman imaging. It was found that the NW has been damaged in Raman mapping but it is not damaged using spatially resolved Raman spectroscopy. The time evolution study of Raman spectra showed damage is happening on surface while core is intact, which can be useful for material processing. Material processing using focused laser beams is now-a-days a widely used technique for various purposes like laser induced crystallization, doping, alloying, inter-diffusion, annealing, oxidation etc. High spatial resolution and position control can be achieved using laser induced processing [154]. Study by Yazji et al. shows that laser can be used for tailoring and manipulating the thermal

conductivity of a single NW, which is of interest for thermoelectric application [155]. However, to enable us to do the desired processing, it is important to understand the process of modification on laser irradiation on InAs NWs. The systematic study of laser irradiation with various laser power densities monitored by time evolution of Raman spectra is presented in this chapter.

**Background:** Sample S1 as noted in chapter 2, contains InAs nanowires of different sizes and shapes. In this sample, the uniform [diameter (d)  $\sim$  500 nm -2  $\mu$ m, length (L)  $\sim$  10-60  $\mu$ m], bent tapered (base d  $\sim$  800 nm- 2.2  $\mu$ m, tip d  $\sim$  300-800 nm, L  $\sim$  30-80 $\mu$ m) and straight tapered (base  $\sim$  800 nm- 2.5  $\mu$ m, tip d  $\sim$  300 – 800 nm, 10-80  $\mu$ m) MNWs are observed using. Here, we will refer name NW when wire  $\sim$  < 1  $\mu$ m, MW when d > 1  $\mu$ m and MNW for tapered when dia varies  $\sim$  1  $\mu$ m to 300 nm. In this chapter, we have used mainly uniform wire and tapered MNWs.

Earlier, Raman imaging was performed on sphere to see the image of InAs sphere. According to Raman selection rule, InAs with Zinc blende structure will have three optical phonons i.e. two degenerate TO and one LO phonon. The optical image is shown in Fig 3.1.1.a. The Raman image is generated by taking the intensity of peak which is range of TO and LO phonon  $\sim$  from 200 to 250  $\text{cm}^{-1}$ . The Raman spectra are shown in Fig 3.1.1.c. The position from 1 to 3 is marked in Raman image which is shown in Fig. 3.1.1.4b and corresponding Raman spectra shows that the TO and LO phonons of InAs are observed  $\sim$  217.5 and 238  $\text{cm}^{-1}$ , respectively which are bulk values of InAs phonons [157] (Fig. 3.1.1.c).

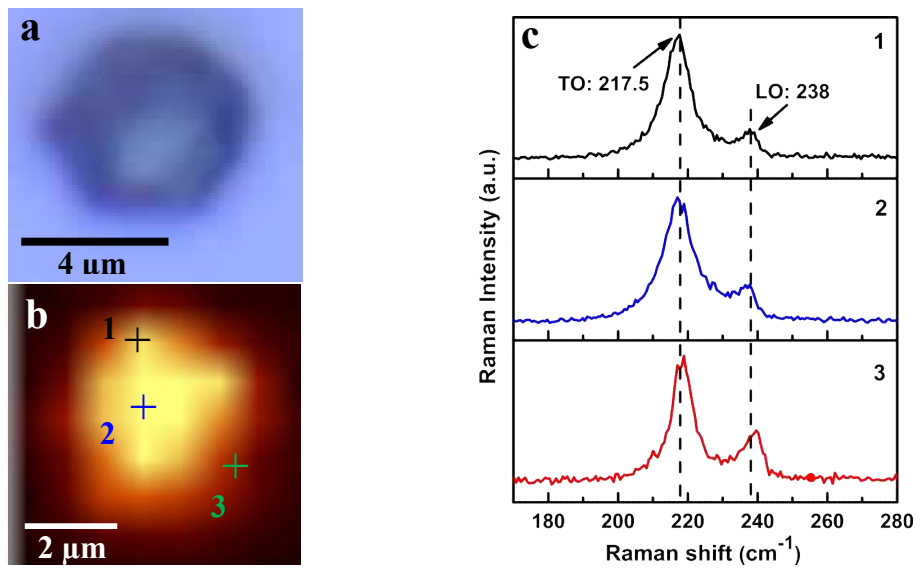


*Fig 3.1.1.1: (a) Optical image of InAs sphere b) Raman mapping generated by taking intensity from 215-220  $\text{cm}^{-1}$  and c) Raman spectra at position 1, 2 and 3 which are marked in the Raman image.*

Raman mapping was performed on the tapered InAs micro-nanowire (MNW), as shown in Fig 3.1.1.2. The optical image is shown inset of Fig. 3.1.1.2a. The diameter of base and tip are  $\sim 1.2 \mu\text{m}$  and  $800 \text{ nm}$ , respectively and length  $\sim 20 \mu\text{m}$ .

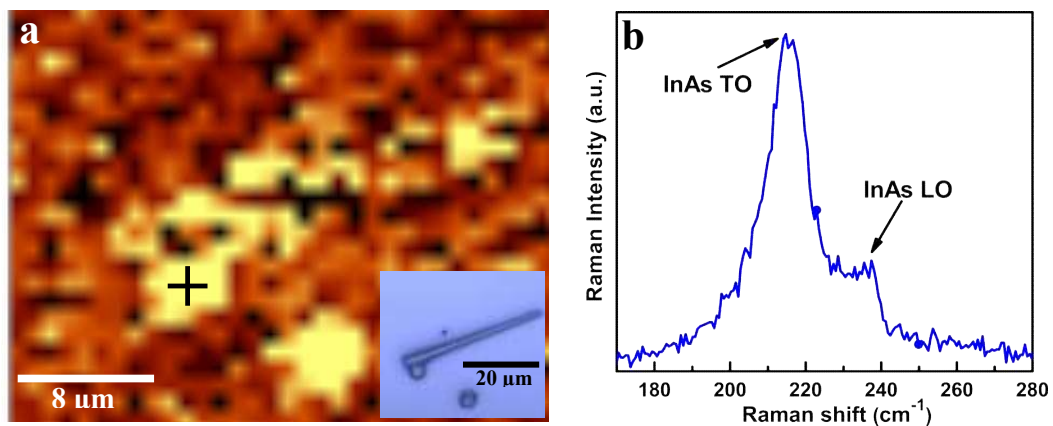


*Fig. 3.1.1.2: (a) Generated Raman image of InAs MNW to take the intensity from 210-220  $\text{cm}^{-1}$ . Inset Fig show optical image of InAs NW before Raman imaging and b) Raman spectra for marked positions on the Raman image.*

The Raman image is generated using intensity of phonon in the range  $\sim 210 - 220 \text{ cm}^{-1}$  which is shown in Fig. 3.1.1.2a. Representative Raman spectrum is shown in Fig 3.1.1.2b. Raman image, shows broken MNW, unlike optical image, so we looked at optical image again (Fig. 3.1.1.3a) after Raman mapping. This shows melting has taken place, where Raman image does not show presence of InAs.

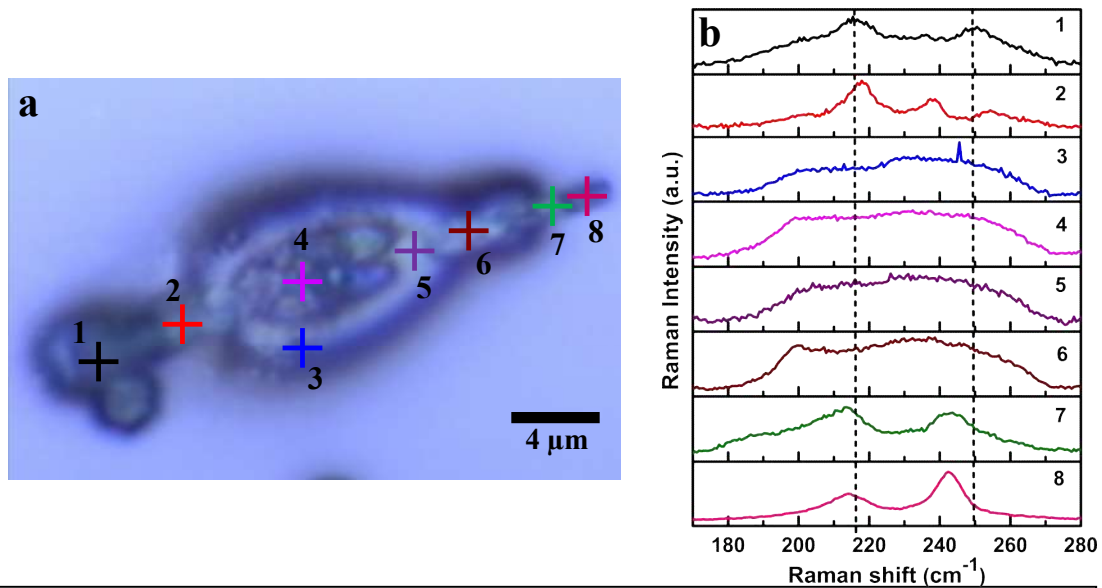


*Fig. 3.1.1.3: (a) Optical image of InAs MNW after Raman mapping (b) Raman spectra which are taken at position marked in optical image.*

After Raman mapping, spatially resolved Raman spectroscopy (SRRS) was performed over MNW region, which shows broad spectrum in  $200-300 \text{ cm}^{-1}$  region (Fig.3.1.13b). Later Raman mapping with lowest possible laser power and acquisition time was performed to note that damage is less (Fig 3.1.1.4b), but still significant.

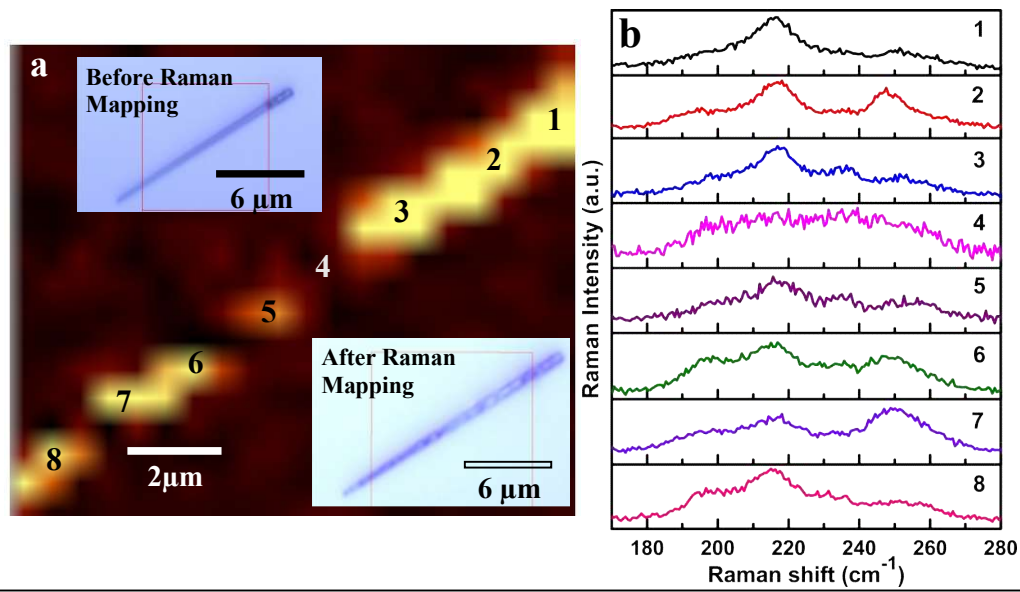


Fig 3.1.1.4: (a) Raman image generated using intensity of phonon in the range of  $150\text{-}300\text{ cm}^{-1}$ , inset shows the optical images of InAs MNW before and after Raman mapping b) Raman spectra for marked positions 1-9 in MNW image.

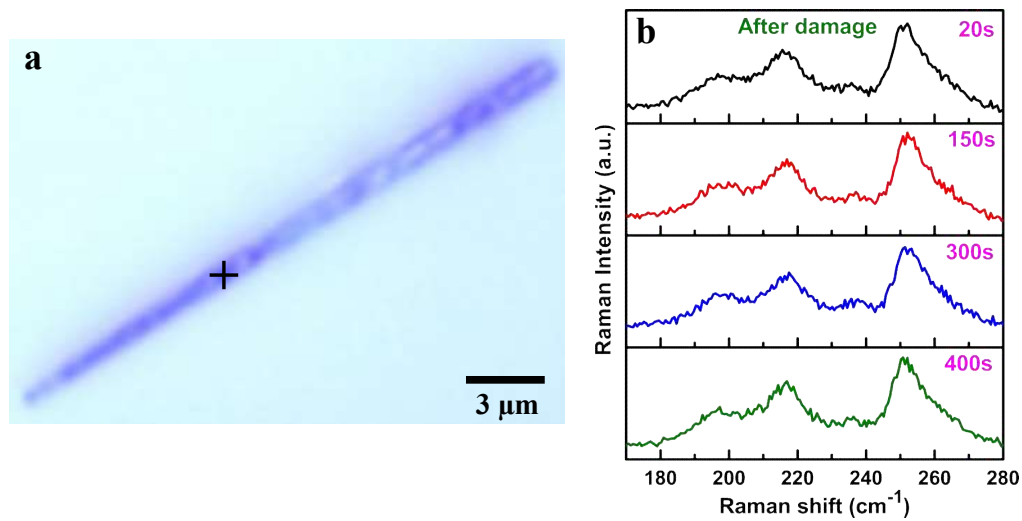


Fig 3.1.1.5: (a) Optical image of InAs MNW after Raman mapping b) Corresponding time dependent Raman spectra.

To understand process of damage, time evolution of Raman spectra was measured on partially damaged but intact MNW, as shown in Fig. 3.1.1.5 b. The spectra show strong asymmetrical additional structure  $\sim 250\text{-}260$ , which changes lineshape and frequency as a

function of time. The Raman spectra and optical image shows that core of InAs seems to be intact, but surface may be damaged /modified.

This local modification of InAs MNW can be used for an advantage, however, for that purpose process needs to be well understood. It has been seen that a local modification on a nanometer scale can be used to control the relevant properties of nanostructures [155- 156, 158].

The systematic study of this time evolution on InAs MNWs is presented in the next section.

## **3.2 Systematic study of Time evolution of Raman spectra on laser irradiation of InAs NWs**

To avoid effect of dimension etc, initially uniform wire was chosen for the systematic time evolution Raman study. Detailed Raman spectra can be generated by using time series Raman spectroscopic measurements.

### **3.2.1 Experimental**

The uniform wire ( $d \sim 900$  nm and  $l \sim 36$   $\mu\text{m}$ ) as shown in the image (inset Fig.3.2.2.1a) is chosen for systematic study of laser power density using 488nm irradiation. All the data shown for this study is on similar dimensioned NWs kept in the same orientation for Raman measurements. The Raman spectroscopy is performed at laser power density (LPD)  $\sim 250$   $\text{kW}/\text{cm}^2$  for 500s by taking 500 data points with acquisition time of 1s. The major changes in Raman spectra are observed after  $\sim 50$ s. Further, no change is observed in Raman spectra over 400 s. Therefore, the time series is chosen for 8 min and Raman spectra is recorded after every 10s i.e. 50 data points. We have performed time series Raman spectroscopy measurements for LPD varying from 30 to 800  $\text{kW}/\text{cm}^2$  for ten discrete LPDs. Each time

series measurement was performed on position spatially separated by 2-3  $\mu\text{m}$  on a NW to avoid heating due to earlier studied time series to affect the next time series. Here, we needed to use two horizontal NW to cover the entire range of LPDs noted above. The duration of time series was decided to be  $\sim 8$  minutes, as the preliminary data on several other NWs showed that over 8 minutes, time evolution of Raman spectra stops i.e. after 8 minutes no major change in Raman spectra is observed.

### 3.2.2 Systematic laser power dependence study of surface modification on laser irradiation

On the basis of consolidated observations made in the different laser power density regime, data is divided in the three different regimes of power density i) 30 - 140  $\text{kW}/\text{cm}^2$  (low LPD: LLPD) in which only TO and LO like mode are observed, ii)  $\sim 200$ -500  $\text{kW}/\text{cm}^2$  (medium LPD: MLPD) in which strong variation in additional mode and iii)  $\sim 600$ -800  $\text{kW}/\text{cm}^2$  (high LPD: HLPD) in which oscillatory behaviour in intensity ratio of TO (InAs) / additional mode is observed.

Above threshold value of LPD  $\sim 140$   $\text{kW}/\text{cm}^2$ , additional modes other than predicted by group theory for InAs are observed, which show constant change in intensity and frequency. Two major possibilities were considered, i) The additional modes are from InAs and may be related to different structure or occur due to disorder and ii) They belong to oxidation or melting of InAs. He [159] and Yazji et al. [155] has reported melting of GaAs and InAs NWs, respectively. The detailed analysis considering the above is given in the following.

**LLPD region (30 -150  $\text{kW}/\text{cm}^2$ ):** The optical image of NW is shown as an inset in Fig. 3.2.2.1a, which shows time evolution of Raman spectra (10s to 500s) at 30  $\text{kW}/\text{cm}^2$ . At this LPD, only strong TO and a very weak LO phonons are observed  $\sim 214$  and  $237.5$   $\text{cm}^{-1}$  with

FWHM  $\sim 12$  to  $5$   $\text{cm}^{-1}$ , respectively. During the whole time series, no changes in TO phonon frequency is observed. At increased LPD to  $\sim 100$   $\text{kW}/\text{cm}^2$  and  $140$   $\text{kW}/\text{cm}^2$  also shows similar behavior (Fig. 3.2.2.1a and b) of TO phonon. Further, increase LPD  $\sim 140$   $\text{kW}/\text{cm}^2$ , no changes occur except increases in intensity of TO phonon which is expected at higher LPD. In this region which is named as low LPD  $\sim 30$ - $150$   $\text{kW}/\text{cm}^2$ , we have observed only TO and LO phonon mode of InAs.

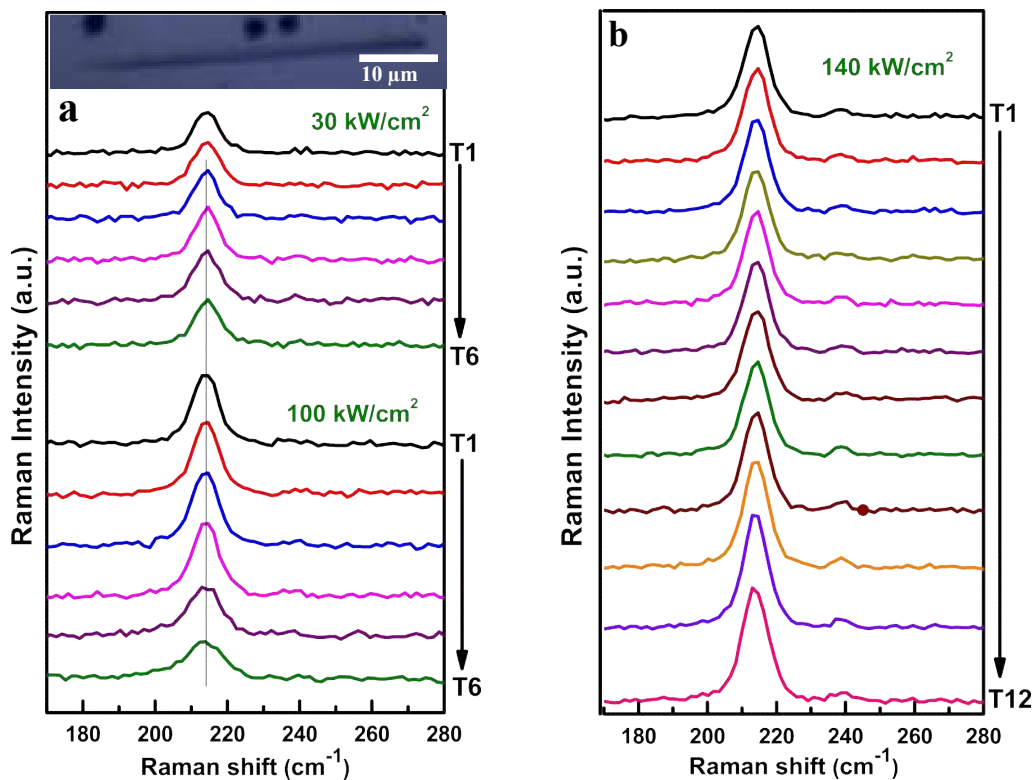
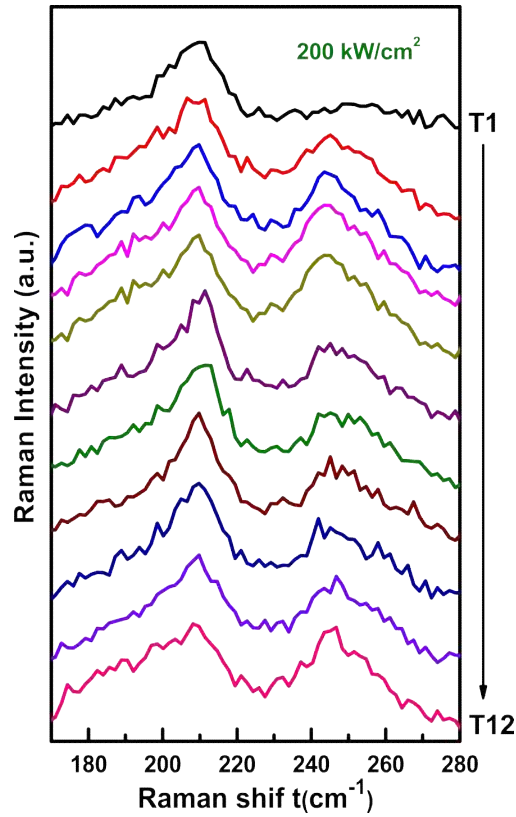


Fig 3.2.2.1: (a) Time evolution of Raman spectra of the InAs NW (image shown in the inset) from T1 (10s) to T6 (500s), showing top and bottom 6 spectra at LPD  $\sim 30$  and  $100$   $\text{kW}/\text{cm}^2$ , respectively and b) Time evolution of Raman spectra from T1 (10s) to T12 (500s) at LPD  $\sim 140$   $\text{kW}/\text{cm}^2$ .

**MLPD (200 - 500  $\text{kW}/\text{cm}^2$ ):** As the power density is increased to  $\sim 200$   $\text{kW}/\text{cm}^2$ , a completely different phenomenon is observed. The time evolution of Raman spectra is shown in Fig 3.2.2.2. Starting from T1 (at 10s) to T12 (at 500s). Two broad structures at 215 and 245  $\text{cm}^{-1}$  start appearing and their relative peak intensity varies with time. Large asymmetry

is observed in lower frequency side of TO (InAs) which is indicating that some new modes are present there.



*Fig 3.2.2.2: Time evolution of Raman spectra of the InAs NW from T1 (10s) to T12 (500s) at LPD  $\sim 200 \text{ kW/cm}^2$*

Hereafter, we show data on the second wire with  $d \sim 800 \text{ nm}$  and  $L \sim 36 \mu\text{m}$ . Since, it has slightly different dimensions, we have repeated time series with similar LPDs i.e.  $\sim 200$  and  $250 \text{ kW/cm}^2$  (Fig. 3.2.2.3). Here, we observed major changes as observed in Fig 3.2.2.2 after 200s (T6) and similarly upto 100s for  $250 \text{ kW/cm}^2$ .

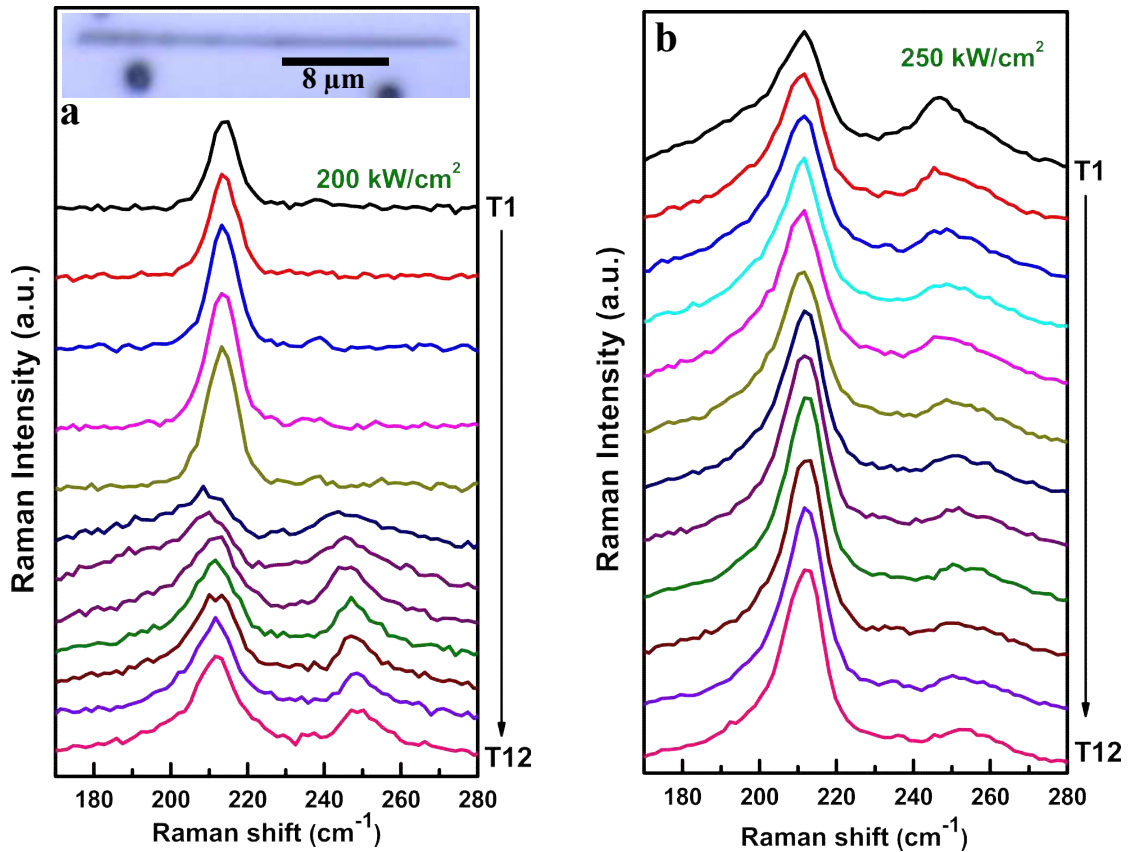
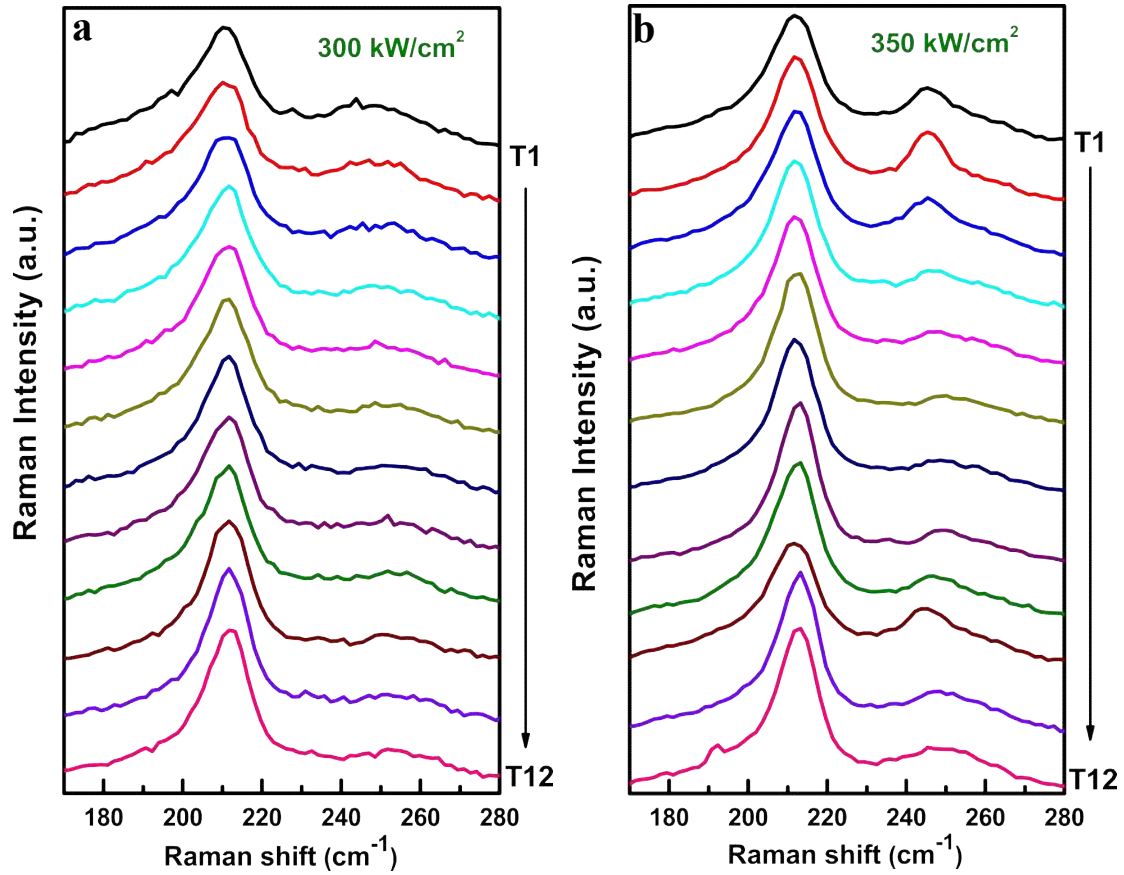


Fig 3.2.2.3: (a) and (b) time evolution of Raman spectra of the InAs NW (image shown in the inset) from T1 (10s) to T12 (500s) at LPD  $\sim 200$  and  $250 \text{ kW/cm}^2$ , respectively

Time evolution of Raman spectra at  $300$  and  $350 \text{ kW/cm}^2$  (Fig 3.2.2.4) show spectra similar to  $250 \text{ kW/cm}^2$ . When LPD is increased to  $\sim 450 \text{ kW/cm}^2$ , drastic change in the intensity of additional mode is observed as well as the frequency of the mode changes to  $\sim 245 \text{ cm}^{-1}$  at 10s (T1). With time increases, the intensity of this additional mode increases w.r.t. TO phonon. The line shape of additional mode varies from T1 to T9. Further, at T9, the frequency of this mode is blueshifted to  $250 \text{ cm}^{-1}$  from  $245 \text{ cm}^{-1}$  (T1). Before analyzing it further, we need to know the frequencies and relative intensities of these additional modes.



*Fig.3.2.2.4: (a) and (b) Time evolution of Raman spectra of the InAs NW (image shown in the inset) from T1 (10s) to T12 (500s) at LPD  $\sim$  300 and 350 kW/cm<sup>2</sup>, respectively*

For this purpose, we have deconvoluted these Raman spectra using minimum required Lorentzians. Raman spectra with deconvoluted peaks are shown in Fig 3.2.2.5b for time at T1 (10s), T2 (200s), T3 (300s), T4 (400s) and T5 (500s). In Fig. 3.2.2.5b, at T1, strong and weak additional peaks are observed at  $\sim$  192, 243 and 180, 258 cm<sup>-1</sup>, respectively. The peak  $\sim$  192 cm<sup>-1</sup> blue shifts to 197 at T5 (500s). The peak  $\sim$  243 cm<sup>-1</sup> first redshifts and then blue shifts from 100 to 500s. The broad mode shifts  $\sim$ 258 and 253 cm<sup>-1</sup>. At T5, strong mode appears at  $\sim$  254 cm<sup>-1</sup> and all other modes disappear.

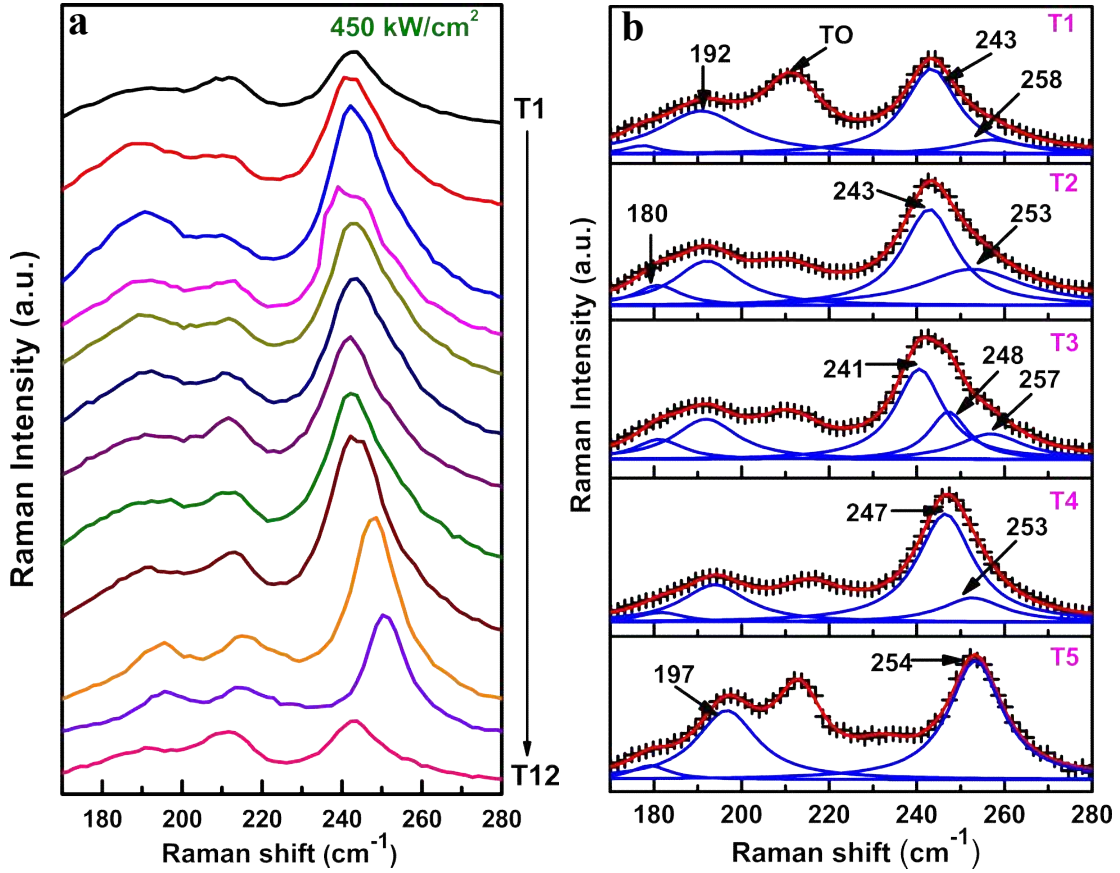


Fig.3.2.2.5. (a) Raman spectra of the time series from T1 (10s)-T12 (500s) At LPD  $\sim 450 \text{ kW/cm}^2$  and (b) Deconvoluted Raman spectra showing the time evolution of the peaks in the range of 180-200, 240-258  $\text{cm}^{-1}$  from T1(10s) to T5(500s). Cumulative fit (red solid line) to the raw data (+) and separate Lorentzian fits are shown with blue solid line.

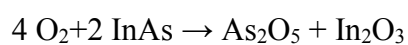
At T3, three mode  $\sim 241, 248$  and  $257 \text{ cm}^{-1}$  coexist. The frequency and FWHM of these mode are changing  $\sim 2\text{-}5$  and  $3\text{-}5 \text{ cm}^{-1}$ , respectively which will be further investigated. Initially, peak  $\sim 241 \text{ cm}^{-1}$  gains in intensity significantly with a fall in intensity of mode  $\sim 253 \text{ cm}^{-1}$ , whereas, the opposite occurs at later time (T5). At later time (500s), mode  $\sim 247 \text{ cm}^{-1}$  disappears ultimately, whereas modes  $\sim 254$  and  $197 \text{ cm}^{-1}$  appear and persist till end of the measurement as shown in T5 of Fig.3.2.2.5b. Here, important point to note is that peaks in the range of  $\sim 180\text{-}200 \text{ cm}^{-1}$  are observed along with peaks in the range  $\sim 240\text{-}260 \text{ cm}^{-1}$ , which

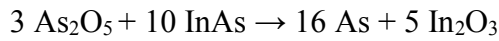
indicates that the origin of lower and higher frequency peaks  $\sim 180\text{-}200\text{ cm}^{-1}$  and  $240\text{-}260\text{ cm}^{-1}$  is same.

The first possibility of additional peaks in the range  $\sim 240\text{-}245\text{ cm}^{-1}$  is considered to be a Plasmon -LO phonon coupled mode ( $L^+$ ), due to photoexcited carriers. The LO Phonon-Plasmon mode interaction results in the formation of two hybrid excitations of the Longitudinal-Optical-Phonon-Plasmon modes denoted by  $L^+$  (at frequency higher than LO) and  $L^-$  (at frequency lower than LO). In case of  $L^+$  mode, its intensity should increase with excitation power density followed by a blueshift in frequency. However, in the present study, we find that observed phonon redshifts from  $244$  to  $240\text{ cm}^{-1}$  at still higher powers. Furthermore, Phonon-Plasmon coupling in InAs nanowires is reported by several authors [160-162], where L- mode is mostly observed  $\sim 232\text{ cm}^{-1}$  and  $L^+$  lies at much higher frequency range, which is difficult to be identified in the spectra for power densities  $200\text{-}500\text{ kW/cm}^2$  [160]. Hence, the possibility of the additional modes being coupled Plasmon-phonon mode is ruled out. Next the possibility considered is a thermal oxidation of InAs due to laser irradiation, as the experiment was performed in the ambient conditions. While performing these measurements it was found that the phonon frequency and intensity changes with time. In the low LPD, no appreciable change occurs in the NW spectra with evolution of time. Most interesting observations are made in the MLPD regime.

It is important to mention here that no report is available so far in the literature, which can explain the observation of the peaks in the range of  $\sim 240\text{-}245\text{ cm}^{-1}$  and  $180\text{-}190\text{ cm}^{-1}$  in InAs NW and the changes in their relative intensity as a function of time and excitation power density. Among the additional modes mentioned above, only peaks at  $257\text{-}258\text{ cm}^{-1}$  and  $198\text{ cm}^{-1}$  are well reported, which are attributed to double degenerate  $E_g$  mode ( $198\text{ cm}^{-1}$ ) and the  $A_{1g}$  mode ( $257\text{ cm}^{-1}$ ) of crystalline arsenic (As). There are several reports on the native oxide/ thermal oxide grown on III-V semiconductors like GaAs and InAs bulk and

their NWs on thermal oxidation by laser heating or other methods, where these two peaks of crystalline As were observed [155,159,163]. Yazji et al. reported observation of amorphous (broad hump  $\sim 220\text{ cm}^{-1}$ ) and crystalline ( $198$  and  $257\text{ cm}^{-1}$ ) form of arsenic (As) at different power density level of laser heating of a GaAs NW [155]. J. He et al. also observed crystalline As peaks in their study of Raman mapping of laser induced changes of InAs NW [159]. The frequency positions of some of the additional Raman modes in the present study are observed close to the As related peaks, although they clearly appear as additional separate peaks with respect to those of As. Here, we have observed Raman spectra is changing in time. To identify these additional modes in the range of  $\sim 180\text{-}195$  and  $240\text{-}255\text{ cm}^{-1}$ , we now explore the possibility of chemical changes in the InAs nanowires, which are expected to take place due to thermal oxidation on InAs NW surface in the ambient conditions. In addition to the formation of elemental As several oxides can also form in the non-equilibrium condition, which may give rise to the additional Raman peaks observed in the present study. Hollinger et al. have reported a detailed comparative study of thermal oxidation of GaAs and InAs by growing thin native oxide layer on InAs and GaAs by ultraviolet and thermal oxidation. They have identified the thermal oxides formed on those materials by comparing core level binding energy, intensities and valance band spectra with corresponding bulk material using X-ray Photoelectron Spectroscopy (XPS) [164]. They have reported that the chemical composition of InAs and GaAs can be controlled by thermodynamically and kinetically from UV to thermal oxidation. They also have predicted that the following reaction could occur in InAs depending upon the thermal oxidation condition.





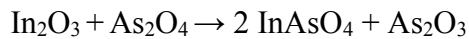
According to Schwartz et al. reaction (3.2) would be favoured under weak oxidation condition, reaction (3.1) in intermediate condition, and reaction (3.3) in strong oxidation condition [163]. Hollinger et al. [164] have calculated the Gibb's free energy for the binary and ternary oxides of InAs and showed that in InAs, InAsO<sub>4</sub> has the lowest energy of formation at 300 K. They also detected ternary InAs<sub>x</sub>O<sub>y</sub> along with As to be present on InAs surface upon thermal oxidation at 350°C for 2 hr. Even though InAs<sub>x</sub>O<sub>y</sub> does not exist in thermodynamic equilibrium, it could exist in metastable conditions at moderate oxidation temperature [163]. Following Hollinger and Schwartz et al [164-165], we have explored if observed Raman peaks correspond to these metastable oxides of InAs. To the best of our knowledge, there are two reports on Raman spectra of InAsO<sub>4</sub>; one by Schwartz et al. [164], where Peaks ~ 201, 245, 326, 400-450 cm<sup>-1</sup> and in the range of ~ 750- 900 cm<sup>-1</sup> in the Raman spectra are attributed to crystalline InAsO<sub>4</sub> powder. Flynn et al. [166] recorded the Raman spectra of the claudetite phase of As<sub>2</sub>O<sub>3</sub>, where along with other frequencies ~ 192 and 248 ± 2 cm<sup>-1</sup> were also observed. Bahfenne et al. [167] also reported that few natural and synthesized minerals, which are like crystals containing As<sub>x</sub>O<sub>y</sub> ions, exhibit peaks at ~ 244 cm<sup>-1</sup> in the Raman spectra. This is to be noted that time evolution i.e initially increase and then decrease of 240-244 cm<sup>-1</sup> mode is followed by mode occurring at ~ 180 and ~ 325, ~ 400 - 435 cm<sup>-1</sup>. Similarly, mode at ~ 192 cm<sup>-1</sup> follows the mode at ~ 248 and ~ 252 cm<sup>-1</sup> in intensity variation. We, therefore, consider that the corresponding combination of modes have same origin. Based on the above discussion, we assign the Raman peaks observed in the

present study at different laser power density and time as follows:  $\sim 257-258$  and  $\sim 198$   $\text{cm}^{-1}$  peaks to crystalline As;  $\sim 180$ ,  $\sim 240-244$ ,  $\sim 306-326$ ,  $\sim 400-435$  and  $\sim 817$   $\text{cm}^{-1}$  modes to  $\text{InAsO}_4$ , and  $\sim 248-254$ , and  $\sim 192$   $\text{cm}^{-1}$  modes to Claudette phase of  $\text{As}_2\text{O}_3$ . The small mismatches in frequency, relative intensity and non-occurrence of some of the peaks between the present study and the reported ones could be due to the difference in the form, preparation method, purity, anhydrous or hydrous state and proportion of the sub-oxides in the oxides. Based on our assignment of the additional modes we explain our observed time evolved Raman data at MLPD as follows:

- 1) From using above understanding of origin of different peaks and their NPD dependence, in we could differentiate three different paths followed for chemical reactions involved in oxidation process in three different LPD regimes.
- 2) They are appropriately noted as Weak, intermediate and strong LPD regimes. In the weak region at LPD  $\sim 200$   $\text{kW}/\text{cm}^2$  (Fig. 3.2.2.3a), time series initiates with observation of As peak at  $\sim 256$  and  $198$   $\text{cm}^{-1}$ , which decreases with time and modes at  $\sim 249$ ,  $192$  and  $244$ ,  $181$   $\text{cm}^{-1}$  modes start emerging along with As modes in their wings. As time progress, the intensity of oxide modes increases.



or



- 3) Further, at intermediate LPD  $\sim 250-350$   $\text{kW}/\text{cm}^2$ , intermediate path of oxidation i.e eq. (3.1) is favoured, and the oxidation process starts producing  $\text{As}_x\text{O}_y$  (in the form of  $\text{As}_2\text{O}_5$ ,  $\text{As}_2\text{O}_4$  etc.).  $\text{As}_x\text{O}_y$  can produce  $\text{InAsO}_4$  through the chemical processes.
- 4) At higher LPD  $\sim 450$   $\text{kW}/\text{cm}^2$ , strong oxidation path is followed, which shows drastic changes in Raman spectra. Initially peak  $\sim 243$   $\text{cm}^{-1}$  along with  $258$   $\text{cm}^{-1}$  are observed (Fig.3.3.2.5), which suggests formation of  $\text{InAsO}_4$  and As via favored chemical reactions

(3.3), (3.4) and (3.5). At later time three peaks  $\sim 241$ ,  $248$  and  $257 \text{ cm}^{-1}$  are observed, which are attributed to  $\text{InAsO}_4$ ,  $\text{As}_2\text{O}_3$  and  $\text{As}$ .

The time evolution of Raman spectra show competition among the metastable oxides ( $\text{InAs}_x\text{O}_y$ ,  $\text{As}_x\text{O}_y$  and  $\text{As}$ ) and their coexistence ( $\sim 241$ ,  $\sim 247$ - $254$ , and  $\sim 257 \text{ cm}^{-1}$ ) as shown in Fig.3.2.2.5b. Here, gain of one mode at the expense of the other is indicative of competition of different processes i.e. formation/decomposition of the metastable compounds from/into one another. Detection of  $\text{As}$  related peak ( $\sim 258 \text{ cm}^{-1}$ ) along with  $\text{InAsO}_4$  ( $15 \text{ cm}^{-1}$ ) at later time (T3) could be attributed to formation of  $\text{As}$  following the chemical reaction 4. Formation and decomposition of  $\text{InAsO}_4$  may be simultaneously active during the oxidation process. Some peaks are common in more than one oxides in the  $\text{As}_x\text{O}_y$  family, e.g.  $\sim 243 \text{ cm}^{-1}$ :  $\text{As}_2\text{O}_5$  and  $\text{InAsO}_4$ ;  $\sim 198 \text{ cm}^{-1}$ :  $\text{As}$  and  $\text{As}_2\text{O}_4$  etc. Therefore, it is difficult to assign every peak unambiguously as at the metastable condition, a mixture of more than one oxides is expected to coexist in the oxide layer. Here, the Raman modes  $\sim 180$ - $190$ ,  $240$ - $245 \text{ cm}^{-1}$ ,  $191$ - $195$ ,  $248$ - $253 \text{ cm}^{-1}$  and  $196$ - $200$ ,  $256$ - $260 \text{ cm}^{-1}$  are attributed to  $\text{InAs}_x\text{O}_y$ ,  $\text{As}_x\text{O}_y$  and  $\text{As}$ . Observation of peaks  $\sim 240$ - $245$  and  $248$ - $253 \text{ cm}^{-1}$  along with other related peaks are attributed to these chemical reactions.

**HLPD (600-800 kW/cm<sup>2</sup>):** Very different and interesting Raman spectra is observed at LPD  $> 600 \text{ kW/cm}^2$ . As the LPD is increased to  $> 600 \text{ kW/cm}^2$ , formation and decomposition of  $\text{InAsO}_4$  ( $240$ - $245 \text{ cm}^{-1}$  and related modes) is no more observed. Unlike, slow transformation of the oxides from one form to another i.e. the step  $\text{InAs}_x\text{O}_y \rightarrow \text{As}_2\text{O}_3 \rightarrow \text{As}$  observed at medium power density level ( $200$ - $500 \text{ kW/cm}^2$ ), very fast transformations are observed as shown in Fig.3.2.2.6a. The peak  $\sim 250 \text{ cm}^{-1}$  shows direct formation of  $\text{As}$  is observed at  $\sim 800 \text{ kW/cm}^2$  at T1 (10s) in Fig. 3.2.2.6a. Surface of the NW became dark after performing the experiment as marked A in the Fig.3.2.2.6b. We performed the same experiment with  $442 \text{ nm}$

excitation laser and it shows direct melting of the NW within few seconds (marked B). Intensity of this As mode shows periodic change as shown in Fig. 3.2.2.6c.

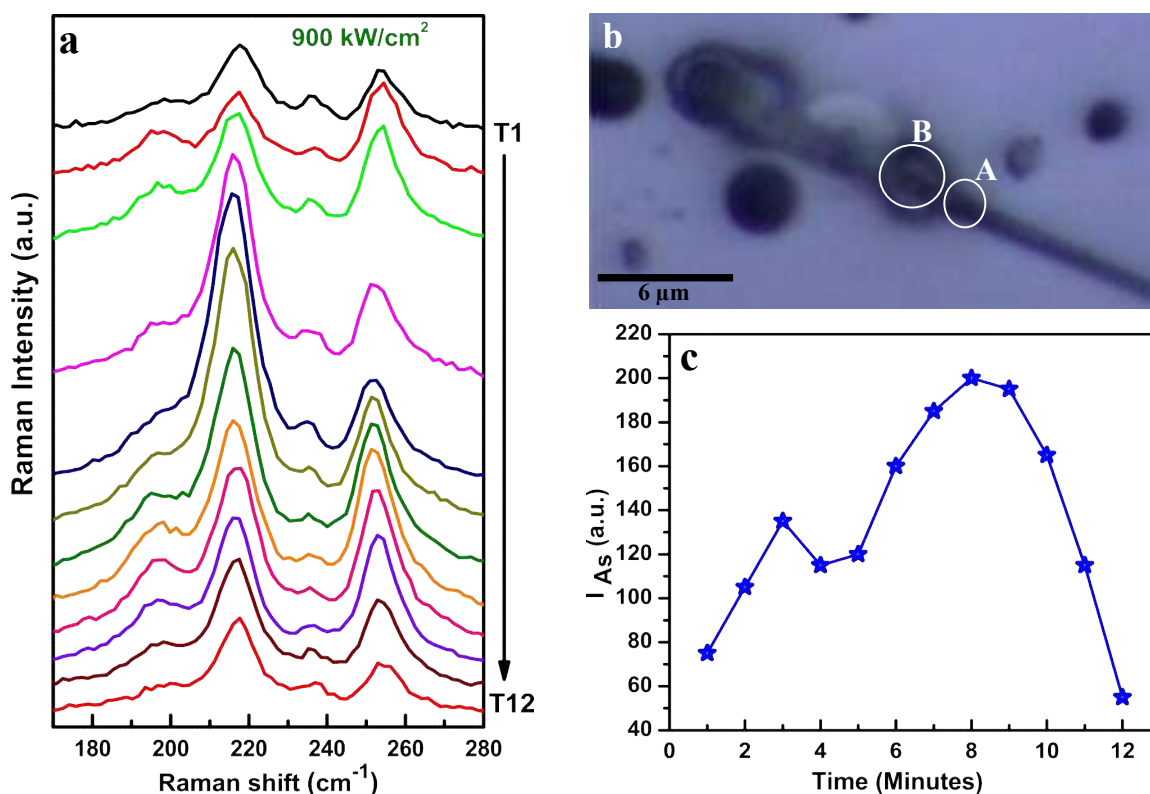


Fig. 3.2.2.6: (a) Time evolution of Raman spectra of InAs NW at the incident laser (488nm) power density of 900 kW/cm<sup>2</sup>. (b) Optical image after laser irradiation and (c) variation of intensity of As mode with time.

Two points are to be noted here. In this power regime, In<sub>2</sub>O<sub>3</sub> is also expected to be produced. However, no mode related to indium oxide is observed. It may be due to microscopic volume and very small scattering cross section of that compound. This observation is supported by the earlier reports of GaAs and InAs oxidation, where no indium oxide /gallium oxide related peak is observed in the Raman spectra [155, 159].

The second important point to be noted is that the intensity of TO mode of InAs remains very low as compared to the aforementioned oxides and As and it does not show any

monotonic redshift and broadening with time due to heating in the whole power density range studied here. The possible reason may be that before the heat is transmitted deep in the NW structure, it is consumed by the top surface to go under various chemical changes and this does not allow the whole NW to be heated up uniformly. The moment  $240\text{ cm}^{-1}$  and related modes start appearing, the scattered light dazzles indicating a huge increase in scattering.

**Variation of TO phonon frequency:** During the 8-16 min continuous laser irradiation experiment at lower power density  $\sim 30\text{ kW/cm}^2$ , TO like mode of InAs is observed  $\sim 214\text{ cm}^{-1}$  with asymmetry and does not show any observable shift in frequency below  $100\text{ kW/cm}^2$  power density. The frequency of bulk InAs is  $217.5\text{ cm}^{-1}$  [157]. The TO like mode is redshifted from that of bulk value. In chapter 4, we will investigate this mode further in the context of different types of NWs i.e. tapered, bent and uniform diameter grown in the same sample i.e. under same growth conditions. As the laser power density is increased above  $100\text{ kW/cm}^2$ , the TO like mode redshifts by  $3\text{-}4\text{ cm}^{-1}$  then blueshifts ( $\text{LPD} > 250\text{ kW/cm}^2$ ) by  $2\text{-}5\text{ cm}^{-1}$  with time evolution at maximum LPD  $\sim 764\text{ kW/cm}^2$ . In the whole time span it shows a reduction in FWHM by  $5\text{-}6\text{ cm}^{-1}$ . This red and blueshift of the TO like mode with time evolution and increase in LPD will be further discussed in chapter 6.

### 3.2.3 Time evolution of Raman spectra under different ambient conditions

In an additional experiment of time evolution study at  $\sim 250\text{ kW/cm}^2$  for NW ( $d \sim 800\text{ nm}$  and  $36\text{ }\mu\text{m}$ ), a very interesting observations is noted for NW placed nearly perpendicular to orientation (Fig.3.2.3.1a) studied earlier. A mode  $\sim 244$  increases in intensity with the redshift and then decreases with blue shift. This was attributed to formation of hydrous and unhydrous  $\text{InAsO}_4$  by performing Raman spectroscopy under wet, dry and normal ambient conditions.

The time evolution of Raman spectra starts with  $\sim 244 \text{ cm}^{-1}$  mode with FWHM  $\sim 12 \text{ cm}^{-1}$ , which intensifies significantly as shown in Fig 3.2.3.1a. The optical image of NW is shown in the inset of Fig. 3.2.3.1b. The intensity of this mode is very large as compared to TO mode. With time increases, at T8 (100s), this 244 mode is observed  $\sim 240 \text{ cm}^{-1}$  which is redshifted  $\sim 4 \text{ cm}^{-1}$  with narrowing FWHM  $\sim 6 \text{ cm}^{-1}$ . During this time, from T8-T11 (100s-200s), this 244 mode is very sharp. At some stage, the intensity of this mode surpasses that of Si substrate.

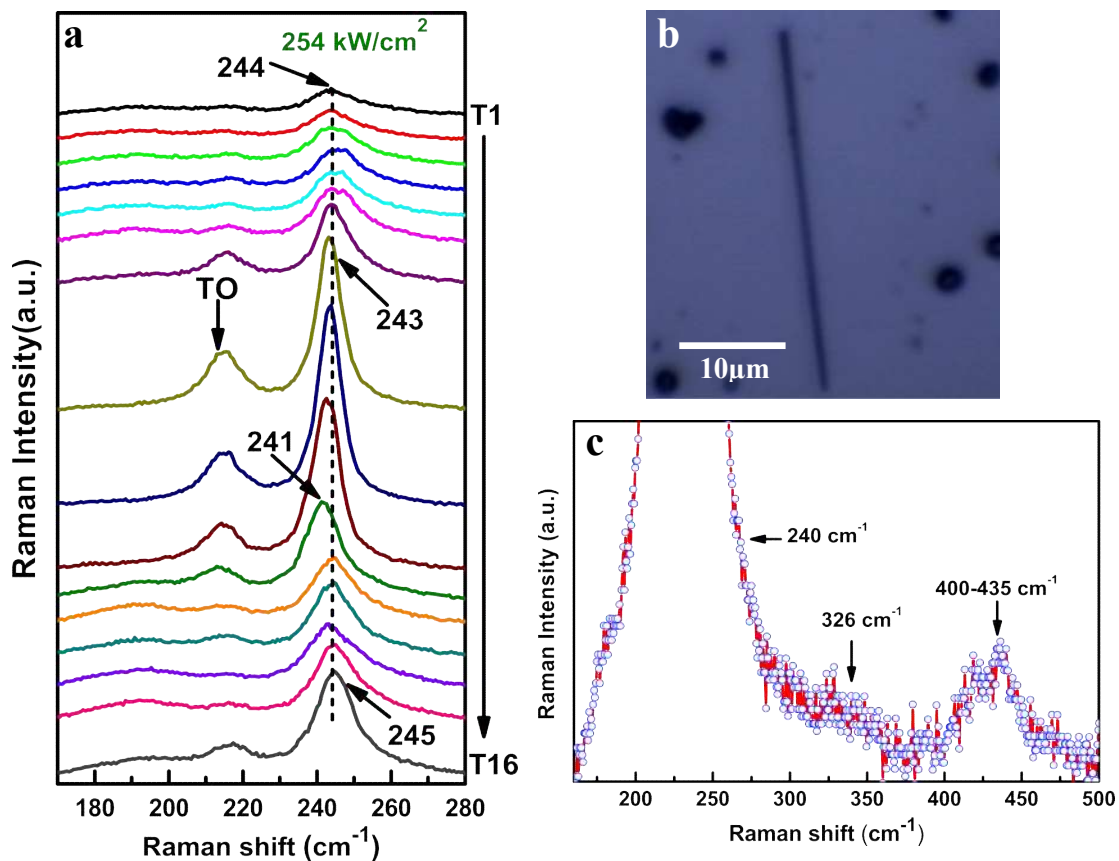


*Fig.3.2.3.1: (a) Raman spectra of the time series from T1(10s)-T16(500s) at LPD  $\sim 254 \text{ kW/cm}^2$ , (b) Optical image of InAs NW and (c) Raman spectra at T1(10s)*

Further, as time increases, at T16 (500s) the  $240 \text{ cm}^{-1}$  mode blueshifts to  $\sim 245 \text{ cm}^{-1}$  with an increase in its FWHM  $\sim 14 \text{ cm}^{-1}$  (Fig. 3.2.3.1a). The mode in the range of  $180\text{-}190 \text{ cm}^{-1}$  is

also observed along with  $244\text{ cm}^{-1}$  mode which indicates that this mode is due to  $\text{InAsO}_4$ . Here, during this time series, we have also observed some new higher frequency Raman modes  $\sim 326, 400\text{-}435\text{ cm}^{-1}$ . If heating is considered to be the reason i.e. tensile stress due to heating, redshift is accompanied with reduced FWHM. Further at later time i.e. more heating, this mode blueshifts. Therefore, redshift due to heating is ruled out. Intensity enhancement and redshift of  $\sim 244\text{ cm}^{-1}$  mode is followed by evolution of several other modes  $\sim 400\text{-}435$  and  $\sim 600\text{-}830\text{ cm}^{-1}$  also. In literature, Gomez et al. have discussed Raman spectra of chemically synthesized indium arsenate dihydrate ( $\text{InAsO}_4 \cdot 2\text{H}_2\text{O}$ ) powder, where several bending and lattice modes  $\sim 182, 240, 266, 306, 425, 438, 476\text{ cm}^{-1}$  and stretching modes in the range of  $\sim 817\text{-}892\text{ cm}^{-1}$  are reported [168]. The observed peaks i.e.  $\sim 241, 181, 265, 425\text{-}438\text{ cm}^{-1}$  closely match with those of  $\text{InAsO}_4 \cdot 2\text{H}_2\text{O}$  [168], indicating that redshift may be due to formation of  $\text{InAsO}_4 \cdot 2\text{H}_2\text{O}$  from  $\text{InAsO}_4$  by absorbing the atmospheric moisture. In the later stage of time series  $\sim 240\text{ cm}^{-1}$  mode blueshifts to  $\sim 245\text{ cm}^{-1}$  again leading to formation of possibly anhydrous  $\text{InAsO}_4$ . Alternately, the red and blueshift could be associated with development/relaxation of stress in the oxide layer. However, this needs further experimental confirmation. Since, it is hydrous v/s anhydrous, it was considered to give suitable environment for generation of one over the other and check the behaviour under laser irradiation. In this study time evolution of Raman spectra was recorded using i) under ambient condition /normal, ii) in Water environment and iii) under silica jel environment. NW chosen has dimension and orientation similar to studied above. The optical image of wire is shown inset of Fig. 3.2.3.2 and corresponding Raman spectra at point is shown in Fig. 3.2.3.2. At LPD  $\sim 200\text{ kW/cm}^2$ . In Fig. 3.2.3.2, the Raman spectra is showing that the formation of  $\text{InAsO}_4$  is started at  $\sim 244\text{ cm}^{-1}$  and with progress in time, it is blue shifted  $\sim$  from  $\sim 243$  to  $246\text{ cm}^{-1}$  (Fig 3.2.3.2). Intensity of this mode is decreasing as time increases.

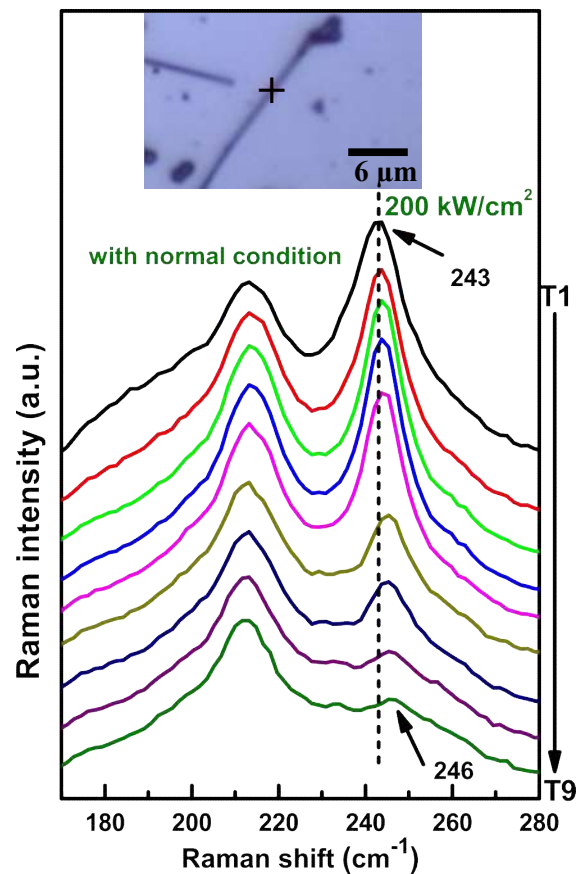


*Fig.3.2.3.2: Raman spectra from T1 (10s) to T9 (500s) at ambient condition with 488 nm excitation at 200 kW/cm<sup>2</sup> and inset show the optical image of NW (d ~ 1  $\mu\text{m}$  and l ~ 20  $\mu\text{m}$ ).*

To excite Raman spectra in water environment, 442 nm excitation was used, as appropriate condition to excite these modes could not be attained using 448 nm laser power available. The Raman spectra clearly shows oxide mode initially at ~ 240  $\text{cm}^{-1}$  and with time, the mode is continually blueshifted ~ from 240 to 249  $\text{cm}^{-1}$  during 8 min Here, the Raman spectra suggests formation of  $\text{InAs}_2\cdot 2\text{H}_2\text{O}$  due to water environment of sample.

Further, we have performed similar experiment with Silica gel on same NW with different position by 442 nm excitation at 450 kW/cm<sup>2</sup> (Fig. 3.2.3.3a). At T1 (10s) the mode is ~ 244 cm<sup>-1</sup>, suggesting formation of anhydrous InAsO<sub>4</sub>. This is expected as nearby moisture is absorbed by silica gel (Fig.3.2.3.2b) making it dry and therefore forbidding formation of hydrous InAsO<sub>4</sub>.

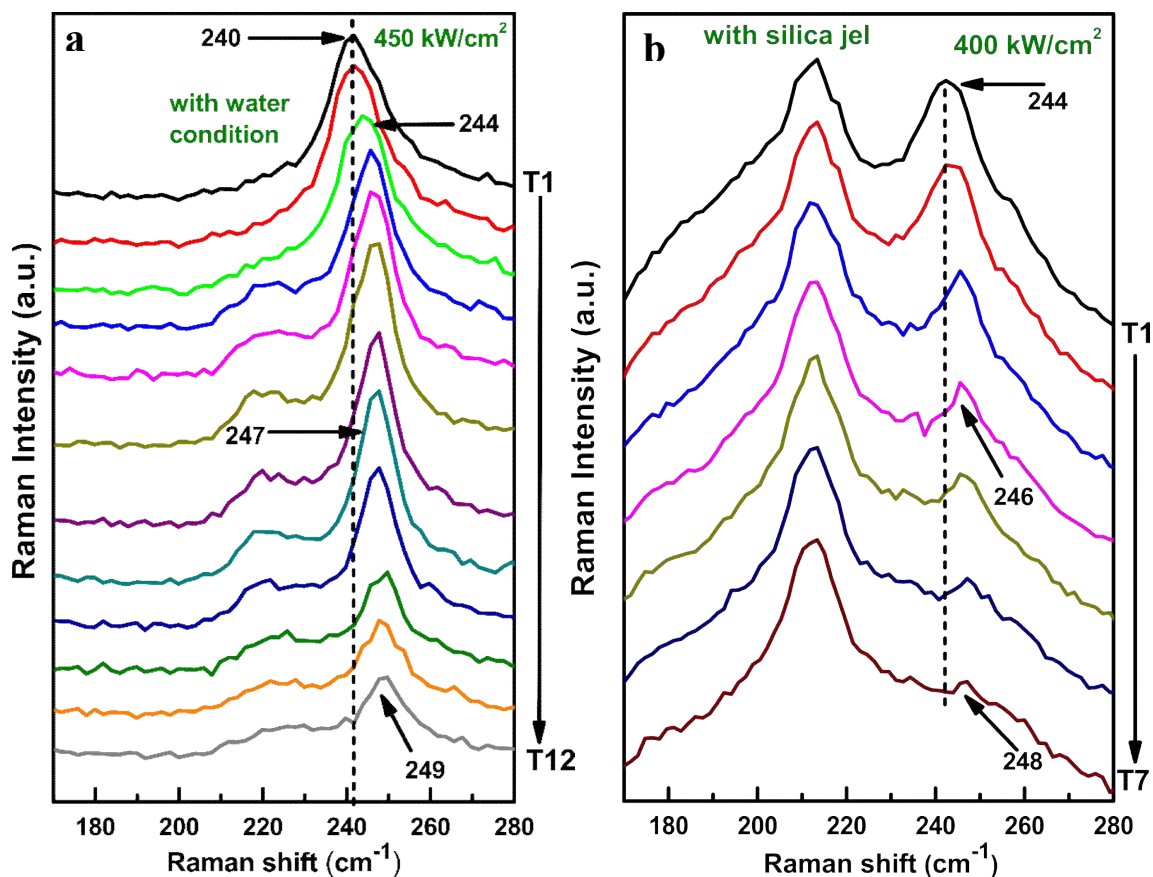


Fig.3.2.3.3: (a) and (b) Raman spectra from T1 to T12 and T7 in water and silica gel environment with 442 and 488 nm excitation at 450 and 400 kW/cm<sup>2</sup>, respectively.

This mode at later time blue shifts to ~ 248 cm<sup>-1</sup> which shows formation of As<sub>2</sub>O<sub>3</sub> due to continuous laser heating. These experiments unambiguously establish that ~ 240 and 244 cm<sup>-1</sup> modes originate from InAsO<sub>4</sub>·2H<sub>2</sub>O and anhydrous InAsO<sub>4</sub>, respectively.

### 3.3 Conclusion

Systematic study of time evolution of chemical changes on the surface of an InAs nanowire (NW) on laser irradiation using laser power densities (LPD) in the range 30 kW/cm<sup>2</sup> to 800 kW/cm<sup>2</sup> for a time span of 8-16 minutes was performed. Chemical changes were monitored using time series Raman spectra taken during entire duration.

For a NW of 800 nm diameter thermal oxidation starts at a threshold power density of ~ 200 kW/cm<sup>2</sup>. Different path (Chemical reactions) of oxidation are followed depending on laser power density used for irradiation. In a time evolution of Raman spectroscopy, it is found that these reactions compete and few end products like like InAsO<sub>4</sub>, As<sub>2</sub>O<sub>3</sub> co-exist for different LPDs at different time duration of irradiation. In the medium power density range, a mixture of three compounds i.e. crystalline InAs<sub>x</sub>O<sub>y</sub>, As<sub>x</sub>O<sub>y</sub> and As is observed, where the concentration of each compound varies with time. At higher power density, layer by layer removal of As is observed from the top surface of the NW without damaging the InAs NW core.

Thus, time evolution of Raman spectroscopy is used to probe chemical changes probe i.e. to study metastable states formed during laser irradiation, which is otherwise extremely difficult to detect by any other technique with such uniqueness. Position controlled laser induced chemical modification on a nanometer scale, without changing the core of the NW, can be useful for NW based device fabrication.

To have control on this process, one needs to understand correlation of these chemical processes with excited temperature using laser irradiation. This will be looked into in chapter 5. Time evolution study showed variation of TO phonon frequency from 214 cm<sup>-1</sup> to 212 - 220 cm<sup>-1</sup>. Before getting into time evolution in the range 212 to 220 cm<sup>-1</sup>, the difference of TO phonon frequency ~214 cm<sup>-1</sup> from that of bulk 217 cm<sup>-1</sup> is studied and discussed in

chapter 4. The study of time evolution of TO phonon frequency and apparent difference in Raman spectra of differently oriented InAs NWs is discussed in chapter 6.

## **Chapter -4**

# **Correlation of Strain and Polytypism in InAs Nanowire**

*“Science is the knowledge of consequences and dependence of one fact upon another” \_\_\_\_\_ Thomas Hobbes*

#### 4.1 Introduction

InAs micro-nanowires (MNWs) have potential to play an important role in high-speed optoelectronic material because of its high electron mobility [136]. Most of the III-V semiconductors like InAs, InSb, GaAs, GaSb, etc. have zinc blende (ZB) structure, whereas, nitrides (GaN, InN etc.) have wurtzite (WZ) structure in their bulk form. However, in nanowires (NWs) of these materials, it is found that they can crystallize in both ZB and WZ structures [169-182]. Since, WZ and ZB structure of the same material are expected to have different optoelectronic properties, it is important to understand the various manifestations of the polytypism. Raman spectroscopy is sensitive to composition, crystalline quality, electronic band structure, size and aspect ratio of NWs [183-187]. In addition, Raman selection rules can provide information about the crystal structure of the material under study. Raman spectroscopy is especially useful for study of MNWs, as density of MNWs is low and it is difficult to study them using more conventional techniques, like X-ray diffraction (XRD). In our earlier study of laser power dependent time evolution of Raman spectra of InAs MNW (diameter (d)  $\sim 1 \mu\text{m}$ ), a TO like mode  $\sim 214 \text{ cm}^{-1}$  [188] was noted, whereas, for bulk InAs, TO phonon frequency is  $\sim 217.5 \text{ cm}^{-1}$  [189]. In the present study, we investigate this observed red shift in InAs MNW, using spatially resolved Raman spectroscopy (SRRS) on several MNWs of different kinds. This is an attempt to answer a question, whether, the origin of the red shift lies in polytypism and if so, what is the correlation? In particular, for InAs and GaAs NWs polytypism have been studied by several groups using different techniques [169-171]. Dependence of polytypism on NW diameter, i.e. change of phase from ZB to WZ with reducing diameter has been revealed by some recent studies [172-175]. However, it may be

important to note that all these reported works are for uniform diameter NWs in the range of 80-200 nm [170-175].

Unlike most of the reported work, where NWs are grown using Au catalyst [172,174-176, 190-193], InAs MNWs study presented here are grown using self-catalyst (In droplet) MOCVD [142]. Further, it is important to note that we have studied only one sample in which, we have observed MNWs of diameter varying between 2.2  $\mu\text{m}$  to 200 nm and length varying between 20 - 80  $\mu\text{m}$ . Uniform, tapered and tapered bent MNWs are formed in one single Si (001) substrate with very low density [142]. Thus, first there is a need to validate the study of small diameter (80-200 nm) NWs for these MNWs, as larger diameter MNWs are not expected to have pure ZB structure and then to investigate the effect of polytypism [175, 191, 194, 195]. This is achieved using SRRS along the length of these MNWs, which shows the variation in frequency of InAs phonons. Different possibilities are considered, including polytypism for understanding this variation, while establishing the polytypism in these MNWs.

#### **4.2 Spatially resolved Raman spectroscopy study of InAs MNWs and spheres/Si (001)**

In previous chapter 3, the frequency of TO like phonon of InAs is observed in the range of  $\sim 212$ - $217 \text{ cm}^{-1}$  and LO phonon of InAs is observed  $\sim 237.5 \text{ cm}^{-1}$  on tapered MNW and uniform NWs. The reported value of bulk TO and LO phonon of InAs  $\sim 217.5$  and  $237 \text{ cm}^{-1}$  [189, 170]. In our case, only TO phonon of InAs NW is redshifted upto  $\sim 5 \text{ cm}^{-1}$  as compared to bulk and but interesting point to note is that LO phonon variation is much less  $\sim 1 \text{ cm}^{-1}$ . For systematic study of the variation of TO phonon frequency in InAs NW, we have performed spatially resolved Raman spectroscopy (SRRS) on InAs MNWs of different kinds.

### 4.2.1 Uniform diameter NWs

InAs MNWs of various dimensions, morphology and tapering factor grown on Si (001) substrate under the same external growth conditions are studied using SRRS. Raman spectra were recorded at several locations along the length of the NW. Long tapered NW of varying diameter, NW with uniform diameter and InAs disc like structures with different diameters were studied. At the center across the diameter, the Raman spectra from all the nanostructures show dominantly TO mode indicating (110) orientation of the top surface planes. In some cases, small intensity LO mode appears additionally  $\sim 237 \text{ cm}^{-1}$ . Appearance of LO mode is probably related to disorder and due to the collection of scattered light from the side facets, which are not perpendicular to the incident light. In our case the FWHM of the TO and LO phonon are found to be  $\sim 6 \text{ cm}^{-1}$  and  $3\text{-}4 \text{ cm}^{-1}$ , respectively, indicating a good crystalline quality of the NWs.

The SRRS is performed on many uniform NWs with different dimensions at different locations along the length of wire. The optical image of wire is shown in Fig. 4.2.1.1a which has diameter  $\sim 1200 \text{ nm}$  and length  $\sim 15 \mu\text{m}$ . The representative SRR spectra is shown in Fig. 4.2.1.1b. We observe strong mode  $\sim 214 \text{ cm}^{-1}$ , which can remain constant over the length of the NW. Further, SRRS is performed on different dimensioned NWs to see the variation if any, in TO phonon frequency. The position is marked in optical image from 1 to 4 in Fig. 4.2.1.2a where, corresponding Raman spectra is recorded along the length of wire (Fig. 4.2.1.2b). The diameter and length of uniform wire are  $\sim 1 \mu\text{m}$  and  $1 \sim 8 \mu\text{m}$ , respectively. Similarly, at this NW, the TO phonon frequency is observed  $\sim 213.5 \text{ cm}^{-1}$  with an asymmetric line shape. No variation is observed along the length of wire. For various uniform NWs studied, frequency of this strong mode varies from  $\sim 214 \text{ cm}^{-1}$  ( $d \sim 1200 \text{ nm}$ ) to  $\sim 213 \text{ cm}^{-1}$  ( $d \sim 600 \text{ nm}$ ) for different diameters along with the change in line shape.

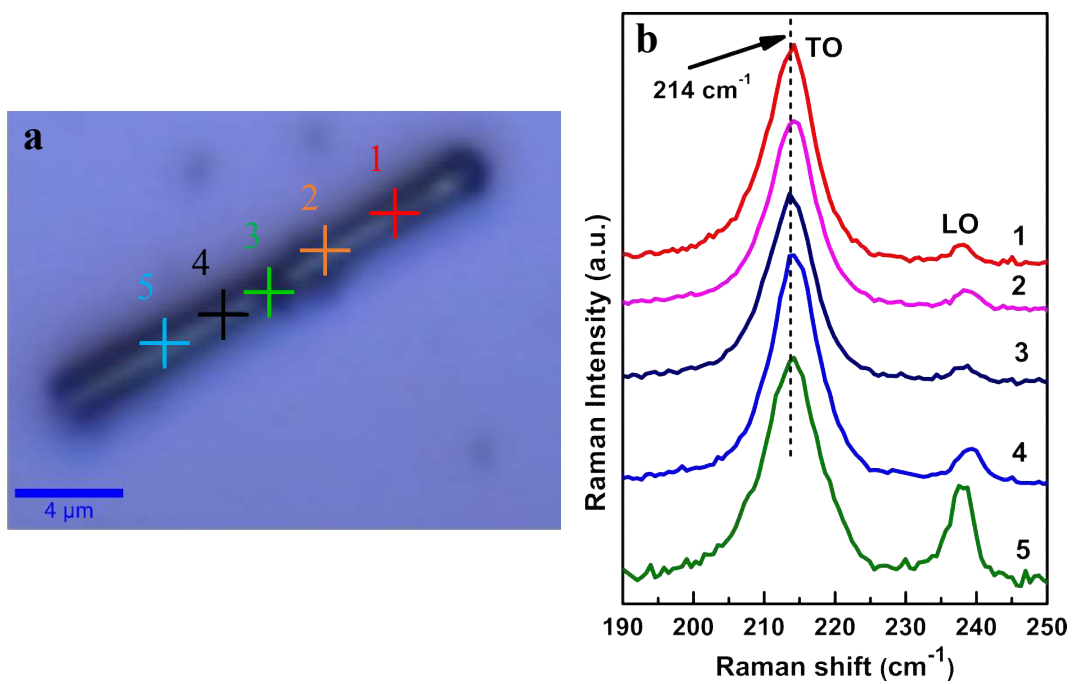


Fig.4.2.1.1: (a) Optical image of uniform InAs MNW (dia  $\sim 1.2 \mu\text{m}$ ) and (b) Spatially resolved Raman spectra (SRRS) at positions (1-5) as marked in the optical image.

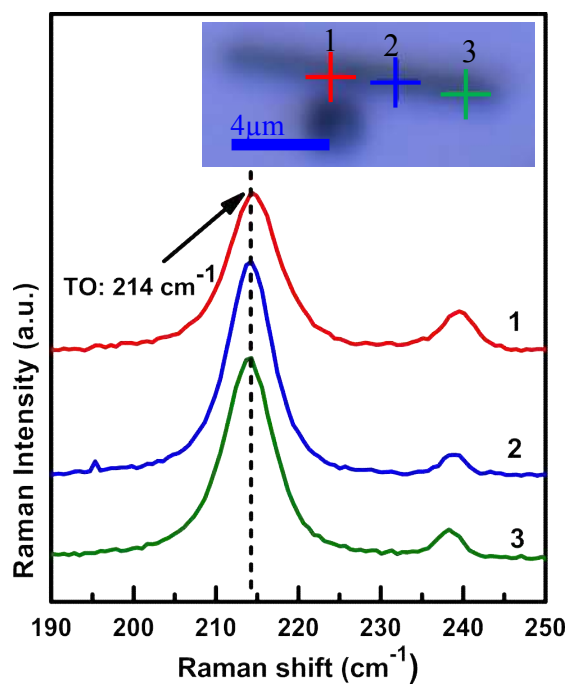


Fig.4.2.1.2: SRR spectra at positions (1-3) as marked in the optical image, which is shown inset (InAs NW: dia  $\sim 0.8 \mu\text{m}$ ).

### 4.2.2 Bent NWs

Further, several bent tapered MNWs are studied as well as different types of bents i.e. sharp and smooth bents. First, SRRS is performed on sharp bent tapered MNW and the optical image of sharp bent tapered MNW is shown in Fig. 4.2.2.1a. The diameter of base is  $\sim 1.3 \mu\text{m}$ , tip is  $d \sim 400 \text{ nm}$  and length is  $\sim 20 \mu\text{m}$ . Representative Raman data for sharp MNWs is shown in Fig. 4.2.2.1b at position 1 to 7 which is marked in optical image (Fig. 4.2.2.1a). The frequency of TO phonon is observed  $\sim 218 \text{ cm}^{-1}$  at base position 1 with an asymmetry on lower frequency side (LFS). Further, we have observed the TO phonon redshifts to  $\sim 213 \text{ cm}^{-1}$  as diameter decreases towards tip. The LO phonon redshifts for 1 to 4 from 238 to 237  $\text{cm}^{-1}$  and no variation for position 5 to 7. The position 4 is at the sharp bent position of MNW.

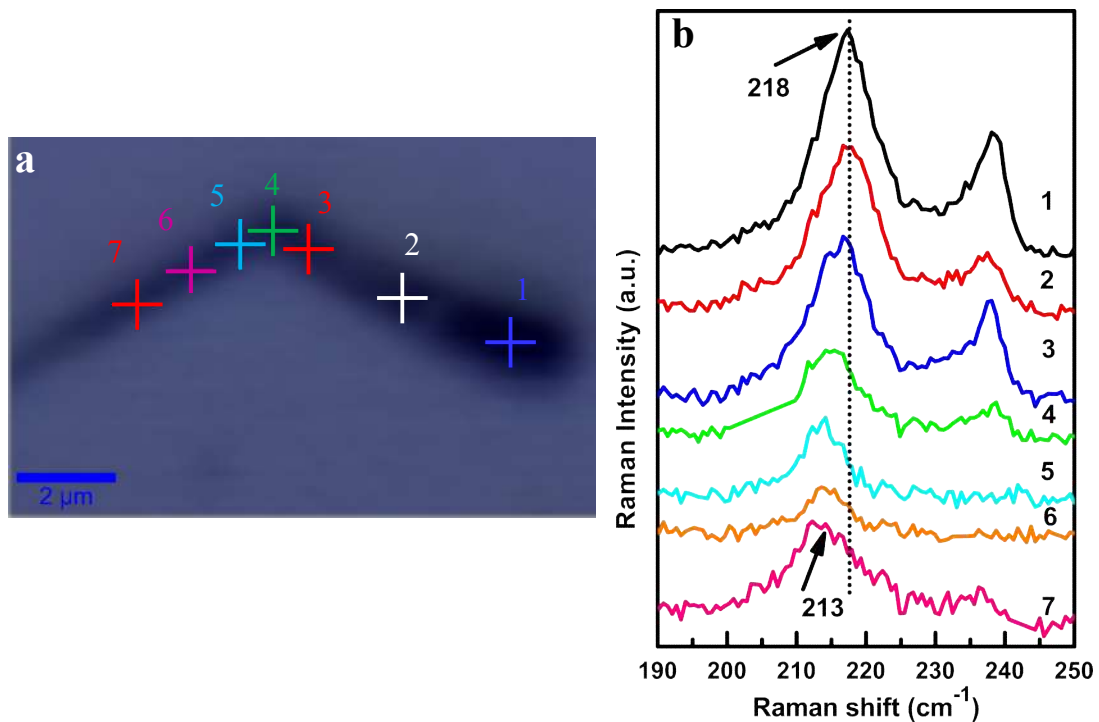
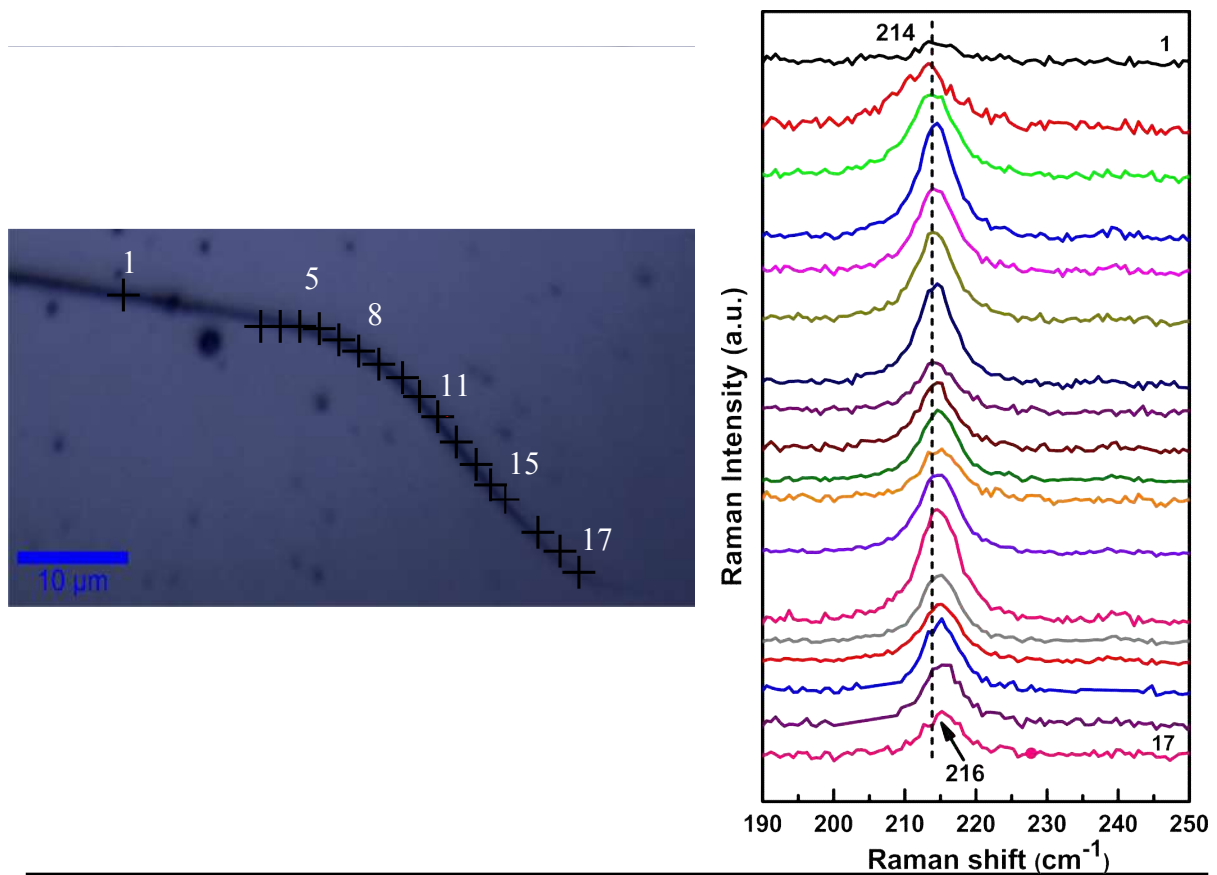


Fig. 4.2.2.1: (a) Optical image of sharp bent tapered MNW (base dia  $\sim 1.3 \mu\text{m}$  and tip  $\sim 400 \text{ nm}$ ), (b) SRR spectra at positions (1-7) as marked in the optical image.

Further, SRRS is performed on smooth bent tapered MNW to see the difference in frequency of TO phonon. The optical image of wire is shown in Fig. 4.2.2.2a which have

base and tip diameter  $\sim 800$  nm and  $\sim 400$  nm, respectively and length  $\sim 120$   $\mu\text{m}$ . The SRR is shown in Fig. 4.2.2.2b at position from 1 to 17 marked in Fig.4.2.2.2a. The TO phonon is blueshifted  $\sim 2$   $\text{cm}^{-1}$  as going towards smooth bending. It is important to note that Raman spectra for spatial positions from base to tip show an opposite behavior, i.e. in sharp bent MNW, strong mode red shifts as MNW reduces in diameter, whereas, it blue shifts for smooth bent MNW.



*Fig. 4.2.2.2: (a) Optical image of smooth bent tapered MNW (base dia  $\sim 800$  nm and tip  $\sim 400$  nm) and (b) SRRS at positions (1-8) as marked in the optical image.*

These observations indicate that redshift or blueshift of TO phonon may be related to either bent or decrease in diameter. Before, we discuss the origin of these red and blue shifts, it may be interesting to see Raman spectra of long straight tapered MNWs.

### 4.2.3 Tapered micro-nanowires (MNWs)

The two optical images of MNW are shown in which base and tip part is focused in Fig. 4.2.3a and 4.2.3b, respectively. Fig. 4.2.3c clearly show a monotonic red shift from  $\sim 218 \text{ cm}^{-1}$  to  $\sim 212 \text{ cm}^{-1}$  in the TO phonon frequency as we move from the larger diameter base region to smaller diameter tip region from position 2 to 6 marked in Fig 4.2.3a and 3b. Base region with diameter  $\sim 2 \mu\text{m}$  shows TO position  $\sim 217\text{-}219 \text{ cm}^{-1}$  and with a gradual redshift with reducing diameter, TO frequency is recorded at  $211\text{-}212 \text{ cm}^{-1}$ , where the diameter reaches a value  $\sim 400 \text{ nm}$ . It is important to note that line shape of this mode is asymmetric and changes along the length of MNWs as shown in Fig. 4.2.3.

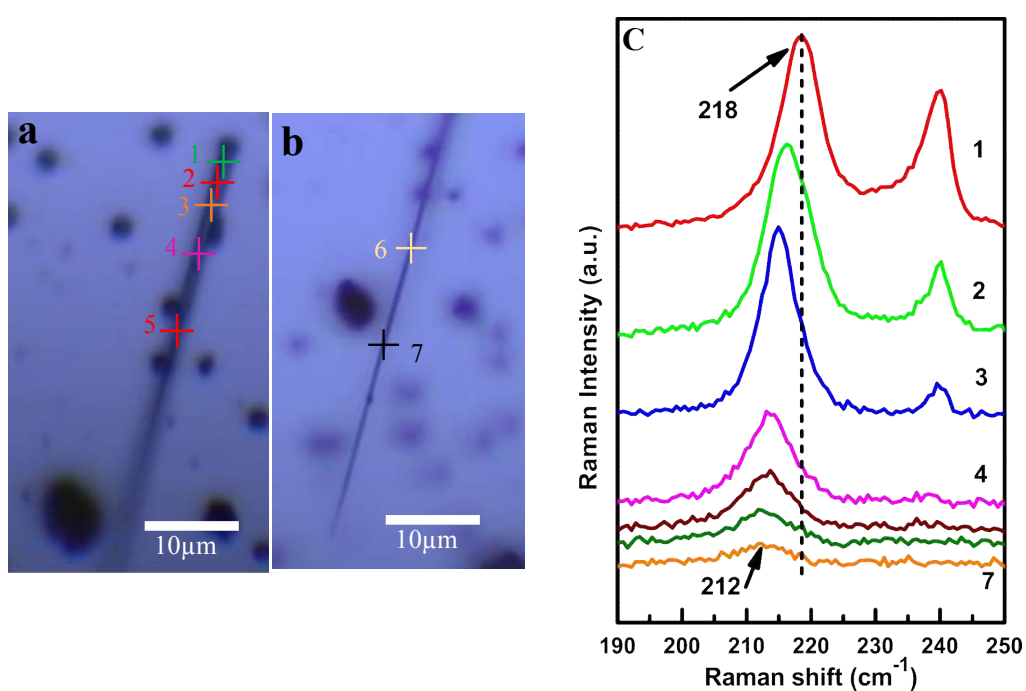


*Fig. 4.2.3: (a) Optical image of straight tapered MNW, wherein objective is focused near the base (dia  $\sim 2 \mu\text{m}$ ), (b) Optical image of same wire, wherein objective is focused at the tip ( $\sim 400 \text{ nm}$ ) and c) SRRS at positions (1-7) as marked in both optical images.*

It is also noted that FWHM is increasing as diameter decreases. The Raman data of points 7 is not plotted as signal to noise ratio is poor; however, it shows a further red shift. The SRRS data is performed on many such tapered MNWs and Raman spectra and similar observation is noted. This shows that continuous redshift of TO phonon is related to decreases in diameter and not the bent. The origin of the redshift of TO phonon frequency by 5-6  $\text{cm}^{-1}$  along the length of the  $\sim$ NW is further explored. The local heating is expected to lead to redshift along with broadening, as reported earlier for individual InAs NWs [155, 201]. In particular, for InAs, a pronounced redshift in the LO frequency is expected for disorder-induced scattering due to the large dispersion compared to the very flat dispersion of the TO branch [Fig. 1(e) from ref 170], when confinement effect on phonons is considered. However, LO phonon does not show much red shift like TO phonon and thus confinement effect is ruled out as a possible explanation. We shall come back to heating due to laser.

All representative data shows (Fig. 4.2.1, 4.2.2 and 4.2.3) that in all uniform, bent and tapered MNWs, respectively maximum two peaks are observed in Raman spectra, one strong  $\sim 212\text{-}218 \text{ cm}^{-1}$  (TO phonon) and sometimes a weak peak  $\sim 238\text{-}239 \text{ cm}^{-1}$  (LO phonon). Mode  $\sim 212\text{-}218 \text{ cm}^{-1}$  shows large amount of variation in frequency and line shape, which is one of the major part of the study presented here. It may be noted that the both TO and LO phonons are blueshifted to  $\sim 218 \text{ cm}^{-1}$  and LO  $\sim 239 \text{ cm}^{-1}$ , respectively. The strong LO phonon mode may be due to contribution from InAs sphere lying next to that point, as can be seen from the image (Fig. 4.2.3.1). To investigate this, SRR is performed on similar spheres as described in the following.

#### 4.2.4 Spheres

The SRR is performed on InAs spheres at different locations on the sphere i.e. center and edge of the sphere, as shown in Fig 4.2.4a & b. The frequency of TO and LO phonon of InAs are observed  $\sim 218$  and  $239$   $\text{cm}^{-1}$ . It is interesting note here that TO phonon is symmetric but LO phonon is asymmetric in line shape unlike for NWs. Raman spectra for positions 1 and 2 are fitted using 3 Lorentzians. TO and LO phonon frequency are  $\sim 218.3$  and  $239$   $\text{cm}^{-1}$ , respectively and additional mode appears  $\sim 235.5$   $\text{cm}^{-1}$ . This confirms that Raman spectrum in position 1 in Fig. 4.2.3c, is due to sphere lying close to the position. The additional mode observed may be either Plasmon-LO phonon coupled mode or surface optical phonon [160-162].

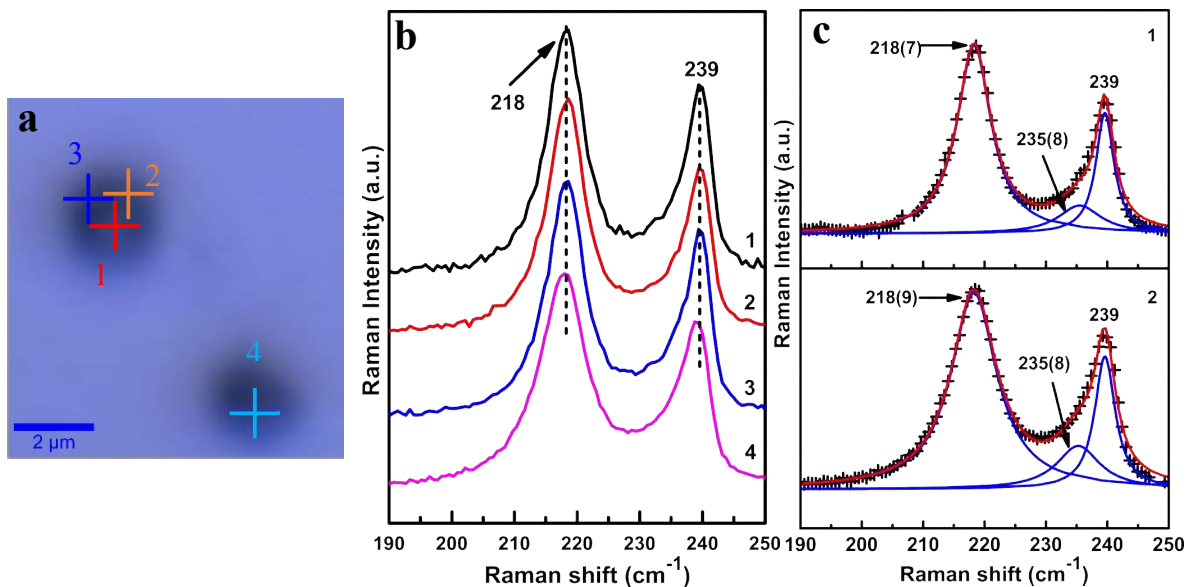


*Fig.4.2.4: (a) optical image of spheres, (b) SRRS at position 1-4 and (c) Cumulative fit (red solid line) to the raw data (+) and separate Lorentzian fits are shown with blue solid line.*

The observation of both TO and LO phonons in backscattering geometry suggests non-epitaxial growth of InAs spheres on Si (001) substrate, as only LO phonons are allowed in backscattering geometry from (001) surface of cubic InAs.

### 4.3 Understanding red and blue shift in SRR of InAs MNWs

With this background, the origin of red and blue shift of the frequency of TO phonon and its lineshape in these MNWs is explored in the following. Coming back to the red shift observed in long straight uniform and tapered MNWs, two possible origins, i) Heating due to laser irradiation, and ii) residual stress can be considered as causes for the same. All Raman spectra shown above is excited using 488 nm with laser power density  $\sim 30 \text{ kW/cm}^2$ . At this laser power, heating effect is discarded as a possible origin of red shift from our earlier (chapter-3) laser power dependent time evolution Raman study of NWs [188], wherein we show that for  $\sim 30 \text{ kW/cm}^2$ , no change is observed over time evolution of 8 minutes [Fig. 3.2.2.1] for 800 nm NW. Further, for smaller diameter NWs, heat transfer is expected to be higher thus leading to lower rise in temperature. Therefore, we consider stress to be the cause of red as well as blue shift observed in these MNWs. In the following, we discuss the cause of this residual stress in these MNWs.

A recent study of Fu et al. [202] has revealed that NW with smaller diameter suffer from larger redshift compared to the NW of larger diameter due to tensile strain. The first possibility to be consider is strain due to lattice mismatch between InAs and Si substrate. Critical layer thickness for InAs on Si substrate is estimated to be  $28 \text{ \AA}$ . We rule out this as the reason for redshift as i) thickness of our InAs NW  $\sim 400 \text{ nm} - 2 \text{ }\mu\text{m}$ : relaxed, ii) Observation of TO phonon in BS configuration indicates non epitaxial growth on Si (001).

Next, possibility considered for the residual stress [169 176] is polytypism observed in III-V NWs grown under various conditions [169-182]. In the bulk form, all III-V semiconductors except nitrides have ZB structure, however, recent studies shows that III-V NWs grow with polytypism i.e. alternate ZB and WZ structure along the growth axis under certain growth condition for smaller diameters ( $<100\text{nm}$ ). Recently, this is studied in detail by some groups using different techniques [169-171]. Growth mapping studies are discussed

in the following to know the about the possibility of polytypism for MNWs studied above.

#### 4.3.1 Growth mapping studies of InAs NWs reported in literature

Several growth-mapping studies with growth parameter variation in specially in V/III ratio and growth temperature are reported on InAs NWs grown using MOCVD [172, 174-175]. In these NWs, the WZ and ZB structure appears as a stacking fault in InAs NWs along the growth direction. Content of WZ to ZB phase in these nanowires is found to depend on various growth parameters such as growth temperature, metal nanoparticle diameter, V/III ratio, total mass flow etc.

**Effect of growth temperature, V/III ratio for growth of different diameter NWs:** The growth temperature and V/II ratio are important about NW growth because the NW grow in a particular temperature range it is called mass flow region. If the temperature is less than mass flow window, then thin film will be grow and if it is higher than nanoparticle will be grow. Most authors have reported [172, 174-175] that the crossover (WZ to ZB structure) diameter graph becomes broader and shifts to larger diameter as growth temperature changes from 480<sup>0</sup>C to 420<sup>0</sup>C for V/III ratio ~ 130 with Au-catalyst method. The size/diameter of InAs NW is dependent on size of nucleating metal nanoparticle sizes. For large diameter, crystal structure is not sensitive to V/III ratio, however it is very sensitive to V/III ratio for smaller diameter [175].

Increasing in growth temperature has favored ZB or WZ depending on the range of temperature as well as V/III ratio [173, 175-176, 182]. In totality, growth-mapping studies, especially for InAs NWs, suggest that the change from ZB to WZ content is not necessarily a smooth function of change in growth parameters. It may be important to note that very small change of V/III ratio/temperature/mass flow may significantly change crystal structure content, whereas, over a large change of these growth parameters, their hardly any change in

the content [182]. Several such studies performed using V/III ratio (varying from 20-220) and temperature (varying from 380 to 500°C) suggest that our growth conditions (growth temperature  $\sim 425$  °C and V/III ratio  $\sim 250$ ) may lead to mainly ZB structure. The effect of growth parameters on the formation of WZ/ZB structure in a NW is complicated and observations reported in literature are summarized in Table 4.3.1.

*Table 4.3.1: Consolidation of results of growth mapping studies [172, 174-175]*

Diameter d (nm)	Growth temperature (°C)	V/III ratio	Structure
d >150 nm	420	130	Pure ZB
d < 50 nm	480	130	Pure WZ
d >100-150 nm	380	220	Pure ZB
d $\sim$ 50 nm	410	30	Pure ZB
d $\sim$ 30 nm	410	20	Pure WZ

### 4.3.2 Understanding correlation of strain and polytypism in InAs NWs

Although, we mentioned earlier that red and blue shift and variation in line shape of TO phonon discussed above may be due to polytypism in these MNWs, however, presence of polytypism needs to be confirmed for these MNWs. Spatially resolved polarized Raman spectroscopy is performed in order to obtain information on the polytypism for these MNWs. Before performing polarized Raman spectra, it may be interesting to see trend observed in these MNWs on analysis of unpolarized Raman data considering polytypism in these MNWs.

#### 4.3.2.1 Understanding polytypism in InAs MNWs:

For the two possible structures ZB and WZ, number of atoms per unit cell are 2 and 4, respectively. Thus, total number of optical phonon modes are 3 and 9 in ZB and WZ, respectively. Out of these,  $A_1(\text{TO})$ ,  $E_1(\text{TO})$ ,  $A_1(\text{LO})$  and  $E_1(\text{LO})$  modes lie very close (within

$\sim 0.5 \text{ cm}^{-1}$ ) in phonon frequencies for WZ, which are also close to TO and LO phonons for ZB structure [190]. However, difference between  $E_{2h}$  and TO phonon modes is expected to be  $\sim 6.3 \text{ cm}^{-1}$  for WZ InAs [190] and this, therefore can be used to get information about the presence of ZB and WZ phases in InAs MNWs. Recent studies have suggested that the red shift of TO phonon frequency could be related to polytypism observed in the Ga/InAs NWs [169-170]. Through polarization and azimuthal-dependent Raman measurements they have attributed the TO phonon  $\sim 217$  to bulk ZB TO,  $214 \text{ cm}^{-1}$  to WZ mode and  $210 \text{ cm}^{-1}$  mode to WZ mode. Considering the possibility of presence of  $E_{2h}$  and TO phonon in the asymmetric TO phonon noted above, all the spectra of Fig.4.2.1. - 4.2.4, are deconvoluted with minimum required Lorentzians i.e. either two or three. Upon deconvolution, two modes; lower frequency ( $\omega_l$ ) and higher frequency ( $\omega_h$ ) are noted.

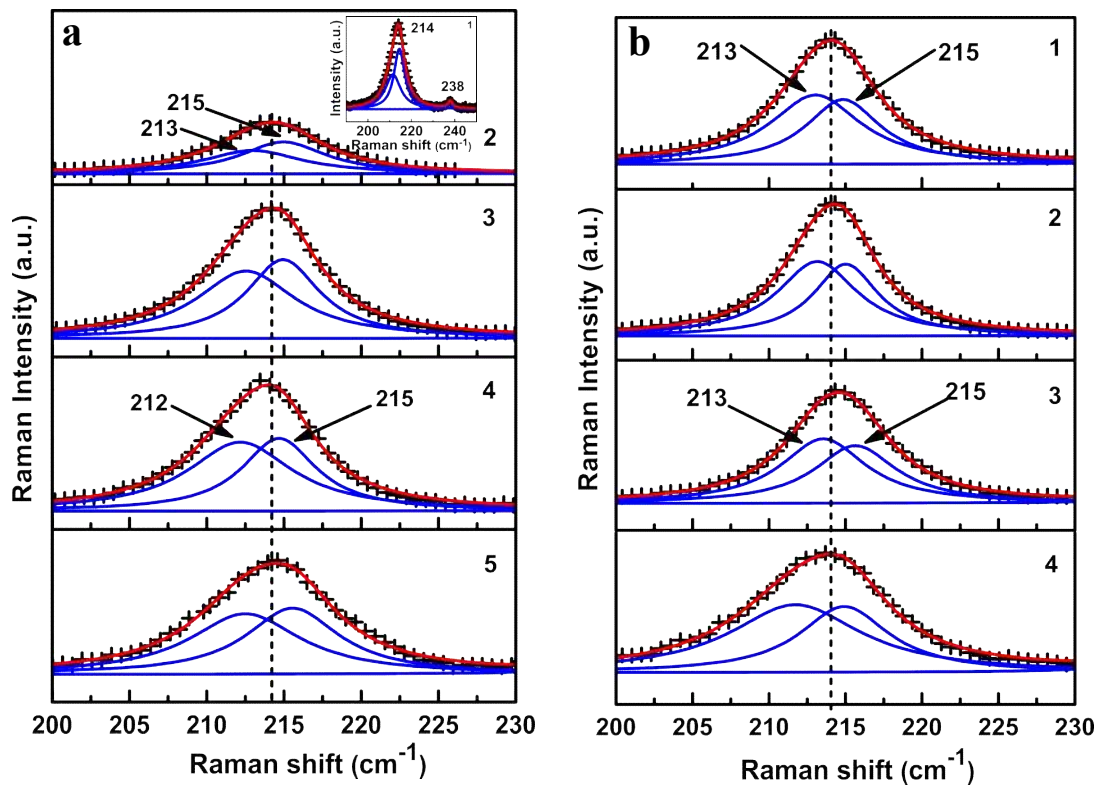


*Fig. 4.3.2.1.1: (a) and (b) SRR spectra at positions (2-5) as marked in the optical image (Fig.4.2.1.1a). Inset of Fig.4.3.1.1a shows Raman spectrum for position 1 marked in the optical image (Fig.4.2.1.1a). Cumulative fit (red solid line) to the raw data (+) and separate Lorentzian fits are shown with blue solid line.*

For the uniform diameter wire, the frequency of  $\omega_l$  and  $\omega_h$  mode are observed to be  $\sim 213 \text{ cm}^{-1}$ ,  $\sim 215 \text{ cm}^{-1}$  for dia  $\sim 1200 \text{ nm}$  (Fig. 4.3.2.1.1a) and  $1000 \text{ nm}$  (Fig. 4.3.2.1.1b), throughout the length of the wire. For the tapered MNW frequency of  $\omega_h$  and  $\omega_l$  varies from  $\sim 218$  and  $215 \text{ cm}^{-1}$  at the base ( $d \sim 1.6 \mu\text{m}$ ) to the tip ( $d \sim 400 \text{ nm}$ ), where  $\omega_h$  disappears and  $\omega_l$  reaches the value of  $\sim 213 \text{ cm}^{-1}$ . It is interesting to observe that as we progress from position 1 to 2,  $\omega_l$  mode is appearing and at further position 3, the intensity of  $\omega_h$  mode is decreasing. The  $\omega_l$  and  $\omega_h$  are red shifted to  $\sim 216 \text{ cm}^{-1}$  and  $214 \text{ cm}^{-1}$ , respectively.

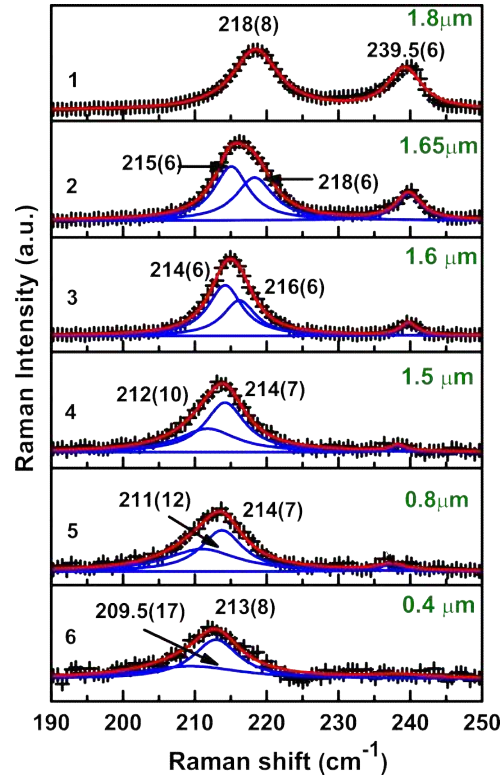


*Fig. 4.3.2.1.2: SRRS at positions (1-6) as marked in both optical images (4.2.3.1a and b). Cumulative fit (red solid line) to the raw data (+) and separate Lorentzian fits are shown with blue solid line.*

At position 4 to 6 where the diameter reaches a value  $\sim 400 \text{ nm}$ ,  $\omega_h$  disappears and  $\omega_l$  dominates till position 6, one new mode starts appearing  $\sim 211 - 209 \text{ cm}^{-1}$  (FWHM increases from position 4 to 6), when  $\omega_l$  reaches a frequency value of  $\sim 213 \text{ cm}^{-1}$ . As one can see,  $\omega_l$  and  $\omega_h$  observed here are very close in frequency (within  $\sim 2 \text{ cm}^{-1}$ ) and depending on the

fraction of ZB/WZ the identification of  $\omega_l$  and  $\omega_h$  as  $E_{2h}$  and TO (ZB + WZ/ZB), respectively, may or may not be correct. Specially, as it's not feasible to have any supporting information via more conventional techniques like transmission electron microscopy (TEM) or XRD in this case. Therefore, before we go into detail discussion about generation of stress in MNW due to presence of both ZB and WZ phases, we perform polarization dependent Raman measurements to identify the origin of phonon frequencies obtained on deconvolution.

#### 4.3.2.2 Confirmation of polytypism using Polarized Raman spectroscopy

The z direction is chosen parallel to growth axis of MNW, which is (111) for ZB and (0001) for WZ structure. It is well established that NW growth happens along (111) ZB and or (0001) WZ directions [169-170, 173, 175, 194, 196-197]. Before, we go further, it may be appropriate to discuss the reasoning behind the formation of ZB and WZ phases in InAs NWs.

The schematic of the geometry of polarized Raman measurement is shown in Fig. 4.3.2.2.1.

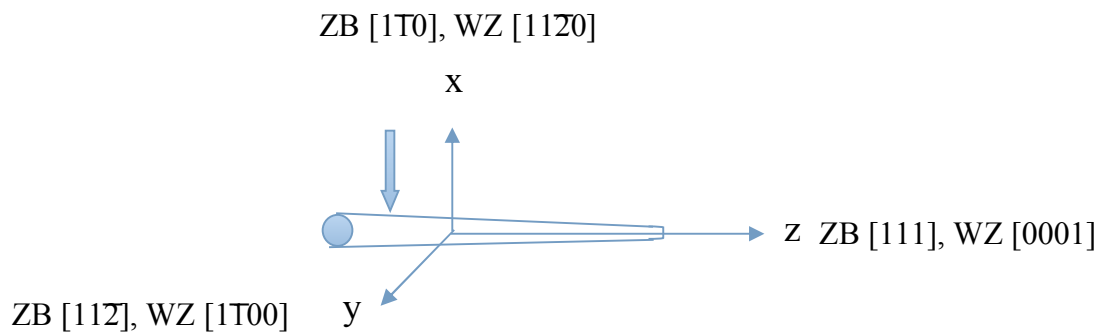


*Fig.4.3.2.2.1: Schematic diagram of the Raman scattering configuration w.r.t. NW axis taken to be in Z direction for back scattering geometry. The x and x axes are the incident and scattering polarization. Z-axis is taken to be [111] and [0001] for ZB and WZ phases, respectively.*

The atomic arrangements in these two structures are very close to each other along the above mentioned directions except for the azimuthal rotation [198-199]. In addition, difference between minimum energy for ZB and WZ phases is calculated to be very small in the range -18 to -9 meV/atom for III-N, 3 to 12 meV/atom for III-V and -1.1 to 6 meV/atom

for II-VI group [173, 198-199]. Therefore, existence of both phases for II-VI and III-N can be considered to be a finite possibility and has been already observed for InN [203-205] and CdS [206-209] in bulk form. However, most III-V's except some nitrides shows cubic structure in bulk form. However, NW of III-V's like GaAs, InAs stabilizes in pure WZ, ZB and mixed phases depending on growth conditions [169-174,194-195,197-198]. Volker et al. have reported that the bulk energy per atom pair for ZB phase is lower than WZ bulk energy, therefore, the stable phase is ZB in bulk material in this case [173], however, for NWs, the WZ phase has lower surface energies than ZB phase for corresponding crystalline orientations in the same material. This effect is expected to stabilize the WZ structure for sufficiently thin NW, that is, when the surface-to-volume ratio is high enough [172-173, 198] However, in our case, where diameters range from 2  $\mu\text{m}$  to 400 nm, this need not be the case. Therefore, it is more important to do polarization studies to first confirm the possibility of existence of both the ZB and WZ in studied MNWs, as described below.

The z direction is considered to be MNW growth direction. For cubic structure, x, y are chosen to be direction  $[1\bar{1}0]$ ,  $[11\bar{2}]$ ; perpendicular to growth directions (111), as earlier noted for several InAs NWs grown using MOCVD [169-171, 195]. The back scattering is taken to be along x  $[1\bar{1}0]$  direction following earlier reports on InAs, GaAs nanowires grown using MOCVD [169-171, 195]. We have performed Raman measurement on a single uniform MNW with a laser light 488 nm in two polarization configuration  $x(z,z)\bar{x}$  and  $x(y,y)\bar{x}$  i.e. incident as well as scattered light is polarized i) parallel and ii) perpendicular to MNW axis, respectively. Raman selection rules suggests that the TO phonon of ZB/WZ and  $E_{2h}$  of WZ are allowed in  $x(y,y)\bar{x}$  geometry, and only TO phonons of ZB/WZ are allowed in  $x(z,z)\bar{x}$  geometry (Table 4.3.2.2.) [169].

Table 4.3.2.2: Raman selection for different Raman scattering configurations [169].

$x(z,z)\bar{x}$	TO : ZB & A <sub>1</sub> (TO) : WZ
$x(y,y)\bar{x}$	TO : ZB , A <sub>1</sub> (TO) : WZ & E <sub>2h</sub> :WZ

Thus, we find that Polarized Raman study using only these two configurations can give the information about the presence of WZ and ZB phases for InAs MNWs. The optical image of uniform NW ( $d \sim 600$  nm) is shown in Fig 4.3.2.2.2a and b, which is oriented in plane horizontally and vertically on Si substrate, respectively. The observation of red shift of the asymmetric peak  $\sim 3.5$  cm<sup>-1</sup> in  $x(y,y)\bar{x}$  configuration compared to that of  $x(z,z)\bar{x}$  configuration, where E<sub>2h</sub> is expected to dominate the spectra, indicates that  $\omega_1$  is indeed E<sub>2h</sub> phonon of WZ structure. Hermann et al. [170] has observed that the intensity of TO phonon is more as compared to E<sub>2h</sub> mode in  $x(z,z)\bar{x}$  and intensity of E<sub>2h</sub> mode is higher than TO mode in  $x(y,y)\bar{x}$  configuration.

They have supported the observance of this ratio using HRTEM experiment. We also observe for  $x(y,y)\bar{x}$  configuration redshift of TO like phonon as compared to spectra in  $x(z,z)\bar{x}$  configuration, confirming TO phonon is dominant in  $x(z,z)\bar{x}$  configuration and  $x(y,y)\bar{x}$  spectra contains both E<sub>2h</sub> and TO phonons ( $\lambda_{exc} \sim 4880\text{\AA}$ ). Similar observations are reported earlier for III-V NWs for diameters in the range  $\sim 100$  nm [169-170, 190]. It is reported that TO phonon observed in InAs, GaAs NWs ( $\sim 100$  nm with both ZB (111) and WZ (001) as growth axis) are mainly due to ZB phase [169-170, 190]. Following this understanding and considering variation in line shape and increased dominance of E<sub>2h</sub> in  $x(y,y)\bar{x}$  confirms, presence of both WZ and ZB phases.

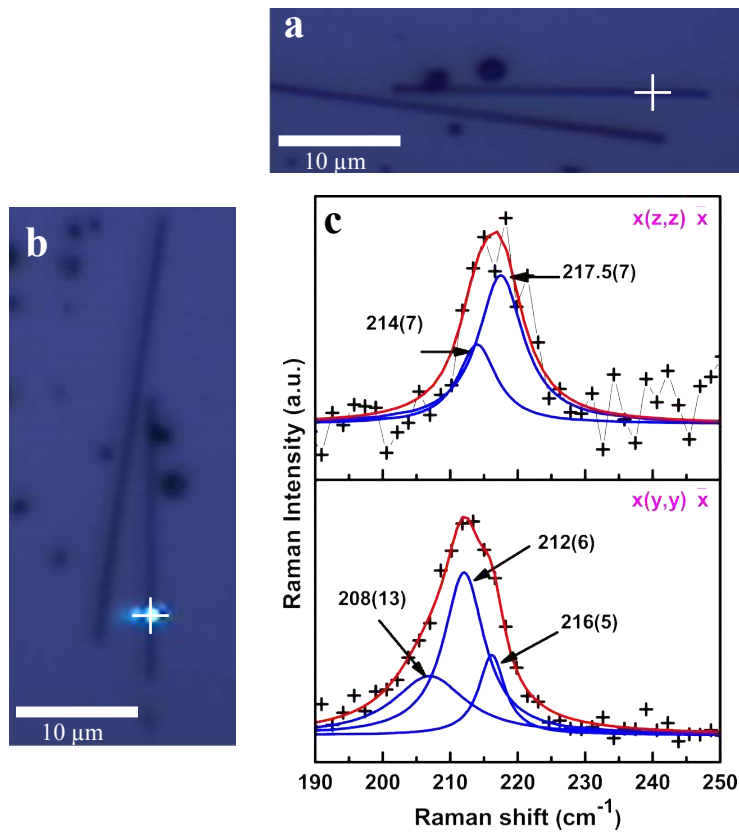


Fig. 4.3.2.2.2: (a) Optical image of uniform wire (dia  $\sim 600$  nm) a) in horizontal direction, b) in vertical direction and c) Polarized Raman data in  $x(z,z)\bar{x}$  and  $x(y,y)\bar{x}$  configuration at positions as marked in optical image (a) and (b), respectively. Cumulative fit (red solid line) to the raw data ( $+$ ) and separate Lorentzian compartments are shown with blue solid line.

Further, it may be important to note that unpolarized data is found to replicate Raman data in  $x(y,y)\bar{x}$  configuration probably due to its large signal in this configuration. In  $x(y,y)\bar{x}$  configuration, the one lower frequency side mode is also observed  $\sim 208$   $\text{cm}^{-1}$  with large FWHM  $\sim 13$   $\text{cm}^{-1}$ . Hermann et al. [170] have reported from the range of 201-210  $\text{cm}^{-1}$  due to the silent mode  $B_{1H}$  of WZ structure. Silent mode is not Raman active, however presence of mix structure/disorder of WZ and ZB phase leads to breaking of translation symmetry/Raman selection rules and these silent modes become observable.

First, the unpolarized Raman spectroscopy is performed on tapered MNW for base ( $d \sim 2 \mu\text{m}$ ), center ( $d \sim 1.2 \mu\text{m}$ ) and tip (800 nm) position, which are marked in optical image as shown in Fig. 4.3.2.2.3a. The  $\omega_l$  and  $\omega_h$  vary from 215 and 218.5 to 213 and 217  $\text{cm}^{-1}$  in unpolarized Raman spectra (Fig 4.3.2.2.3b) as going from base to tip. Further, polarization dependent Raman measurement is also performed on tapered MNWs. In polarized Raman spectra,  $\omega_l$  and  $\omega_h$  varies from  $\sim 216$  to  $\sim 213 \text{ cm}^{-1}$  and  $\sim 218$  to  $\sim 217 \text{ cm}^{-1}$  in  $x(z,z)\bar{x}$  configuration, whereas, from  $\sim 214$  to  $\sim 213 \text{ cm}^{-1}$  and  $\sim 217.5$  to  $\sim 216 \text{ cm}^{-1}$  in  $x(y,y)\bar{x}$  configuration, respectively for MNW going from base (Fig. 4.3.2.2.3c) to tip (Fig. 4.3.2.2.3e). The line shape and width of these modes  $\sim 215 \text{ cm}^{-1}$  in  $x(y,y)\bar{x}$  geometry suggests that frequencies of  $\omega_l$  to  $\omega_h$  comes closer continuously from base to tip. The relative intensity ratio of the two phonons, however, does not seem to change significantly in the unpolarized Raman data (Fig. 4.3.2.2.3b). In  $x(z,z)\bar{x}$  configuration, the intensity of  $\omega_h$  is higher as compared to  $\omega_l$  and according to Raman selection rule for ZB and WZ, only the TO of ZB and WZ is allowed in this configuration. In this case, we have fitted two types of same spectra by changing the initial parameter. The fitting is chosen on the basis of 1) chi square should be close to 1 and 2) error in fitting parameters should be less. Fittings shown in figures have error in frequency and FWHM in the range  $\pm 0.2$  to  $0.6$  and  $\pm 0.2$ - $0.8 \text{ cm}^{-1}$ . The redshift and line shape variation for this mode in  $x(y,y)\bar{x}$  configuration compared to that  $x(z,z)\bar{x}$  confirms  $\omega_l$  mode as  $E_{2h}$  and  $\omega_h$  peak as TO phonon of either WZ or ZB and thereby presence of WZ and ZB phases in these MNWs. The presence of  $E_{2h}$  phonon with very small intensity in  $x(z,z)\bar{x}$  geometry may be due to disorder of WZ and ZB phase which is leading to breaking of translation symmetry.

This is further discussed in the next section. The above analysis suggests that the studied tapered and uniform MNWs show the presence of both ZB and WZ phases of InAs and  $\omega_l$  to  $\omega_h$  are identified as  $E_{2h}$  (WZ) and TO (ZB or WZ) phonons.

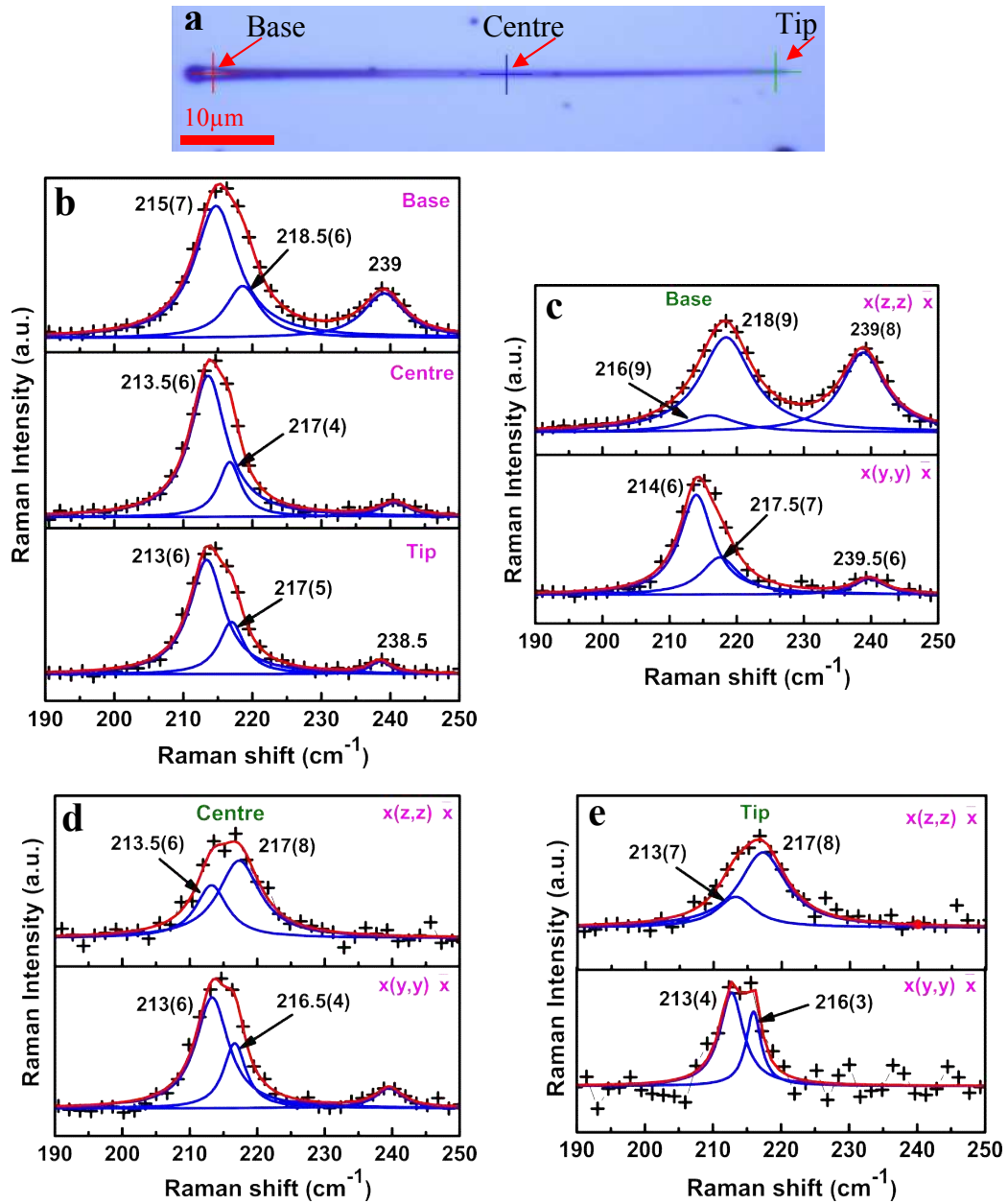


Fig. 4.3.2.2.3: (a) Optical image shows tapered MNW (base dia  $\sim 2 \mu\text{m}$  and center dia  $\sim 1.6 \mu\text{m}$  and tip  $\sim 800 \text{nm}$ ), (b) unpolarized Raman data at position marked for base, center and tip, (c), (d) and (e) Polarized Raman data for base center and tip position, respectively in  $x(z,z)$  and  $x(y,y)$  configuration. Cumulative fit (red solid line) to the raw data (+) and separate Lorentzian fits are shown with blue solid line.

As in uniform diameter MNWs, it is also found that unpolarized Raman data is replica of  $x(y,y)$  data in frequency and lineshape. In the following, we present SRRS study of

several such tapered and uniform MNWs in order to understand correlation of diameter and frequency of  $E_{2h}$  (WZ) and TO (ZB) phonons.

### 4.3.2.3 Diameter dependence of polytypism in InAs NWs

SRR data taken at different positions along the length on several MNWs. The  $E_{2h}$  and TO phonon frequencies obtained from deconvolution of dominant structure (210-218  $\text{cm}^{-1}$ ) are plotted for the corresponding diameters in Fig. 4.3.2.3.1. Before discussing this plot. It is important to discuss how diameter is determined here. The optical images for all the MNWs have been recorded for selection of SRR data. However, some places diameter  $\sim 400$  nm is closer to diffraction limit, but not below the diffraction limit; as optical images are obtained from white light source.

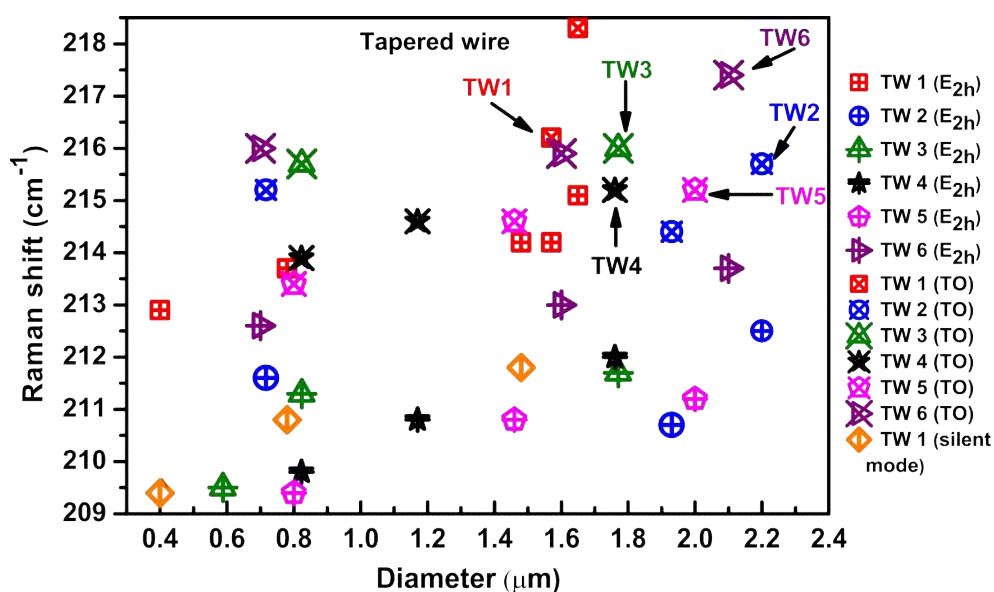


Fig.4.3.2.3.1: Shows diameter v/s frequency for 6 Tapered wires (TW1-6: Table-4.3.2.3.2). Here cross (X) and Plus (+) represent TO and  $E_{2h}$  phonon for TW 1-6,

Nevertheless, we have confirmed correlation of optical and AFM images for few nanowires, which shows that AFM gives values  $\sim 50-100$  nm less than which is noted from the optical image and we have used the Further, one to one correspondence using optical

image. Using diameter obtained from optical images, consistently for all MNWs is found to be suitable procedure here.

All spectra show two main structures, one strong peak  $\sim 212 - 217 \text{ cm}^{-1}$  and other weaker peak  $\sim 238 - 239 \text{ cm}^{-1}$ . The deconvoluted Raman spectra are shown for base (2 and  $1.65 \mu\text{m}$ ), center (1.9 and  $1.6 \mu\text{m}$ ) and center ( $\sim 0.8 \mu\text{m}$ ), tip ( $< 0.8 \mu\text{m}$ ) position with similar diameter range in Fig 4.3.2.3.2a and 3b, respectively. The first is deconvoluted into two phonons as  $\omega_l$  (lower frequency: range  $\sim 210 - 214 \text{ cm}^{-1}$ :  $E_{2h}$  phonon) and  $\omega_h$  (higher frequency:  $\sim 214.5-218 \text{ cm}^{-1}$ : TO phonon) phonons.

*Table 4.3.2.3.2: Diameter of base, center and tip positions for tapered wires (TW) designated as 1, 2, 3, 4, 5 and 6 for which phonon frequency are plotted in Fig. 4.3.2.3.1.*

	<i>Base D (<math>\mu\text{m}</math>)</i>	<i>Centre D (<math>\mu\text{m}</math>)</i>	<i>Tip D(<math>\mu\text{m}</math>)</i>
TW 1(L- 80 $\mu\text{m}$ )	1.57	0.78	0.4
TW 2 (L- 24 $\mu\text{m}$ )	2.2	1.93	0.717
TW 3 (L- 61 $\mu\text{m}$ )	1.77	0.824	0.588
TW 4(L- 49 $\mu\text{m}$ )	1.76	1.17	0.823
TW 5(L- 32 $\mu\text{m}$ )	2	1.46	0.8
TW 6(L- 62 $\mu\text{m}$ )	2.1	1.6	0.78

However, for some very long MNWs, lower frequency phonon in the range of  $\sim 206-209 \text{ cm}^{-1}$  is a broad mode with  $\text{FWHM} \geq 10 \text{ cm}^{-1}$ , wherein corresponding  $\omega_h$  lies in the range  $\sim 210-214 \text{ cm}^{-1}$ , for positions on MNWs, which is closer to the tip. These  $\omega_l$ 's are assigned as silent  $B_1$  mode and corresponding  $\omega_h$  mode as  $E_{2h}$  phonon of WZ phase of InAs. The silent mode is considered being allowed due to disorder. It is important to note that frequency alone cannot be used to assign this mode to be either  $E_{2h}$  or silent mode.  $\text{FWHM} \sim 11-17 \text{ cm}^{-1}$  (Fig.

4.3.2.3.4b for TW1) is an important indicator to be considered. Thus, assignment is done considering FWHM and trend of the MNW Raman spectra shown beforehand, i.e. for larger diameter part of the MNW (TW1), wherein FWHM and intensity ratio of  $\omega_l$  and  $\omega_h$  are expected to show corresponding change.

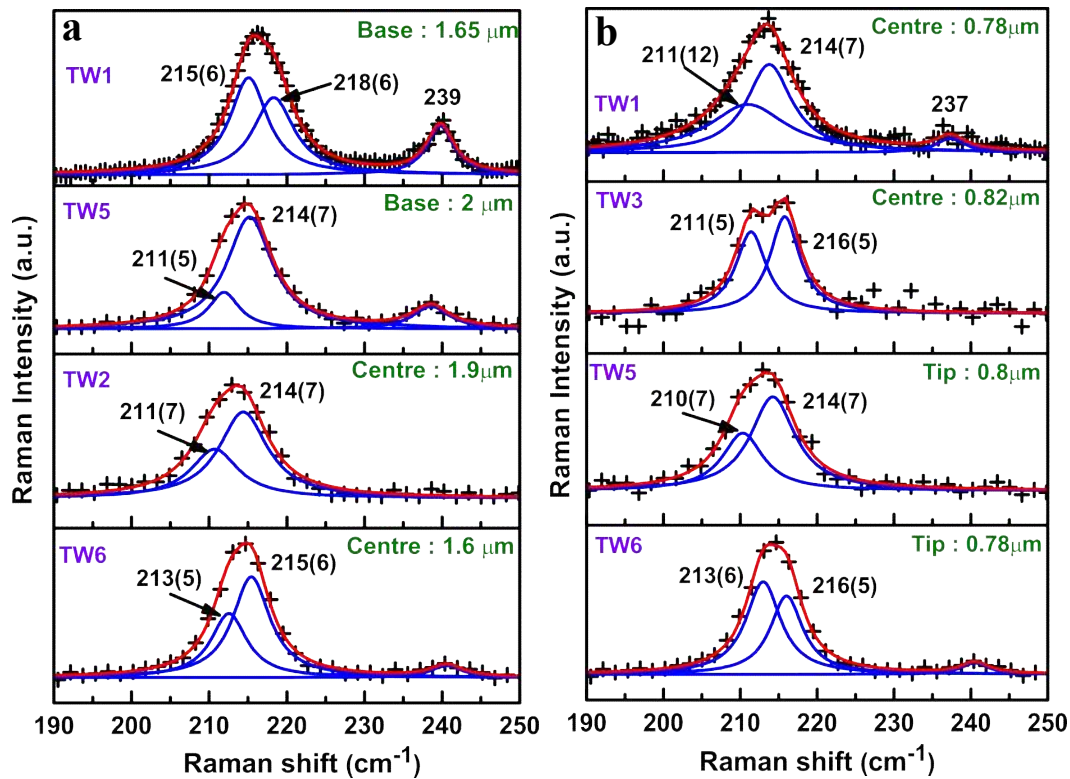


Fig 4.3.2.3.2: (a) and (b) Shows Cumulative fit (red solid line) to the raw data (+) and separate Lorentzian fits are shown with blue solid line for TW 1,5,2,6 at base and center and 1,3,5,6. For center and tip position, respectively.

This observation is made mainly for very long tapered MNWs. Similar observations were made earlier by Hörmann et al.[170] For most other tapered and uniform MNWs, the FWHM of  $\omega_l$  and  $\omega_h$  varies from  $\sim 4$  to  $8 \text{ cm}^{-1}$  (Fig. 4.3.2.3.2a [TW1-6] and Fig. 4.3.2.3.2b [TW1-6]) and are assigned to  $E_{2h}$  and TO phonons, respectively. Frequencies of  $E_{2h}$  and TO phonon from deconvoluted Raman spectra for six TWs are consolidated in Fig 4.3.2.3.2.

It is interesting to note that the variation observed in value of the frequency for  $E_{2h}$  and TO is quite large, especially for  $E_{2h}$ . Further, it is found that this seems to depend not only on

diameter (absolute value), but also on its position on the tapered MNW i.e. if the diameter measured is at the base or center or tip of the MNW.

Thus, Fig. 4.3.2.3.1 and 4.3.2.3.2 states that although, residual strain varies with diameter and shows increase in WZ content as diameter decreases for a tapered MNWs, it however does not uniquely depend on the diameter in these MNWs. This further suggest that although, external growth conditions are same, difference in local growth conditions (seeding/nucleating sites) decides if grown wire would be uniform diameter/tapered and with what phase content i.e. WZ/ZB content ratio.

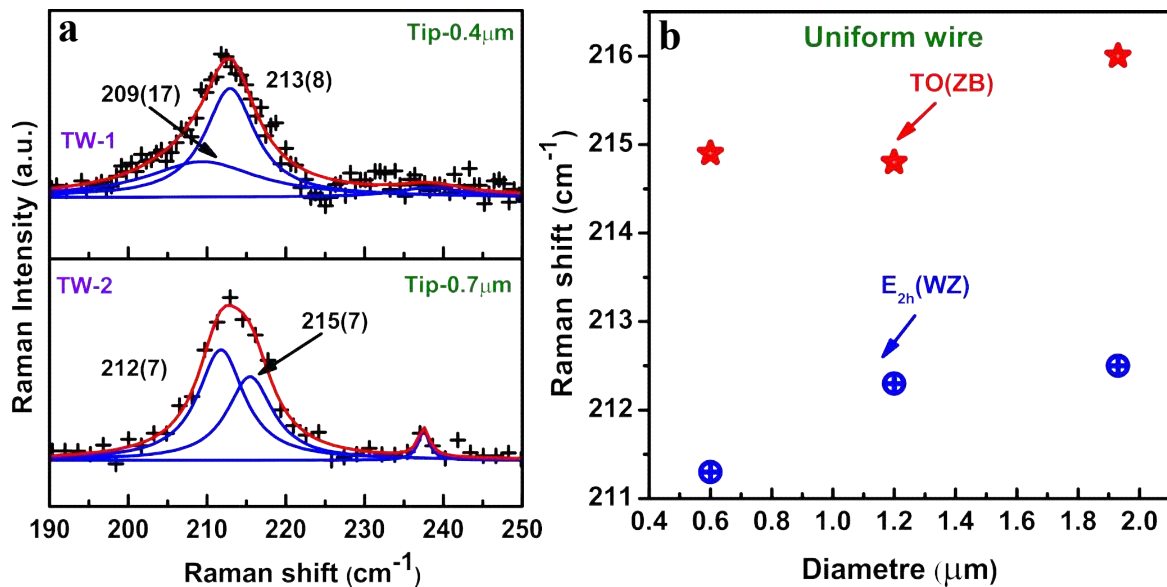


Fig.4.3.2.3.3: (a) Cumulative fit (red solid line) to the raw data (+) and separate Lorentzian fits are shown with blue solid line for TW 1,2 and b) Shows diameter v/s frequency for 3 uniform wires. Symbols (X) and (+) show E<sub>2h</sub> and TO, respectively.

In the following, we discuss these results in the light of polytypism observed in InAs MNWs. In uniform NWs, the frequency and FWHM of E<sub>2h</sub> and TO phonons remains constant along the length of NW, which suggest that content of WZ and ZB phase does not change along the length of NW. Fig. 4.3.2.3.3a and 5b show that for uniform diameter strain varies linearly with the diameter. Further, the frequency of E<sub>2h</sub> and TO phonon redshifts as the

diameter decrease from 1.2  $\mu\text{m}$  to 600 nm as shown in Fig 4.3.2.3.5b, suggesting that the content of ZB phase increases with diameter.

#### 4.3.2.4 Wavelength dependent Raman spectroscopy:

In principal, intensity ratio of  $E_{2h}$  and TO phonon may give us some clue about change in WZ/ZB content, considering the earlier reports, which suggests that TO phonon observed is mainly due to ZB phase and the fact that  $E_{2h}$  and TO phonon show blue and redshift respectively from that of the bulk phonon values [169-171, 190]. Further, Zardo et al. has shown that  $E_{2h}$  and TO, LO phonons shows very different resonance Raman profiles ( $E_{2h}$  peaks  $\sim 2.4$  eV and TO peak  $\sim 2.7$  eV) for WZ and ZB phonons from InAs NW [171, 190, 210-211]. Hence, the ratio may not be commensurate with the content of ZB to WZ phases, when measured with 488/514.5 nm excitations. Further, wavelength dependent polarized Raman spectroscopy is performed at the same position of an InAs MNW for 488 (Fig. 4.3.2.4a) and 441.6 nm (Fig 4.3.2.4b) excitations to further confirm that TO and LO phonons are coming from ZB or WZ phase. From these Raman spectra, one can see that intensity of LO and TO increases drastically at 441.6 excitation as compared to 488 nm excitation. In  $x(y,y)\bar{x}$  configuration,  $E_{2h}$  and  $A_1(\text{TO})$  phonons of WZ structure and TO (ZB) phonons are allowed. At 441.6 nm excitation, the TO phonon dominates in both  $x(y,y)\bar{x}$  and  $x(z,z)\bar{x}$  configurations, however intensity ratio of  $E_{2h}$  to TO phonon decreases as compared to 488 nm excitation. This resonance enhancement in TO and LO phonon clearly brings out that TO and LO phonons are originating from ZB phase. The relative intensity of TO and  $E_{2h}$  depends mainly on four parameters i.e. selection rule/scattering configuration, resonance enhancement, fraction of WZ and ZB phases. The Resonance Raman enhancement can lead to breaking of Raman selection rules and hence the relative intensity of these TO (ZB) and  $E_{2h}$  (WZ) may not represent the fraction of phases with Raman data taken using 4880A or 5145A which are

most commonly used techniques. In our case the  $E_{2h}$  and TO modes are quite close due to presence of significant amount of ZB and WZ phase. This sometimes leads to a large error in intensity obtained through fitting, as frequencies are very close.

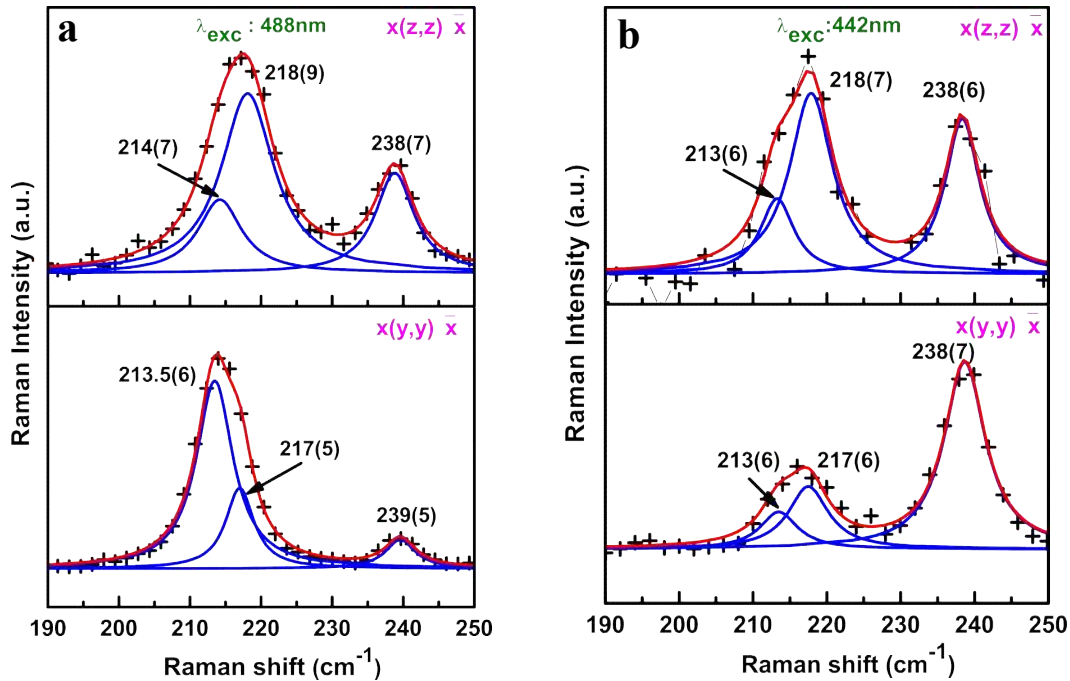


Fig.4.3.2.4: (a) and (b) Polarized Raman data performed with 488 nm and 442 nm excitation, respectively at same wire and at similar position in  $x(z,z)$  and  $x(y,y)$  configuration for uniform wire (dia  $\sim 1.2 \mu m$ ). Cumulative fit (red solid line) to the raw data (+) and separate Lorentzian compartments are shown with blue solid line.

The intensity ratio of TO and  $E_{2h}$  therefore cannot be guiding parameter for obtaining fraction of ZB to WZ phase. Nevertheless, this clearly establishes that the TO phonon observed in unpolarized data is mainly due to ZB phase. In the following effect of polytypism is discussed.

#### 4.3.2.5 Correlation of strain and polytypism in InAs MNWs

In continuation of the above discussion, although, intensity ratio is not a good measure of ZB/WZ ratio, it is noted that as WZ content increases, TO phonon frequency (ZB) shows red

shift, indicating tensile stress, whereas,  $E_{2h}$  phonon frequency (WZ) shows blue shift, suggesting compressive stress. Similar results have been noted earlier for GaAs and InAs uniform NW of diameter  $\sim 100-200$  nm [169-170]. To the best of our knowledge, this is the only related study for III-V NWs. In this context, it may be important to note here, that the stress generated is not due to lattice mismatch occurring in an epitaxial growth (ZB phase / WZ phase alternating as substrate and grown layer) as suggested by Zardo et al.[169, 212].

The preferred growth direction of III-V NWs has been known to be (111) cubic and for II-VI NWs is known to be (0001) for mixed phase growth in III-V NWs [169-170, 190, 198]. It is also known that (111) cubic and (0001) hexagonal are equivalent directions i.e. atomic placement in the two directions for two types of atoms is very similar and can go from one to another with slight azimuthal rotation and therefore for NWs such change of phase is observed [199]. When such stacking fault of change in phase from ZB to WZ happens, it is expected to manifest itself in two ways, i) breaking of selection rules and or ii) generation of strain in the ZB and WZ due to presence of the other. The TO phonon frequency of bulk InAs is found to be  $\sim 217.5$   $\text{cm}^{-1}$  [189, 170, 195, 210-211] and  $E_{2h}$  of WZ is calculated to be  $\sim 211 \pm 1 \text{cm}^{-1}$  [190].

Although, lattice parameters for ZB and WZ phases are different, as expected due to geometric reconfiguration of the unit cell, the faces/planes (111 for ZB and 0001 of WZ) have almost same atomic arrangement except azimuthal rotation. That is to say, although, growth is epitaxial in nature in the direction of growth axis, the phase and planes are different, so that atomic arrangements are similar for two cases. However, atomic arrangements differ significantly in other planes/directions. Similar strain generated due to polytypism is studied for (ZB/WZ) layered SiC thin films [213]. Based on various experimental studies, the strain due to polytypism in ZB and WZ structures is correlated to formation of 2H, 4H and 6H, 3C as more stable unit cell structure in case of polytype growth direction, thereby changing

lattice constant in the perpendicular direction too. This in turn leads to either compressive or tensile stress, value of which depends on percentage of hexagonality and internal cell parameter [176, 200, 213-218]. Theoretically, also, these are found to be minimum energy configuration/s due to changed next near neighbor interactions and therefore, the strain generated is expected to be proportional to content of the other polytype [176]. We attribute the generation of strain due to polytypism in MNWs to be the same and hence they can be used to calculate ratio of content ZB to WZ phase once calibrated to do so. For this, more systematic study along with other technique which can probe this content independently is required, which will be pursued separately and is out of scope of this paper. In the following, however, we can comment upon relative change in ZB to WZ content ratio. The effect of WZ/ZB fraction for uniform and tapered MNWs with different diameter is further studied using temperature dependent Raman spectroscopy measurements. Zardo et al. [169] have studied variation in phonon frequency of  $E_{2h}$  (WZ phase) and  $E_1$  (TO: ZB) with change in relative percentage of WZ and ZB for a uniform diameter GaAs NW. They have varied percentage of WZ and ZB along the length of NW by changing V/III ratio during the deposition. They have observed that the percentage of WZ varies from 98% at one end of NW to 32% in the center and near 0% at another end of NW by High Resolution TEM measurement. All our observations regarding blue and red shift for tapered and uniform MNWs and understanding developed about WZ/ZB ratio for the same is commensurate with observations made by Zardo et al. [169] for above mentioned GaAs NW. At this juncture, it is important to note that FWHM decreases for both TO and  $E_{2h}$  phonons (Fig. 4.3.2.2.2 and 4.3.2.2.3) in  $x(y,y)\bar{x}$  Raman scattering configuration than that in  $x(z,z)\bar{x}$  configuration. This clearly brings out the fact that crystalline quality of the material in the direction of NW axis is poorer than perpendicular to it. This is easy to understand as there are many stacking faults due to ZB and WZ structure along the length of MNW axis, whereas, crystalline quality is

much better perpendicular to the MNW axis. As lateral dimension decreases i.e. as we go from base to tip, overall crystalline quality increases. The stacking faults disorder mentioned above can lead to breaking of selection rule, allowing small intensity of  $E_{2h}$  in  $x(z,z)\bar{x}$  configuration as mentioned in the earlier section.

#### 4.4 Effect of strain on temperature dependent properties of InAs NWs

When temperature increases lattice constant is expected to increase so will the force constant. However, when there is residual strain in the MNW due to polytypism, it is expected to affect temperature dependent properties like thermal conductivity, specific heat, linear thermal expansion etc. In the following Temperature dependent Raman spectra is measured on a MNW at three points (base, center and tip) to study effect of strain on thermal expansion coefficient.

##### 4.4.1 Spatially resolved Temperature dependent Raman study: Effect of polytypism

In order to avoid contributions due to all possible variations as noted above, temperature dependent, polarization dependent Raman measurements and atomic force microscopy measurements is performed on the same tapered MNW with same position for obtaining one to one correlation. The optical image of a MNW studied is shown in Fig. 4.4.1.1a.

Since, polarized Raman data and line shapes of unpolarized Raman data clearly suggests presence of two peaks for a structure  $\sim 212-218 \text{ cm}^{-1}$ , we have fitted spectra from 80 K to 300 K for base to tip with three Lorentzian function for LO, TO and  $E_{2h}$  keeping frequency of the  $\omega_{LO}$ ,  $\omega_{TO}$ ,  $\omega_{E_{2h}}$ , width ( $\Gamma_{LO}$ ,  $\Gamma_{TO}$ ,  $\Gamma_{E_{2h}}$ ) and intensities of LO, TO,  $E_{2h}$  as fitting parameters.

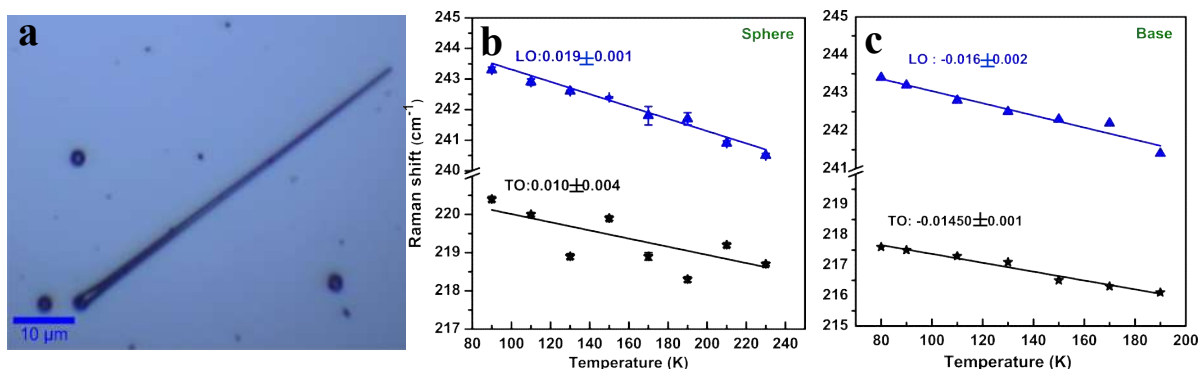


Fig.4.4.1.1: (a) Optical image of InAs MNW. Frequency v/s temperature plot showing linear fit for TO and LO frequency for (b) sphere and (c) base position. The Error bar corresponds to the standard error to  $\omega$  as obtained from nonlinear least square fit to the spectra. The solid line are the best fit to the data points, from which slope are calculated in Fig. (b) and (c).

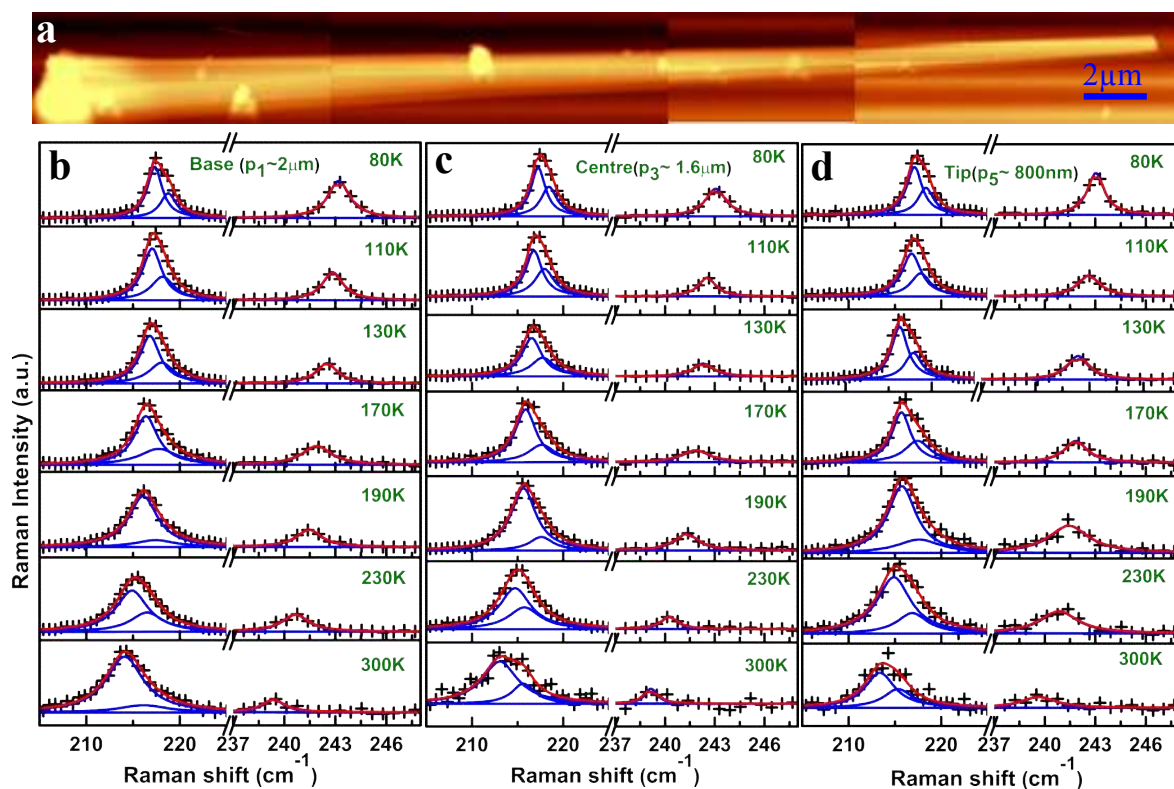


Fig.4.4.1.2: (a) Show the AFM image of InAs MNW, (b), (c) and (d) show the temperature dependent Raman spectra in the temperature range 300K to 80K for base ( $\sim 2 \mu\text{m}$ ), center ( $\sim 1.6 \mu\text{m}$ ) and tip ( $\sim 800 \text{ nm}$ ) position, respectively. Cumulative fit (red solid line) to the raw data (+) and separate Lorentzian fits are shown with blue solid line.

Before going further, we shall like to note that due to significant mixing of phases as noticed from the frequencies of E<sub>2h</sub> and TO phonons, we believe that in our case, calculation of fraction using following equation may not be feasible.

$$\left(\frac{d\omega}{dT}\right)_{Total} = x \left(\frac{d\omega}{dT}\right)_{WZ} + (1-x) \left(\frac{d\omega}{dT}\right)_{ZB} \quad (4.1)$$

Further, temperature dependent Raman spectroscopy is performed at InAs sphere to get the value of  $(d\omega_{TO}/dT)_{ZB}$  because the sphere have pure ZB structure. The  $d\omega_{TO}/dT$  obtained  $\sim 0.010 \text{ cm}^{-1}/\text{K}$  by from graph of TO, LO phonon frequency vs temperature which is shown in Fig. 4.4.1.1.

$$\left(\frac{d\omega}{dT}\right)_{WZ} = \left(\frac{d\omega}{dT}\right)_{TE} + \left(\frac{d\omega}{dT}\right)_S \quad (4.2)$$

$$\left(\frac{d\omega}{dT}\right)_{ZB} = \left(\frac{d\omega}{dT}\right)_{TE} + \left(\frac{d\omega}{dT}\right)_S \quad (4.3)$$

Panda et al. [211] have reported the  $d\omega_{E2h}/dT_{WZ}$  and  $d\omega_{TO}/dT_{ZB}$  are  $\sim -0.005$  and  $-0.009 \text{ cm}^{-1}/\text{K}$ , respectively. Putting these values in equation 1, we get  $x = -1.3$ , an unfeasible value for concentration, with  $d\omega/dT_{total} \sim -0.01450$  (Fig 4.4.1.1).

This suggests that the contribution of residual stress needs to be exclusively taken into account and secondly phonons both originating from ZB and WZ phases need to be treated separately, as they undergo different kind of stress. Thus equation (1) for our case can be written as, [211]. Where, TE and S refer to change in frequency as a function of temperature due to thermal expansion and residual stress, respectively. Frequencies v/s temperature of deconvoluted peaks is plotted in Fig. 4.4.1.3 (a, b, c) for base (P<sub>1</sub>), center (P<sub>3</sub>) and tip (P<sub>5</sub>) for the tapered MNW.

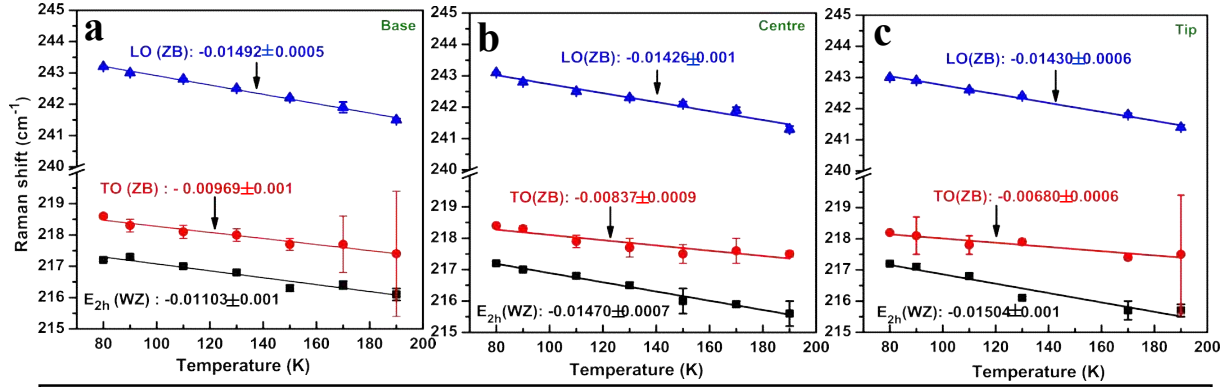


Fig.4.4.1.3. Frequency  $\nu$ /s temperature plot showing linear fit for TO, LO and  $E_{2h}$  frequencies for (a) base, (b) center and (c) tip position. The Error bar corresponds to the standard error to  $\omega$  as obtained from nonlinear least square fit to the spectra. The solid line are the best fit to the data points, from which slope are calculated in Fig. (a)-(c).

It may be appropriate to note here that unlike others, [210-211, 171, 219] we are able to resolve peak  $\sim 212$ - $218$  cm<sup>-1</sup> into two peaks i.e. TO phonon and  $E_{2h}$ . This has become feasible, as unlike others, we have observed Raman data for larger MNWs, which have larger ZB content. Whereas, earlier reported work is mainly on smaller NWs ( $\sim 100$  nm), wherein, WZ is a dominant phase [170-171, 190, 211, 219]. The slope of the plots for  $E_{2h}$  and TO phonons  $d\omega/dT_{E_{2h}}$ ,  $d\omega/dT_{TO}$  and  $d\omega/dT_{LO}$  are calculated for base ( $P_1 \sim 2$   $\mu$ m),  $P_2$  ( $\sim 1.7$   $\mu$ m), center ( $P_3 \sim 1.6$   $\mu$ m),  $P_4$  ( $\sim 1$   $\mu$ m) and tip ( $P_5 \sim 800$  nm) and for uniform NW ( $P_8 \sim 500$  nm (Fig. 4.4.1.4) are tabulated in table 4.4.1.1. One can clearly see that for TO and LO phonons, frequencies are less than that for bulk ZB [211, 219- 221] and for  $E_{2h}$ , it is greater than that of bulk WZ [211].

Since, major contribution of TO and LO phonon is due to ZB, the equation 4.2 and 4.3 are applied to  $E_{2h}$  and TO, LO phonons, respectively.

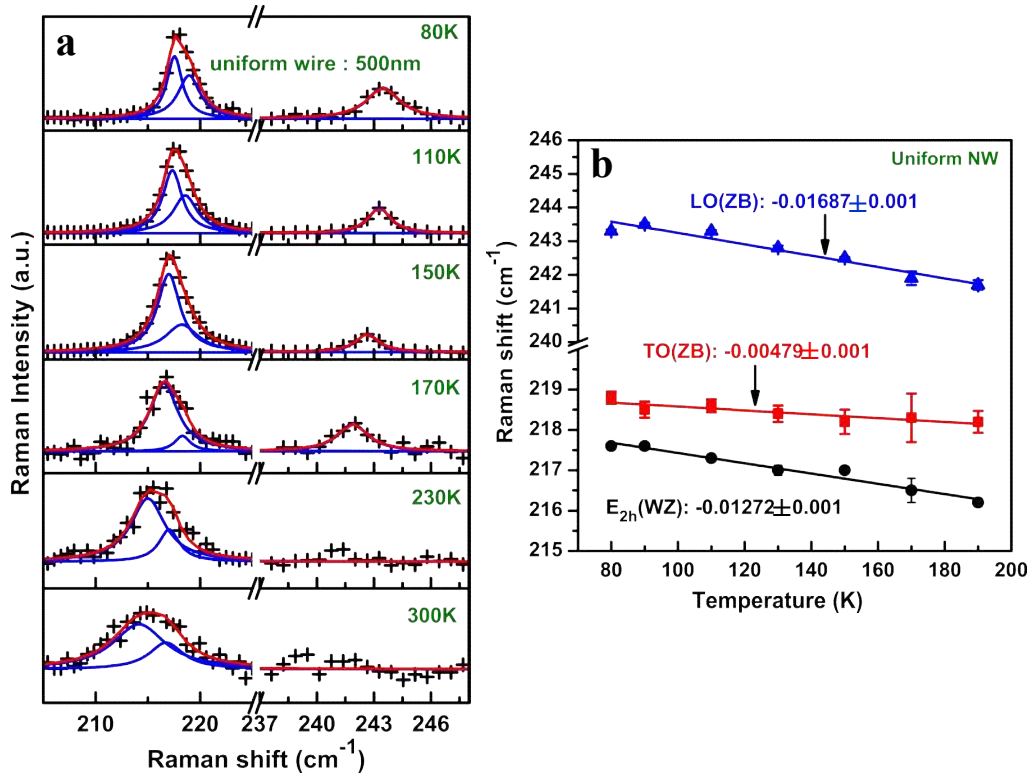


Fig. 4.4.1.4: (a) The temperature dependent Raman spectra in the temperature range 300K to 80K for uniform NW (dia  $\sim$  500 nm). Cumulative fit (red solid line) to the raw data (+) and separate Lorentzian fits are shown with blue solid line and b) Frequency v/s temperature plot showing linear fit for TO, LO and  $E_{2h}$  frequencies for uniform wire. The solid line are the best fit to the data points.

The calculated contribution of strain to the  $d\omega/dT_{E_{2h}, TO}$  and LO and are tabulated in table 4.4.1.2 for a tapered MNW and a uniform wire. It can clearly be seen from table IV that  $d\omega/dT_{E_{2h}}$  due to strain increases as we go from base to tip, however for TO and LO phonons  $d\omega/dT_{TO}$  and LO the same can be said but with much lesser certainty (marked in red/bold).

The uncertainty can be correlated to lesser content of WZ. It is already noted that WZ content increases from base to tip and the trend of  $d\omega/dT$  contribution for these phonons also changes accordingly as given in table 4.4.1.1. The large error bars observed for some points in  $\omega$  v/s T plots are mainly due to two reasons i) intensity of the TO/ $E_{2h}$  is much smaller w.r.t. the other and ii) frequency s of the two are too close and hence, determination of position has larger uncertainty. The reason for smaller TO and  $E_{2h}$  intensity is also two fold, i) smaller

content of ZB/WZ phase and ii) changing of resonance itself due to different mixture of ZB to WZ phase [211, 219].

*Table 4.4.1.1. Frequencies of  $E_{2h}$  ( $\omega_l$ ) and TO ( $\omega_h$ ), intensity ratio of TO to  $E_{2h}$  phonons at 300K and 80K and  $d\omega_{E_{2h}}/dT$ ,  $d\omega_{TO}/dT$ ,  $d\omega_{LO}/dT$  for different positions on a tapered MNW and for a uniform NW are summarized.*

	$\omega_l$ , $\omega_h$ and ratio of $\omega_h/\omega_l$ at 300K	$\omega_l$ , $\omega_h$ and ratio of $\omega_h/\omega_l$ at 80K	$d\omega_{E_{2h}}/dT$ (cm <sup>-1</sup> /K)	$d\omega_{TO}/dT$ (cm <sup>-1</sup> /K)	$d\omega_{LO}/dT$ (cm <sup>-1</sup> /K)
Base (P <sub>1</sub> ~ 2 μm)	214.1, 216.1 and 0.17	217.2, 218.6 and 0.5	-0.01103 ± 0.001	-0.00969± 0.001	-0.01492± 0.0005
P <sub>2</sub> ~ 1.7 μm	213.4, 215.4 and 0.35	217.4, 218.5 and 0.49	-0.01412± 0.001	-0.00955± 0.001	-0.01482± 0.0007
Center (P <sub>3</sub> ~ 1.6 μm)	213, 215.6 and 0.31	217.2, 218.4 and 0.6	-0.01470± 0.0007	-0.00837 ± 0.0009	-0.01426± 0.001
P <sub>4</sub> ~ 1 μm	213.2, 215.5 and 0.38	217.4, 218.6 and 0.32	-0.01483± 0.001	-0.00805± 0.0008	-0.01431± 0.0008
Tip (P <sub>5</sub> ~ 800 nm)	213.3, 215.3 and 0.52	217.1, 218.3 and 0.57	-0.01504± 0.001	-0.00680± 0.0006	-0.01430± 0.0006
uniform NW (P <sub>8</sub> ~ 500 nm)	213.6, 216.5 and 0.75	217.5, 218.9 and 0.8	-0.01272± 0.001	-0.00479± 0.001	-0.01687± 0.001

Therefore, we concentrate on sign of  $d\omega/dT_{E_{2h}, TO}$  and  $LO$  due to stress (Table 4.4.1.2), which is more definitive in nature and explain the same in the following.

*Table 4.4.1.2: Strain component of  $(d\omega_{E_{2h}}/dT)_S$ ,  $(d\omega_{TO}/dT)_S$  and  $(d\omega_{LO}/dT)_S$  for different positions on a tapered MNW and for a uniform NW are summarized.*

diameter	$(d\omega_{E_{2h}}/dT)_S$ ( $\text{cm}^{-1}/\text{K}$ )	$(d\omega_{TO}/dT)_S$ ( $\text{cm}^{-1}/\text{K}$ )	$(d\omega_{LO}/dT)_S$ ( $\text{cm}^{-1}/\text{K}$ )
$P_1 \sim 2 \mu\text{m}$ (TW: Base)	$-0.0060 \pm 0.001$	<b><math>+0.0003 \pm 0.001</math></b>	$+0.0020 \pm 0.0005$
$P_2 \sim 1.7 \mu\text{m}$	$-0.0091 \pm 0.001$	<b><math>+0.0005 \pm 0.001</math></b>	$+0.0022 \pm 0.0007$
$P_3 \sim 1.6 \mu\text{m}$ (TW: Center)	$-0.0097 \pm 0.0007$	$+0.0016 \pm 0.0009$	$+0.0027 \pm 0.001$
$P_4 \sim 1 \mu\text{m}$	$-0.0098 \pm 0.001$	$+0.0020 \pm 0.0008$	$+0.0026 \pm 0.0008$
$P_5 \sim 800 \text{ nm}$ (TW :Tip)	$-0.0100 \pm 0.001$	$+0.0032 \pm 0.0006$	$+0.0027 \pm 0.0006$
$P_8 \sim 500 \text{ nm}$ (Uniform NW)	$-0.0077 \pm 0.001$	$+0.0052 \pm 0.001$	<b><math>+0.0001 \pm 0.001</math></b>

The in-plane thermal expansion of WZ ( $\alpha_a$ ) is less compared to thermal expansion of ZB. As we decrease the temperature, the change in length of WZ is small compared to change in ZB. In order to match atomic arrangement of ZB length (substrate layer), WZ will feel further compressive strain and therefore  $E_{2h}$  (WZ) will blue shift on decrease in temperature giving rise to negative contribution to  $d\omega/dT_{E_{2h}}$ . Whereas, exactly opposite will happen for ZB on WZ, where mode frequency will red shift due to generation of tensile strain on

decrease in temperature. This will give positive contribution of  $d\omega/dT_{TO,LO}$ . The negative and positive  $d\omega/dT$  for  $E_{2h}$  and TO phonon, respectively can thus be explained as due to difference in thermal expansion of WZ and ZB phases of InAs.

#### 4.4.2 Calculation of effective Thermal expansion for WZ structure

Using this temperature dependent Raman data, we estimate thermal expansion of WZ phase of InAs as described in the following. The temperature dependent Raman shift,  $\Delta\omega(T)$  at temperature T relative to the frequency  $\omega_0$  at room temperature can be written as,[222]

$$\Delta\omega(T) = \Delta\omega_{TE}(T) + \Delta\omega_S(T) + \Delta\omega_A(T) \quad (4.4)$$

Where  $\Delta\omega_{TE}(T)$ ,  $\Delta\omega_S(T)$ ,  $\Delta\omega_A(T)$  denote the frequency shift due to thermal expansion, interfacial strain and anharmonicity in lattice, respectively. In present case the range of temperature effect is taken to be below Debye temperature (250K) [211, 223] to avoid significant contribution due to anharmonicity. Therefore, we can neglect the anharmonic part. In an isotropic approximation, the term  $\Delta\omega_{TE}(T)$  and  $\Delta\omega_S(T)$  are given by [222, 224] for WZ,

$$\Delta\omega_{TE}(T) = -\omega \left[ \exp \left\{ -\gamma \int_0^T [\alpha_c(\tilde{T}) + 2\alpha_a(\tilde{T})] d\tilde{T} \right\} - 1 \right] \quad (4.5)$$

$$\Delta\omega_S(T) = -\omega_0 \gamma (2 + \beta) \left[ \left( 1 + \varepsilon_g \right) \frac{1 + \int_{T_g}^T \alpha_{ZB}(\tilde{T}) d\tilde{T}}{1 + \int_{T_g}^T \alpha_{WZ}(\tilde{T}) d\tilde{T}} - 1 \right] \quad (4.6)$$

Where  $\alpha_c$  and  $\alpha_a$  are the temperature dependent coefficient of linear thermal expansion parallel and perpendicular to the hexagonal c axis.  $\varepsilon_g$  is average residual strain. Here, in our case this average residual strain is present due to mixed structure of ZB and WZ. The contribution of change in frequency due to change in temperature is expected due to interfacial strain. This interfacial strain in turn is arising due to difference in ZB and WZ thermal expansion, which is approximated to single WZ layer on ZB and vice versa (Fig. 4.4.2), as we are dealing with average values of frequency, strain and WZ/ZB content over

the scattering volume of Raman spectra. With this consideration, we can write  $\Delta\omega_{TE}(T)$  for ZB [225] as,

$$\Delta\omega_{TE}(T)=\omega_0 \left[ \exp \left\{ -3\gamma \int_0^T \alpha(T) dT \right\} - 1 \right] \quad (4.7)$$

$$\omega_s(T) = -\omega_0 \gamma (2+\beta) \left[ \left( 1 + \varepsilon_g \right) \frac{1 + \int_0^T \alpha_{WZ}(T) dT}{1 + \int_0^T \alpha_{ZB}(T) dT} - 1 \right] \quad (4.8)$$

$$\Delta\omega_s(T) = -\omega_0 \gamma (2+\beta) \left[ \left( 1 + \varepsilon_g \right) \frac{1 - \alpha_{WZ}(T_g - T)}{1 - \alpha_{ZB}(T_g - T)} - 1 \right] \quad (4.9)$$

Growth temperature i.e. 698 K and  $\varepsilon_g$  is average residual strain, which is now calculated from Raman spectra at 300 K.  $\gamma$  is gruneisen parameter i.e. 1.21 for bulk InAs [226] which does not have strong temperature dependence and hence it is neglected for the region considered. The temperature dependent thermal expansion of ZB is taken from Sirota et al. which varies from  $4.52 \cdot 10^{-6}$  to  $2.25 \cdot 10^{-6}/K$  for temperature variation from 300 K to 80 K [227].  $\omega_0$  is transverse optical phonon frequency,  $\beta$  is ratio of elastic constant [228].

$$\Delta\omega_s(T) = (\omega_T - \omega_{300}) - (T-300) \cdot d\omega_{ZB}/dT \quad (4.10)$$

It is calculated from frequency at temperature in the range of 80 K- 190 K.  $d\omega_{ZB}/dT$  for TO phonon is taken to be  $-0.01 \text{ cm}^{-1}/K$  [47]. Taking these parameters, we have calculated the effective thermal expansion coefficient of WZ for base, center and tip position i.e.  $\Delta\omega_s$  (ZB/WZ) is taken to be happening due to difference in thermal expansion of two phases.

Here  $\Delta\omega_s$  (ZB/WZ) is taken to be the average value ZB/WZ phase. It varies with temperature from 190 K to 80 K for base  $\sim 13$  to  $10 \cdot 10^{-6} /K$ , center  $\sim 20$  to  $14 \cdot 10^{-6} /K$  and tip  $\sim 24$  to  $19 \cdot 10^{-6} /K$ . It is appropriate to note here that accuracy of these values is highest at 80 K, as TO phonon frequency shows lowest uncertainty i.e.  $218 \pm 0.06 \text{ cm}^{-1}$ , unlike  $217 \pm 1.5 \text{ cm}^{-1}$  at 190 K.

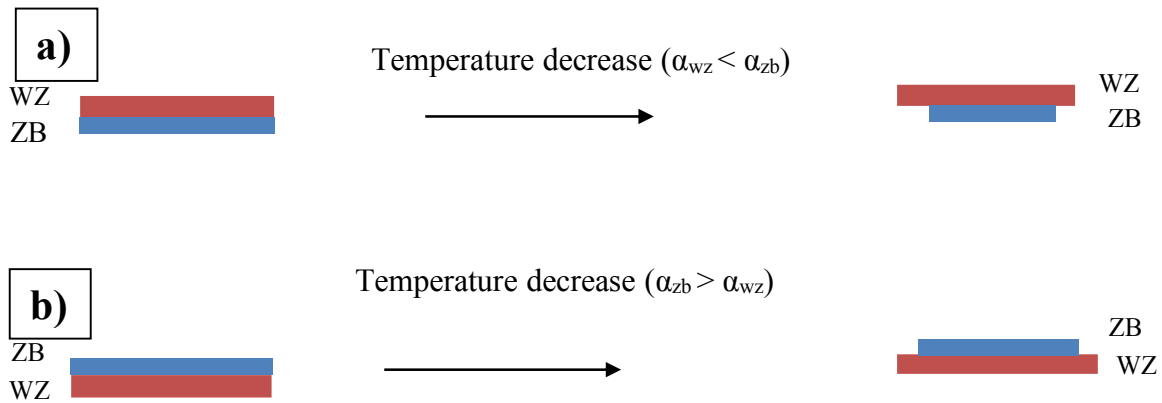


*Fig. 4.4.2: Schematic diagram showing effect of difference in thermal expansion on generation of strain when, (a) the ZB is taken as a substrate and WZ is taken as a layer and (b) the WZ is taken as a substrate and ZB is taken as a layer.*

The effective in-plane thermal expansion of WZ is increasing from base to tip. This is consistent with the fact that compressive stress on WZ is reducing as we go from base to tip due to increase in percentage of WZ towards tip position, which increases the hexagonality and getting close to 2H structure. Thus, the in-plane lattice constant of WZ is increasing and accordingly the thermal expansion of WZ is increasing. However, one must remember that for this calculation, constant thermal expansion coefficient for ZB phase is taken, which may not be the case in reality. This approximation is expected to give overestimated values for thermal expansion coefficient for WZ.

#### 4.5 Revisiting Raman spectra of bent MNWs

With the above understanding, it may be interesting to revisit SRR spectra of bent MNWs (Fig. 4.5a). For smooth bent (Fig. 4.5b), from position 1 to 8, as we are going from larger (800 nm) to smaller (400 nm) diameter, it starts blue shifting right before the bend occurs and continues till it reaches the tip. More such data on smooth and sharp bent MNWs reveals that

sharp bent is observed, wherever there is sudden change in diameter. The sudden change in diameter may lead to development of larger strain due to sudden and larger change in WZ/ZB ratio, thus giving rise to sharp bent.

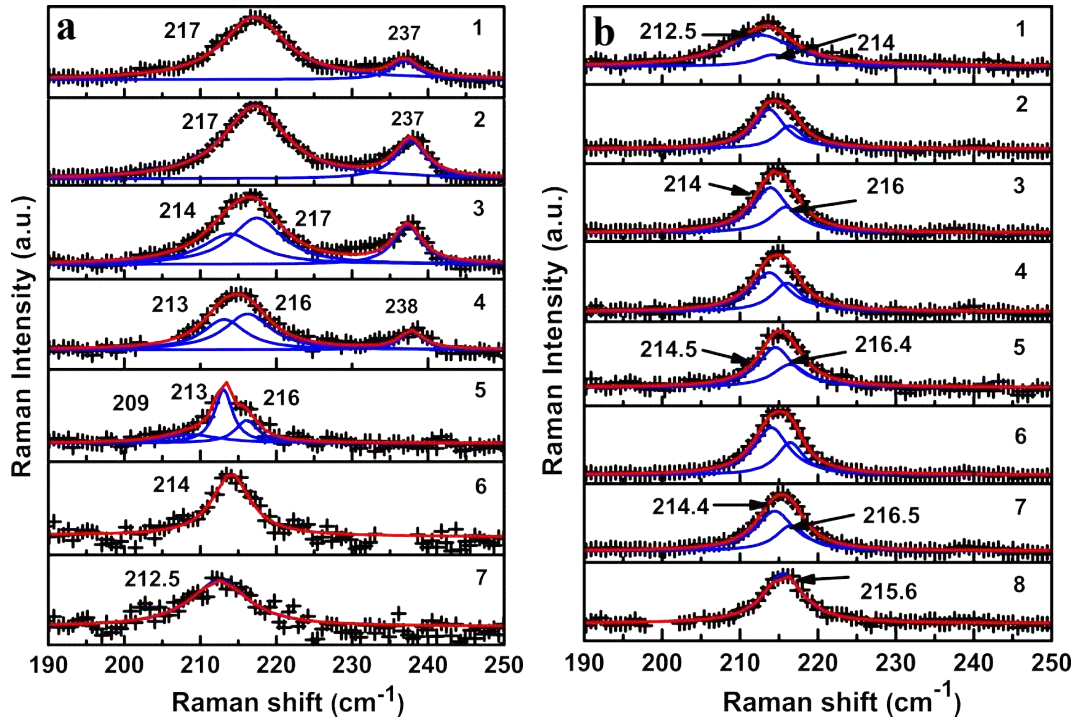


Fig. 4.5: (a) SRR spectra at positions (1-7) as marked in the optical image (Fig. 4.2.2.1a), (b) SRRS at positions (1-8) as marked in the optical image (Fig. 4.2.2.2a). Cumulative fit (red solid line) to the raw data (+) and separate Lorentzian fits are shown with blue solid line.

It is further interesting to note that sharp bent has probably lead to relaxation of the stress in the MNW and hence thereafter it shows red shift, as per change in diameter observed for tapered MNWs. Important to the contrast here that for smooth bent MNWs (Fig. 4.5b), instead continuous blue shift is observed for both the modes (TO and  $E_{2h}$ ) even after smooth bent although diameter is decreasing there too. This suggests that smooth bent has not allowed complete relaxation of the stress generated. One more observation needs to be mentioned here, i.e. reduction in  $E_{2h}$  and TO phonon frequency  $s$  going from  $x(z,z)\bar{x}$  to  $x(y,y)\bar{x}$  geometry as phonons are polarized in Z and Y directions may be due to biaxial strain

in the growth direction. Both these aspects are being further investigated and will be published elsewhere.

#### 4.6 Conclusion

To elucidate the frequency shift observed in TO phonon of InAs in large diameter (~800 nm) microwire, several uniform, tapered and bent InAs micro-nanowires (MNWs) are studied using spatially resolved Raman spectroscopy. Growth mapping studies of metal organic vapor phase epitaxial grown InAs NWs of diameter ~100-200 nm reported in literature suggest MNWs of large diameter (500 nm -2  $\mu\text{m}$ ) to have pure zinc blende (ZB) structure. However, spatially resolved unpolarized, polarized and wavelength dependent Raman spectroscopy has established presence of mixed phases in large diameter uniform and tapered MNWs. This is found to lead to strained ZB and wurtzite (WZ) structures present in these InAs MNWs. The strain was further studied using spatially resolved temperature dependent Raman spectroscopy. This shows that there is significant contribution of stress to temperature dependent behavior of phonon frequencies under these conditions and it has -ve and +ve contribution to  $d\omega/dT$  for WZ and ZB phase, respectively. This can be explained using relative thermal expansion coefficients of ZB and WZ phases. Considering the heterostructure and knowing thermal expansion of ZB phases, we have calculated effective thermal expansion of WZ, which increases from base to tip, consistent with increase in lattice constant of WZ i.e. relaxation of compressive stress from base to tip. Further, it is found that as grown bent MNWs formation is associated with sudden change of diameter and consequently ZB to WZ content.



## **Chapter -5**

**Understanding thermal oxidation of  
InAs micro-nanowires on laser  
irradiation, using simulated  
temperature**

*“The science of today is the technology of tomorrow” — Edward Teller*

## 5.1 Introduction

Semiconductor nanowires (NWs) are important building blocks of future optical, electronic and solar cell devices [229]. Their electrical and optical properties depend on their dimensions and surface. For device applications, it is often necessary to form insulators on the surface and or surface passivation of these nanowires [230]. Formation of native oxide is the easiest way to do so and many physical and chemical processes are used for this purpose [164]. For fine tuning of NW properties, modification of surface and dimensions using laser irradiation is considered to be one of the important method [229, 231-232], as it is considerably fast and good control over the material processing can be achieved.

For III-V bulk/nanowires, it is known that various oxides are formed under different oxidation conditions and InAs particularly presents one of the most complicated processes [164, 188]. Under strong oxidation conditions, presence of Group V metalloids is observed in native oxides on III-V surface, which can strongly influence absorption, leakage current, dielectric breakdown strength etc. [233]. Thus, it is important to know precisely, what is the composition of the modified surface under certain oxidation condition, in order to use it appropriately. Recently, several reports on laser irradiation of III-V NWs (GaAs, InAs) have demonstrated that the oxidation [229, 231-232, 188] and subsequently melting of nanowires are thermal effects [155, 234, 159]. Thus, in order to gain control over various oxidation processes, it is imperative to know temperature at the surface of NW, subjected to the laser irradiation. Stoke and anti-Stokes Raman spectroscopy is often used for estimating the rise in local temperature on laser irradiation. However, since the wavelengths we are using lie in the regime, where, Resonance Raman scattering of InAs occurs; Stokes/anti-Stokes intensity ratio can give incorrect temperature value and hence should not be used for obtaining local

temperature [235]. The other way to know the temperature at the surface of InAs NW, is to simulate the temperature rise at the surface of NW on laser irradiation, which is applied in this work. There exist few reports of temperature simulation using 2D geometry, which is used for corroboration of melting of the InAs NWs and oxidation of suspended NW under high Laser power density (LPD) [229, 231-232, 234, 159]. To the best of our knowledge, this is the first systematic study being reported on the corroboration of simulated temperature and different stages of oxidation processes of InAs NW. Oxidation processes are monitored using time evolution of Raman spectra. In this work, we first establish corroboration between Raman spectra of a chosen InAs NW as a function of time and LPDs and corresponding simulated temperature, covering entire range of oxidation processes. The transient temperature is simulated under various experimental conditions, using finite element method (FEM) with “ANSYS” software considering 3D geometry [236]. This simulated temperature is further used to predict oxidation processes for randomly chosen NWs on laser irradiation with different LPDs for examining the general applicability of this methodology in nanotechnology.

The various oxidation processes leading formation of  $\text{InAsO}_4$ ,  $\text{As}_2\text{O}_3$ , As in various quantities, are understood to be function of temperature. In this chapter, we present simulation of temperature at the surface of InAs NW under given conditions (laser power density, irradiation time, substrate, ambient conditions etc.). Temperature simulations are performed using ANSYS software using finite element method. The simulated temperature corroborates well with the corresponding oxide formations, i. e. weak oxidation for small amount of As,  $\text{As}_2\text{O}_3$ ,  $\text{InAsO}_4$  for temperature  $> 630$  K, intermediate oxidation for larger amount of  $\text{InAsO}_4$  and moderate quantity of  $\text{As}_2\text{O}_3$  for temperature  $\sim 680 - 725$  K and strong oxidation leading to large quantity of  $\text{InAsO}_4$ ,  $\text{As}_2\text{O}_3$  and As, for temperature  $\sim 925$  K. The simulated temperature above  $\sim 1100$  K and its corroboration with Raman spectra suggest this

higher temperature actually corresponds to lower temperature in the range of 600-1000 K, wherein second layer oxidation starts. Corroboration of simulated temperature and Raman spectra taken for random conditions like diameter, aspect ratio, power density etc. was also inspected. It shows that in the geometry factor, not only diameter, but also an aspect ratio is a critical parameter which determines the temperature at the surface of InAs NW. This further emphasizes importance of temperature simulation in order to enable us to use it for required surface modification.

**Background of this work:** In our previous work, we have systematically studied time evolution of Raman spectra as a function of LPD incident on InAs nanowire (NW: D1:  $d \sim 800$  nm and length  $\sim 36$   $\mu\text{m}$ ) [188]. Results of these experiments along with the existing literature on oxidation of bulk InAs identifies formation of  $\text{InAsO}_4$ ,  $\text{As}_2\text{O}_3$ ,  $\text{In}_2\text{O}_3$  and elemental As. Thus, for the controlled surface modification of NWs, it is essential to envisage the rise in the local temperature due to laser irradiation. Stoke and anti-Stokes Raman spectroscopy is another method for estimating the rise in local temperature on laser irradiation. However, the laser wavelength (2.54 eV) used for exciting Raman spectra is in the vicinity of E1 band gap of InAs ( $\sim 2.5$  eV) [141, 169]. In this case, the Raman cross section is dominated by the resonance term, and hence, Stokes/anti-Stokes intensity ratio is not expected to be only the function of phonon occupation number. Therefore, this ratio can give incorrect value and hence should not be used for obtaining local temperature [235]. Therefore, we simulate the local temperature by solving heat transfer equation numerically using finite element program in ANSYS [237].

## 5.2 Theory of temperature simulation

For the above mentioned reason as well as to enable us to predict the surface modification for different lasers wavelengths and laser powers, we have simulated the local temperature by solving heat transfer equation analytically [238].

When incident laser energy generates heating of the material, this heat is transferred in the material by conduction, whereas, convection and radiation causes the heat to flow from material surface to the ambient. In conduction, the energy is transferred from the more energetic to less energetic particles of a material through their interaction. The rate equation for one dimensional case is given by [239],

$$q_x = -K \frac{dT}{dx} \quad (5.1)$$

The heat flux  $q_x$  ( $W/m^2$ ) is the transfer rate of heat in the  $x$  direction per unit area perpendicular to the direction of heat transfer,  $K$  is the thermal conductivity of the material. Convection is the transportation of heat transfer between a fluid in a motion and bounding surface because of temperature difference between surface and fluid (surrounding). Heat transfer in through convection on the surface is given by,

$$q = h (T_s - T_\infty) \quad (5.2)$$

Where,  $q$  is the convection heat flux ( $W/m^2$ ),  $T_s$  (K) is the temperature at material surface, (K) is the ambient temperature and  $h$  is the convection coefficient ( $W/m^2 K$ ).

At a finite temperature, thermal radiation is the energy emitted by the material. The radiation energy is transported by electromagnetic waves. The net rate of heat exchange between the surface and it's environment due to radiation is given by:

$$q = \epsilon \sigma (T_s^4 - T_\infty^4) \quad (5.3)$$

Where,  $q$  is the radiation heat flux,  $\epsilon$  is the emissivity of material,  $\sigma$  is the Stefan- Boltzmann constant ( $\text{W/m}^2 \text{K}^4$ ).  $T_s$  and  $(K)$  are described above. Thus, heat transfer in  $x$  direction is given by,

$$q_{\text{in}} = -K \frac{dT}{dx} + h(T_s - T_{\infty}) + \epsilon\sigma(T_s^4 - T_{\infty}^4) \quad (5.4)$$

Temperature rise due to laser heating is simulated by solving the heat transfer equation using thermal properties of the solid. Considering a homogenous medium in which temperature gradient exists, temperature distribution is expressed in Cartesian coordinates. Next, we consider that the energy transfer will occur from the top of the surface of NW by conduction. The conservation energy is required for this volume, as given by the equation,

$$E'_{\text{in}} + E'_g - E'_{\text{out}} = E'_{\text{st}} \quad (5.5)$$

Where,  $E_{\text{in}}$  is an incident energy,  $E_g$  is heat source term which is associated with the thermal heat generation,  $E_{\text{out}}$  is the outflow heat and  $E_{\text{st}}$  is the internal thermal heat stored by the material and thus, heat balance equation is given by this:

$$\frac{\partial^2 T}{\partial x^2} + \frac{\partial^2 T}{\partial y^2} + \frac{\partial^2 T}{\partial z^2} + \frac{q}{K} = \rho c_p \frac{\partial T}{\partial t} \quad (5.6)$$

Here,  $q$  is the heat flux rate,  $\rho$  is the density of material and  $c_p$  is the specific heat. This is the time dependent condition, however, under steady state condition, there will be no change in the amount of energy stored and thus, equation 5.6 reduced to,

$$\frac{\partial^2 T}{\partial x^2} + \frac{\partial^2 T}{\partial y^2} + \frac{\partial^2 T}{\partial z^2} + \frac{q}{K} = 0 \quad (5.7)$$

### 5.2.1 Convergence check for meshing Sizes and choice of other parameters for temperature simulation

The test data is chosen to be the Raman spectra for LPD  $\sim 200 \text{ kW/cm}^2$ , at  $\sim 200\text{s}$  (Fig. 5.2.1), which shows initiation of oxidation of InAs NW for the range of data considered. It has been

reported that in literature oxidation of (bulk) InAs at temperatures  $\geq 625$  K results in the formation of  $\text{InAsO}_4$ , As and  $\text{As}_2\text{O}_3$  in small quantity [230, 164, 240].

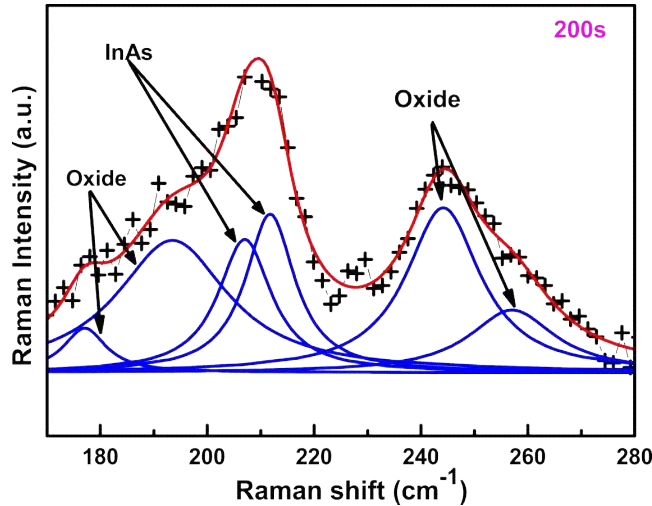


*Fig. 5.2.1: Raman spectra at 200s at laser power density (LPD)  $\sim 200$  kW/cm<sup>2</sup>. Cumulative fit (red solid line) to the raw data (+) and separate Lorentzian fits are shown with blue solid line.*

Using heat conduction equation, first, we simulate local temperature by solving equation 5.6 analytically in 2-dimensional (D) geometry. However, the obtained steady state temperature ( $\sim 310$  K) is much lower for the process expected from Raman spectra i.e  $\geq 625$  K [240]. We can solve the heat transfer equation by different methods i.e. finite element method (FEM), finite difference method (FDM), finite volume method (FVM), boundary element method (BEM) [237, 239, 241]. All the methods are equivalent for using it for thermal analysis, however, available ANSYS uses FEM, which gives better accuracy also. In FEM, we divide volume in many sub-regions which is called element and all sub-regions are connected at the nodes. The values have to be simulated at each node. In this, the assumption we consider is that a variation within an element and the continuous variable is replaced by piece-wise continuous functions which is defined in the element in terms of the nodal values. In the

following, we discuss simulation of local rise in temperature in InAs NW on laser irradiation using FEM.

### 5.2.1.1 2D geometry

Initially, the rise in temperature of the NWs subjected to laser irradiation is estimated by considering the 2D geometry in ANSYS using FEM. Here the assumption is that the heat transfer occurs through the thickness and length of NW, whereas in remaining direction it is considered to be infinite dimension. At 1.6 mW ( $\sim 200 \text{ kW/cm}^2$ ) with thermal conductivity of InAs  $\sim 27 \text{ W/mK}$  [242-243], the simulated steady state temperature (at 500s) on the surface of InAs comes out be  $\sim 344 \text{ K}$  (Fig. 5.2.1.1). Temperature profile is shown in Fig. 5.2.1.1. Here, the red color in temperature profile suggests maximum temperature at surface of InAs NW and blue color suggests minimum temperature on Si substrate. The temperature obtained is for steady state condition and considering perfect contact between InAs NW and Si substrate.

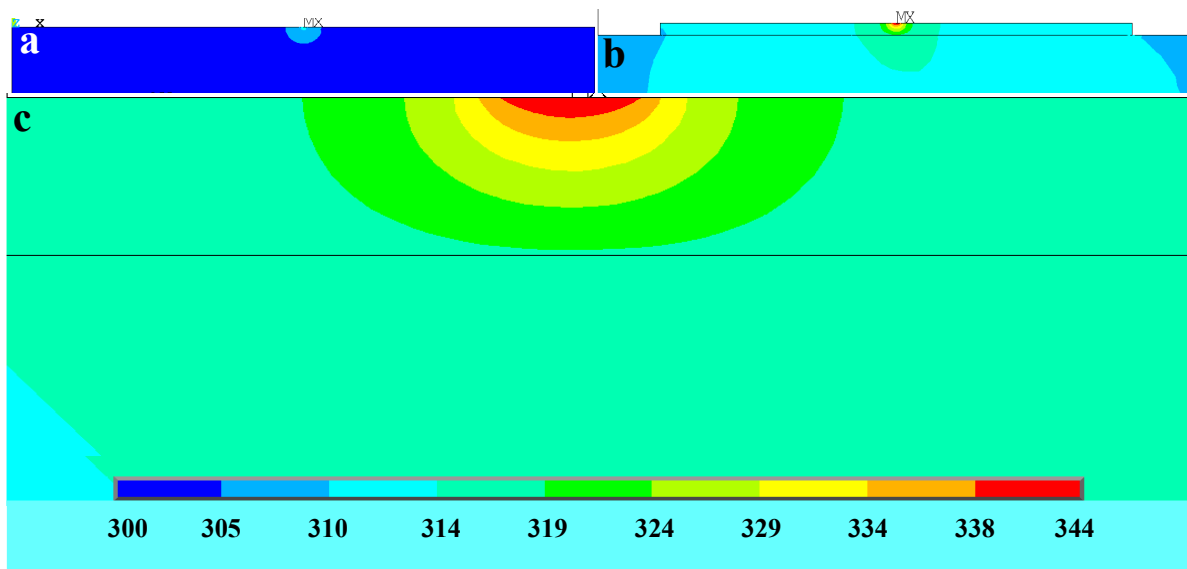


Fig 5.2.1.1: (a) The blue color is showing temperature profile of Si substrate, (b) cyan color is showing temperature profile of InAs NW and (c) Zoom image of temperature profile of InAs NW.

However, this estimated temperature lies much below the expected value of  $\geq 625$  K (at 200s) i.e. there exists inconsistency between the simulated temperature and observed Raman spectra. To look into this, first, we have reproduced the simulation results given in He et al. [159, 234]. Next, other possible reasons for mismatch are looked into. The temperature rise at the surface (at the laser spot) of the material is expected to be dependent on the geometry, thermal conductivity of the material, absorption coefficient, reflectivity of excitation wavelength, heat generated, environment, thermal contacts between substrate and NW etc. In addition to looking at choices of parameters noted above, it is felt that since for NW, semi-infinite geometry in lateral direction is far from reality and may not give a correct result. Therefore, first change made is to consider full 3D realistic geometry (schematic 1) for further simulations [244].

### 5.2.1.2 3D geometry

Thus, in order to resolve the inconsistency noted between Raman spectra and simulated temperature, we perform simulations in 3D geometry considering actual dimensions.

Dimensions in the schematic shown in the Fig. 5.2.1.2.1. are noted in  $\mu\text{m}$ .

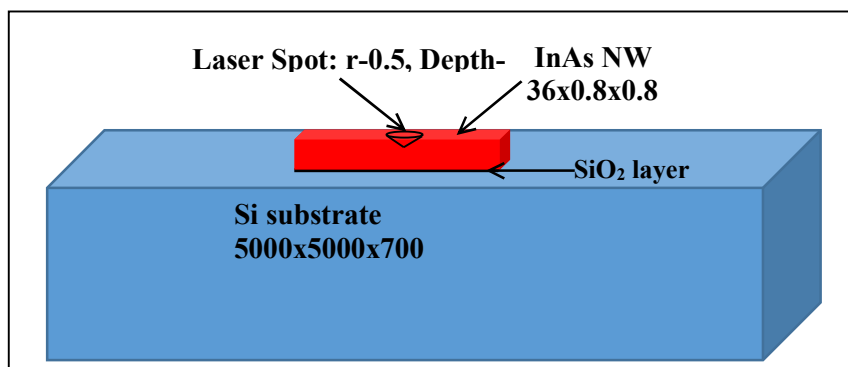


*Fig.5.2.1.2.1: 3D Schematic of InAs nanowire with Gaussian laser spot with penetration depth  $\sim 22$  nm on Si substrate with 5 nm SiO<sub>2</sub> layer. All dimensions are in  $\mu\text{m}$ .*

All parameters used are consolidated (bulk InAs) in Table 5.2.1.2.

Table 5.2.1.2. Parameters of bulk InAs, Si, used in the temperature simulations.

Parameters	Si	InAs
Thermal conductivity (W/ $\mu\text{mK}$ )	$1.3 \times 10^{-4}$ *	$27 \times 10^{-6}$ **
Specific heat (J/Kmol)	0.7 <sup>+</sup>	0.25 <sup>++</sup>
Density (gm/ $\mu\text{m}^3$ )	$2.33 \times 10^{-12}$ * <sup>+</sup>	$5.68 \times 10^{-12}$ * <sup>+</sup>
Size ( $\mu\text{m}^3$ )	5000x5000x700	36x0.8x0.8

\*: [245], \*\*: [242], [197], +: [246], ++: [247], \*+: [248], +\*: [249]

### **Convergence of meshing size for InAs, Si and laser spot volume:**

First, we check for convergence of meshing size for each of the subsection like, laser spot i.e. heat generation volume, NW (InAs), substrate (Si) etc. Initial meshing size of Si substrate and InAs NW is taken to be  $\sim 600 \mu\text{m}$  and  $0.5 \mu\text{m}$ , respectively and convergence of meshing size of cylindrical volume of laser spot is checked over the range  $\sim 0.5$  to  $0.015 \mu\text{m}$  (Fig. 5.2.1.2.2a). The simulated temperature comes out to be  $\sim 382 \text{ K}$ , when the convergence is reached for the meshing size of  $\sim 0.015 \mu\text{m}$ . Next, we fixed meshing size of NW and cylindrical volume  $\sim 0.5$  and  $0.020 \mu\text{m}$ , respectively and varied the meshing size of Si from 1200 to  $200 \mu\text{m}$ . However, we did not observe any significant change in the simulated temperature ( $\sim 382 \text{ K}$ ). We have considered meshing size of Si substrate in the range of 1200 -  $200 \mu\text{m}$  such that nodes of meshing of InAs can be connected to nodes of meshing of Si substrate (Fig. 5.2.1.2.2b). Further, we fixed meshing size of Si substrate and cylindrical volume  $\sim 600$  and  $0.020 \mu\text{m}$ , respectively and varied meshing size of InAs NW from  $0.5$  to  $0.16 \mu\text{m}$ .

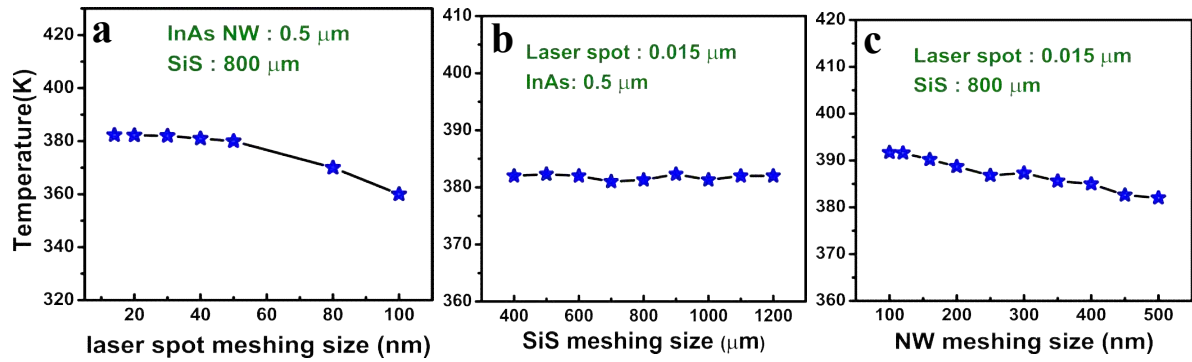


Fig.5.2.1.2.2: Meshing size convergence graph for (a) laser spot, (b) Si Substrate (SiS) and (c) InAs NW.

The meshing size for InAs NW is converged  $\sim 0.16 \mu\text{m}$  and obtained temperature  $\sim 395 \text{ K}$  (Fig. 5.2.1.2.2c). Convergence graph for various meshing sizes for laser spot (Fig. 5.2.1.2.2a), Si substrate (Fig.5.2.1.2.2b) and InAs NW (Fig.5.2.1.2.2c) is shown above.

We take further look at meshing size variation of InAs NW. Fig 5.2.1.2.3 shows two plots, one transient temperature vs time duration and other variation of temperature with meshing size at different duration. Both reflects convergence appropriately.

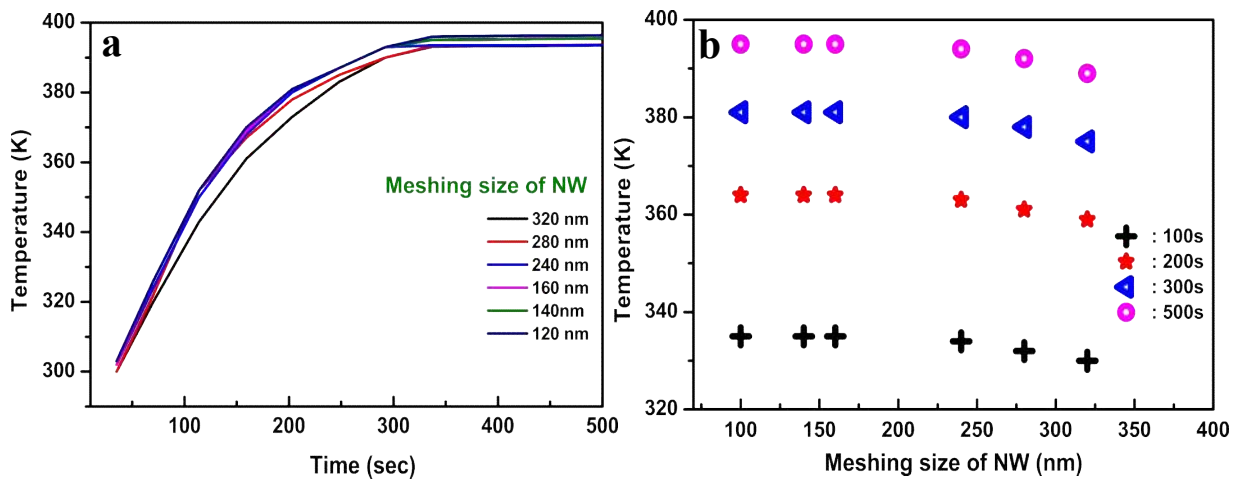
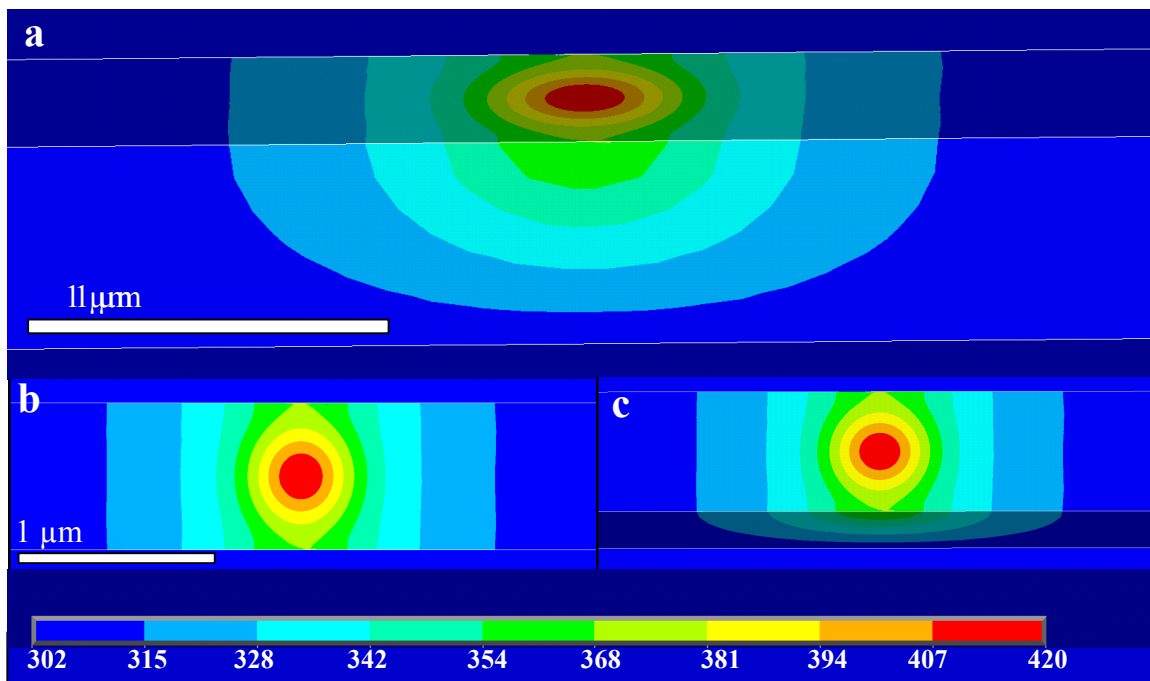


Fig.5.2.1.2.3: (a) Show graph between temperature and laser irradiation time and (b) temperature and meshing size of NW.

Thus, temperature simulation is performed assuming perfect contact between InAs NW and Si substrate, where, load i.e. heat generation  $- 0.09264 \text{ W}/\mu\text{m}^3$  (laser power: 1.6 mW) is

applied in a cylindrical volume of laser spot on InAs NW with convection (in air:  $5 \times 10^{-12}$  W/ $\mu\text{m}^2\text{K}$  [239]) on side and upper face of Si substrate as well as InAs NW and ambient temperature is taken to be 300 K.

We looked for reasons for this inconsistency and found that InAs NWs were grown on Si substrate used without RCA cleaning and therefore, SiO<sub>2</sub> layer ( $\sim 5$  nm) is expected to present on Si surface [250]. Since, the thermal conductivity of SiO<sub>2</sub> is much less and thus, it is expected to make difference in the heat flow. This is accounted for by considering a thin layer of SiO<sub>2</sub> on Si surface for further simulation (schematic 5.2.1.2.1).



*Fig.5.2.1.2.4: (a) 3D temperature profile view for InAs nanowire (NW:  $d \sim 800$  nm,  $L \sim 36\mu\text{m}$ ) on Si substrate, (b) and (c) show the front and side tilted view of temperature profile, respectively.*

The length and width of SiO<sub>2</sub> layer is considered is to be equal to that of InAs NW in order to connect meshing nodes with Si. With the thermal conductivity ( $0.2 \times 10^{-6}$  W/ $\mu\text{m K}$ ) of 5 nm [250] SiO<sub>2</sub> layer, the steady state temperature is  $\sim 500$  K, which still does not match with the experimental results. In this case, simulated temperature at the surface of NW comes out to be  $\sim 420$  K (temperature profile: Fig. 5.2.1.2.4) with optimized meshing sizes taken for

cylindrical volume (heat generation), InAs NW and Si substrate as  $\sim 600$ ,  $0.16$  and  $0.014 \mu\text{m}$ , respectively. However, this value is still much less than needed to explain the Raman spectrum (Fig. 5.2.1) in discussion. It is important to note here that thermal conductivity of zinc blende (ZB) InAs is considered, although it is known there exist polytypism in these NWs [251]. In order to account for polytypism thermal conductivity of wurtzite (WZ) InAs  $\sim 10 \text{ W/mK}$  [197] is taken for simulations discussed hereafter. Since, exact ratio of WZ/ZB content is not known, the minimum value possible is considered to obtain maximum possible rise in temperature. Till now, we have not considered reflectivity losses explicitly, cylindrical volume for laser spot with reflectance  $\sim 45\%$  (for  $488 \text{ nm}$ : 252) and Gaussian intensity profile of the laser spot are considered for next level of simulations. Thus, accounting for Gaussian profile, heat generated  $q(x, y, z)$  at a point  $(x, y, z)$  within a volume is given by [253]:

$$q(x, y, z) = \frac{6\sqrt{3} Q}{\alpha b c \pi\sqrt{\pi}} \exp\left(-\frac{3x^2}{a^2} - \frac{3y^2}{b^2} - \frac{3z^2}{c^2}\right) \quad (5.8)$$

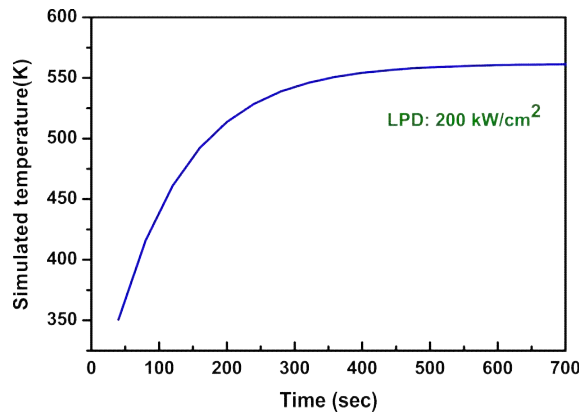


*Fig.5.2.1.2.5: (a) Show graph between temperature and laser irradiation time.*

Using the optimized parameters, we obtained temperature at  $10\text{s} \sim 320 \text{ K}$  and steady state temperature at  $500\text{s} \sim 550 \text{ K}$  as shown in Fig. 5.2.1.2.5. It is important to note here that in this simulation, our assumption is perfect contact between Si and InAs NW, which is not feasible in real condition. The pre-annealing step at  $625^\circ\text{C}$  is done before growth of InAs NW

for this sample and thus, some cracks are expected to be created on Si substrate, on which these InAs NW may be formed [142]. Considering this there is a good possibility that perfect contact between NW and Si substrate may not be a reality. Taking into account actual circular NW geometry, only mid line contacts between InAs NW and SiO<sub>2</sub> layer are considered. The morphology of InAs NW is checked using atomic force microscopy (AFM: chapter 2: Fig 2.5.3.), whereas, we have considered cuboid shape of InAs NW in this simulation in order to simplify the simulation.

#### **Contacts area between InAs and Si volume:**

Considering the above, we have simulated the temperature for elemental contact area 12%, 14%, 22%, and 44% between SiO<sub>2</sub> layer and InAs NW. It is important to note that variation in simulated temperature from perfect contact to 44% contact area is within 1K. Thus, we find that the simulated temperature comes out to be ~ 630 K and ~ 720 K at 200s and 500s, respectively for 12% contact area, whereas, initial (~10s) and steady state (~500s) temperatures are ~ 580, 510, 310 K and ~ 700, 640, 660 K is for contact area 14%, 22% and 44%, respectively. The temperature obtained taking 12% contact area, matches with required temperature for the oxidation process at 200s.

Next we check, what is the variation in temperature with change in number of substeps over the entire temperature range studied (Fig. 5.2.1.2.6). This shows that the 20 number of substeps is a suitable number, which gives correct result in reasonable time and this number will be taken for all further simulations.

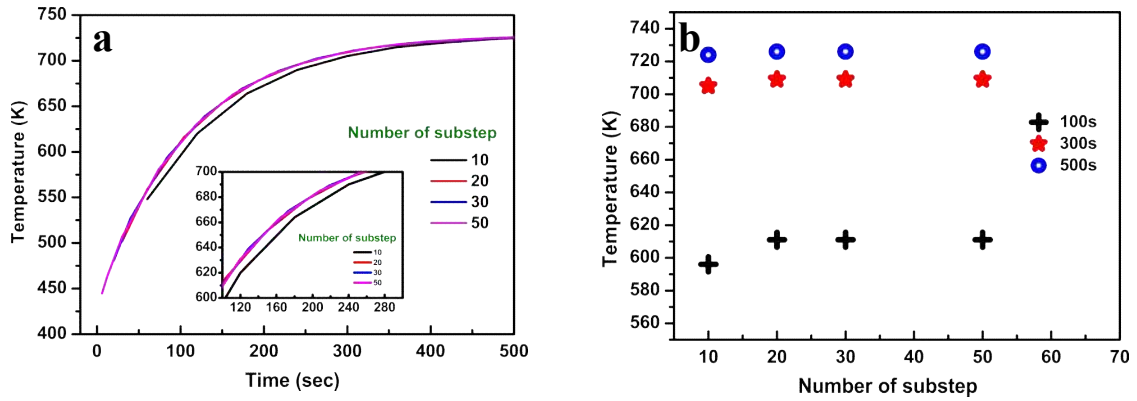


Fig.5.2.1.2.6: Show graph between temperature and (a) laser irradiation time and (b) number of step, respectively.

Time evolution of the simulated temperature, thus (12 % elemental contact area) obtained at the surface of InAs NW at the central point of laser spot is shown in Fig. 5.2.1.2.7a and b for 200 and 636 kW/cm<sup>2</sup> laser power density, respectively.

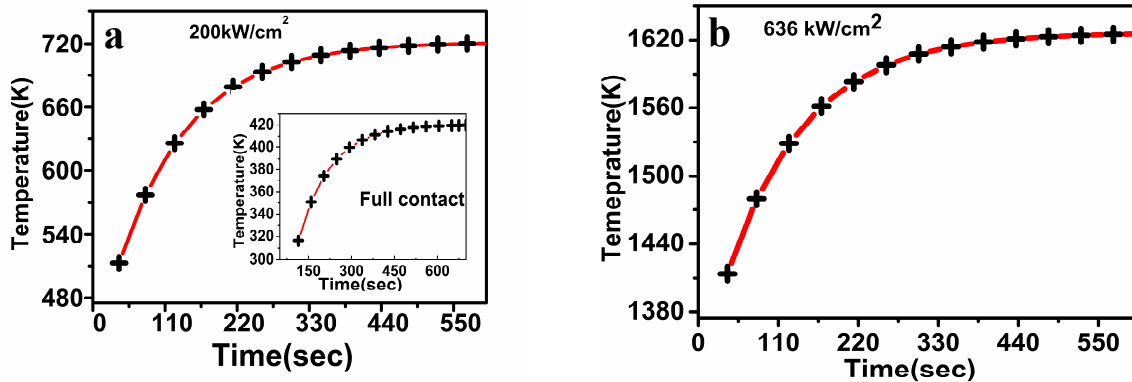


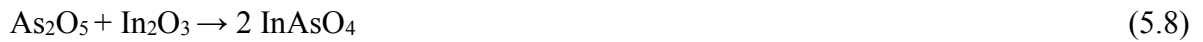
Fig.5.2.1.2.7: (a) and (b) Simulated temperature at the surface of InAs (center of laser spot) as a function of irradiation time for laser power density  $\sim 200$  kW/cm<sup>2</sup> and 636 kW/cm<sup>2</sup> for 12 % elemental contact area, respectively. Right inset shows simulated temperature under same conditions with perfect contact.

Now that we get expected temperature for our case, using same parameters and considerations, we again simulate temperature using 2D geometry and could obtain steady state temperature  $\sim 575$  K. This shows that to obtain correct temperature on laser irradiation of a NW ( $\sim$  hundreds nm) lying on a substrate ( $\sim$  few mm), simulation using actual 3D geometry is important. Error bar for the maximum simulated temperature is estimated to be  $\sim$

$\pm 25$  K, considering measurement errors/uncertainty for various input parameters. Using above parameters temperature is simulated for all laser irradiation conditions i.e. for all LPDs and for time duration of 600s. Corroboration of this simulate temperature with time evolution of Raman spectra is discussed in the next section.

### 5.3 Corroboration of time evolution Raman spectra and simulated temperature

To begin with the results of temperature simulations are consistently corroborated with experimentally observed Raman spectra over a duration of 8 minutes for LPD  $\sim 200$  kW/cm<sup>2</sup>. Keeping the same parameters, we further investigate the predictability of these temperature simulations against observed Raman spectra for different LPDs and irradiation time. For this purpose, we first consolidate different chemical processes occurring due to the oxidation of bulk InAs and their corresponding temperature ranges. Three regions of chemical reactions have been identified and named as weak, intermediate and strong reactions following Schwartz et al. [163, 165] The temperature required for weak oxidation is  $\geq 625$  K [164] and formation of InAsO<sub>4</sub> [240], As and As<sub>2</sub>O<sub>3</sub> is expected in this case [163-165] The weak process (WP) reactions are,



The reaction (5.8), (5.9) and (5.10) are denoted by WP1, WP2 and WP3, respectively. When we keep sample in ambient, small quantity of As<sub>2</sub>O<sub>3</sub> or As<sub>2</sub>O<sub>5</sub> are expected to form at room temperature [254-255]. According to Swartz, reaction WP3 would be favored under weak oxidation condition [163, 165], resulting in small As<sub>2</sub>O<sub>3</sub> and As related peaks. Further, at slightly higher temperature, intermediate processes (IP) reactions are,



The reaction (5.11) and (5.12) are denoted by, IP1 and IP2, respectively. Schwartz et al. and Hollinger et al. further suggests that the expected temperature for formation of  $\text{As}_2\text{O}_3$  by intermediate level oxidation reaction of InAs is in the range from 700 - 733 K [163-165], resulting in broader  $\text{As}_2\text{O}_3$  related peaks. Further, at higher temperatures, strong oxidation processes (SP),



Reaction (5.13) and (5.14) are denoted by SP1 and SP2 leading to large quantity formation of  $\text{As}_2\text{O}_3$  and As [256]. Further, large amount of  $\text{InAsO}_4$  is formed by the reaction



The reaction (5.15) is denoted as SP3 [164-165]. These strong oxidation processes have been reported for temperature  $\sim 930$  K for long time duration of  $\sim 2-4$  days. However, for instantaneous reaction the temperature required may be greater than 930 K. It is reasonable to take this temperature  $> 1000$ K and check against our results. On further increase in temperature, As is formed by decomposition of  $\text{InAsO}_4$ ,



The reaction (5.16) can be denoted as SP4 [165]. All these reactions and corresponding temperatures are consolidated in Table 5.3.1

**Table 5.3.1:** Consolidation of various oxides formed in weak, intermediate and strong interaction regimes, corresponding Raman peak frequencies and temperature for these oxidation processes.

Processes	Resulting product, Raman mode (FWHM) ( $\text{cm}^{-1}$ )	Temperature (K)
Weak		$\geq 630^{\text{a,c}}$
WP1	InAsO <sub>4</sub> : 180-190 and 240-244 (10-15)	
WP2	As <sub>2</sub> O <sub>3</sub> : 190-195 and 245-248 (15-20)	
WP3	As: 196-198 and 256-258 (15-20)	
Intermediate		$\geq 730^{\text{a,b}}$
IP1	InAsO <sub>4</sub> : 180-190 and 240-244 (10-15): W	
IP2	As <sub>2</sub> O <sub>3</sub> : 190-195 and 248-254 (10-15): W	
Strong		$\geq 1000^{\text{a,c}}$
SP1	As <sub>2</sub> O <sub>3</sub> : 190-195 and 248-254 (10-15): S	
SP2	As: 198 and 256-258: W	
SP3	InAsO <sub>4</sub> : 180-190 and 240-244 (15-25)	
SP4	As: 198-200 and 256-260: S	

a : [165] ,      b : [163-164],      c : [256]

To develop correlation between Raman spectra and simulated temperature, we have simulated time evolution of temperature for LPDs used in the range of 30 to 636 kW/cm<sup>2</sup>. The simulated steady state temperature (300 - 450 K) for LPD ~ 30-100 kW/cm<sup>2</sup> is commensurate with the Raman spectra, [188] which does not show any oxidation peak. In Fig. 5.3.1a, b, c and d, we show correlation of temperature and Raman spectra as a function of time at LPD ~ 100, 200, 254, 445 kW/cm<sup>2</sup>, respectively.

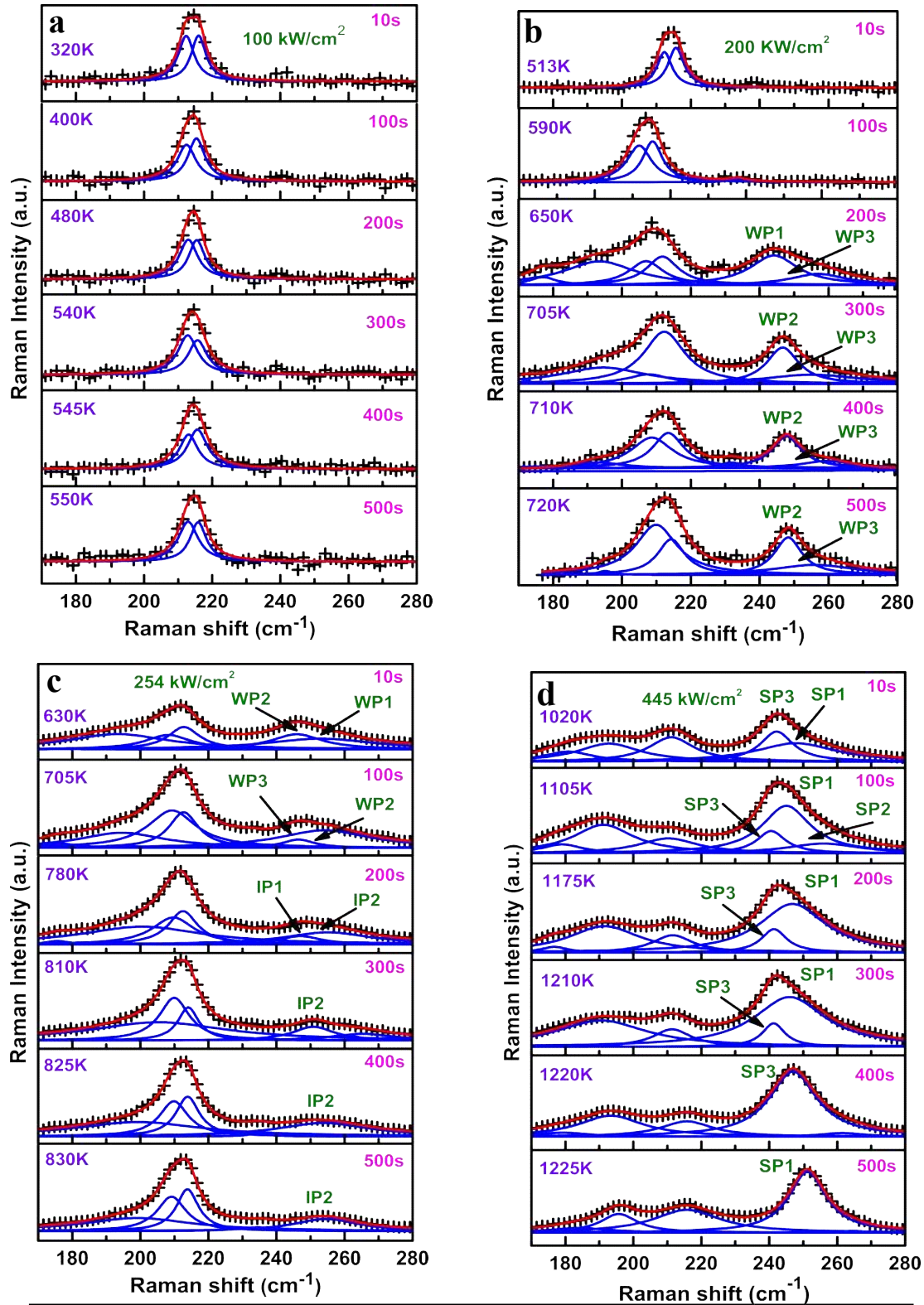


Fig. 5.3.1: (a) Raman spectra along with simulated temperature (a) Time evolution using 488nm laser irradiation of D1 with laser power density (LPD)  $\sim 100 \text{ kW/cm}^2$ , (b) for LPD  $\sim 200 \text{ kW/cm}^2$ , (c) for LPD  $\sim 254 \text{ kW/cm}^2$  and (d) for LPD  $\sim 445 \text{ kW/cm}^2$ . Cumulative fit (red solid line) to the raw data (+) and separate Lorentzian fits are shown with blue solid line.

At  $\sim 200$ s for  $200 \text{ kW/cm}^2$ , (Fig. 5.3.1b), oxide modes are observed  $\sim 195$ ,  $245$ - $248$  and  $255$ - $256 \text{ cm}^{-1}$ . Intensity and peak positions of these modes are indicative of the weak oxidation, which matches well with the obtained temperature of  $650 \text{ K}$ , where formation of  $\text{InAsO}_4$  and  $\text{As}$  takes place by WP1 and WP3 (Table – 5.3.1). Consistently, at  $500$ s ( $\sim 720 \text{ K}$ ) Raman spectra is dominated by  $\text{As}_2\text{O}_3$ . At LPD  $\sim 254 \text{ kW/cm}^2$ , Raman spectra shows that above  $100$ s ( $\sim 700 \text{ K}$ ) suggest the oxidation reaction is going from weak (WP1-WP3) to intermediate (IP1 and IP2) oxidation when temperature  $> 720 \text{ K}$ . At higher LPD  $\sim 445 \text{ kW/cm}^2$  (Fig. 5.3.1d), the simulated temperature reaches  $\sim 1020$ - $1225 \text{ K}$ , where observed peaks in Raman spectra are in the range  $\sim 247$ - $254$  and  $192 \text{ cm}^{-1}$ . Intensity of these peaks w.r.t. to optical phonon of  $\text{InAs}$  ( $\sim 215 \text{ cm}^{-1}$ ) indicates formation of  $\text{As}_2\text{O}_3$  by SP1 and peaks in the range  $\sim 244$ - $246$  and  $183 \text{ cm}^{-1}$  suggest formation of  $\text{InAsO}_4$  by SP3 (Table 5.3.1). The crystalline  $\text{As}$  ( $\sim 198$  and  $256$ - $258 \text{ cm}^{-1}$ ) is formed by SP4, along with  $\text{InAsO}_4$  (strong intensity) and by SP2 with  $\text{As}_2\text{O}_3$  mode (weak intensity) at  $\sim 1020 \text{ K}$  ( $\sim 10$ s).

Thus, Raman spectra clearly shows that occurrences of different process i.e. WP, IP, SP are consistent with temperature value up to  $1150 \text{ K}$  i.e. Raman spectra is commensurate with the simulated temperature for the whole time evolution data of  $\sim 8$  minutes for four discrete powers studied in the range  $100$ - $445 \text{ kW/cm}^2$  up to  $1150 \text{ K}$  (Fig. 5.3.1a, b, c and d). However, above  $300$ s, the simulated temperature obtained is  $>1220 \text{ K}$ , which is above the melting point ( $\sim 1215 \text{ K}$ ) [257] of  $\text{InAs}$ . The higher simulated temperature  $>1200 \text{ K}$  suggests that the NW should melt, however, there is no evidence of the same in either Raman spectra or in the optical image. We shall revisit this issue later in this section.

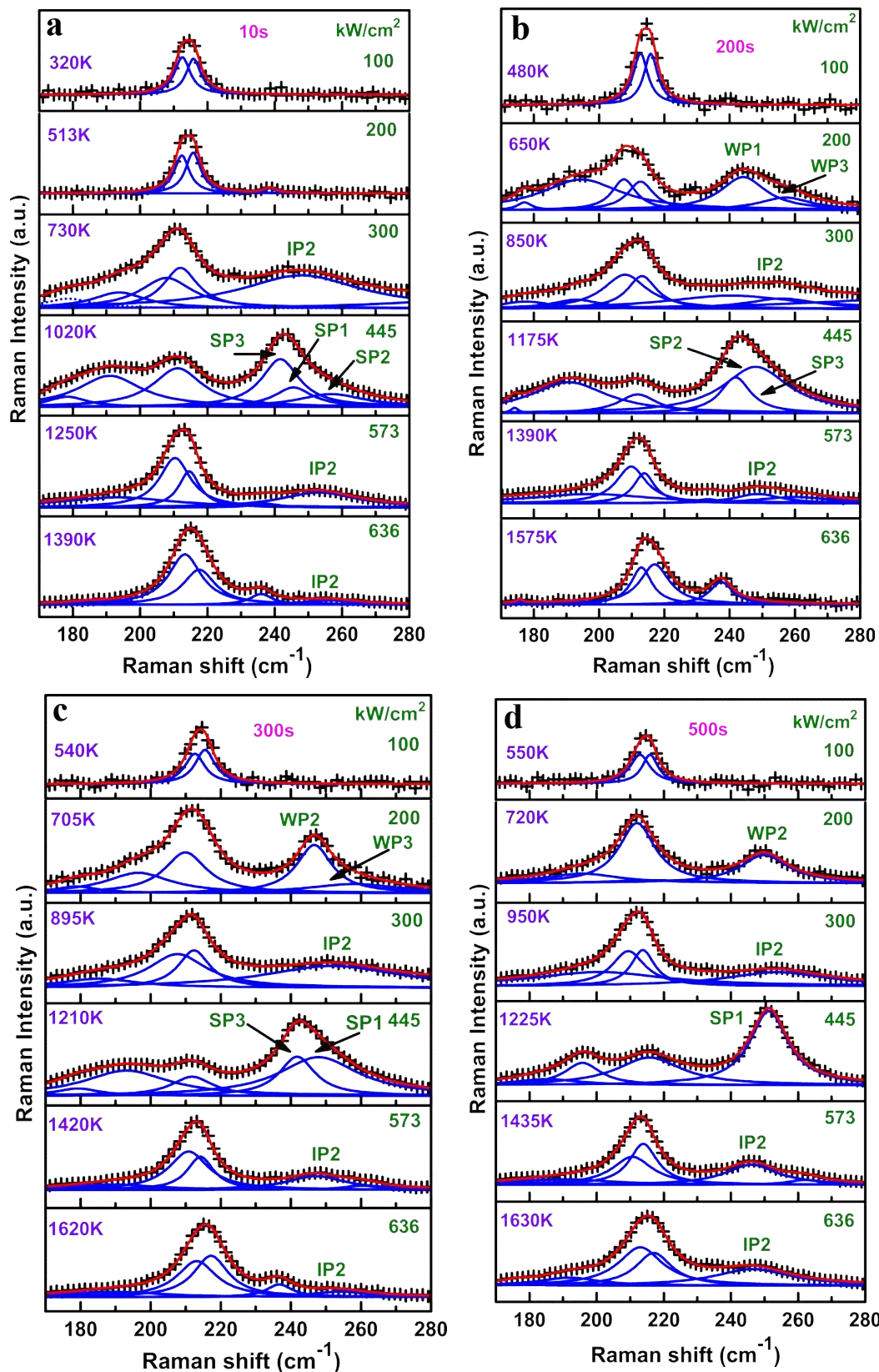


Fig. 5.3.2: Raman spectra along with simulated temperature (a), (b), (c) and (d) for irradiation time of 10s, 200s, 300s and 500s, respectively at all discrete LPDs from 100  $\text{kW}/\text{cm}^2$  to 636  $\text{kW}/\text{cm}^2$ . Cumulative fit (red solid line) to the raw data (+) and separate Lorentzian fits are shown with blue solid line.

Further, we look into the corroboration of Raman spectra with simulated temperature as a function of LPDs after particular time duration to clearly bring out origin of oxidation processes being thermal in nature. Raman spectra for different LPDs after irradiation time of 10s, 200s, 300s and 500s are shown in Fig. 5.3.2a, b, c and d, respectively. (Fig. 5.3.2a) with corresponding temperature noted for each spectrum. At  $\sim 10$ s (Fig. 5.3.2a), we can see that no oxide is formed till LPD  $\sim 200$  kW/cm<sup>2</sup>. For LPD  $\sim 300$  kW/cm<sup>2</sup>, Raman spectra shows formation of amorphous As<sub>2</sub>O<sub>3</sub> oxide via IP2 consistent with the temperature  $\sim 730$  K. For LPD  $\sim 445$  kW/cm<sup>2</sup>, peaks related to As<sub>2</sub>O<sub>3</sub>, InAsO<sub>4</sub> and elemental As are observed in the range of 248-253, 241-243 and 258 cm<sup>-1</sup>, respectively which are formed via SP1, SP3 and SP2 consistent with simulated temperature  $\sim 1020$  K. The RS above 1200K will be discussed later. For Raman spectra at 200s (Fig. 5.3.2b), the weak process already started for LPD  $\sim 200$  kW/cm<sup>2</sup> consistent with simulated temperature of 650 K. Consistent with simulated temperature 850 and 1175, products related to IP2 and SP1, SP2 & SP3 processes are observed. It is important to note here that RS similar to 200s is observed for 300s (Fig. 5.3.2c) and 500s (Fig. 5.3.2d).

This is an important observation that steady state is reached in simulated transient temperature graphs by 500s (Fig.5.2.1.2.5) and further temperature rise is very small of the order of  $\sim 30$ K, from 200 to 500s. Raman spectra is commensurate with this understanding. Raman spectra for LPDs  $\sim 100$  kW/cm<sup>2</sup> to 636 kW/cm<sup>2</sup> shows evidence of oxidation process from WP1 to SP4 corresponding to simulated temperature noted in respective Raman spectra till temperature reaches  $\sim 1200$  K.

To summarize above results, one can say that with the time evolution or increase in LPD, temperature rise increases and first weak, later Intermediate and then strong processes take place, as observed in Raman spectra. In several spectra, products of more than one processes are observed. Although, all the processes from WP1 to SP4 follow the simulated

temperature, as a function of LPD and time evolution, Raman spectra for temperature above ~1200 K cannot be explained using understanding developed above

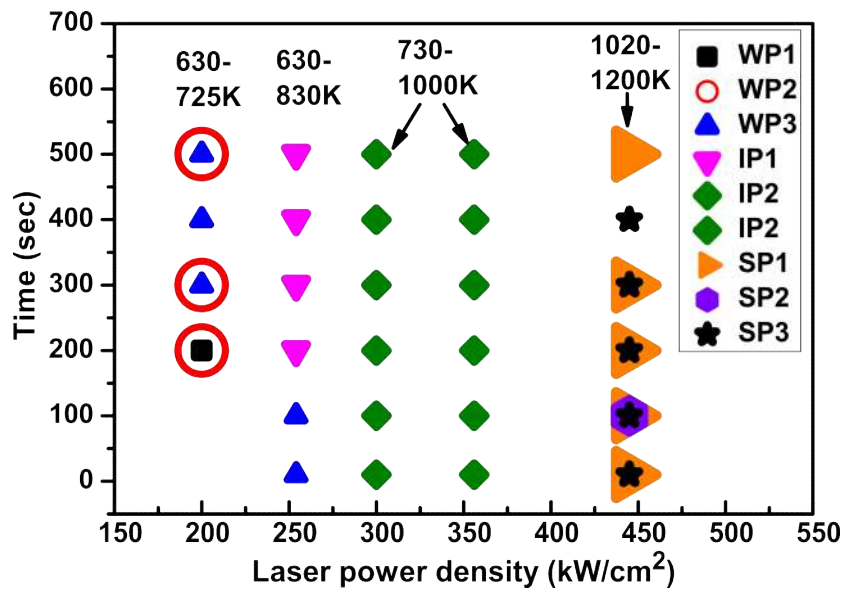


*Fig. 5.3.3: Consolidation of time evolution of simulated temperature and various oxidation processes as a function of LPDs for a NW (DI).*

It is important to note that no significant changes are observed between 200s to 300s for most LPDs, which is also commensurate with the transient temperature simulation, wherein, major temperature rise occurs between 10-200s and there onwards saturation of temperature sets in (Fig 5.3.1a to d and 5.3.2a & b). The correspondence of time evolution of Raman spectra to different processes (Table 5.3.1) under weak, intermediate and strong oxidation for different laser powers studied are consolidated in Fig. 5.3.3.

Time dependent Raman spectra are shown in Fig. 5.3.4a and b for LPDs ~ 573 and 636 kW/cm<sup>2</sup>, respectively.

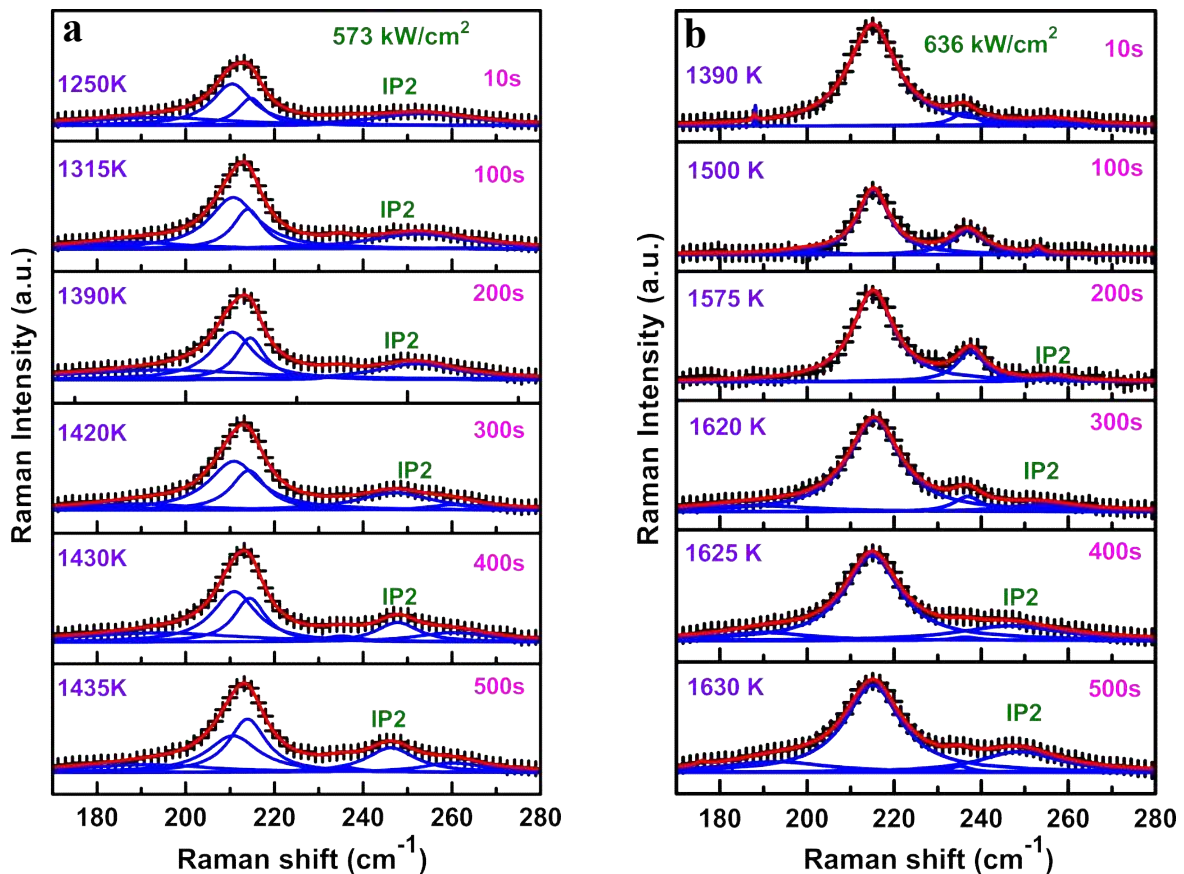


Figure 5.3.4: Raman spectra along with simulated temperature (a) Time evolution using 488nm laser irradiation of D1 with laser power density (LPD)  $\sim 573 \text{ kW/cm}^2$  and (b) for LPD  $\sim 636 \text{ kW/cm}^2$ . Cumulative fit (red solid line) to the raw data (+) and separate Lorentzian fits are shown with blue solid line.

Salient features of the data are,

- 1) Major rise in temperature is in first 200s. From 200s to 300s temperature rise is slow and steady state is reached from 400 to 600s for all the laser irradiation conditions considered. This is commensurate with changes observed in the Time evolution of Raman spectra for different LPDs
- 2) As time passes, higher temperature reaction products along with lower temperature reaction products overlap in certain regions.
- 3) The initial temperature (at 10s) and process occurring at that time changes from no oxidation to SP oxidation commensurate with increase in LPDs.

4) For temperatures above 1150 K, as obtained by FEM analysis, the Raman spectra cannot be explained based on the above understanding.

5) For incident LPD  $\sim 500\text{-}600\text{ kW/cm}^2$ , the FEM analysis leads to the simulated temperatures 1250-1630 K. Although, melting point of bulk InAs is  $\sim 1215\text{ K}$ , no melting of the NW is observed in Raman spectra. In concurrence to this, optical image taken after the Raman measurement does not show any melting of NWs.

This inconsistency between experimental observation and simulated temperature can be understood as at this LPD, large scattering of laser is observed due to the powder formation of elemental As and  $\text{As}_2\text{O}_3$ , which is leading to decrease in the intensity of laser reaching at the NW. Additionally, heat is used up in evaporation of elemental As and all this actually lowers the temperature at the surface of InAs. The As evaporation temperature is  $\sim 900\text{ K}$  [258]. Simultaneously, Laser beam is incident on the next layer of InAs, while temperature at the surface is lowered. Taking this into account, we can analyze observed Raman data in the temperature range 1250-1630 K giving rise to WP-IP processes, depending on several parameters. One can clearly see that when, temperature rises above 1250 K, wherein, already (temperature range  $\sim 1000\text{-}1200\text{ K}$ ) SP processes have been observed, subsequent Raman spectra show processes occurring at lower temperatures like lower SPs or IPs for all Raman spectra (Fig. 5.3.1, 5.3.2 and 5.3.3.). It is Important to note that at higher simulated temperature range from 1210-1650 K, IP2 is observed in the time evolution of Raman spectra for LPDs  $\sim 573$  (Fig. 5.3.4a) and  $636\text{ kW/cm}^2$  (Fig. 5.3.4b) for the entire range from 10 to 500s suggesting that temperature rise is not taking place as expected. This is consistent with the above interpretation that temperature above 1200K is not actually reached and cooling effect is started. This is brought out in Fig. 5.3.5 where top three and bottom three Raman spectra for LPD  $\sim 573\text{ kW/cm}^2$  and  $300\text{ kW/cm}^2$  at 10, 200 and 500s,

respectively are plotted. It is clear from Fig. 5.3.5 that Raman spectra for temperatures 1200-1450 K are similar to the RS observed at lower temperatures  $\sim$  700- 950 K.

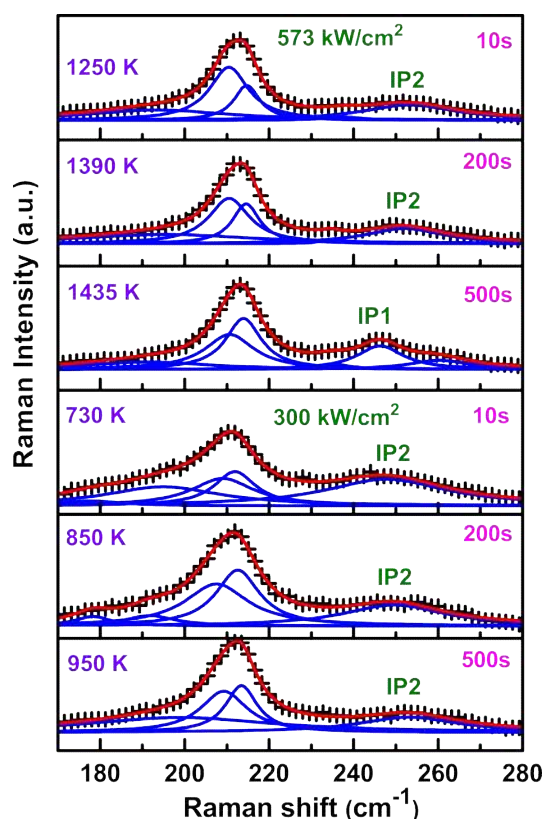


Figure 5.3.5: Raman spectra along with simulated temperature (a) top and down three time evolution using 488nm laser irradiation of D1 with laser power density (LPD)  $\sim$  573 and 300 kW/cm<sup>2</sup>, respectively. Cumulative fit (red solid line) to the raw data (+) and separate Lorentzian fits are shown with blue solid line.

One can note that when temperature rises above 1250 K, subsequent Raman spectra show processes occurring at lower temperatures like IP (730 K-1000 K) or WP (630 K - 720 K) for all Raman spectra (Fig. 5.3.1 to Fig. 5.3.4). Here, when simulated temperature  $>$ 1250 K, the oxidation of first layer is complete and As byproduct that is generated gets evaporated. In this process of evaporation temperature decreases and the second layer oxidation starts from weak/intermediate oxidation process. It is important to note that this process has been noted as oscillatory behavior of intensity of the phonon ( $\sim$  250 cm<sup>-1</sup>) related to elemental As, which shows layer by layer removal of As and it corresponds to temperature  $>$ 1200K [188]. This understanding gives satisfactory corroboration of the simulated temperature for the

complete power dependent time evolution Raman spectra of a studied InAs NW. In the next section, we investigate general applicability of this methodology to predict/control the surface modification using laser irradiation.

#### **5.4 General applicability of this methodology**

To investigate general applicability of the process, the methodology is applied to other NWs with different diameter and aspect ratio grown on the same Si substrate. For this purpose, we repeated experiment on other InAs NWs, randomly choosing the irradiation LPDs. Herein, we use the same input for the temperature simulation of these NWs on laser irradiation except their dimensions. Meshing size convergence was checked for all the NWs separately and we have fixed elemental contact area between SiO<sub>2</sub> and InAs i.e. 12 % which is used in the above simulation.

##### **5.4.1 Application to different diameter NWs and same aspect ratio**

For this purpose, we have chosen NW of diameter larger than earlier by 100nm with similar aspect ratio. Laser irradiation experiment monitored by time evolution of Raman spectra is performed on this InAs NWs using randomly chosen LPDs. The time evolution Raman spectra for NW (D2:  $d \sim 0.9 \mu\text{m}$  and length  $\sim 36 \mu\text{m}$ ) is shown at LPD  $\sim 230$  and  $254 \text{ kW/cm}^2$  in Fig 5.4.1a and b, respectively. At LPD  $\sim 230 \text{ kW/cm}^2$ , the weak oxidation is observed from the Raman spectra and again simulated temperature is obtained  $\sim 630 \text{ K}$  which is started of weak process then further, as time increases, the weak process (WP1-WP3) is converted into intermediate (IP1 and IP2) from temperature range 800-820 K. At higher LPD  $\sim 250 \text{ kW/cm}^2$ , the Raman spectra is well corroborated with simulated temperature in the range 720-950 K for intermediate process.

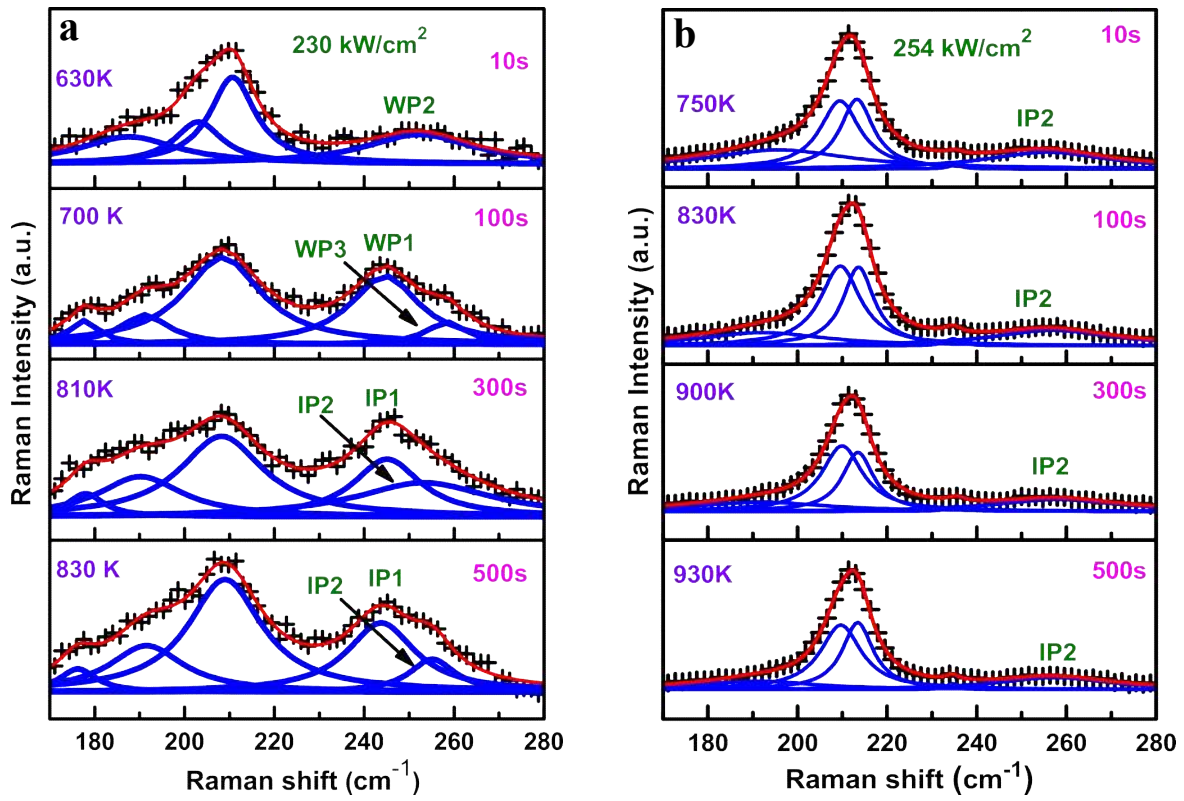


Figure 5.4.1: Raman spectra along with simulated temperature (a) and (b) Time evolution for 488nm laser irradiation with laser power density (LPD)  $\sim 200$  and  $254$   $\text{kW}/\text{cm}^2$ , respectively for irradiation time of 10s, 100s, 300s and 500s. Cumulative fit (red solid line) to the raw data (+) and separate Lorentzian fits are shown with blue solid line.

### 5.4.2 Application to NWs with very different diameter and aspect ratio

The next InAs NW (D3) chosen is of dia  $\sim 900$  nm and length  $\sim 8$   $\mu\text{m}$ , i.e. with increased diameter and much different aspect ratio. Figure 5.4.2.1a and 1b shows simulated temperature  $\sim 1200$  K to  $1650$  K corresponding to IP and SP processes observed in time evolution of Raman spectra for LPDs  $\sim 764$   $\text{kW}/\text{cm}^2$  and  $900$   $\text{kW}/\text{cm}^2$ , respectively. These IP process are second layer IP processes similar to Fig. 5.3.5 for observed for D1 NW. It is also interesting to note that consistent with the understanding developed above, simulated temperature  $>1650$

K for D3 at LPD  $\sim 900 \text{ kW/cm}^2$  shows SP processes completing the cycle of second layer modification.

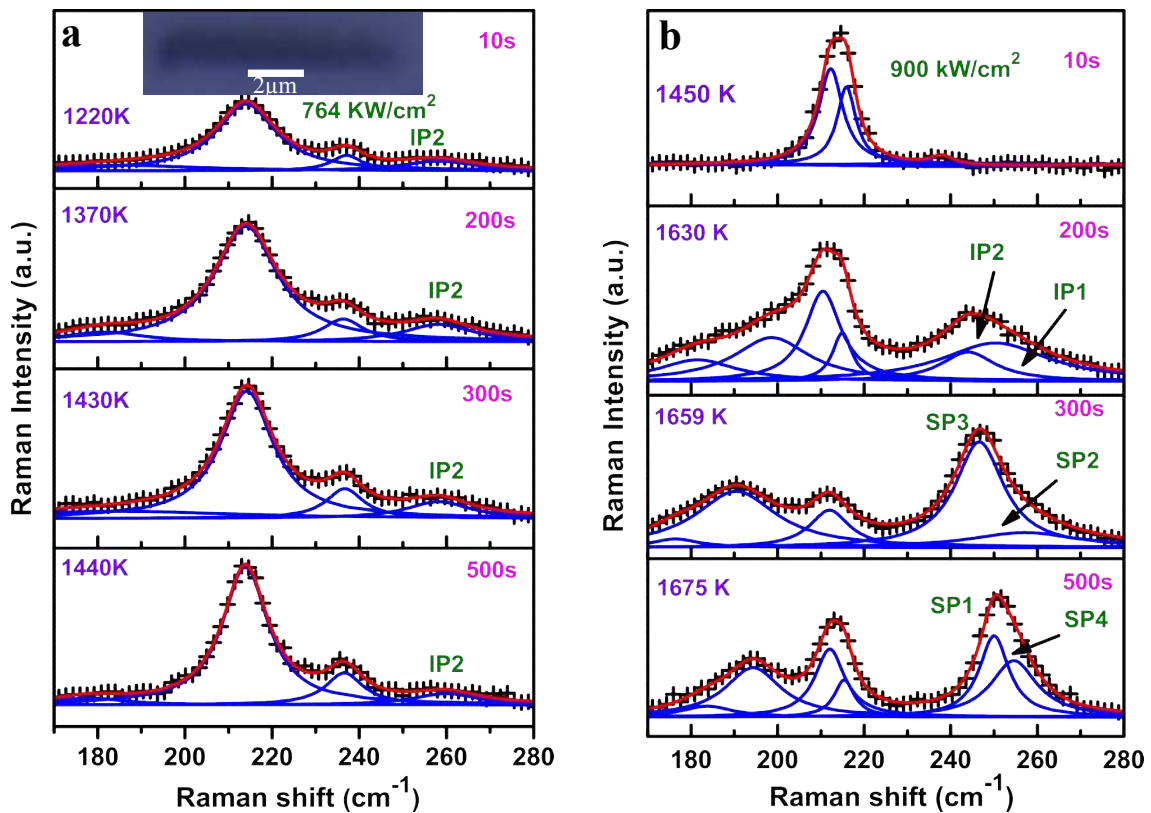
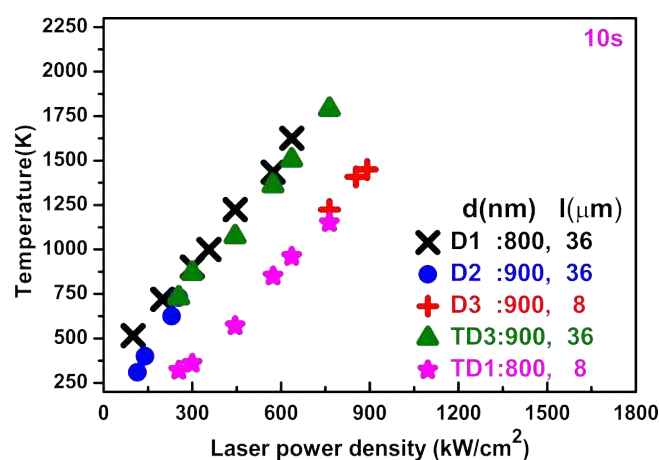


Fig. 5.4.2.1: Raman spectra along with simulated temperature for D3 InAs NW (optical image: inset,  $d \sim 90 \text{ nm}$  and  $l \sim 8 \mu\text{m}$ ) (a) and (b) Time evolution for 488nm laser irradiation with laser power density (LPD)  $\sim 764$  and  $900 \text{ kW/cm}^2$ , respectively. Cumulative fit (red solid line) to the raw data (+) and separate Lorentzian fits are shown with blue solid line.

This temperature was not reached in D1, as we have irradiated it with lower LPDs only. Fig. 5.4.2.1b shows time evolution of Raman spectra at highest LPD  $\sim 900 \text{ kW/cm}^2$ , giving initial temperature to be  $\sim 1400 \text{ K}$ . Here, the time evolution is progressive i.e. starting from very less oxidation at 10s, suggesting As generated is probably evaporated and again new layer oxidation has started with WP, and proceeds to IP and SP processes as time progresses thereby increasing the temperature nominally. Thus simulated temperature  $> 1250$

K, although, may not be the actual temperature, they can be used as guidelines of re-occurrence of oxidation cycle for the new InAs layer.



*Fig. 5.4.2.2: Consolidation of simulated temperature for different NWs at 10s as a function of LPDs.*

These diameter and aspect ratio dependent results are consolidated and presented in Fig. 5.4.2.2.

We have extrapolated the temperature simulation for D1 and D3 to TD1 and TD3 by changing their length from 36 to 8 and 8 to 36, respectively. It suggests that decrease in length decreases the rise in temperature, as sink becomes closer to heat generation region. It further shows that not only diameter, but the aspect ratio is also an important parameter for simulation of temperature on laser irradiation.

This methodology was further applied to InAs NWs grown elsewhere [143] by MOCVD. The NW is grown at growth temperature  $\sim 420^{\circ}$  C and V/ III ratio  $\sim 40$  with Au catalyst method [143]. These NWs are isolated using ultra-sonicator and further, transferred on other Si substrate which dimensions have  $\sim 3000 \times 2000 \times 700 \mu\text{m}^3$ . In this sample, diameter and aspect ratio of NWs are much different then studied earlier as compared to previous sample. The diameter and length of NW are in the range of  $\sim 100\text{-}800$  nm and  $\sim 1 \mu\text{m}$  to  $20 \mu\text{m}$ , respectively. These were measured using AFM (chapter 2: Fig. 2.5.3). The

temperature simulation is performed on many NW but we have shown the simulation for two NWs which have dia  $\sim 200$  and  $250$  nm and length  $\sim 4.5$  and  $5.4$   $\mu\text{m}$ . Fig. 5.4.3a, shows Raman spectra along with simulated temperature for InAs NWs of two different dimensions with two LPDs as representative data.

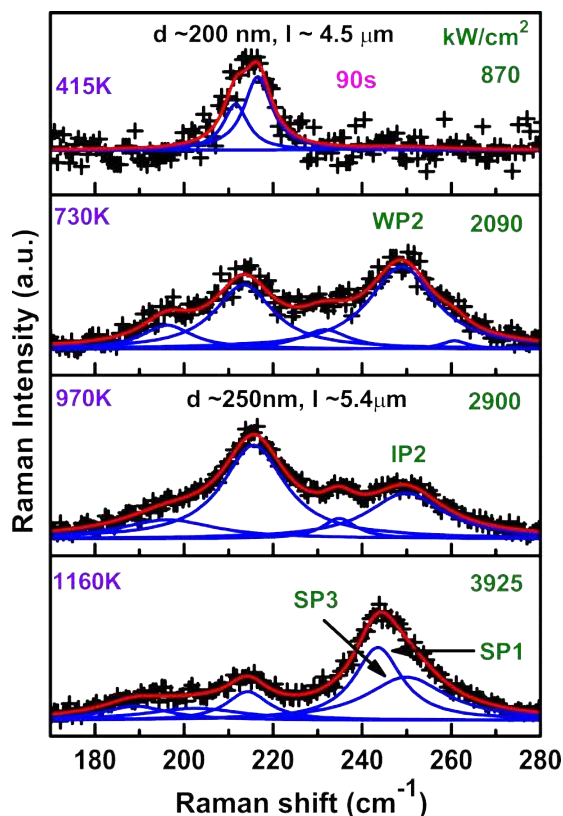


Fig. 5.4.2.3: For two different nanowires with dia  $\sim 200$  nm and length  $\sim 5$   $\mu\text{m}$ , grown elsewhere and transferred on the Other Si substrate for different LPDs at 90s. Cumulative fit (red solid line) to the raw data (+) and separate Lorentzian fits are shown with blue solid line.

Here, we have first simulated the temperature for one NW using various LPDs and used it for first check for initiation of oxidation. Simulated temperature considering perfect contact corroborates well with Raman spectra using various LPDs for several such NWs. Further, meshing size convergence is checked again, as dimensions of NWs is quite different. Meshing size convergence for Si, InAs and cylindrical volume is found at 600, 0.05 and 0.005  $\mu\text{m}$  and are used for further simulation studies. It is important to note here that LPDs used are required to be order of magnitude large in order to obtain oxidation, as diameter of

these NWs are in the range of  $\sim 200$  nm, much smaller than used for the above study ( $\sim 800$  nm) and further, since they are transferred on Si, they are in better contact with the substrate. Correlation between simulated temperature and Raman spectra (Fig. 5.4.2.3), clearly establishes the predictability of FEM based approach for estimation of temperature, which enables the controlled modification of the surface and dimension of InAs NWs.

This study suggests that growth method, diameter, aspect ratio all are important parameters in determination of temperature at the surface (laser spot) of InAs NWs. The above study further validates the importance of temperature simulation in predicting / controlling required surface modification.

## 5.5 Conclusion:

We have simulated the transient temperature at the surface of laser irradiated InAs NW (diameter  $\sim 800$  nm) using Finite element method (“ANSYS” software) for different laser power densities (LPDs) and corroborated the same with different thermal oxidation processes mediated by the rise in temperature. The oxidation processes are identified as weak reactions WP1, WP2, WP3, intermediate temperature reactions IP1, IP2 and higher temperature strong reactions SP1, SP2, SP3 & SP4, using time evolution of Raman spectra for various LPDs. Salient features of the study are,

- 1) Both Raman spectra and simulated temperature reach steady state at  $\sim 8$  minutes.
- 2) The only variable parameter used is number of contacts to match the data at 200s for 200 kW/cm<sup>2</sup> LPD. All other data at all points i.e. upto 500s and for several LPDs from 30 to 636 kW/cm<sup>2</sup>, shows good corroboration of Raman spectra and temperature up to  $\sim 1150$  K.
- 3) The higher simulated temperature ( $\sim 1200$ - $1700$  K) does not show any damage, although, melting point of InAs  $\sim 1215$  K. The reason is understood to be that these higher temperatures are actually not reached, due to scattering of light occurring from large quantities of As<sub>2</sub>O<sub>3</sub> &

As formed at the temperature  $>1150\text{K}$ . In addition, evaporation of As is expected to further lower the temperature in this situation. Raman spectra observed for higher simulated temperatures are also commensurate with this understanding.

4) The applicability of this methodology is further confirmed, using randomly chosen NWs grown on the same substrate along with NWs (grown elsewhere: diameter  $\sim 200\text{ nm}$ ) isolated and transferred on other Si substrate, both irradiated at randomly chosen LPDs.

The study of laser irradiation of InAs NWs with various laser power densities for NWs i) grown under different conditions, ii) covering large range of diameters and aspect ratio and iii) directly grown on the Si substrate or isolated and transferred on the Si substrate, shows that growth method, diameter, aspect ratio are important parameters in determining the temperature at the surface of InAs NWs subjected to laser irradiation. The necessity of temperature simulation for predicting temperature rise on laser irradiation of a semiconductor NW is important, as usual Stokes/anti-Stokes Raman measurement cannot give correct temperature due to resonance Raman scattering with visible excitation sources. Thus, the above study validates the importance of temperature simulation in predicting / controlling the required surface modification for other III-V NWs useful in nanotechnology.

The study thus establishes predictability of various oxidation processes for given NW dimensions, laser power density and irradiation time, thereby ascertaining importance and applicability of the temperature simulation in controlling surface modification of randomly chosen InAs NWs using laser irradiation. This methodology can be used to control the oxidation process as desired for using NWs in device technology, where oxidation is used for creating an insulating layer.

The Raman data presented in this chapter is of the same geometry/orientation of NWs to avoid complications related to Raman scattering configuration. It is to be noted that

very different Raman spectra are observed for orthogonally oriented NWs for similar LPDs, which is investigated further and makes the content of chapter-6.

## Chapter 6

**Understanding the effect of NW orientation on time evolution of Raman spectra from laser irradiated InAs NWs**

*“Bad times have a scientific value. These are occasions a good learner would not miss” \_\_\_\_\_ Ralph Waldo Emerson*

## 6.1 Introduction

Local surface modification of NWs is often required for various nanotechnology applications and laser irradiation is found to be an easy and precise method for this purpose [259-261]. The process of thermal oxidation using laser irradiation reduces thermal conductivity on the surface. Several reports suggest/show various applications of low thermal conductivity e.g. thermo-electric [259] and photo thermo-electric devices as a solar thermo-electric generator [154, 260]. The oxide layer on InAs NW is used in device application like metal oxide field effect transistor [261]. With the surface modification process being thermal oxidation, it is important to understand the correlation of processes with both temperature and the NW orientation, in order to use it for required applications. Raman spectroscopy is an ideal technique to study these local variations using laser irradiation on a single semiconductor nanowire as, it is capable of giving information of oxidation, strain, crystalline quality, crystal structure etc. of an isolated NW. In earlier chapter 5 [262], we have studied the correlation between simulated transient temperature and time evolution of Raman spectra on InAs NWs and established that simulated temperature can be used to predict /control the required surface modification. Conventional way of Stokes-anti Stokes measurements for calculation of the temperature at the laser irradiated InAs NW surface does not give correct temperature due to resonance enhancement of InAs phonons. Therefore, simulation of temperature is important for estimating temperature under laser irradiation of InAs NW [262]. All NWs studied in the above mentioned work were oriented similarly in the plane. In the present chapter, we investigate the differences observed in time evolution of Raman spectra for differently oriented NWs (in plane) using polarized Raman spectroscopy. Polarization

dependence (incident light) of photoemission electron microscopy [263], photoluminescence [264] and Raman spectroscopy [190, 170-171, 195] on InAs nanowires have been investigated. First two have been studied using NWs of diameter  $\sim$ 100-150 nm, which shows antenna effect, wherein coupling of light to the NW depends on polarization of incident light w.r.t. the NW axis [31, 265]. As we have studied earlier, Raman spectra for InAs nanowires (dia.: 2  $\mu$ m – 200 nm and length: 80 - 4  $\mu$ m) depicts Raman selection rules in polarized Raman spectra [251, 266]. However, we observe major differences in time evolution of oxide related peaks in unpolarized Raman spectra for differently oriented InAs NWs for the same/similar simulated temperature. To the best of our knowledge orientation dependence of unpolarized Raman spectra of NW on laser irradiation has not been studied/reported earlier. One report by Tanta et al. discusses surface dependent oxidation due to different transition kinetics for [0001] and [01T0] surfaces [229]. Laser antenna effect studies show evidence of effect of laser coupling on NW orientation [45,265]. The systematic investigation of the effect of orientation on time evolution of Raman spectra shows that the differences in unpolarized Raman spectra are related to formation of oriented crystalline oxide on the surface of InAs NWs on laser irradiation. Further, Raman spectroscopy study further shows that at higher simulated temperatures  $>$  950 and  $>$ 1300 K, grey and black elemental arsenic are formed, respectively, as the end product of oxidation processes. Being layered materials, few layers obtainable via laser irradiation can lead to properties like graphene.

## 6.2 Raman spectra of differently oriented InAs NWs

In previous chapter [262], we have established a correlation between simulated transient temperatures at the surface of an InAs nanowire (NW) on laser irradiation with the time evolution of Raman spectra. All NWs studied were oriented similarly for Raman data presented in the earlier chapter. Transient temperature simulations were performed with

ANSYS software using finite element method for solving the heat transfer equation on laser irradiation of InAs NWs [262]. In the simulation, we have considered a 3D geometry in which actual dimensions of Si substrate and InAs NW are used. The laser spot volume (focal spot area x penetration depth) is considered, where the heat is generated. The penetration depth is  $\sim 22$  nm for 488 nm, which is smaller than the depth of focus. Further details of temperature simulation can be found in chapter 5. One representative simulated 3D steady state temperature profile for one InAs NW ( $\sim 4 \times 0.35 \times 0.35 \mu\text{m}^3$ ) lying on the Si substrate ( $\sim 3000 \times 2000 \times 700 \mu\text{m}^3$ ) is given in the Fig. 6.2.3.3. Transient temperature for laser irradiation time upto 500 s, at the laser spot is also plotted in the same figure. The simulated temperature referred, hereafter in the chapter is at the laser spot area from where Raman spectra is also being measured. This temperature is thus corroborated with the measured Raman spectra. Interestingly, we find that differently oriented NWs show different time evolution of Raman spectra on laser irradiation with similar laser power densities (LPDs). To understand this variation, temperature is first simulated for all time evolution of Raman spectra recorded for different NWs and LPDs. The simulation is performed in a similar way as noted above and detailed in chapter 5. Temperature simulation allowed us to use understanding developed earlier chapter [262], where effect of laser irradiation is well described in terms of local increase in temperature on laser irradiation with evolution of time for different LPDs.

### **6.2.1 Differences in time evolution of unpoalrized Raman spectra from in-plane horizontally and vertically oriented NW**

Here, we will refer to the in plane orientation of NWs as shown in Fig.6.2.1.1a, as horizontal (H) and perpendicular to that as vertical (V) in the frame of reference being described (Fig. 6.2.1.1b: nearly V). Both NWs shown in optical images (Fig.6.2.1.1) have

similar dimensions i.e. diameter ( $d$ )  $\sim 800$  nm and length ( $l$ )  $\sim 36$   $\mu\text{m}$  are denoted as D1 (Fig.6.2.1.1a) and D2 (Fig.6.2.1.1b). Raman peaks  $\sim 180$ - $190$ ,  $240$ - $245$   $\text{cm}^{-1}$ ;  $190$ - $195$ ,  $246$ - $252$   $\text{cm}^{-1}$  and  $196$ - $200$ ,  $256$ - $260$   $\text{cm}^{-1}$  are due to formation of  $\text{InAsO}_4$ ,  $\text{As}_2\text{O}_3$  and  $\text{As}$ , respectively by the weak (W), intermediate (I) and strong oxidation processes (SP) described and consolidated in table 5.3.1 [262] of chapter 5 [262, 188]. All Raman spectra are deconvoluted using minimum Lorentzians required as per lineshape of entire spectra and possibility of presence of relevant oxide modes. It may be appropriate to mention here that all data presented in earlier chapter 5 are for H oriented InAs NWs. Fig.6.2.1.1c, d and e clearly brings out differences in Raman spectra for H and V oriented NWs, wherein, top three and bottom three Raman spectra shown are for D1(H) and D2 (nearly V) NWs, respectively. Simulated temperature in each case is also noted along with the spectrum. Significant differences in Raman peak positions and relative intensities are observed on these differently oriented NWs i.e. D1 and D2 for same simulated temperature (Fig.6.2.1.1c, d and e). The frequency of the transverse optical phonon (TO) mode of InAs is observed at  $\sim 213$ ,  $215$   $\text{cm}^{-1}$  in D1 and D2 NW, respectively for simulated temperature in the range  $\sim 300$  K and this is almost constant up to simulated temperature  $\sim 500$  K. Here, we are referring to the  $\text{TO}^*$  mode, which is actually a combination of TO phonon of zinc blende (ZB) and  $\text{E}_{2\text{h}}$  phonon of wurtzite (WZ) structure, when polytypism exists [251]. Henceforth, this combination mode will be referred to as the  $\text{TO}^*$  mode.

Important observations about  $\text{TO}^*$  and (longitudinal optical) LO phonons of InAs from Fig.6.2.1.1c, d and e are consolidated as follows,

i) For D1 NW, at simulated temperature  $\sim 630$  -  $710$  K,  $\text{TO}^*$  mode is redshifted by  $2$ - $3$   $\text{cm}^{-1}$  with as increase to FWHM  $\sim 20$   $\text{cm}^{-1}$ , which can be related to the effect of heating. The FWHM of  $\text{TO}^*$  mode for D1 and D2 NWs at  $300$  K is  $\sim 10$   $\text{cm}^{-1}$ . For D2 NW, the  $\text{TO}^*$  frequency redshifts  $\sim 1$   $\text{cm}^{-1}$  with increase in FWHM to  $\sim 17$   $\text{cm}^{-1}$  (Fig.6.2.1.1c).

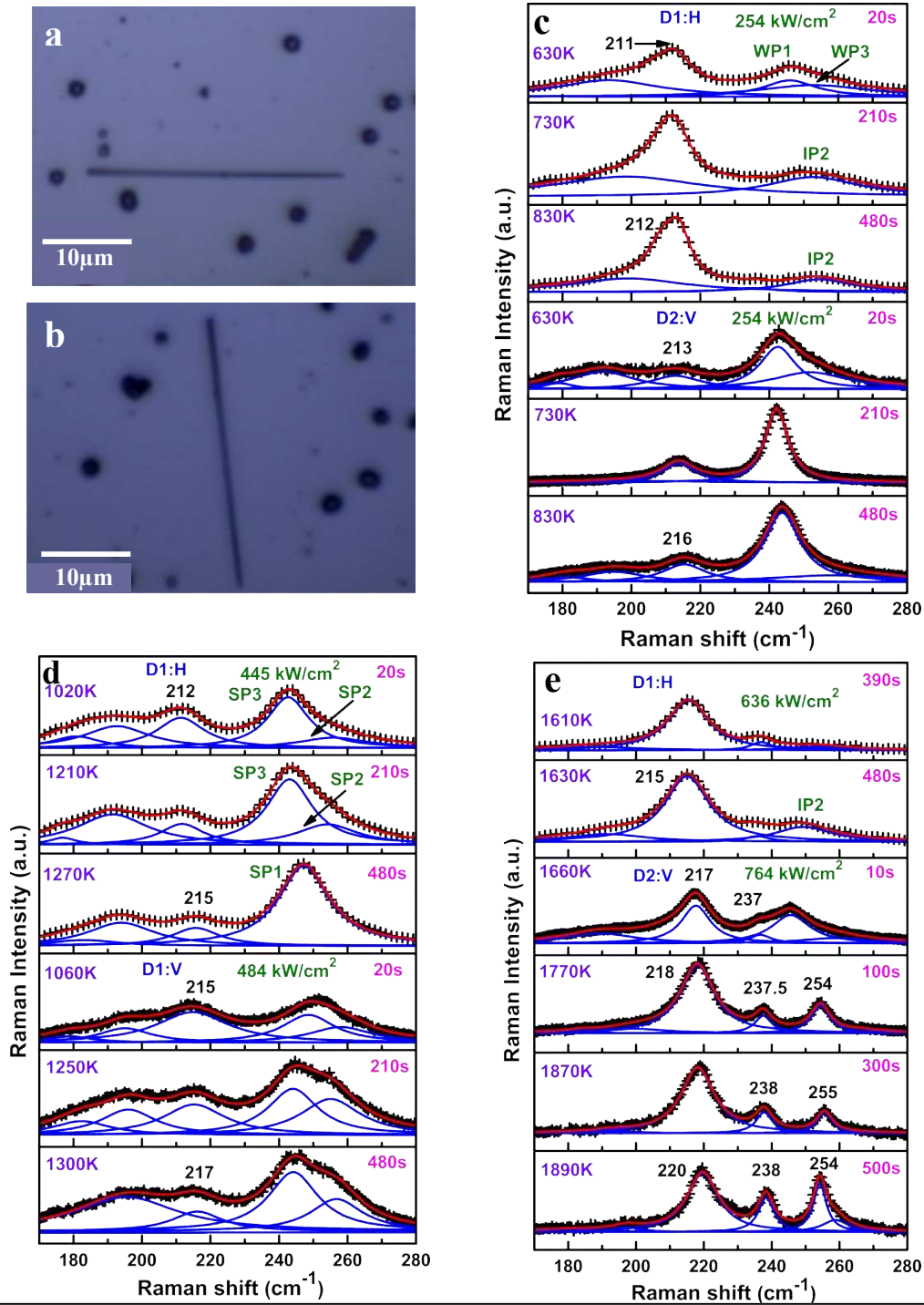


Fig. 6.2.1.1: (a) and (b) show optical images of InAs NWs D1 and D2 oriented in-plane horizontally (H) and nearly vertically (V) on Si substrate, respectively. (c), (d) and (e) show time evolution of Raman spectra for 20s, 210s and 480s in which top three Raman spectra are for D1 and bottom three Raman spectra for D2. Cumulative fit (red solid line) to the raw data (+) and separate Lorentzian fits are shown with blue solid line.

ii) Further, in the simulated temperature range  $\sim 1000$ - $1300$  K, TO\* mode is blueshifted to  $\sim 215$ ,  $217$   $\text{cm}^{-1}$  along with reduction in FWHM to  $\sim 12$  and  $15$   $\text{cm}^{-1}$  for D1 and D2 NWs, respectively (Fig.6.2.1.1d).

iii) At very high simulated temperature between  $1600$ - $1900$  K, we observe that for D2 NW, TO\* phonon further blue shifts from  $\sim 217$  to  $220$   $\text{cm}^{-1}$ . It further narrows down to FWHM  $\sim 8$   $\text{cm}^{-1}$  along with reappearance of LO like mode  $\sim 237$   $\text{cm}^{-1}$  (Fig.6.2.1.1e). For D1, the LPDs used are of smaller value and therefore simulated temperature  $>1650$  K is not reached.

In the previous work, we have noted that the simulated temperature above  $1200$  K may not actually be reached due to evaporative cooling effect of volatile As, generated as a byproduct. Reduction in laser power reaching InAs NW, due to scattering losses (from oxide powder), is expected to further decrease the temperature [262]. Thus, additional blue shift and reduction in FWHM can be related to this reduced temperature. However, both blueshift and reduction in FWHM can be related to this reduced temperature. However, both blueshift and FWHM values are indicative of cooling below the room temperature, which seems as an improbable proposition. This prompted us to look for a different explanation for blueshift and narrowing of WHM of TO\* mode. In this regard, it is interesting to note that modes  $\sim 220$ ,  $237$  and  $254$   $\text{cm}^{-1}$  are also observed at simulated temperature  $\sim 1900$  K for D2 NW (Fig.6.2.1.1e). These observations were further confirmed using another set of NWs, D3(H) NW with  $d \sim 900$  nm,  $l \sim 8$   $\mu\text{m}$  and D4 (V) NW with  $d \sim 600$  nm,  $l \sim 12$   $\mu\text{m}$ , oriented in H and V (nearly) directions in a frame of reference as shown inset of Fig.6.2.1.2a. The simulated temperature ranges for chosen LPDs is  $\sim 1400$ - $1700$  K. It is important to recall here that earlier, we have shown that when simulated temperature  $>1250$  K, the oxidation of first layer is complete and As byproduct that is generated gets evaporated and the second layer oxidation starts from weak/intermediate oxidation process [262].

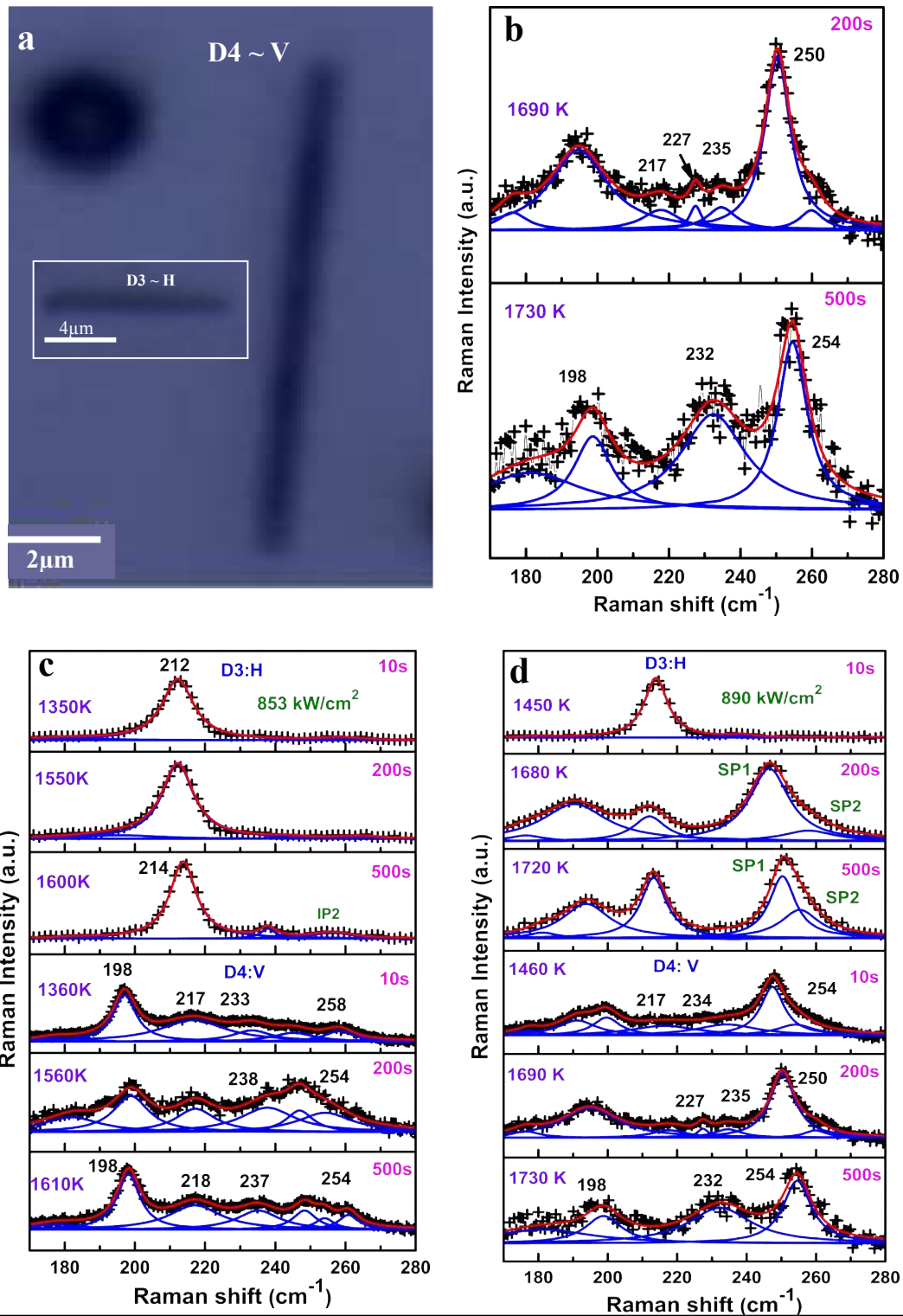
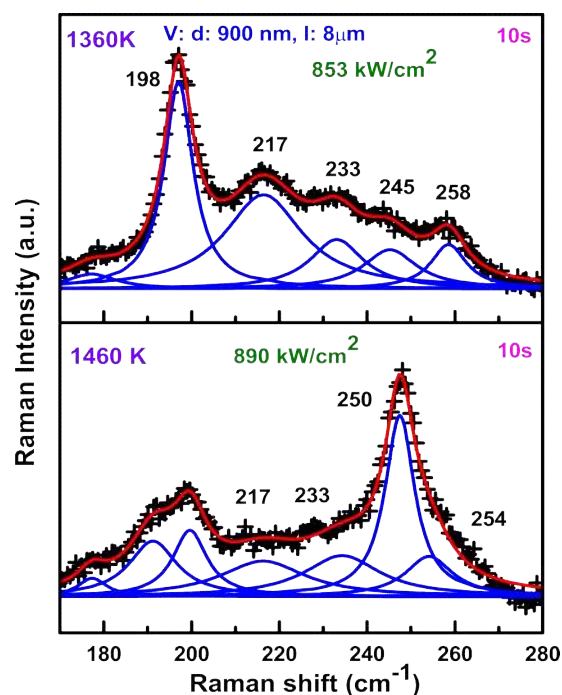


Fig.6.2.1.2: (a) show optical images of InAs NW for D3 (inset) and D4 oriented in-plane horizontally (H) and nearly vertically (V) on Si substrate. (b) Show time evolution of Raman spectra for 200s and 500s for D4. (c) and (d) show time evolution of Raman spectra for 10s, 200s and 500s in which top three Raman spectra are for D3 and bottom three Raman spectra for D4. Cumulative fit (red solid line) to the raw data (+) and separate Lorentzian fits are shown with blue solid line.

The observations for these NWs are as follows,

1. Raman spectra show that the intensity of oxide peaks is less for D3 (H) NW as compared to the D4 (V) NW (Fig.6.2.1.2c).
2. For D4 (V) NW, TO phonon of elemental As ( $\sim 198 \text{ cm}^{-1}$ ) mode is much stronger as compared to D3 (H) wire for simulated temperature in the range 1380 to 1630 K (Fig.6.2.1.2c).
3. For D4 NW, at simulated temperature range  $\sim 1400$ - 1630 K, intensity of TO\* peak is less as compared to D3 NW (Fig.6.2.1.2c). To get a clear picture of various fitted peaks for D4 (V) NW at simulated temperature  $\sim 1360$ , 1460 K in Fig.6.2.1.2c and d respectively; fitting is separately shown in Fig. 6.2.1.3.



*Fig. 6.2.1.3: Fitting of Raman spectra of Fig. 6.2.12c and d at simulated temperature at 1360 and 1460 K on D4 NW in near vertical geometry. Cumulative fit (red solid line) to the raw data (+) and separate Lorentzian fits are shown with blue solid line.*

Bottom two Raman spectra from Fig.6.2.1.2d are separately shown in Fig. 6.2.12b for clarity. The TO\* peak is absent as well as some new modes start appearing  $\sim 225$ , 232-234  $\text{cm}^{-1}$  for D4 NW (Fig.6.2.1.2c and d). Since intensities of these modes are very small, fitting

uncertainties are large and hence frequency positions should be taken within few  $\text{cm}^{-1}$ , only. It may further be noted that deconvolution of Raman spectra in Fig.6.2.1.2b (at 1730 K) shows presence of a very small  $\text{TO}^*$  mode, which cannot be fitted/deconvoluted and hence, affects the fitting on the lower frequency side.

Two possibilities are considered for the above observed differences in Raman spectra excited with similar LPDs on H and V oriented InAs NWs or for similar simulated temperatures.

- (1) Difference in coupling of incident laser light with different orientation of NW giving rise to different level of oxidation i.e. due to difference in laser coupling different temperature may be expected.
- (2) Difference in Raman selection rules (RSR) for oxides and InAs for two configurations leading to different Raman spectra. This possibility is considered even for unpolarized data, as when the NW orientation is changed and incident polarization remains same, due to well defined growth axis this leads to different Raman scattering configurations.

At room temperature, the TO phonon of ZB and  $E_{2h}$  phonon of WZ phases show tensile and compressive stress in NW, respectively due to presence of the other phase [251]. The blueshift of TO and  $E_{2h}$  phonon with narrowing of FWHM can be related to annealing effect at high temperature leading to relaxation of stress and reduction in disorder. However, heating may not relax the stress generated due to presence of the other crystal phase, but only can reduce additional mechanical tensile stress generated in the structure due to other reasons like defects/disorder and lead to blueshift and narrowing of FWHM. These points need to be investigated systematically.

## 6.2.2 Polarized Raman spectroscopy

To elucidate points noted above, polarization dependent Raman spectroscopy is performed. Since, we did not have the sample studied above with us anymore, new set of samples were chosen for further investigation. Initially, we needed to check that above observations are repeated on new set of InAs NWs grown using MOCVD on Si (111) [143] and transferred on other Si substrate, which are then used for further investigation. Once, we could repeat the above observations on these NWs, unpolarized Raman spectroscopy is performed on the new set of InAs NWs for horizontally oriented InAs NW (D5:  $d \sim 250$  nm and  $l \sim 3$   $\mu\text{m}$ : Fig.6.2.2.1a) by changing incident polarization parallel (z) and perpendicular (y) to NW axis. Following the same procedure given in chapter 5, using finite element method (ANSYS), we first back simulate LPD values to obtain required oxidation process (temperature). Here, actual size of Si substrate ( $L \times W \times T$ :  $3000 \times 2000 \times 700$   $\mu\text{m}^3$ ) and InAs NWs are ( $L \times W \times T$ :  $3-8 \times 0.25-0.4 \times 0.25-0.4$   $\mu\text{m}^3$ ) were used for the simulation. The convergence of meshing size for these simulations was checked and optimized values taken for Si substrate  $\sim 400-500$   $\mu\text{m}$ , InAs NW  $\sim 0.06-0.07$   $\mu\text{m}$  for different NWs. Meshing size for heat generating region is taken to be  $\sim 0.015$   $\mu\text{m}$ , as in chapter 5. It may be appropriate to note here that oxidation temperatures i.e.  $>750$  K are obtained at very high LPD ( $> 1000$   $\text{kW}/\text{cm}^2$ ) for these NWs, as they have smaller diameter and aspect ratio, further, method of preparation has led to better contact between NW and substrate (Fig.6.2.2.1) [262].

Here, z direction is considered to be the NW growth direction i.e. [111] for ZB and [0001] for WZ structure. The x, y axes are chosen to be along the directions [1T0] and [11Z0] {out of plane}, [11Z] and [1T00] {in plane} perpendicular to growth directions, respectively. The back scattering is taken to be along x direction. At simulated temperature  $\sim 750$  K, oxide peaks are not observed, when incident polarization is in y direction (Fig.6.2.2.1b), while intermediate oxidation is observed, when incident polarization is in z direction (Fig.6.2.2.1c).

According to Raman selection rules for ZB and WZ structures, TO phonon of ZB and  $A_1(\text{TO})$  phonon of WZ phase are allowed in  $x(z,z)\bar{x}$  as well as  $x(y,y)\bar{x}$  and  $E_{2h}$  is allowed only in  $x(y,y)\bar{x}$  configuration [251].

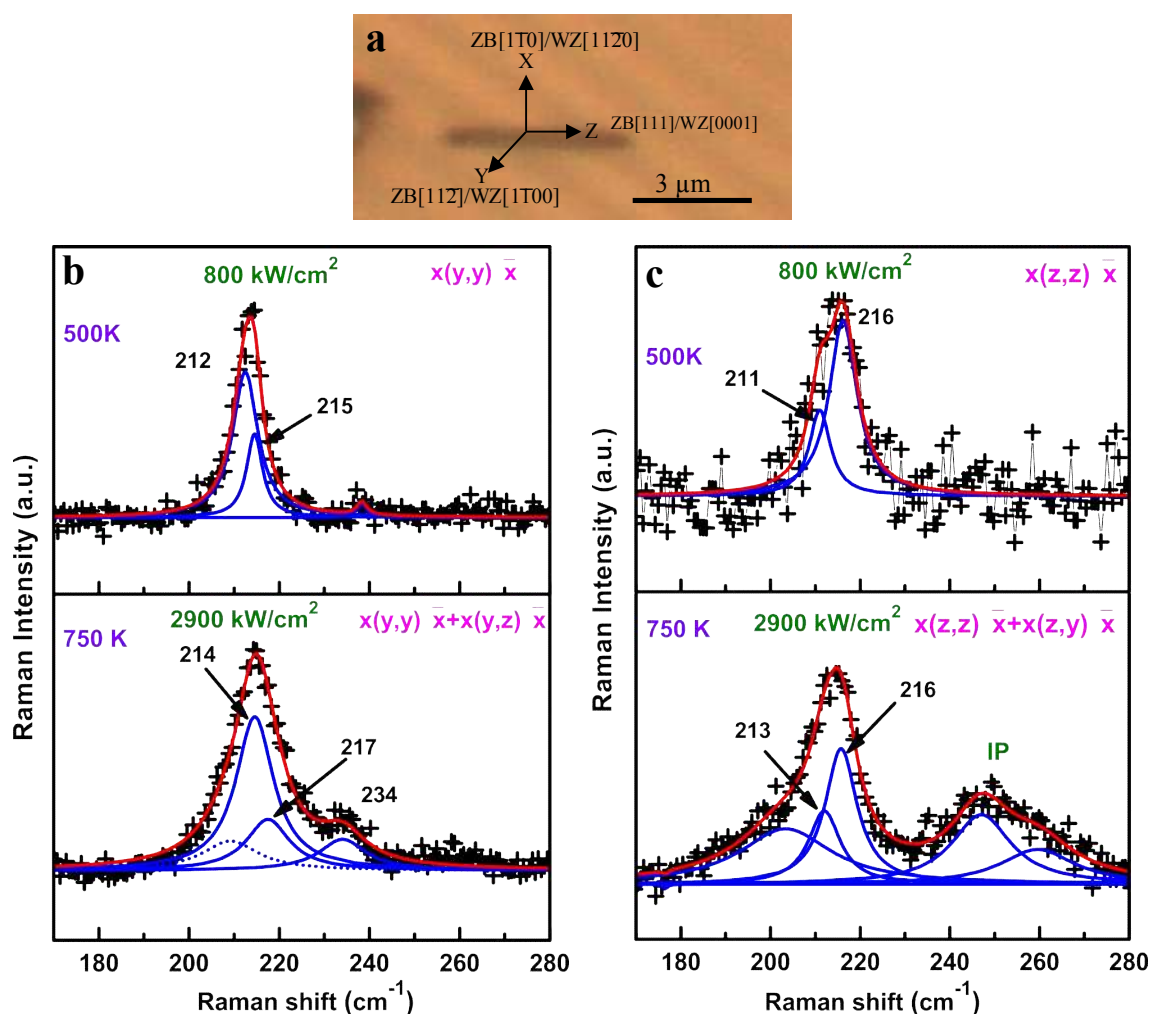


Fig.6.2.2.1: (a) Optical image of InAs NW D5 on Si substrate and the inset shows schematic used for Raman scatterings configuration. (b) Polarized and unpolarized Raman spectra with incident polarization parallel and perpendicular to NW axis. . Cumulative fit (red solid line) to the raw data ( + ) and separate Lorentzian fits are shown with blue solid line.

The difference in line shape of TO\* mode in Fig.6.2.2.1b and c. for 500 K in  $x(y,y)\bar{x}$  and  $x(z,z)\bar{x}$  configuration is suggestive of polytypism observed in InAs NWs, as studied earlier [251, 266]. When incident polarization is in Z direction, the TO\* mode is observed to be redshifted with increased FWHM as compared to when incident polarization is in y

direction. In addition, oxide modes are not observed, when incident polarization is in y direction. The question, which needs to be answered is whether these observations are related to higher temperature rise in  $x(z,z+z,y)\bar{x}$  configuration. Given the above information, we can attribute it to either different laser coupling or RSR or both to some extent. To find out which of the two is actually responsible for the difference observed in Raman spectra, detailed polarized Raman spectroscopy was performed on D6 ( $d \sim 250$  nm and  $l \sim 8$   $\mu$ m). Raman spectroscopy is performed on a single uniform NW in two polarization configuration  $x(z,z)\bar{x}$  and  $x(y,y)\bar{x}$  i.e. incident as well as scattered light is polarized i) parallel and ii) perpendicular to NW axis, respectively.

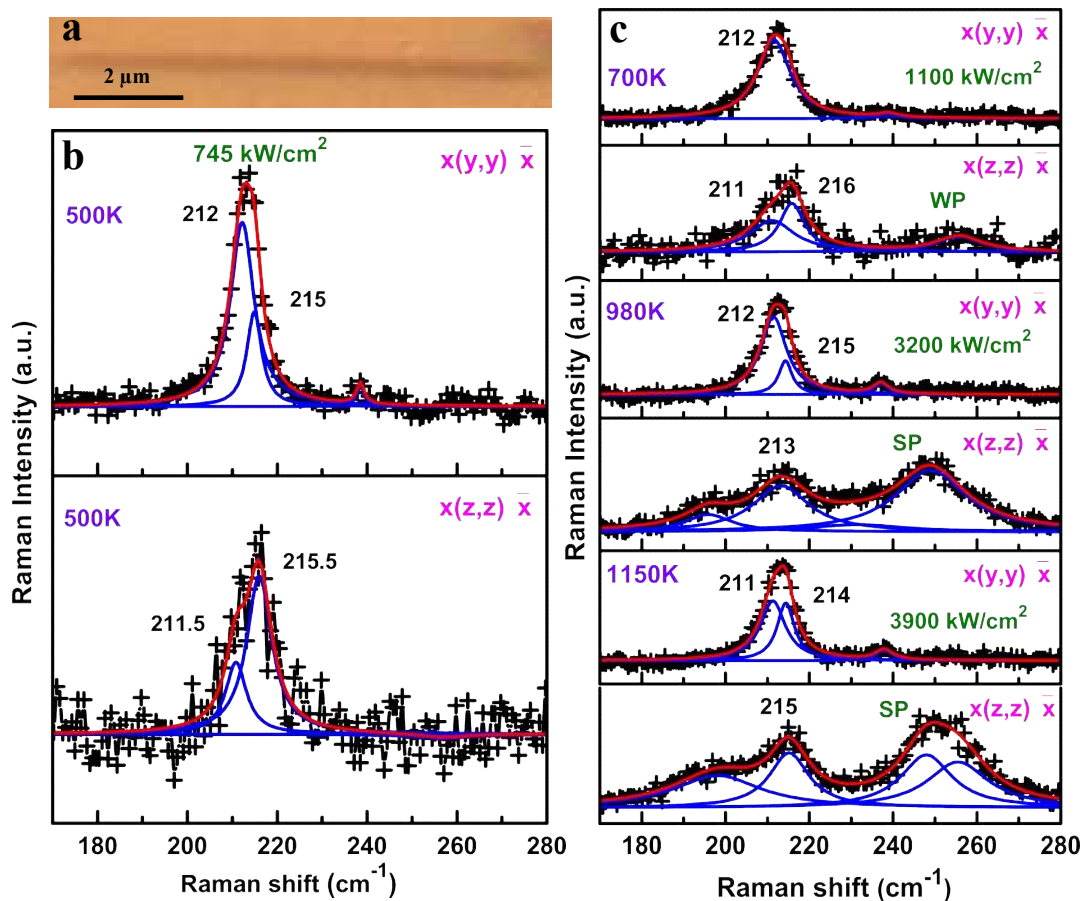


Fig.6.2.2.2: (a) Shows optical image of for InAs NW D6 on Si substrate. (b) Polarized Raman spectra for various LPDs showing oxide modes observable only in  $x(z,z)\bar{x}$  configuration. Cumulative fit (red solid line) to the raw data (+) and separate Lorentzian fits are shown with blue solid line.

This experiment is done on first  $x(y,y)\bar{x}$  configuration and then  $x(z,z)\bar{x}$  configuration on the same position on the NW for LPDs: 800, 1100, 3200, 3900 kW/cm<sup>2</sup>. The optical image of NW is shown in Fig.6.2.2.2a. The Raman spectra are shown in Fig.6.2.2.2b at low LPD  $\sim$  745 kW/cm<sup>2</sup> in which we did not observe any oxide related modes in both configuration as temperature (simulated temperature  $\sim$  500 K) reached is not enough to form oxides. In Fig.6.2.2.2c, weak to strong oxidation processes are observed in  $x(z,z)\bar{x}$  configuration at simulated temperature range from 700- 1150 K, while no trace of oxide related modes can be seen in  $x(y,y)\bar{x}$  configuration at the same simulated temperatures.

This is indicative of the dominant effect being RSR of oxide peaks. In addition to that, the TO\* phonon frequency is blue shifted  $\sim$  2-3 cm<sup>-1</sup> in  $x(z,z)\bar{x}$  configuration as compared to  $x(y,y)\bar{x}$  due to existence of polytypism [251]. Larger FWHM in  $x(z,z)\bar{x}$  as compared to  $x(y,y)\bar{x}$  configuration can be attributed to stacking fault disorder of ZB and WZ phases along the NW growth direction [ZB:111] or [WZ:0001] [251].

Here, the coupling effect considered is difference in coupling of incident light with the NW, depending on angle made by polarization of incident light with the NW axis. For the bulk material, the Raman scattering intensity is proportional to the excitation frequency, scattering volume, intensity of incident light and RSR for a given crystal symmetry and scattering configuration. However, for NWs one more term gets added in the calculation of Raman scattering intensity i.e. internal electric field enhancement due to NW dimensions. When the NW diameter is much less than the incident wave length ( $d \ll \lambda$ ), it is known that the Raman scattering intensity is proportional to the internal electric field intensity inside the NW of the incoming plane wave [45, 265]. The internal electric field depends on the NW dimensions ( $d, \lambda$ ) as well as the angle between incident electric fields with NW axis. Although, diameters of NWs studied lie in the range from 900 nm to 200 nm, which is not

expected to show strong antenna effect, for the sake of completeness, it is also considered as one of the possibilities.

### 6.2.3 Two-step polarized Raman spectroscopy

To investigate, if RSR is indeed the dominant effect in our case, following two-step Raman spectroscopy experiment is designed. In the first step, the polarization dependent Raman spectroscopy in two configurations is performed i.e.  $x(y,y)\bar{x}$  and  $x(z,z)\bar{x}$  at very low and high LPDs  $\sim 800 \text{ kW/cm}^2$ , 5200 and 6000  $\text{kW/cm}^2$ .

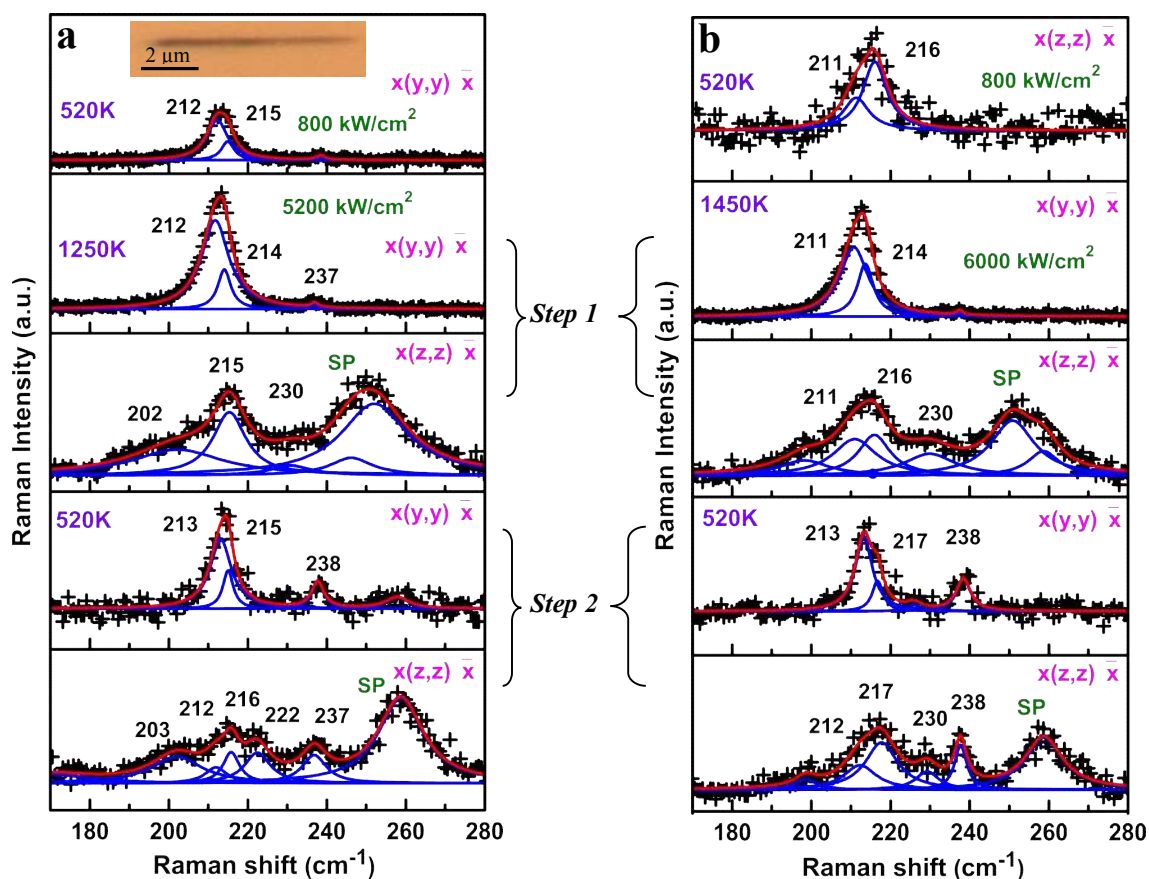


Fig.6.2.3.1: (a) and (b) shows polarized Raman spectra at lower LPD followed by Raman spectra and laser irradiation with higher LPD and later Raman spectra at lower LPD to check the effect of polarization configuration v/s polarized irradiation for D7 NW. Cumulative fit (red solid line) to the raw data (+) and separate Lorentzian fits are shown with blue solid line.

In second step, the same position is probed by Raman spectroscopy in both configurations with low LPD  $\sim 700 \text{ kW/cm}^2$ , where no oxidation is expected [262]. The objective of this experiment is that in step 2, if oxide modes can be observed in both configurations then it can be considered to be due to coupling of incident light with NW axis and if results presented in Fig.6.2.2.2 are repeated, then it is safe to conclude that the observance of oxidation is related to Raman selection rules for oxide modes. Fig.6.2.3.1a and b, in step 2 shows that no oxide modes are observed in  $x(y,y)\bar{x}$  configuration in step 1 or step 2, however oxide peaks are observed in  $x(z,z)\bar{x}$  configuration. This experiment confirms that Raman selection rules for oxide modes is the origin of the difference in unpolarized Raman spectra in differently oriented InAs NWs irradiated with LPDs leading to same simulated temperatures.

It is very interesting that laser irradiation of zinc blende InAs produces oxides which have structures different than zinc blende, but still dominantly oriented along specific direction. This gives rise to Raman spectra, which follows Raman selection rules. There is very limited literature regarding this effect and mainly for thermally annealed bulk InAs film. For  $\sim 700$  and  $800 \text{ K}$  for InAs (111) wafer, it leads to amorphous  $\text{As}_2\text{O}_3$ ,  $\text{In}_2\text{O}_3$  and  $\text{InAsO}_4$  formation, respectively [267, 163]. Whereas, for InAs (111) at  $>750 \text{ K}$ , Schwartz et al. show formation of crystalline formations of  $\text{As}_2\text{O}_3$ ,  $\text{In}_2\text{O}_3$  [163] while Yamaguchi et al show that annealing InAs (001) wafer at  $700\text{-}900 \text{ K}$  gives rise to polycrystalline  $\text{As}_2\text{O}_3$ ,  $\text{In}_2\text{O}_3$  [230]. Literature suggests that in  $700\text{-}800 \text{ K}$  range amorphous oxides may be formed and at higher temperatures polycrystalline/crystalline oxides may be formed. The data presented above also suggests that  $\sim 700 \text{ K}$ , amorphous oxides are formed and above  $900 \text{ K}$ , crystalline oxides with preferred orientations are formed on laser irradiation of InAs NWs. Our study further leads to very important understanding that even unpolarized Raman data can give information about orientation of oxides in case of NWs and therefore, needs to be looked into carefully. One interesting observation is made in Fig. 6.2.3.1 that additional modes  $\sim 222$  and  $230 \text{ cm}^{-1}$ , other

than InAs ( $\sim 214, 237 \text{ cm}^{-1}$ ) and oxide modes ( $\sim 190\text{-}200, 250\text{-}260 \text{ cm}^{-1}$ ) appear in Raman spectra for step 2 only and not in step 1. In addition to that, the TO\* mode is blue shifted by  $\sim 2 \text{ cm}^{-1}$  and FWHM is also reduced (Fig. 6.2.3.1b).

To understand this further and to find out its correlation with higher simulated temperature, we have performed polarized Raman spectroscopy for two incident polarization y and z at intermediate LPD  $\sim 2900 \text{ kW/cm}^2$  to get the oxidation of InAs NW (D8: diameter  $\sim 350 \text{ nm}$  and length  $\sim 4 \mu\text{m}$ ). In step 2, the same position is probed by Raman spectroscopy in four configurations  $x(z,z)\bar{x}$ ,  $x(z,y)\bar{x}$ ,  $x(y,y)\bar{x}$  and  $x(y,z)\bar{x}$  at low LPD  $\sim 800 \text{ kW/cm}^2$ .

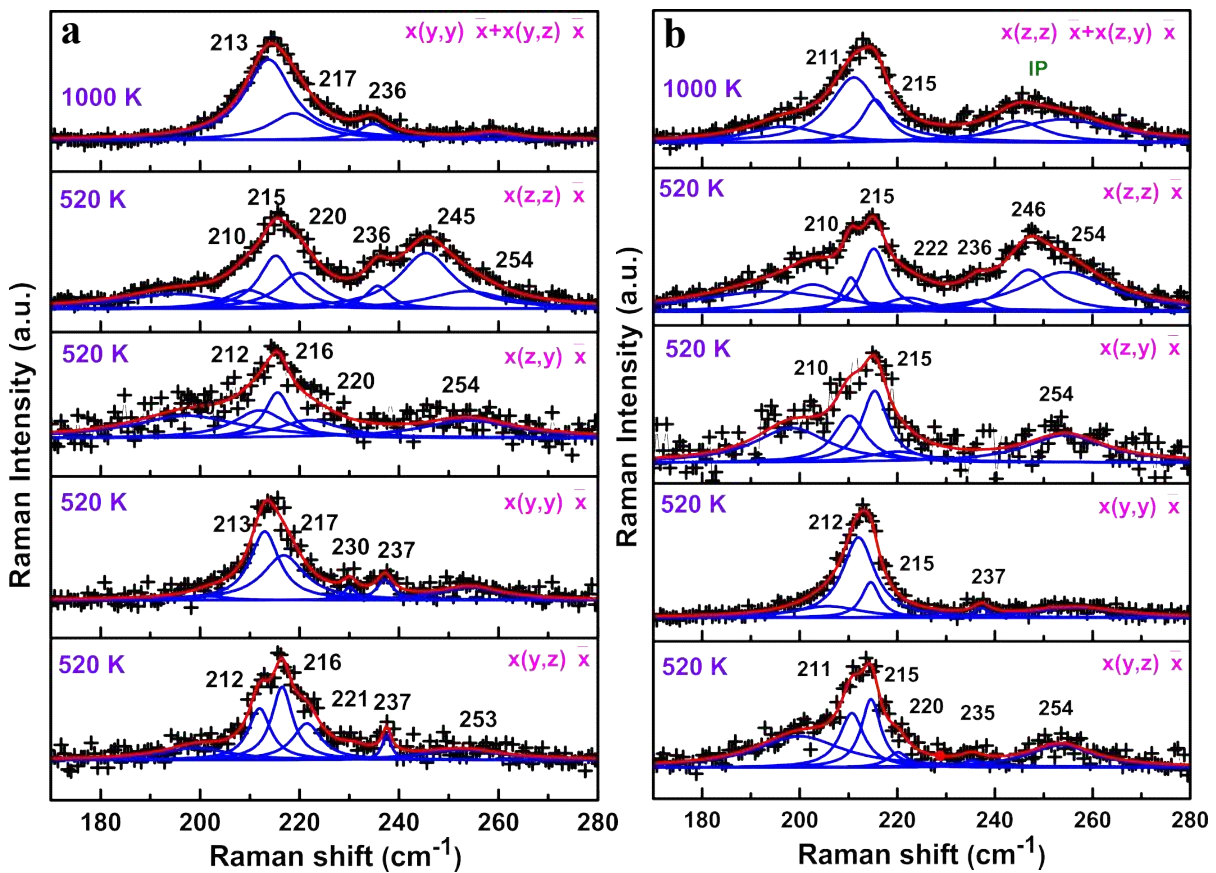


Fig.6.2.3.2: (a) and (b) Show unpolarized Raman spectra for higher LPD ( $\sim 2900 \text{ kW/cm}^2$ ) with incident polarization perpendicular and parallel to NW axis, respectively, followed by Lower LPD ( $\sim 800 \text{ kW/cm}^2$ ) Raman spectra in 4 different polarization configuration for D8 NW. Cumulative fit (red solid line) to the raw data ( $+$ ) and separate Lorentzian fits are shown with blue solid line.

The Raman spectra are shown in Fig. 6.2.3.2a and b. In step 1, 220-222  $\text{cm}^{-1}$  mode is not observed while in step 2, this mode is prominently observed and the highest intensity of this modes is noted in  $x(z,z)\bar{x}$  and  $x(y,z)\bar{x}$  configuration. In Fig. 6.2.3.2a and b for  $x(z,y)\bar{x}$  configuration, the signal to noise ratio is poor however, from the better Raman spectrum (Fig. 6.2.3.2a) of the two, peak positions are identified and same set is used for fitting in the other spectrum..

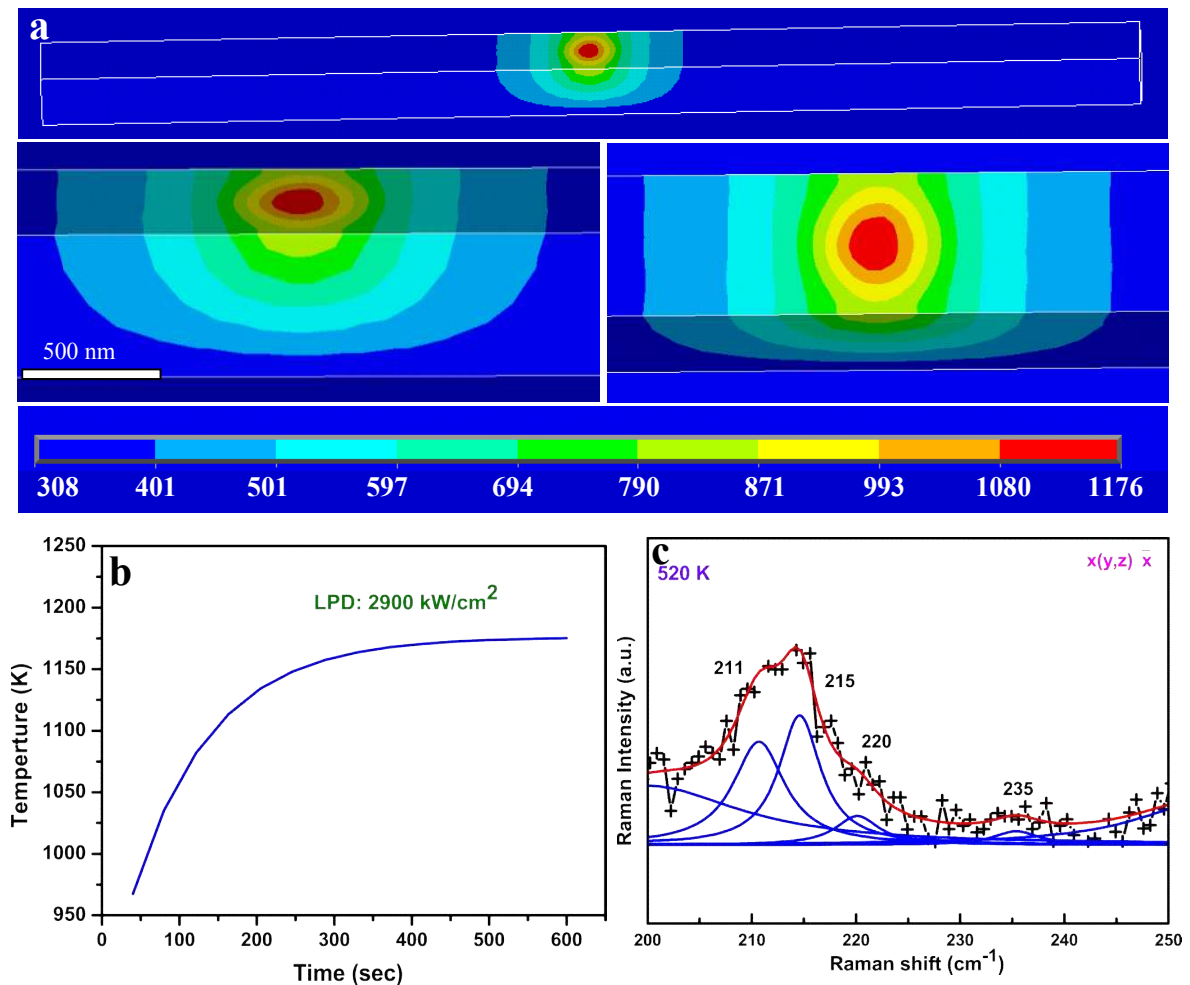


Fig.6.2.3.3: (a) Simulated 3D temperature profile view for InAs nanowire (D8: NW:  $d \sim 350 \text{ nm}$ ,  $L \sim 4 \mu\text{m}$ ) on Si substrate (complete NW and part of the NW with different tilts) for LPD  $\sim 2900 \text{ kW/cm}^2$ , b) Simulated transient temperature as a function of laser irradiation time (c) Fitting of Raman spectra of figure 6.2.3.2b in  $x(y,z)\bar{x}$  configuration range from 200-250  $\text{cm}^{-1}$ . Cumulative fit (red solid line) to the raw data (+) and separate Lorentzian fits are shown with blue solid line.

Further, simulated 3D steady state temperature profile for LPD  $\sim 2900$  kW/cm<sup>2</sup> and temperature at the laser spot vs laser irradiation time are shown in the supplementary Fig. 6.2.3.3a and b, respectively. Temperature corresponding to top Raman spectra in Fig. 6.2.3.2a and b is noted at 90s ( $\sim 1000$  K), as per the experiment. Fitting of Raman spectra from 200 to 250 cm<sup>-1</sup> in  $x(y,z)\bar{x}$  configuration of Fig. 6.2.3.2b is shown for clarity in the Fig. 6.2.3.3c. The observation of the Raman mode  $\sim 220$  cm<sup>-1</sup> only at lower LPD indicates that it may be related to cooling effect.

It may be further interesting to find out if, presence of this mode is related to blue shift of TO\* phonon (InAs) from 217 to 220 cm<sup>-1</sup> at simulated temperature range  $\sim 1600$  - 1900 K noted in Fig. 6.2.1.1e. From the above understanding, heating- cooling experiment for InAs NWs, using laser irradiation monitored by unpolarized Raman spectroscopy is expected to give us the clue to the presence of these additional modes.

#### **6.2.4 Heating–cooling experiment: monitored by Raman spectroscopy**

Heating experiment is performed by keeping laser irradiation on for 8 min at LPD  $\sim 230$  kW/cm<sup>2</sup> and 400 kW/cm<sup>2</sup> for D9 ( $d \sim 1$   $\mu$ m and  $l \sim 80$   $\mu$ m). The optical images of InAs NW is taken before and after the experiment, which are shown in Fig. 6.2.4.1a and b, respectively. Further, in cooling experiment, laser was put off and Raman spectra was recorded at LPD  $\sim 30$  kW /cm<sup>2</sup> after every 15 min, till 1 and 2 hours, respectively. It may be noted that temperature range reached in the first case is 700 - 950 K and in the second case, it is  $\sim 1000$ -1280 K. At  $\sim 700$  K (Fig. 6.2.4.1.d), the TO\* mode  $\sim 211$  cm<sup>-1</sup> and As<sub>2</sub>O<sub>3</sub> mode  $\sim 252$  cm<sup>-1</sup> are observed during 8 min. After 15 min of cooling, completely different Raman spectra are observed, as compared during heating (Fig. 6.2.4.1d and e). The frequencies of oxide modes are different for two bottom spectra in Fig. 6.2.4.1d and e. After 2 hours of cooling, we observe different oxide modes  $\sim 254$  cm<sup>-1</sup> with reduced FWHM, along with some

additional modes  $\sim 220$ - $223$  and  $238$   $\text{cm}^{-1}$  other than  $\text{TO}^*$  phonon of InAs, which remains constant  $\sim 217$   $\text{cm}^{-1}$ . After cooling, evolution of these additional modes is indicative of continuation of some chemical process/evolution during cooling, leading to change in chemical composition.

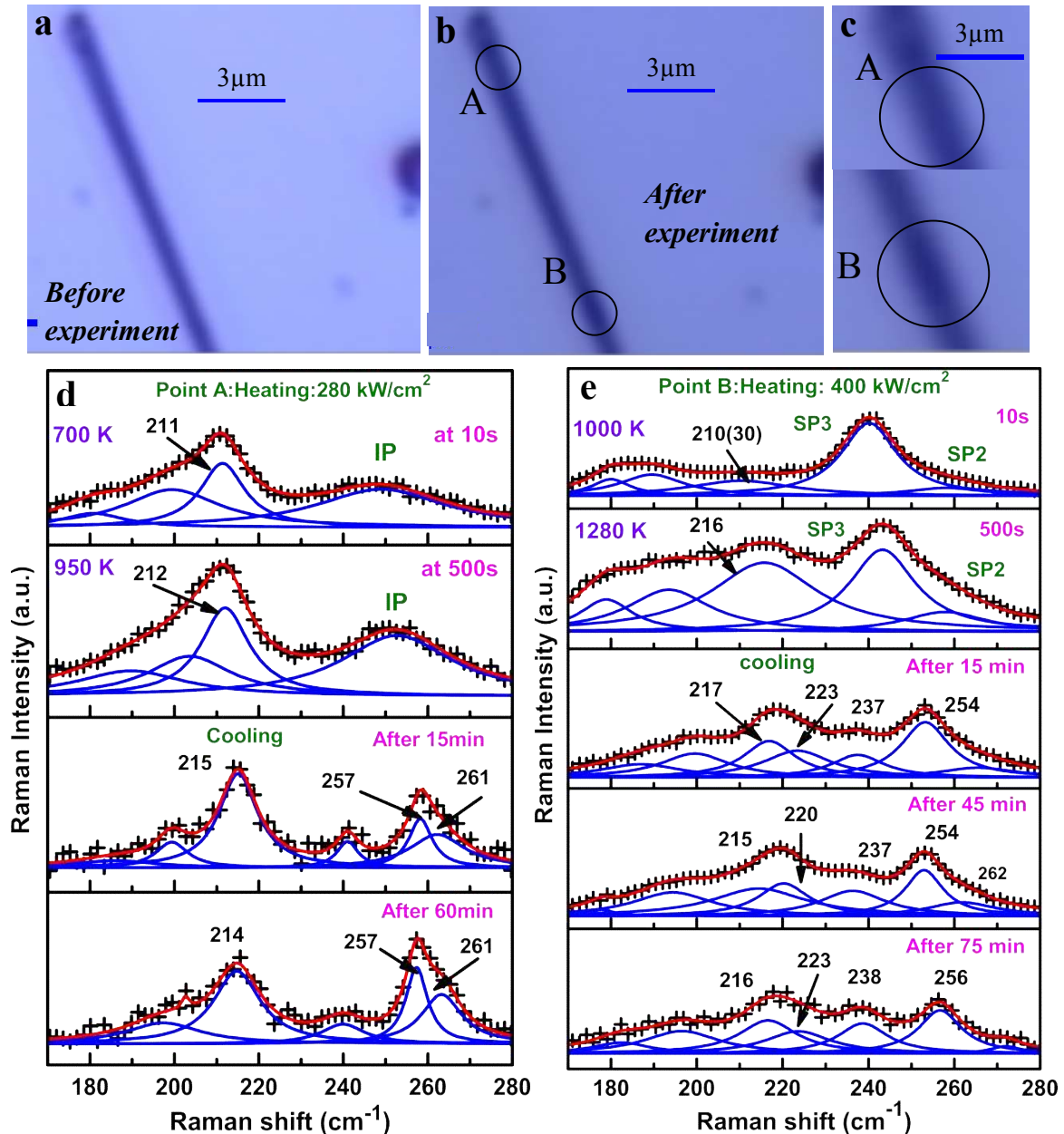


Fig. 6.2.4.1: (a) and (b) Optical image of InAs NW (D8) before and after Raman experiment, respectively. (c) Show the zoomed image of position A and B. (d) and (e) show unpolarized Raman spectra during heating cooling experiments showing formation of Grey and Black allotropes of elemental As on cooling of low and high LPD irradiated InAs NW, respectively. Cumulative fit (red solid line) to the raw data (+) and separate Lorentzian fits are shown with blue solid line.

To investigate this possibility, we looked into possible chemical reactions of these oxides during cooling. For Intermediate processes (IP) and strong processes (SP) of oxidation chemical reaction is showing that the  $\text{As}_2\text{O}_3$  and  $\text{InAsO}_4$  are metastable oxides, which further decomposes into stable elemental As [262].



During cooling, formation of elemental As by IP and SP are only processes possible. Out of the two byproducts  $\text{In}_2\text{O}_3$  and As, these additional peaks do not belong to  $\text{In}_2\text{O}_3$  [ $\sim 133$  and  $231 \text{ cm}^{-1}$  [268]]. Further, the difference in frequency in these two cases, wherein, they get heated to different temperatures to have either IP or SP oxidation, leaves only one possibility i.e. Raman spectra may belong to different allotropes of As. This possibility was further explored. Swartz et al. [233] have reported Raman spectra for different allotropes of elemental As. Raman spectra for i) crystalline gray As has modes at  $\sim 195, 257$  [269],  $200, 260$  [270] and  $198, 257$  [271]  $\text{cm}^{-1}$ , ii) crystalline black As has modes at  $\sim 222, 254$   $\text{cm}^{-1}$  [272],  $224, 233, 256$   $\text{cm}^{-1}$  [273] and iii) amorphous As has broad band at  $\sim 175\text{-}275$  and weak peak at  $\sim 200$  [270, 274-275]  $\text{cm}^{-1}$ . Yazii et al. [155] have also reported Raman modes of amorphous As at  $\sim 220 \text{ cm}^{-1}$  with large FWHM ( $50 \text{ cm}^{-1}$ ). It is also reported that gray ( $E_0 \sim 0.3 \text{ eV}$ ) and black (metallic) As have rhombohedral [276-277] and orthorhombic [278-279] structure, respectively. It may be noted here that for gray As modes  $\sim 198, 257$  and  $262 \text{ cm}^{-1}$  and for black As modes  $\sim 220$  and  $254 \text{ cm}^{-1}$  occur together, confirming formation of gray and black As, respectively. Thus, Raman spectra suggests that cooling after IP and SP processes

leads to formation of grey and black As, respectively. Raman peaks for black and gray As are consolidated in table 6.3.4.

*Table 6.3.4: Consolidation of Raman peaks frequencies for gray and black As from the literature.*

Material	Raman peak
Gray As	195 <sup>+</sup> , 257 <sup>+</sup> , 200 <sup>++</sup> , 260 <sup>++</sup> 198 <sup>+++</sup> , 258 <sup>+++</sup>
Black As	222 <sup>*</sup> , 254 <sup>*</sup> 224 <sup>**</sup> , 233 <sup>**</sup> , 256 <sup>**</sup> : (As <sub>0.83</sub> P <sub>0.17</sub> )

+ : [269], ++ : [270], +++: [271], \* : [272], \*\* : [273]

The formation of specific allotrope of elemental As seems to be determined by history of oxide formation i.e. if it is formed via intermediate or strong interaction processes. This in turn suggests that it depends on the highest temperature reached before cooling. This has been checked for few more laser irradiation experiments, specially for black As. Different allotropes of As exists but grey As is a stable phase, whereas, black As is a metastable phase of arsenic. It may be important to note that there has been no success in the synthesis of pure Black-As due to its metastability [280]. Fig. 6.2.4.1c shows formation of greyish and blackish deposit on InAs NW at A and B point surrounded by blackish and greyish areas, respectively. Both grey and black arsenic have high electrical conductivity due to layered structure and control over growth of only few layers of As can lead to properties similar to graphene [272, 280-283].

With the above understanding, we revisit the data in Fig. 6.2.1.1e, which is fitted to consider possibility of presence of the black As  $\sim 220 \text{ cm}^{-1}$  at higher simulated temperature (Fig. 6.2.4.1a). The top spectrum in Fig. 6.2.4.1a is for unperturbed condition at simulated temperature  $\sim 320 \text{ K}$ , which is expected to be similar to  $\sim 300 \text{ K}$  (room temperature) [262].

After deconvolution, the 217, 220, 238 and 254  $\text{cm}^{-1}$  modes are observed and modes  $\sim 220$ , 238 and 254 are attributed to black As. It may be appropriate to mention here that in Fig. 6.2.1.1 and 2, small intensity of oxide modes (D1 and D3 NWs) are observed due to poor extinction ratio for non-selected polarization from the polarized laser beam. One can further note that the blueshift of  $\text{TO}^*$  mode from  $\sim 215$  to  $217 \text{ cm}^{-1}$  along with its reappearance and narrowing of FWHM from 20 to  $6 \text{ cm}^{-1}$  for simulated temperature range 1000 - 1900 K for D2 NW [Fig. 6.2.1.1d and e], may be due to metamorphic layer formation of InAs (ZB) and or the conversion of WZ phase into ZB phase at higher simulated temperatures.

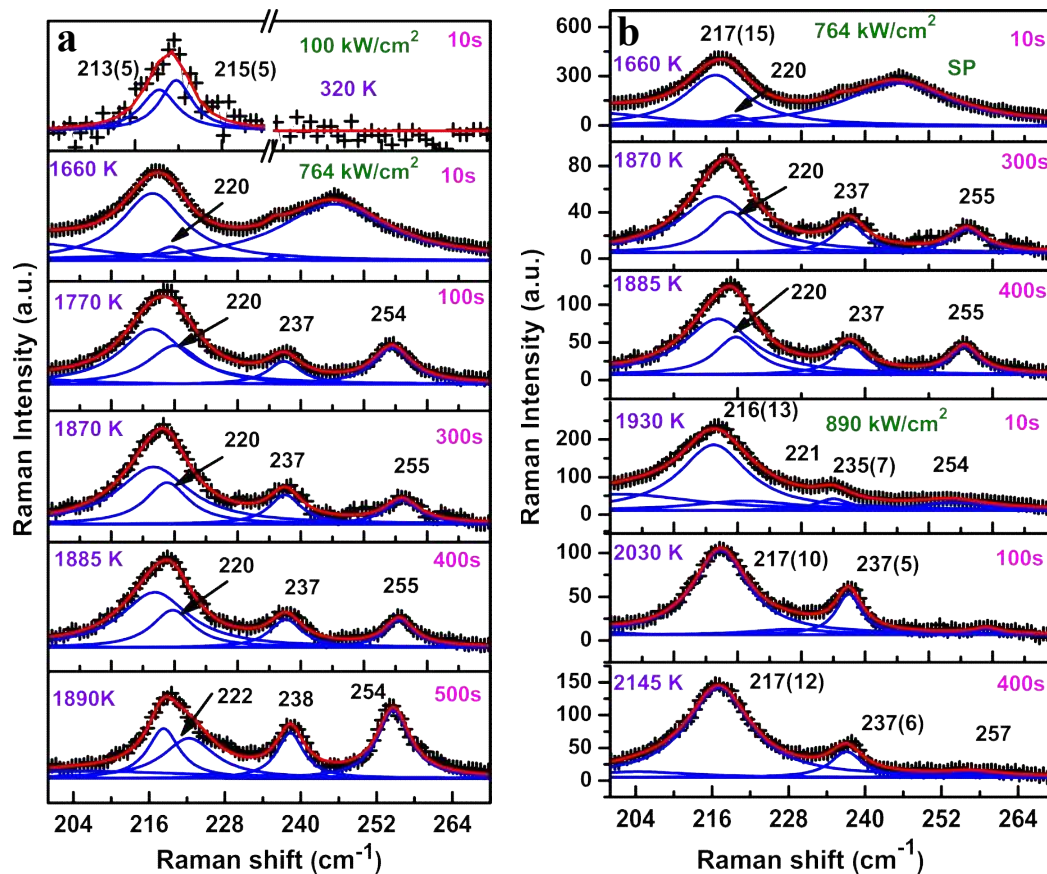


Fig. 6.2.4.2: (a) Raman spectra elucidating apparent large blueshift in  $\text{TO}^*$  phonon as due to formation of black As at higher simulated temperature through fitting of mode  $\sim 220 \text{ cm}^{-1}$ , (b) Raman spectra at  $T > 1600 \text{ K}$  showing decrease and then increase in intensity of  $\text{TO}^*$  mode as temperature increases. Cumulative fit (red solid line) to the raw data (+) and separate Lorentzian fits are shown with blue solid line.

Fig. 6.2.4.1b brings out decrease and then increase in the intensity of dominant ZB TO phonon for two LPDs, further indicating formation of ZB InAs layer during higher simulated temperatures. Similar observation of metamorphic growth of InAs is reported by Yamaguchi et al. [230]. This effect will be further investigated using resonance and TEM.

Resonance Raman spectroscopy is explored as a technique to study polytypism for smaller NWs and is discussed in the following section.

### 6.3 Application of Resonance Raman spectroscopy to study polytypism

In chapter 4, existence of polytypism i.e. presence of both wurtzite (WZ) and Zincblende (ZB) structures in InAs nanowires (NWs) of diameter (d)  $\sim 2 \mu\text{m}$ - 600 nm using polarized Raman spectroscopy is discussed. In the above work we have used NWs of smaller diameter  $\sim 200\text{nm}$  and we find that, as we go towards smaller diameter, certainty with which we can discuss the structures decreases significantly. To improve upon this, alternate study of wavelength dependent unpolarized and Polarized Raman spectroscopy is performed to establish use of Resonance Raman spectroscopy for easily ascertaining presence of both WZ and ZB phases in an isolated InAs nanowires with dia  $< 700 \text{ nm}$ . In the following, NW

Raman spectra of InAs NW (dia  $\sim 650\text{nm}$ ) with 488 nm excitation (Fig. 6.3.1) shows mixed structure i.e presence of WZ and ZB phase. TO ( $\sim 215 \text{ cm}^{-1}$ ) and  $E_{2h}$  ( $\sim 212 \text{ cm}^{-1}$ ) phonon represent ZB and WZ structure, respectively. As noted in chapter 4, we have chosen two configurations  $x(z,z)\bar{x}$  and  $x(y,y)\bar{x}$ , wherein, in the first allows only TO phonon and second configuration allows both TO and  $E_{2h}$  phonon [251]. One may note that  $x(z,z)\bar{x}$  configuration shows poor signal to noise ratio and it is difficult to say anything with good level of certainty. Further, it is also noted in chapter 4 that Raman spectra (RS) of  $x(y,y)\bar{x}$  configuration is similar to unpolarized RS with incident laser polarization in Y direction. In  $x(y,y)\bar{x}$  configuration, both modes are observed and  $E_{2h}$  of WZ dominates which indicates that

polytypism is present in InAs NW. In  $x(z,z)\bar{x}$  configuration, the signal is poor however, the TO phonon of ZB is dominant. The poor signal in  $x(z,z)\bar{x}$  configuration may have three reasons 1) smaller diameter 2) amount of ZB phase may be small because in this configuration, only TO is allowed and 3) low S/N ratio in polarized data. Here, as we go towards smaller diameter, certainty with which we can discuss the structures decreases significantly. It is difficult to say about polytypism using polarization dependent Raman spectroscopy for isolated smaller nanostructures.

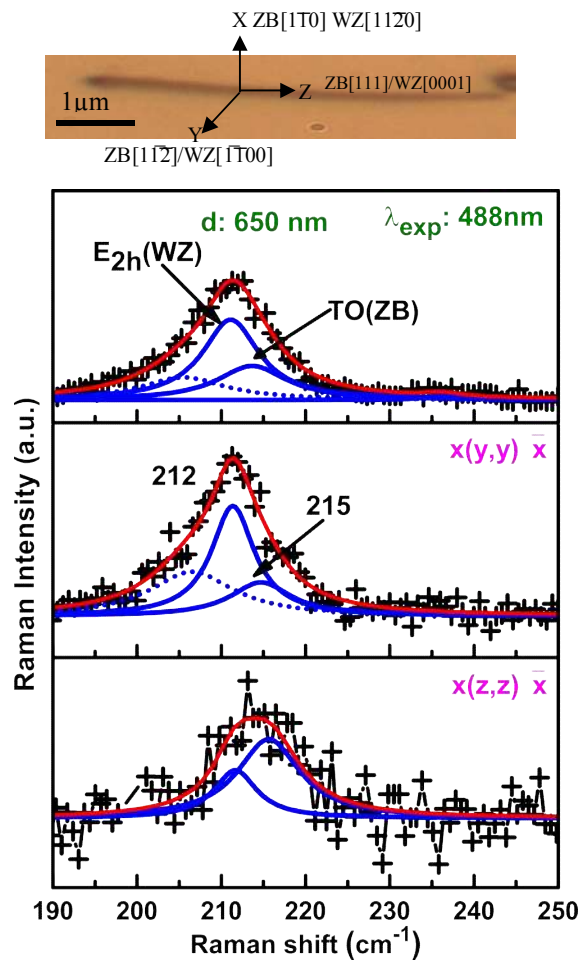


Fig. 6.3.1: Top is the unpolarized Raman spectrum for InAs NW (D9:  $d \sim 650$  nm) and bottom two are the polarized Raman spectra for  $x(y,y)\bar{x}$  and  $x(z,z)\bar{x}$  configuration using 488 nm excitation. Raman configuration are described using Porto's notations. Cumulative fit (red solid line) to the raw data (+) and separate Lorentzian fits are shown with blue solid line.

Wavelength dependent Raman spectroscopy is explored as an alternate method for this purpose, WZ and ZB phase of InAs have different E1 band gaps [171] i.e. E1 and E1+ $\Delta$ 1 for WZ phase: 2.4 and 2.6 and for ZB phase: 2.5, 2.7 eV and may give RS, which can help distinguish presence of WZ and ZB structure.

Arion laser excitations i.e. 514 nm (2.41 eV), 488 nm (2.54 eV), 476 nm (2.61 eV), 458 nm (2.71 eV) are suitable to study resonance behavior for WZ and ZB phase of InAs NW. Further, we have performed the wavelength dependent unpolarized Raman spectroscopy with Y incident laser excitation for low power density  $\sim 200$  kW/cm<sup>2</sup> (avoiding heating effect) on the same wire (Fig. 6.3.2a). Resonance enhancement of E<sub>2h</sub> (WZ) and TO (ZB) is observed at 514 and 458 nm, respectively relative to the other phonon. Other salient features of these Resonance Raman spectra (RRS) are,

- (1) The broad mode observed  $\sim 208$ -210 cm<sup>-1</sup>, which is attributed to silent mode of WZ InAs [251, 170] shows maximum intensity at 514 nm and decreases as we move towards 458nm excitation spectra.
- (2) In chapter 4, we have briefly discussed that LO phonon in these NWs are coming from ZB structure [251] and consistently intensity of LO peak increases at 458 nm compared to 514 nm excitation spectra.
- (3) The frequency of TO\* peak is blueshifted from 213 to 215 cm<sup>-1</sup> as wavelength changes from 514 to 458 nm which further suggests that TO(ZB) dominates at 458 nm.

Thus this data establishes the point that the presence of both ZB and WZ structure in InAs NW can be elucidated using RRS.

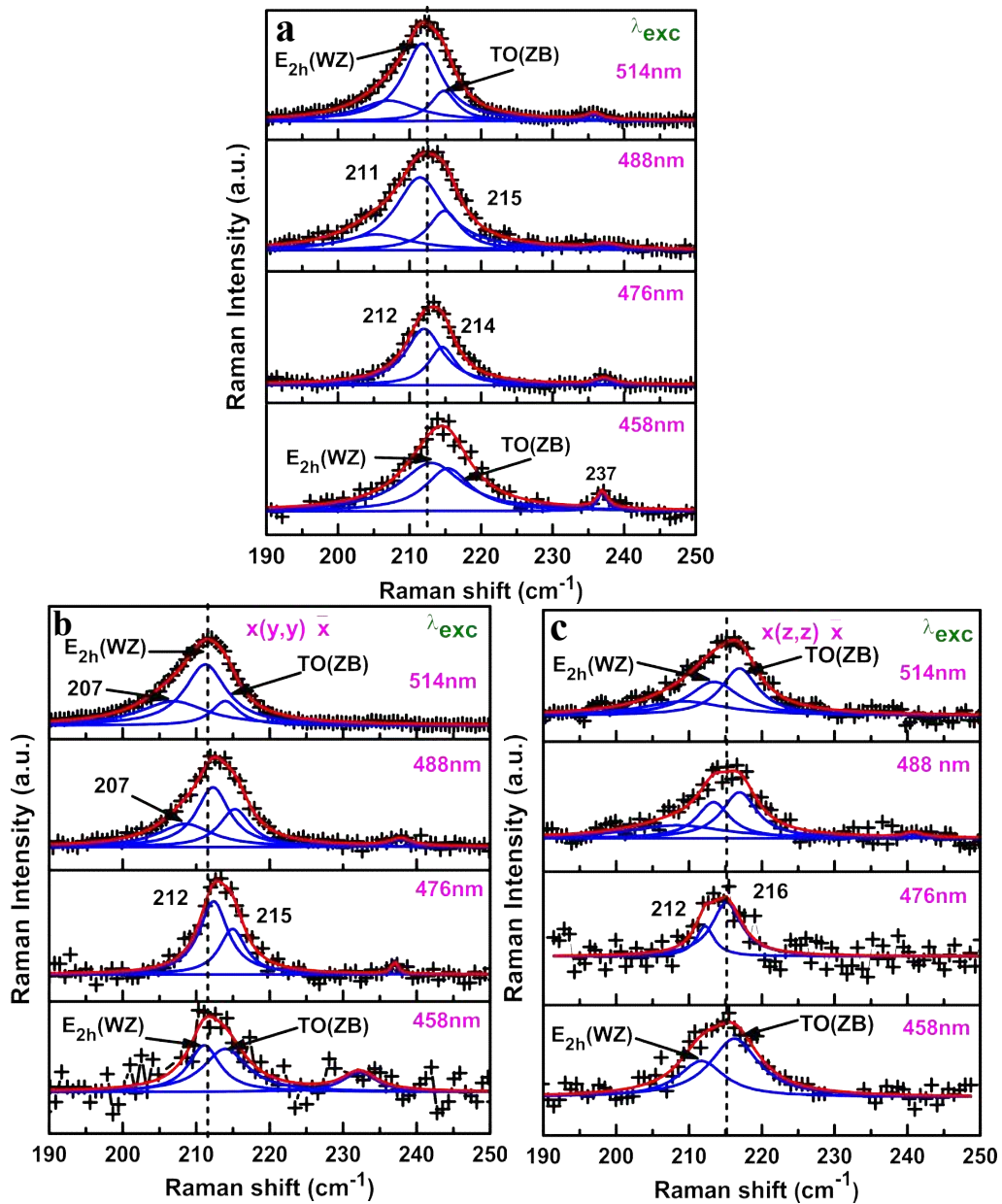


Fig. 6.3.2: a) Wavelength dependent unpolarized Raman spectra, b) and c) wavelength dependent polarized Raman spectra for  $x(y,y)\bar{x}$  and  $x(z,z)\bar{x}$  configuration, respectively using 514, 488, 476 and 458 nm excitation. Cumulative fit (red solid line) to the raw data (+) and separate Lorentzian fits are shown with blue solid line.

Next, we perform wavelength dependent polarized Raman spectroscopy (Fig 6.3.3) at same point to confirm that resonance Raman and polarized Raman indeed gives the same

information. In  $x(y,y)\bar{x}$  configuration (Fig. 6.3.3.a), we have observed similar Raman spectra as observed unpolarized Raman measurement due to the presence of both phonon i.e.  $E_{2h}$  (WZ) and TO (ZB) phonons are allowed in this configuration. The interesting point is noted in Raman spectra of  $x(z,z)\bar{x}$  configuration as shown in Fig. 6.3.3b. According to Raman selection rule, in  $x(z,z)\bar{x}$  configuration, only TO (ZB) phonon is allowed and consistently TO (ZB) is dominant at 514 nm.

### 6.3.1 Resonance Raman spectroscopy for investigation of InAs NWs with diameter <600nm

The unpolarized and polarized Raman spectroscopy are performed on InAs NW (dia ~ 300 nm) with 514 nm for both incident i.e. Y and Z polarization (Fig 6.3.1.1) to show that these spectra replicates  $x(y,y)\bar{x}$  and  $x(z,z)\bar{x}$ , respectively.

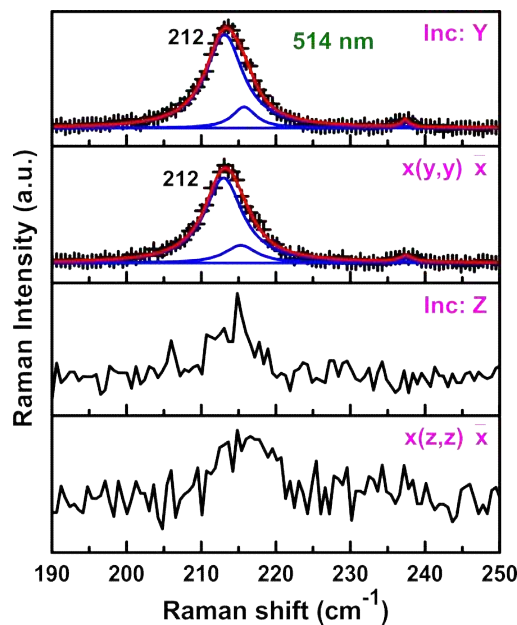


*Fig. 6.3.1.1: Show the Raman spectra by taking incident Y and Z and polarized Raman spectra for  $x(y,y)\bar{x}$  and  $x(z,z)\bar{x}$  configuration using 514 excitation. Cumulative fit (red solid line) to the raw data (+) and separate Lorentzian fits are shown with blue solid line.*

Further, we have chosen two different set of InAs NWs to perform RRS to take incident light polarized either Y or Z direction to measure unpolarized Raman spectra for 514 nm and 458 nm (Fig 6.3.1.2). The diameter and length of the NW are  $\sim 300$  and  $\sim 5 \mu\text{m}$  as shown Fig 6.3.1.2a. RRS is normalized for intensity by considering change in contribution of scattering volume (area \* depth),  $\omega^4$  and no of photons per second as per the wavelength. Further time and power dependence is removed. The number on Y axis, thus reflects intensity variation of phonons as a function of wavelength. The spectra suggests this NW has WZ dominant structure and thus the maximum counts observed ( $\sim 80$ ) at 514 nm as compared to 15 counts at 458 nm in Fig. 6.3.1.2a.

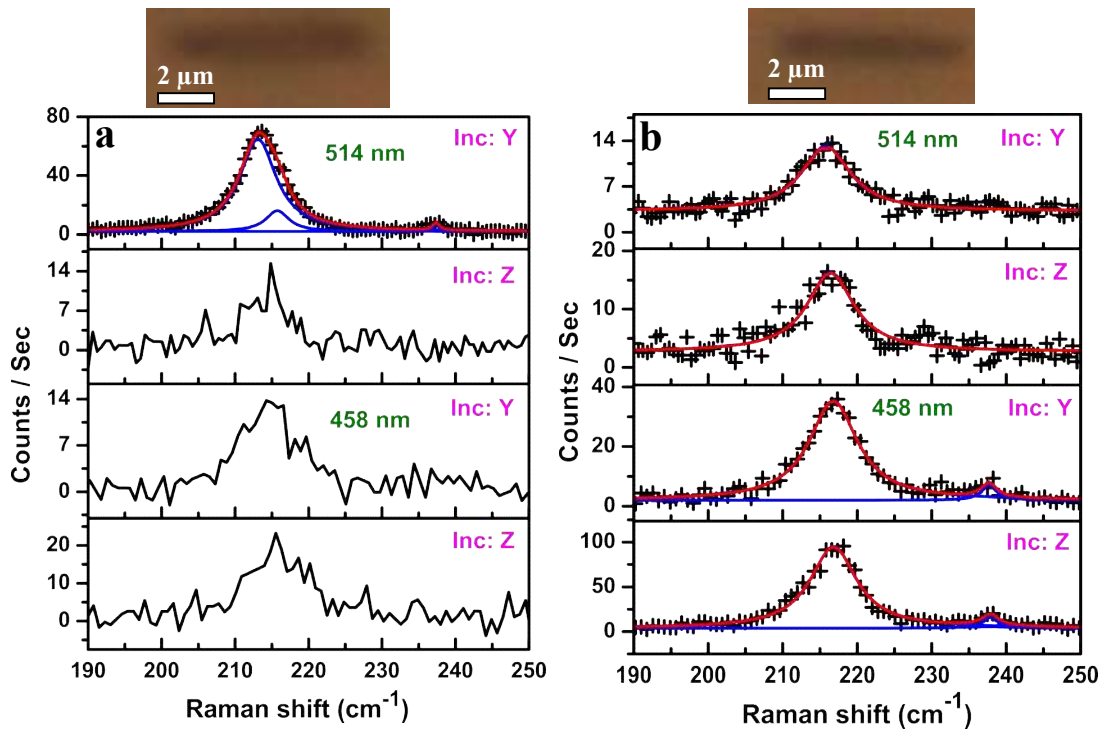


*Fig. 6.3.1.2: a) and b) wavelength dependent unpolarized Raman spectra by taking incident Y and Z for each wavelength 514, 458 nm excitation for diameter 300, 270 nm, respectively. Cumulative fit (red solid line) to the raw data (+) and separate Lorentzian fits are shown with blue solid line.*

Similar experiment is performed using 514 and 458 nm excitation on different NW with dia  $\sim 270$  nm and  $l \sim 4 \mu\text{m}$  (Fig. 6.31.2.b). The TO\* is observed  $\sim 217 \text{ cm}^{-1}$  at both wavelengths

and maximum counts are observed ( $\sim 100$ ) at 458 nm for Z incident RRS. Observation of TO phonon with Lorentzian lineshape at both 458 nm and 514 nm, as well as higher counts in Z incident as compared to Y incident laser polarization confirms that structure is pure ZB. According to Raman selection rule (RSR), the scattering cross section for TO (ZB) in  $x(z,z)\bar{x}$  configuration is two times that of  $x(y,y)\bar{x}$  configuration, as observed (Fig. 6.3.1.2). Thus using Y and Z incident RRS, we have established that WZ and ZB phases can be identified using RRS.

In earlier section, we have observed that at higher simulated temperature  $> 1600$  K, the WZ phase may be converted into pure ZB phase. In next section, we use RRS to obtain information about the structure for smaller nanostructures and investigate the conversion of phase at higher simulated temperature using laser irradiation.

### **6.3.2 Investigation of conversion of wurtzite to zincblende phase on laser irradiation using Resonance Raman spectroscopy:**

As first step, RRS is taken at low LPD  $\sim 800$  kW/cm<sup>2</sup> ( $d \sim 350$  nm and  $l \sim 1.5$   $\mu$ m) at 514, 488 and 458 nm for Y and Z incident laser polarization. In Fig. 6.3.2a, the  $E_{2h}$  (WZ) and TO (ZB) phonon are observed  $\sim 213$  and  $216$  cm<sup>-1</sup>, respectively. The maximum counts at 514 nm suggests that wire have higher WZ content. Further, same position is probed using incident Y laser (488nm) polarization so that oxides modes do not interfere and TO\* mode can be clearly visible at high simulated temperature  $\sim 1300$ - $1400$  K. In Fig. 6.3.2b, top two spectra show strong TO\* and LO mode  $\sim 216$  and  $237$  cm<sup>-1</sup>. These Raman spectra is very similar to Fig 6.3.2. The additional  $227$  cm<sup>-1</sup> is also observed due to formation of black As. After 5 min, the same position is probed at low LPD to take Z incident. The bottom spectra show TO\* and LO phonons  $\sim 217$  and  $237$  cm<sup>-1</sup>. Frequency and Lorentzian line shapes indicate pure ZB phase. Further mode related to black As is also observed. This conversion is further checked

using resonance Raman spectroscopy. The same position is now probed using 514 nm, 488 nm and 458 nm with low LPD  $\sim 800 \text{ kW/cm}^2$  to avoid any further laser heating. In Fig. 6.3.2c, for all Raman spectra single Lorentzian can be fitted to  $\text{TO}^*(\sim 217 \text{ cm}^{-1})$  and LO ( $\sim 237 \text{ cm}^{-1}$ ) phonon. The intensity of TO phonon is largest at 458nm and signal is higher for Z incident laser polarization. It may be important to note here that intensity of TO phonon w.r.t.  $E_{2h}$  phonon depends on three parameters 1) Resonance 2) fraction of phase and 3) Raman selection rule.

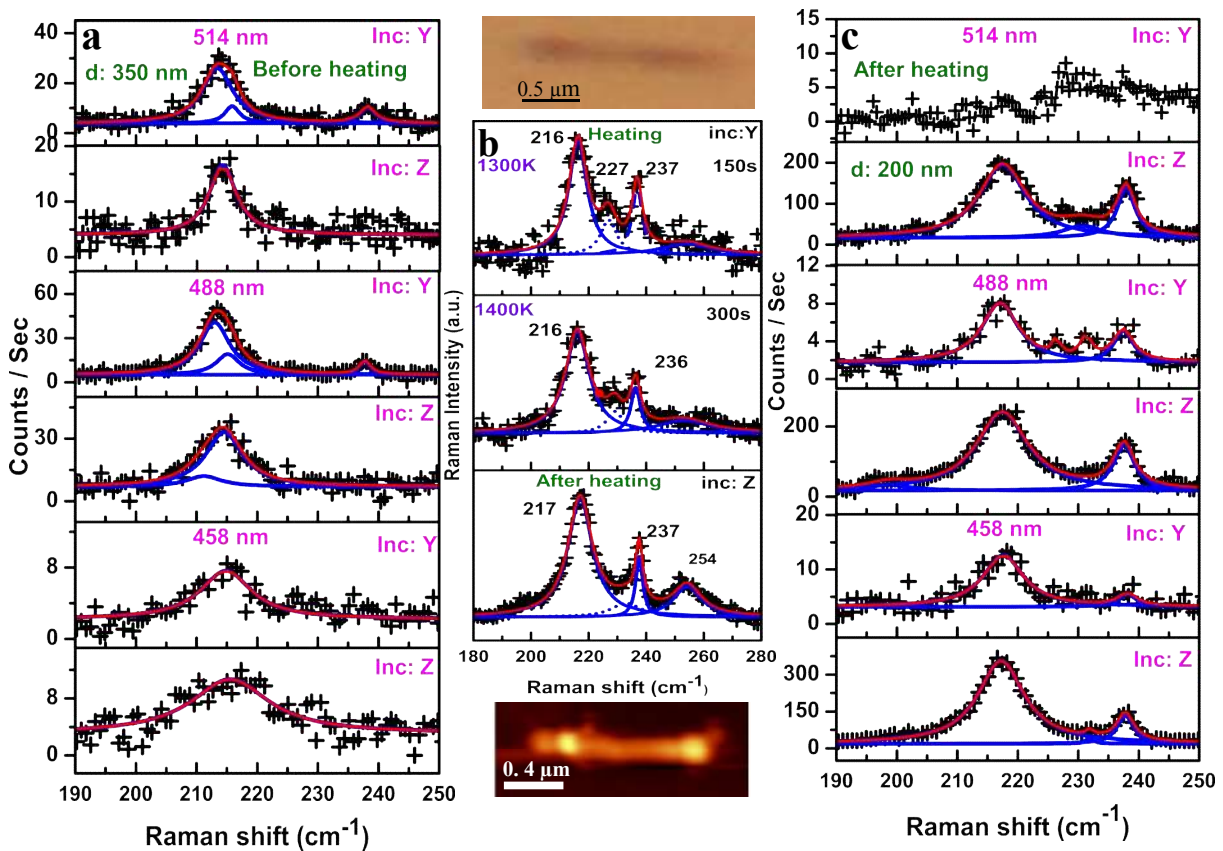


Fig. 6.3.2.a) Before heating, wavelength dependent unpolarized Raman spectra by taking incident Y and Z polarization for each wavelength 514, 488 and 458 nm excitation at LPD  $\sim 800 \text{ kW/cm}^2$ , b) top two Raman spectra are for LPD  $\sim 6500 \text{ kW/cm}^2$  at 150s and 300s for incident Y and bottom Raman spectra is for LPD  $\sim 800 \text{ kW/cm}^2$  after heating, for incident Z using 488 nm excitation. The top and bottom of (b) are optical and AFM images, before and after heating, respectively. c) After heating, wavelength dependent unpolarized Raman spectra by taking incident Y and Z polarization for each wavelength 514, 488 and 458 nm excitation at LPD  $\sim 800 \text{ kW/cm}^2$ . Cumulative fit (red solid line) to the raw data (+) and separate Lorentzian fits are shown with blue solid lines.

According to Raman selection rule of ZB, the scattering cross section is two times larger for Z incident polarization. However, in present case, the counts is  $\sim 20$  times larger for Z incident as compared Y incident polarization. This is rather intriguing. We have performed AFM measurement after heating for this NW, the diameter of wire seems to have reduced from 300 to 200 nm and have dumbel like shape i.e. dimension is reduced in the center, where laser is irradiated. At this diameter antenna effect may occur giving rise to higher intensity in Z incident polarization [45, 265]. This needs to further investigated and is out of scope of this thesis. However, this thermal phenomenon is independently checked using TEM.

This work provides the basis for the application of resonance Raman spectroscopy in obtaining information of polytypism in nanostructures, where, polarized Raman spectroscopy /XRD may not be feasible and local conversion from mix or pure WZ to pure ZB phase can be used for fast electronic devices.

### **6.3.3 Investigation of conversion of wurtzite to zincblende using transmission electron microscopy on thermal annealing**

Conversion of InAs WZ to ZB phase at higher temperature is independently investigated using Transmission Electron Microscope (TEM). The crystalline structure and the growth direction of the NWs are studied using selective area electron diffraction (SAED) and high resolution transmission electron microscopy (HRTEM) using TEM.

For TEM measurements, NWs are isolated from the substrate by ultra-sonication and then two drops of NW solution in water are put on copper grid with carbon film. The diameter and length of InAs NWs on copper grid are found to be in the range of 50-200 nm and few  $\mu\text{m}$ , respectively. The four NWs are chosen for this experiment. SAED is performed

on InAs NWs, NW1 to NW4 and are shown in Fig. 6.3.3.1 and 6.3.3.2. Selected area for SAED measurements is  $\sim 100$  nm. The SAED patterns are analyzed as described in the following. First, we chose 2D unit cell from SAED Laue pattern consisting of three spots 1, 2, 3 and origin O. Then distances are calculated between O and 1:  $d_1$ , O and 2:  $d_2$  and O and 3:  $d_3$  and angles between 1 and 2:  $\theta_1$ , 1 and 3:  $\theta_2$  are measured using TEM Gatan analysis software package. By putting these as input, matching (h,k,l) values for both WZ and ZB phase of InAs are checked using Fortran programme SAED index developed by Dr. Himanshu Srivastava (SUS, RRCAT). The appropriate set of (h,k,l) planes are chosen on the

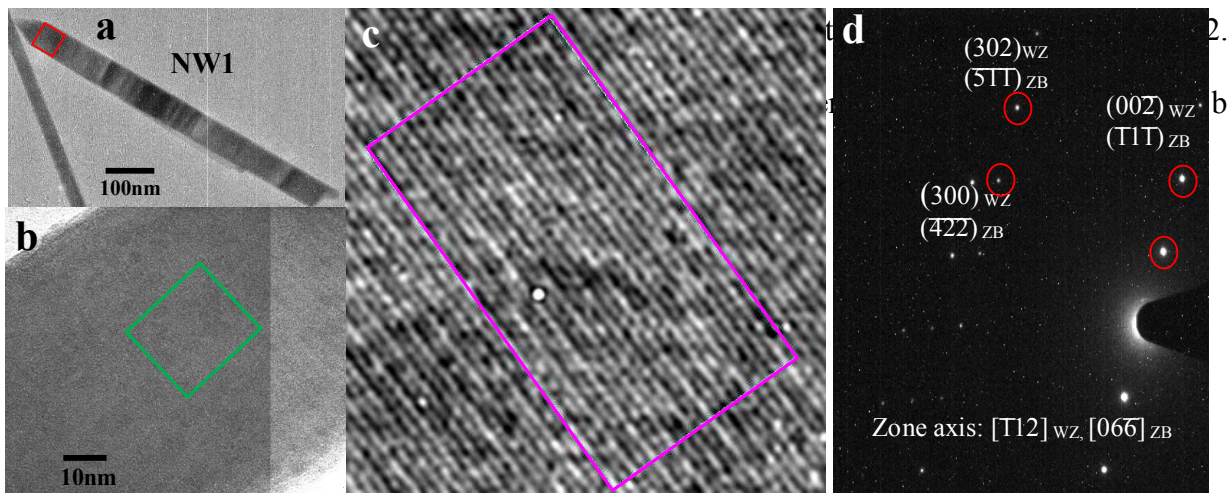


*Fig. 6.3.3.1 (a) TEM image of NW1 and HRTEM was performed on position marked by (red) square, (b) HRTEM image, (c) Filtered image of the region marked in b, inter planer d is calculated over region marked by the rectangle(magenta), and (d) The SAED pattern at the center position of the NW.*

From table 6.3.3.1, we can note that NW1, NW3 both show possibility of presence of WZ and ZB phases. HRTEM of NW1, however, shows presence of WZ phase. The tolerance values needed for matching (h,k,l) planes, as well as stacking faults observable in TEM images indicate mixed phase for NW1 and NW3 [170, 171, 190, 211, 219] It may be

important to note here that mixed phase generates strain in both WZ and ZB phases and hence may require to take higher tolerance for matching (h,k,l) planes in SAED pattern [251].

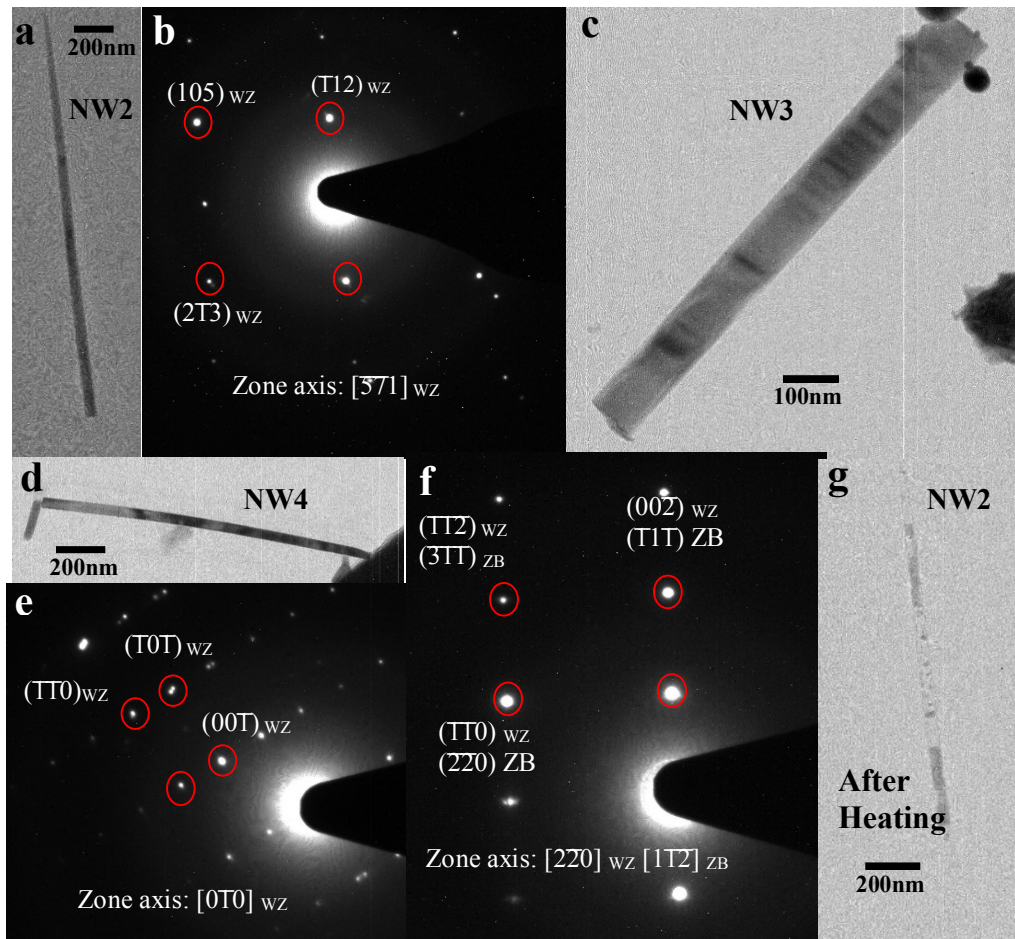


*Fig. 6.3.3.2: (a), (c) and (d) TEM image of NW 2,3 and 4, respectively. (b), (f) and (e) The SAED pattern at the center position of the NW2, 3, 4, respectively. (g) TEM image of NW2 after heating.*

Tolerance value is small for NW3, probably because SAED pattern taken in the center shows single phase region in TEM image (Fig.6.3.3c) and is unstrained, however, TEM image of entire NW3 shows presence of mixed phase. Secondly, both have similar dimensions  $\sim 90 \mu\text{m}$ . SAED patterns of NW2 and NW4 are identified to have pure WZ phase. This is consistent

with their dimensions (~50 nm) [172, 174-175], TEM image (no stacking faults) and low tolerance required for SAED pattern matching.

*Table 6.3.3.1 Consolidation result of SAED and HRTEM for NW1-4.*

NWs Phase /SAED Zone axis		From SAED / HRTEM d (Å <sup>0</sup> )		angle (°)	Tolerance d/θ ( Å <sup>0</sup> /° )	Matching d values (Å <sup>0</sup> )	angle (°)	(h,k,l)
NW1 (Fig. 6.3.3.1d)	d <sub>1</sub>	1.205			0.2/2	1.2366		(300)
WZ / [1T2]	d <sub>2</sub>	3.378	d <sub>1</sub> & d <sub>2</sub>	88.13		3.4976	89.99	(00Z)
	d <sub>3</sub>	1.124	d <sub>1</sub> & d <sub>3</sub>	19.44		1.165	19.47	(302)
ZB / [066]	d <sub>1</sub>	1.205			0.2/2	1.0239		(42Z)
	d <sub>2</sub>	3.378	d <sub>1</sub> & d <sub>2</sub>	88.13		3.4976	90.00	(T11)
	d <sub>3</sub>	1.124	d <sub>1</sub> & d <sub>3</sub>	19.44		1.1658	19.47	(5T1)
HRTEM /WZ		6.6408						(001)
NW2 (Fig. 6.3.3.2b)	d <sub>1</sub>	1.579			0.1/1	1.577		(2T3)
WZ / [571]	d <sub>2</sub>	2.519	d <sub>1</sub> & d <sub>2</sub>	86.17		2.544	86.86	(T12)
	d <sub>3</sub>	1.296	d <sub>1</sub> & d <sub>3</sub>	31.17		1.309	30.91	(105)
NW3 (Fig. 6.3.3.2f)	d <sub>1</sub>	2.219			0.1/1	2.141		(TT0)
WZ / [220]	d <sub>2</sub>	3.586	d <sub>1</sub> & d <sub>2</sub>	90.16		3.4977	89.99	(00Z)
	d <sub>3</sub>	1.873	d <sub>1</sub> & d <sub>3</sub>	31.75		1.8266	31.48	(TTZ)
ZB / [1T2]	d <sub>1</sub>	2.219			0.1/1	2.141		(2Z0)
	d <sub>2</sub>	3.586	d <sub>1</sub> & d <sub>2</sub>	90.16		3.4975	89.99	(T1T)
	d <sub>3</sub>	1.873	d <sub>1</sub> & d <sub>3</sub>	31.75		1.8266	31.48	(3TT)
NW4 (Fig. 6.3.3.2e)	d <sub>1</sub>	3.748			0.1/1	3.7098		(TT0)
WZ / [0T0]	d <sub>2</sub>	6.968	d <sub>1</sub> & d <sub>2</sub>	89.83		6.9955	89.99	(00T)
	d <sub>3</sub>	3.283	d <sub>1</sub> & d <sub>3</sub>	27.90		3.277	27.93	(T0T)

The sample is heated in-situ in TEM to 873 K for 5 minutes and SAED patterns and HRTEM are taken for NWs after temperature stabilizes. It was observed that material got removed from some regions of these NWs due to possible evaporation in high vacuum and good SAED could be obtained from the same position only from NR1. Fig. 6.3.3.3a and b shows TEM images before and after heating, which clearly indicates removal of stacking faults after heating.

The SAED pattern here matches with ZB phase only, with low tolerance values for angle and d value (Table 6.3.3.2). HRTEM could not be obtained for NW1. However, HRTEM of NW5 could be taken and is shown in Fig 6.3.3.4.

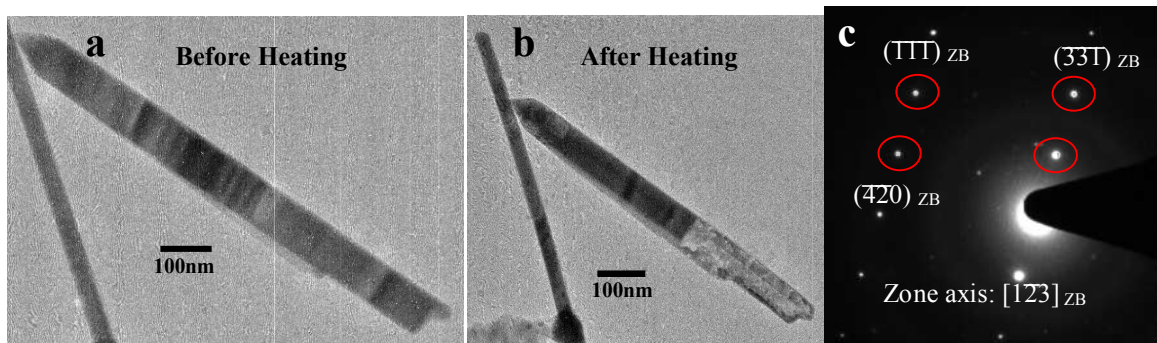


*Fig. 6.3.3.3: (a) and (b) TEM image of NW1 before and after heating, respectively. (c) The SAED pattern after heating at the center position.*

This gives  $d \sim 3.339 \text{ \AA}$  corresponding to ZB (111). From, dimensions of NW5 (~30 nm) and TEM image (before heating), it is expected to be pure WZ phase [172, 174-175]. Thus above study shows that there is phase transformation of InAs NWs from mixed phase/WZ phase to Pure ZB phase on heating ~873 K for 5 minutes.

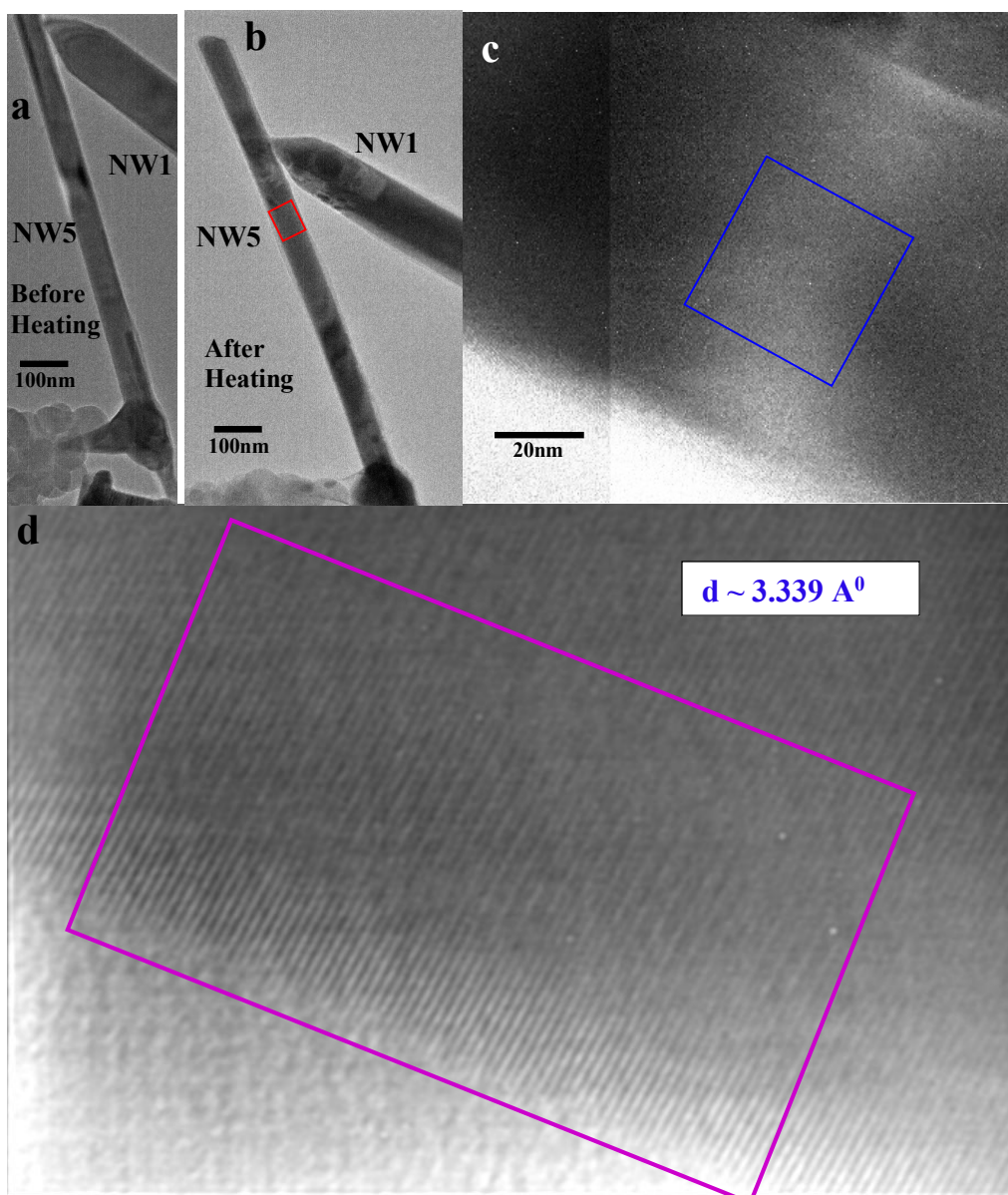


*Fig.6.3.3.4: (a) and (b) TEM image of NW5 before and after heating, respectively. HRTEM was performed on position marked by (red) square (b), (c) HRTEM image, d) Filtered image of the region marked in b, inter planer d is calculated over region marked by the rectangle(magenta)*

Table 6.3.3.2: Consolidation results of SAED for NW1 before and after heating.

NWs Phase /SAED zone axis		From SAED/ HRTEM d (Å <sup>0</sup> )		angle (°)	Tolerance d/θ ( Å <sup>0</sup> /° )	Matching d values (Å <sup>0</sup> )	angle (°)	(h,k,l)
NW1 Fig.(6.3.3.2c)	d <sub>1</sub>	1.205			0.2/2	1.2366		(300)
WZ / [112]	d <sub>2</sub>	3.378	d <sub>1</sub> & d <sub>2</sub>	88.13		3.4976	89.99	(002)
	d <sub>3</sub>	1.124	d <sub>1</sub> & d <sub>3</sub>	19.44		1.165	19.47	(302)
ZB / [066]	d <sub>1</sub>	1.205			0.2/2	1.0239		(422)
	d <sub>2</sub>	3.378	d <sub>1</sub> & d <sub>2</sub>	88.13		3.4976	90.00	(111)
	d <sub>3</sub>	1.124	d <sub>1</sub> & d <sub>3</sub>	19.44		1.1658	19.47	(511)
After heating at 873 K								
NW1 Fig.(6.3.3.3c)	d <sub>1</sub>	1.358			0.1/1	1.3546		(420)
ZB / [123]	d <sub>2</sub>	3.395	d <sub>1</sub> & d <sub>2</sub>	105.86		3.4976	104.96	(111)
	d <sub>3</sub>	1.403	d <sub>1</sub> & d <sub>3</sub>	23.33		1.3898	22.57	(331)

## 6.4 Conclusion

Two nearly perpendicular orientations of InAs NWs are found to show very different unpolarized Raman spectra for similar NWs irradiated with similar laser power density. This is investigated using specially designed polarization dependent Raman spectroscopy experiments. The study shows the difference in Raman spectra is observed for different NW orientation due to differences in Raman selection rules for crystalline oxides generated and not due to any difference in coupling of laser light with NW. This suggests that an unpolarized Raman spectra can lead to incorrect interpretation regarding oxidation processes, if even unpolarized Raman spectra is not looked into carefully. Further, at higher simulated temperatures (~1600 K), TO\* [combination of TO: dominant zincblende: ZB and E<sub>2h</sub>: wurtzite: WZ phonons] phonon blueshifts and FWHM reduces along with reappearance of

TO\* and LO like modes with higher strength. The study shows that both InAsO<sub>4</sub>, As<sub>2</sub>O<sub>3</sub> continue to disintegrate after laser irradiation is stopped, giving rise to different allotropes of elemental As, depending on the highest temperature (> 950/1300 K) reached before cooling. The higher simulated temperatures (>1200K), although, are not actually reached, the different ranges noted, help us separate the effects observed and is found to be very useful in the laser irradiation studies. The formation of specific allotropes of elemental As i.e. gray-As (rhombohedral) and black-As (orthorhombic) during cooling after a intermediate and strong oxidation interaction processes occurs at low (~ 700-950 K) and high (> 1000-1300 K) simulated temperatures, respectively. Both have high electrical conductivity due to layered structure and control over growth of only few layers using laser irradiation envisages properties similar to graphene.

Polarized Raman spectroscopy (PRS) indicates that polytypism (WZ and ZB) is present in the InAs NW (dia ~ 650 nm). However, PRS gives very poor S/N ratio for smaller diameters. As an alternate resonance Raman spectroscopy is investigated using Ar ion laser excitations at 514.5, 488, 476.5, 458 nm. Wavelength dependent Raman spectroscopy of mixed phase, dominant WZ and ZB phase NWs could be well separated on the basis of WZ and ZB phonon resonance enhancement of E<sub>2h</sub>(WZ) and TO(ZB) phonons. Thus it is established that resonance Raman spectroscopy can be used to obtain information about polytypism and can be successfully used for smaller isolated nanostructures, where it may be difficult to use more standard techniques like XRD/polarized Raman spectroscopy. RRS was further used to confirm conversion of WZ phase of InAs NW to ZB phase on laser irradiation at higher simulated temperature > 1300 K. Independently, conversion of WZ/mixed phase of InAs to ZB phase on thermal annealing is confirmed with SAED and HRTEM using in situ thermal annealing in TEM.

The study brings out potential of Raman spectroscopy as online monitoring technique for insulator to metallic surface modification of InAs NWs using laser irradiation. The control gained using laser irradiation with the help of simulated temperature and understanding developed of various processes on laser irradiation can lead to novel device applications. Resonance Raman spectroscopy (RRS) is established as an alternate technique to study polytypism for smaller nanostructures. RRS and TEM are used to study conversion of mixed /WZ phase to ZB phase in InAs NW on laser irradiation and thermal annealing, respectively.

# **Chapter 7**

## **Conclusion**

*“In questions of science, the authority of a thousand is not worth the humble reasoning of a single individual” \_\_\_\_\_ Galileo Galilei*

The aim of research work was to study the individual InAs micro-nanowires (MNWs) using Raman spectroscopy, which was not feasible using conventional techniques like XRD, TEM etc. due to low density and large diameter of NWs. In the MOCVD grown InAs/Si (001) sample under specific growth condition, NWs and MNWs of various morphologies and dimensions are found. Raman spectroscopy (microscopy) for InAs MNW, which are difficult to be studied using either XRD (macroscale technique) or TEM (nanoscale technique) is very suitable to be used as a local probe, along the length of MNWs and NWs. Raman scattering which is a weak process. However, Resonance enhancement of Raman scattering from InAs in the visible allows us to combine specificity of Raman spectroscopy and possibility of obtaining good signal to noise ratio from InAs MNWs/NWs, to study them individually. The InAs is a semi metal and hence, it can be easily affected by small laser power of visible irradiation due to large absorption.

Raman mapping on a single InAs MW (dia  $\sim 1 \mu\text{m}$ ) showed damage and time evolution of Raman spectra. To understand this behavior, systematic time evolution studies of power dependent Raman spectroscopy is performed for laser power densities (LPDs) in the range of 30-900 kW/cm<sup>2</sup> for time duration of 8 min. Three types of time evolution of Raman spectra are observed at these LPDs, which are further classified into different regions i.e. 1) low LPD (30 – 90 kW/cm<sup>2</sup>): No additional modes are observed, 2) medium LPD (100-500 kW/cm<sup>2</sup>): additional modes are observed in the range of 180-200 and 240-260 cm<sup>-1</sup> and the intensity of additional modes varies with time up to 6 min and 3) higher LPD (600-800 kW/cm<sup>2</sup>): Oscillatory behavior of intensity of an additional mode is observed. These observations are attributed to different oxidation paths being followed for InAs NWs under

different power levels of laser irradiation. Raman spectroscopy is used to detect the formation of metastable oxides on InAs NW surface and their transformation from one form to another with time. For a NW studied, thermal oxidation is observed at a laser power density of  $\sim 200$  kW/cm<sup>2</sup>. In the medium power density range (200-500 kW/cm<sup>2</sup>), a mixture of three compounds i.e. crystalline InAs<sub>x</sub>O<sub>y</sub> ( $\sim 240$ - $245$  cm<sup>-1</sup>), As<sub>x</sub>O<sub>y</sub> and As is observed, where, the concentration of each compound varies with time. InAs<sub>x</sub>O<sub>y</sub> transforms into As<sub>2</sub>O<sub>3</sub> and peaks at  $\sim 247$ - $252$  and  $192$  cm<sup>-1</sup> appear. Formation of InAs<sub>x</sub>O<sub>y</sub> and As<sub>x</sub>O<sub>y</sub> reactions compete with each other in the intermediate time span. At higher LPD (600-800 kW/cm<sup>2</sup>) i.e. when strong oxidation processes, these metastable oxides are no more detected, instead oscillatory behavior of elemental As is observed. This indicates layer by layer removal of top surface of the NW. For a NW oriented differently ( $\sim 254$  kW/cm<sup>2</sup>), formation of InAs<sub>x</sub>O<sub>y</sub> is reflected as a sharp peak  $\sim 240$ - $245$  cm<sup>-1</sup>. Time evolution of  $240$  cm<sup>-1</sup> mode is attributed to formation of hydrous and anhydrous InAsO<sub>4</sub> from Raman study under different environment like silica gel and water.

In summary, the time evolution of Raman spectra is used to probe chemical changes on laser irradiation, which is otherwise extremely difficult to detect by any other technique with such uniqueness. Position controlled laser induced chemical modification on a nanometer scale, without changing the core of the NW, can be useful for NW based device fabrication.

The frequency of TO phonon of InAs in these NWs is observed  $\sim 214$  cm<sup>-1</sup> at low laser power density (no damage), which is red shifted as compared the bulk value. Further, the peak  $\sim 212$  -  $218$  cm<sup>-1</sup> is observed with large asymmetry in InAs micro-nanowires (MNWs: diameter:  $2\ \mu\text{m}$  –  $400$  nm) using spatially resolved Raman spectroscopy (SRRS) of uniform,

bent and long tapered MNWs grown on a Si (001) substrate. For uniform NW, the frequency of TO phonon is observed  $\sim 215 \text{ cm}^{-1}$ , which is constant along the length while in tapered MNW, it is redshifts from  $\sim 217$  to  $\sim 212 \text{ cm}^{-1}$  continuously, as diameter decreases from base to tip. The redshift of TO phonon structure in these MNW/NWs is attributed to strain in the MNW/NWs, which is considered to be due to the presence of polytypism in InAs MNW/NWs. TO\* mode (TO phonon structure) is attributed to the superposition of  $E_{2h}$  phonon (wurtzite: WZ) and TO phonon (zinc blende: ZB). Further, polarized and wavelength dependent spatially resolved Raman spectroscopy establishes the presence of WZ and ZB phases in these MNW/NWs. This is found to lead to strained ZB and WZ phases present in these InAs MNW/NWs. However, formation of WZ phase for larger diameter InAs MNW/NWs is not commensurate with existing growth mapping studies. Growth mapping studies of metal organic chemical vapor deposition grown InAs NWs of diameter  $\sim 100\text{-}200 \text{ nm}$  reported in literature suggest MNWs of large diameter ( $500 \text{ nm}$  -  $2 \mu\text{m}$ ) to have pure ZB structure. Small changes in growth condition i.e. growth temperature and V/III ratio, however can change the crystal structures of InAs NW. Further, study of these MNWs suggests that the fraction of WZ to ZB content in a MNW depends not only on the diameter, but also seems to be governed by local growth/seeding conditions. This in turn leads to either tapered or uniform MNW growth under the same growth conditions on a substrate. The variation of phonon frequencies that of bulk value are correlated to the residual stress present in ZB and WZ phases, due to the presence of the other (WZ/ZB) phase. With the above understanding, as grown bent MNWs formation is associated with sudden change of diameter and consequently ZB to WZ content. The stress was further studied for tapered MNW, using spatially resolved temperature dependent Raman spectroscopy. Consistently, temperature dependent Raman data shows that there is a measurable contribution of stress to  $d\omega/dT$ , a positive for ZB and negative for WZ phonons, due to differences in their thermal expansions.

This can be explained using relative thermal expansion coefficients of ZB and WZ phases. Considering the heterostructure and knowing thermal expansion of ZB phases, we calculate effective thermal expansion of WZ, which increases from base to tip. This is consistent with increase in lattice constant of WZ i.e. relaxation of compressive stress from base to tip. Further, effective thermal expansion coefficient of WZ InAs in the presence of ZB phase is calculated to vary in the range  $10 - 19 \times 10^{-6} / \text{K}$  from base to tip of a MNW at  $\sim 80 \text{ K}$ , which is not possible to determine otherwise.

For fine tuning of semiconductor NW properties, modification of surface and dimensions using laser irradiation is being suggested as one of the fast and easy to use methods. The role of temperature simulation is investigated for predicting surface modification of InAs nanowire (NW) using laser irradiation. The surface modification is monitored by Raman spectroscopy. We first establish correlation between simulated temperatures at the surface of a InAs nanowire (NW) with time evolution of Raman spectra, on laser irradiation. Transient thermal simulations are performed with ANSYS software using finite element method, considering actual 3D geometry of the irradiation setup. In the systematic study of laser irradiation (laser power densities  $\sim 30\text{-}636 \text{ kW/cm}^2$ ) over time duration of  $\sim 8$  minutes, the simulated temperature is found to corroborate well with the corresponding oxidation processes e.g. weak (WP), intermediate (IP) and strong (SP), occurring on the surface of InAs nanowire under various laser irradiation conditions. The oxidation processes are identified as weak reactions WP1, WP2, WP3, intermediate temperature reactions IP1, IP2 and higher temperature strong reactions SP1, SP2, SP3 & SP4, using time evolution of Raman spectra for various LPDs. Salient features of the study are,

- 5) Both Raman spectra and simulated temperature reach steady state at  $\sim 8$  minutes.
- 6) The only variable parameter used is number of contacts to match the data at 200s for 200  $\text{kW/cm}^2$  LPD. All other data at all points i.e. upto 500s and for several LPDs from 30 to

636 kW/cm<sup>2</sup>, shows good corroboration of Raman spectra and temperature up to ~ 1150 K.

- 7) The higher simulated temperature (~1200-1700 K) does not show any damage, although, melting point of InAs ~1215 K. The reason is understood to be that these higher temperatures are actually not reached, due to scattering of light occurring from large quantities of As<sub>2</sub>O<sub>3</sub> & As formed at the temperature >1150 K. In addition, evaporation of As is expected to further lower the temperature in this situation. Raman spectra observed for higher simulated temperatures are also commensurate with this understanding.
- 8) The applicability of this methodology is further confirmed, using randomly chosen NWs grown on the same substrate along with NWs (grown elsewhere: diameter ~ 200 nm) isolated and transferred on other Si substrate, both irradiated at randomly chosen LPDs.

The predictability of the methodology was then investigated by applying it to random conditions of NW like diameter, aspect ratio and laser power density etc. for i) NWs found in the same sample and ii) InAs NWs grown elsewhere and transferred on other Si substrate.

The study thus establishes predictability of various oxidation processes for given NW dimensions, laser power density and irradiation time, thereby ascertaining importance and applicability of the temperature simulation in controlling surface modification of randomly chosen InAs NWs using laser irradiation. This methodology can be used to control the oxidation process as desired for using NWs in device technology, where oxidation is used for creating an insulating layer.

Two nearly perpendicular orientations of InAs NWs are found to show very different unpolarized Raman spectra for similar NWs irradiated with similar laser power density. This is investigated using specially designed one step and two step polarization dependent Raman spectroscopy experiments. The study shows the difference in Raman spectra is observed for different NW orientation due to differences in Raman selection rules for crystalline oxides

generated and not due to any difference in coupling of laser light with NW. This suggests that an unpolarized Raman spectra from NWs can lead to incorrect interpretation regarding oxidation processes, if not looked into carefully. Further, at higher simulated temperatures ( $\sim 1600$  K), TO\* [combination of TO: dominant zinc blende: ZB and  $E_{2h}$ : wurtzite: WZ phonons] phonon blueshifts and FWHM reduces along with reappearance of TO\* and LO like modes with higher strength. This is investigated using specially designed heating cooling experiment. The study shows that both  $InAsO_4$ ,  $As_2O_3$  continue to disintegrate after laser irradiation is stopped, giving rise to different allotropes of elemental As, depending on the highest temperature ( $> 950/1300$  K) reached before cooling. The higher simulated temperatures ( $> 1200$ K), although, are not actually reached, the different ranges noted, help us separate the effects observed and is found to be very useful in the laser irradiation studies. The formation of specific allotropes of elemental As i.e. gray-As (rhombohedral) and black-As (orthorhombic) during cooling after an intermediate and strong oxidation processes occurs at low ( $\sim 700-950$  K) and high ( $> 1000-1300$  K) simulated temperatures, respectively. Both have high electrical conductivity due to layered structure and control over growth of only few layers using laser irradiation envisages properties similar to graphene. Further, conversion of WZ phase to ZB phase at higher simulated temperature is also considered responsible for reappearance of TO phonon.

Polarized Raman spectroscopy (PRS) indicates that polytypism (WZ and ZB) is present in the InAs NW (dia  $\sim 650$  nm). However, PRS gives very poor S/N ratio for smaller diameters. Resonance Raman spectroscopy is investigated as an alternate, using Ar ion laser excitations at 514.5, 488, 476.5, 458 nm. Wavelength dependent Raman spectroscopy of mixed phase, dominant WZ and ZB phase NWs could be well separated on the basis of WZ and ZB phonon resonance enhancement of  $E_{2h}$  (WZ) and TO (ZB) phonons. Thus, resonance Raman spectroscopy is established as an useful technique to obtain information about

polytypism. It can be successfully used for smaller isolated nanostructures, where it may be difficult to use more standard techniques like XRD/polarized Raman spectroscopy. Resonance Raman spectroscopy is further used to study conversion of WZ to ZB phase in InAs NW on laser irradiation at higher simulated temperature  $> 1300$  K. Independently, conversion of WZ phase of InAs to ZB phase on thermal annealing is investigated with SAED and HRTEM using in situ thermal annealing in TEM.

Presence of mixed phases in large diameter uniform and tapered MNW/NWs and their variation along the length of MNW is established using spatially resolved Raman spectroscopy. This is found to lead to strained zincblende and wurtzite phases, present in these InAs MNW/NWs. The study further, brings out potential of Raman spectroscopy as online monitoring technique for semi metallic to insulator to metallic surface modification of InAs NWs using laser irradiation. The control gained using laser irradiation with the help of simulated temperature and understanding developed of various processes on laser irradiation can lead to novel device applications. Resonance Raman spectroscopy is established as an alternate technique to study polytypism for smaller nanostructures. Resonance Raman spectroscopy and transmission electron microscopy are used study conversion of WZ phase to ZB phase in InAs NW on laser irradiation and thermal annealing, respectively.

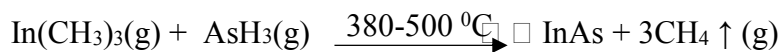
The study paves the way to study polytypism in individual semiconductor NWs along the length and different oxidation processes leading to surface modification, on laser irradiation using Raman spectroscopy.

**Future scope:** Future plan of work includes, study of the WZ to ZB conversion process with thermal annealing using Raman spectroscopy. Further, it is planned to extend simulation of temperature for different geometry of NWs and spheres on laser irradiation and study cooling. It may be interesting to study larger band gap semiconductor NWs with Raman spectroscopy.

# Annexure

### Growth:

InAs nanowires (NWs) are grown by metal organic chemical vapor deposition (MOCVD) [142, 143]. In the MOCVD growth method, the metal organic precursors of group III elements are used, in which metal atoms are bonded with organic radicles. These precursor is used to get high flux of the metal element at low temperature. Similarly, for group V elements, hydrides such arsenic and phosphine gas are used. In the reactor chamber, all reactants are used in the vapor phase i.e. no liquid or solid are present in this method. In the MOCVD growth metal elements are obtained by the pyrolysis process. The growth process takes place in two steps, i) metal organic compound and gas are entered into the reactor followed by homogeneous gas phase mixes and ii) heterogeneous growth takes place when they are reached near or on the heated substrate. The resulting layer that are deposited can be either epitaxial and polycrystalline. An example of a MOCVD growth process for III-V layer can be represented by the equation described below.



Minimization of the homogeneous reaction and maximization of the heterogeneous reaction is achieved by controlling the process parameters. The process parameters depend on various parameters like the geometry of reactor chamber, dimensions, growth temperatures and temperature of the chamber wall, V/III ratio, and pressure/concentration of the elements. These factors control the thermodynamics and kinetics required for the layer growth. The MOCVD process is mainly endothermic and therefore, cold-wall reactor system is used for cooling. The infrared lamp heater gives the thermal energy to the complete growth process. For the growth of InAs NWs tri methyl Indium ((CH<sub>3</sub>)<sub>3</sub>In) and Arsine (AsH<sub>3</sub>) gases are used as source material using low pressure MOVPE machine. The growth temperature zone depends on two factors i.e. (i) decomposition temperature of source material ((CH<sub>3</sub>)<sub>3</sub>In and

AsH<sub>3</sub>) and (ii) surface diffusion of group-III atoms, i.e. indium and incorporation of the adatoms into the NW crystal lattice. The parameters that are used for the growth of InAs NWs are described below briefly.

Set 1( sample 1): The InAs NWs are grown on substrate Si (001) with V/III ratio ~ 250 and growth temperature ~ 425°C by using self-catalyst for a few seconds. The crystal structure is observed as a mixed structure (wurtzite: WZ and zinc blende: ZB) for this sample using spatially resolved polarized Raman spectroscopy. The diameter and length of NWs are observed in the range of ~ 600 nm - 2.5 μm and 10-80 μm, respectively. These samples are grown in semiconductor materials laboratory, materials science division RRCAT, Indore; by our collaborators [142].

Set 2 (samples 2-4): The InAs NWs are grown on substrate Si (111) using Au-catalyst with V/III ratio ~ 40, 30, 100 and for samples 2, 3, 4; respectively. The growth temperature and time duration are kept same for all samples i.e. ~ 420°C and 10 min, respectively. Mixed structure (WZ and ZB), WZ and ZB phases are observed for InAs nanowire samples 2, 3, and 4; respectively. Spatially resolved polarized Raman spectroscopy was used to check the phases observed on InAs nanowires isolated from these samples and dispersed on other Si substrate. The diameter and length of these nanowires are observed in the range of ~ 50 nm - 1 μm and ~ 2 - 20 μm, respectively. These samples are grown in DCMP, MS, TIFR, Mumbai; by our collaborators [143].

# BIBLIOGRAPHY

- [1] L. Filipponi and D. Sutherland “Introduction to Nanoscience and Nanotechnologies” Interdisciplinary Nanoscience Center, Aarhus University, Denmark, pp 2 (2011).
- [2] C. Q. Chen, Y. Shi, Y. S. Zhang, J. Zhu, Y. J. Yan, Phys. Rev. Lett. **96**, 075505 (2006).
- [3] R. H. Baughman, C. Cui, A. A. Zakhidov, Z. Iqbal, J. N. Barisci, G. M. Spinks, G. G. Wallace, A. Mazzoldi, D. D. Rossi, A. G. Rinzler, O. Jaschinski, S. Roth, M. Kertesz, Science **284**, 1340 (1999).
- [4] C. Lee, X. Wei, J.W. Kysar, J. Hone, Science **321**, 385 (2008).
- [5] L. T. Ngo, D. Almecija, J. E. Sader, B. Daly, N. Petkov, J. D. Holmes, D. Erts, J. J. Boland, Nano Lett. **6**, 2964 (2006).
- [6] B. Wu, A. Heidelberg, J. J. Boland, Nat. Mater. **4**, 525 (2005).
- [7] C. Q. Chen, Y. Shi, Y. S. Zhang, J. Zhu, Y. J. Yan, Phys. Rev. Lett. **96**, 075505 (2006).
- [8] Y. Tian, M. R. Sakr, J. M. Kinder, D. Liang, M. J. Mac, Donald ,Richard L.J. Qiu, Hong-Jun Gao, Xuan P.A. Gao, Nano Lett. **12**, 6492 (2012).
- [9] B. Poudel et al., Science **320**, 634 (2008).
- [10] D. Li, Y. Wu, P. Kim, L. Shi, P. Yang, A. Majumdar, Appl. Phys. Lett. **83**, 2934 (2003).
- [11] L. Shi, Q. Hao, C. H. Yu, N. Mingo, X. Kong, Z. L. Wang, Appl. Phys. Lett., **84**, 2638 (2004).
- [12] J. H. Zhou, Q. Jin, J. H. Seol, X. Li, L. Shi, Appl. Phys. Lett., **87**, 133109 (2005).
- [13] Y. Cui, X. Duan, J. Hu and C. M. Lieber, J. Phys. Chem. B **104**, 5213 (2000).
- [14] J. Sarkar, G. G. Khan and A. Basumallick, Bull. Mater. Sci. **30**, 271 (2007).
- [15] F. Favier, E. C. Walter, M. P. Zach, T. Benter and R. M. Penner, Science **293**, 2227 (2001).
- [16] G. Busch Eur. J. Phys. **10**, 254 (1989).
- [17] F. Laeri, F. Schüth, U. Simon, and M. Wark, “Host-Guest-Systems Based on Nanoporous Crystals” Weinheim: Wiley, pp.435 (2003).
- [18] M. Faraday, “Experimental Researches in Electricity”, Bernard Quaritch, London vol. I, pp. 122 (1839).

- [19] T. K. Sarkar, R. Mailloux, A. A. Oliner, M. Salazar-Palma, and D. L. Sengupta, “The History of Wireless” Hoboken: Wiley (2006).
- [20] J. Orton, “Semiconductors and the Information Revolution: Magic Crystals that Made IT Happen” Amsterdam: Academic Press/Elsevier, pp. 35 (2009).
- [21] W. Mönch “Semiconductor Surfaces and Interfaces” Berlin-Heidelberg: Springer (2001).
- [22] Z. A. Smith and K. D. Taylor “Renewable and Alternative Energy Sources: A Reference Handbook” Santa Barbara: ABC-CLIO Inc, pp. 157 (2008).
- [23] M. Grundman “The Physics of Semiconductors” Berlin-Heidelberg: Springer (2006).
- [24] X. Fang, T. Zhai, U. K. Gautam, L. L. L. Wua, Y. Bando, D. Golberg, *Prog. Mater. Sci.* **56**, 175 (2011).
- [25] L. Łukasiak and A. Jakubowski, *Journal of telecommunication and information technology*, 3 (2010).
- [26] A. I. Khan “Pre-1900 semiconductor research and semiconductor device applications,” in *Proc. IEEE Conf. History Electron*, pp.1 (2004).
- [27] D. Chapin, C. Fuller, and G. Pearson, *J. Appl. Phys.* **25**, 676 (1954).
- [28] J. M. Nassar, A. M. Hussain, *Proceedings of the 14th IEEE International Conference on Nanotechnology* (2014).
- [29] G. C. Kumarage, R. P. Wijesundera, V. A. Seneviratne, C. P. Jayalath and B. S. Dassanayake, *Semicond. Sci. Technol.* **32**, 045014 (2017) and references there in.
- [30] J. M. Woodball, and H. J. Hovel, *Appl. Phys. Lett.* **30**, 492 (1977).
- [31] O. Oda “Compound semiconductor bulk materials and characterizations” World scientific publishing, **2** (2007).
- [32] J. Wang and M. Isshiki “Wide-bandgap II–VI semiconductors: growth and properties,” in *Springer Handbook of Electronic and Photonic Materials*, S. Kasap and P. Capper, Springer US: pp. 325 (2006).
- [33] B. H. Kim, M. J. Hackett, J. Park, and T. Hyeon, *Chem. Mater.* **26**, 59 (2014).
- [34] M.-C. Daniel and D. Astruc, *Chem. Rev.* **104**, 293 (2004).
- [35] A. Alagarasi, “Chapter-Introduction to nanomaterials” (2011).
- [36] Peter J. F. Harris “Carbon Nanotube Science: Synthesis, Properties and Applications” Cambridge University Press (2009).
- [37] S. Iijima, **354**, 56 (1991).

- [38] S. Iijima, and T. Ichihashi, **363**, 603 (1993).
- [39] S. Mouras, A. Hamm, D. Djurado and J. C. Cousseins, *Revue de Chimie Minerale*, **24**, 572, (1987).
- [40] M. Sharon, M. Sharon, H. Shinohara and A. Tiwari, “Graphene: An Introduction to the Fundamentals and Industrial Applications”, Wiley: USA (2015).
- [41] R. Rossetti and L. Brus, *J. Phys. Chem.* **86**, 4470 (1982).
- [42] A.P. Alivisatos, *J. Phys. Chem.* **100**, 13226 (1996).
- [43] E. G. Barbagioanni, D. J. Lockwood, P. J. Simpson, and L. V. Goncharova, *J. Appl. Phys.* **111**, 034307 (2012).
- [44] Y. Li, X.-Y. Yang, Y. Feng, Z.-Y. Yuan and B.-L. Su, *Solid State and Materials Sciences*, **37**, 1 (2012).
- [45] G. Chen, J. Wu, Q. Lu, H. R. Gutierrez, Q. Xiong, M. E. Pellen, J. S. Petko, D. H. Werner, and P. C. Eklund, *Nano Lett.* **8**, 1341, (2008).
- [46] H. A. Chaliyawala, Z. Purohit, S. Khanna, A. Ray, R. K. Pati, and I. Mukhopadhyay, *J. Appl. Phys.*, **123**, 213104 (2018).
- [47] E. Bermúdez-Ureña et al. *Nano Lett.* **17**, 747 (2017).
- [48] A. M. Smith and S. Nie, *Acc Chem Res.* **43**, 190 (2010).
- [49] M. Eslamian, *Coatings* **4**, 60 (2014).
- [50] M. C. Rao and M. S. Shekhawat, **22**, 576 (2013).
- [51] J. N. Tiwari, R. N. Tiwari, K. S. Kim, *Prog. Mater. Sci.* **57**, 724 (2012).
- [52] F. F. Vidor, T. Meyers and U. Hilleringmann, *Electronics*, **4**, 480 (2015).
- [53] P. J. Burke “Nanotubes and nanowires”, University of California, Irvine, USA, **44** (2007).
- [54] P. S. Alexopoulos and T. C. O'Sullivan, *Annu. Rev. Mater. Sci.* **20**, 391 (1990).
- [55] I. Khan, K. Saeed, I. Khan, *Arab. J. Chem.* <https://doi.org/10.1016/j.arabjc.2017.05.011> (2017).
- [56] E. C. Dreaden, A. M. Alkilany, X. Huang, C. J. Murphy, M. A. El-Sayed, *Chem. Soc. Rev.* **41**, 2740 (2012).
- [57] J. E. Lee, N. Lee, T. Kim, , J. Kim, T. Hyeon, *Acc. Chem. Res.* **44**, 893 (2011).

- [58] M. Ganesh, P. Hemalatha, M. M. Peng, H.T. Jang, Arab. J. Chem. **10**, S1501 (2017).
- [59] I. Rawal, A. Kaur, Actuators A Phys. **203**, 92 (2013).
- [60] M. Mansha, A. Qurashi, N. Ullah, F.O. Bakare, I. Khan, Z.H.Yamani, Ceram. Int. **42**, 11490 (2016).
- [61] H. Ullah, I. Khan, Z. H. Yamani, A. Qurashi, A, Ultrason. Sonochem. **34**, **484** (2016).
- [62] H. Barrak, T. Saied, P. Chevallier,, G. Laroche, A. M'nif, A.H. Hamzaoui, Arab.J. Chem. <http://dx.doi.org/10.1016/j.arabjc.2016.04.019> (2016).
- [63] M. Shaalan, M. Saleh, M. El-Mahdy, M. El-Matbouli, Nanomed. Nanotechnol. Biol. Med. **12**, 701 (2016).
- [64] S. Thomas, B.S.P. Harshita, P. Mishra, S. Talegaonkar, Curr. Pharm. Des. **21**, 6165 (2015).
- [65] S. Sun, Science **80**, 1989 (2000).
- [66] T. Hisatomi, J. Kubota, K. Domen, Chem. Soc. Rev. **43**, 7520 (2014).
- [67] Z. L. Wang, Adv. Mater. **15**, 432 (2003).
- [68] Iijima S. Nature **354**, 56 (1991).
- [69] V. N. T. Satyanarayana, S. Kuchibhatla, A.S. Karakoti, D. Bera, S. Seal, Prog. Mater. Sci. **52**, 699 (2007).
- [70] R. R. LaPierre et al., Phys. Status Solidi RRL **7**, 815 (2013).
- [71] R. R. LaPierre, M. Robson, K. M. Azizur-Rahman and P. Kuyanov, J. Phys. D: Appl. Phys. **50**, 123001 (2017).
- [72] C. Couteau, A. Larrue, C. Wilhelm, and C. Soci, Nanophotonics **4**, 90 (2015).
- [73] H. Chen, L. Chen, J. Zhao, R. Yang, IEEE Sensors Journal **13**, 949 (2013).
- [74] M. H. Huang et al. Science **292**, 1897 (2001).
- [75] J. C. Johnson, H. J. Choi, K. P. Knutsen, R. D. Schaller, P. Yang and R. J. Saykally Nature Mater **1**, 106 (2002).
- [76] Y. Li, F. Qian, J. Xiang, and C. M. Lieber, Material Today, **9**, 18 (2006).
- [77] S. W. Chung, J. Y. Yu and J. R. Heath, Appl. Phys. Lett. **76**, 2068 (2000).
- [78] Y. Cui, X Duan, J. Hu and C. M Lieber, J. Phys. Chem. B **104**, 5213 (2000).
- [79] Y. Huang, X. Duan, Y. Cui and C. M Lieber, Nano. Lett. **2**, 101 (2002).

- [80] M. S. Gudiksen, L. J. Lauhon, J. Wang, D. C. Smith and C. M. Lieber, *Nature* **415**, 617 (2002).
- [81] M. H. Huang et al., *Science* **292**, 1897 (2001).
- [82] J. R. Kim, H. Oh, H. M. So, J. J. Kim, J. Kim, C. J. Lee and S. C. Lyu, *Nanotechnology* **13**, 701 (2002).
- [83] X. Duan, Y. Huang and C. M. Lieber, *Nano. Lett.* **2** 487 (2002).
- [84] M. H. Huang. *Adv. Mater.* **13** 113 (2001).
- [85] X. Duan, Y. Huang, Y. Cui, J. Wang and C. M. Lieber, *Nature* **409**, 66 (2001).
- [86] V. Derycke, R. Martel, J. Appenzeller and P. Avouris, *Nano Letts* **1**, 453 (2001).
- [87] K. Nielsch, R. B. Wehrspohn, S. F. Fischer, H. Kronmiller, J. Kirsehner and U. Gosele *Mater. Res. Soc. Symp. Proc.* **9** 636 (2001).
- [88] S. Sun, C. B. Murray, D. Weller, L. Folks, and A. Moser, *Science* **287**, 1989 (2000).
- [89] T. M. Whitney, J. S. Jiang, P. C. Searson, and C. L. Chien, *Science* **261**, 1318 (1993).
- [90] D. AlMawlawi, N. Coombs, and M. Moskovits, *J. Appl. Phys.* **70**, 4421(1991).
- [91] L. D. Hicks and M. S. Dresselhaus, *Phys. Rev. B* **47**, 16631 (1993).
- [92] J. Heremans, C. M. Thrush, Z. Zhang, X. Sun, M. S. Dresselhaus, J. Y. Ying and D. T. Morelli, *Phys. Rev. B* **58**, 10091 (1998).
- [93] R John Bosco Balaguru and BG Jeyaprakash. Quantum size effect, electrical conductivity and Quantum transport. NPTEL, India, 2013
- [94] A. Bid, A. Bora, and A. K. Raychaudhuri, *Phys. Rev. B* **74**, 035426 (2006).
- [95] S. Maitrejean, R. Gers, T. Mourier, A. Toffoli, and G. Passemar, *Microelectron. Eng.* **83**, 2396 (2006).
- [96] W. Steinhogel, G. Schindler, G. Steinlesberger, and M. Engelhardt, *Phys. Rev. B* **66**, 075414 (2002).
- [97] G. Schindler, G. Steinlesberger, M. Engelhardt, and W. Steinhogel, *Solid- State Electron* **47**, 1233 (2003).
- [98] W. Steinhogel, G. Schindler, G. Steinlesberger, M. Traving, and M. Engelhardt, *International Conference on Simulation of Semiconductor Processes and Devices, SISPAD* unpublished pp. 27 (2003).
- [99] H. Li and F. Sun, <http://dx.doi.org/10.5772/52592>.

- [100] N. Anttu, “Nanophotonics in absorbing III-V nanowire arrays” Thesis (2013).
- [101] H. J. Joyce, *Progress in Quantum Electronics* **35**, 23 (2011).
- [102] E. D. Minot et al., *Nano Lett.* **7**, 367 (2007).
- [103] M. H. Huang, S. Mao, H. Feick, H. Yan, Y. Wu, H. Kind, E. Weber, R. Russo, and P. Yang *Science* **292**, 1897 (2001).
- [104] Y. Cui, Q. Wei, H. Park, and C. M. Lieber, *Science*, **293**, 1289 (2001).
- [105] J.-I. Hahm and C. M. Lieber, *Nano Lett.* **4**, 51, 2004.
- [106] M. Fang, N. Han, F. Wang, Z.-X. Yang, S. P. Yip, G. Dong, Jared J. Hou, Y. Chueh and J. C. Ho, *J. Nanomater.* **2014**, 702859 (2014).
- [107] R. Agarwal, C. J. Barrelet, and C. M. Lieber, *Nano Lett.* **5**, 917 (2005).
- [108] A. H. Chin, S. Vaddiraju, A. V. Maslov, C. Z. Ning, M. K. Sunkara, and M. Meyyappan *Appl. Phys. Lett.* **88**, 163115 (2006).
- [109] H. T. Ng, J. Han, T. Yamada, P. Nguyen, Y. P. Chen, and M. Meyyappan, *Nano Lett.* **4**, 1247 (2004).
- [110] T. Bryllert, L.-E. Wernersson, T. Lowgren, and L. Samuelson, *Nanotechnology* **17**, S227, (2006).
- [111] E. Lind, A. I. Persson, L. Samuelson, and L.-E. Wernersson, *Nano Lett.*, **6**, 1842 (2006).
- [112] J. Wang, M. S. Gudiksen, X. Duan, Y. Cui, and C. M. Lieber, *Science*, **293**, 1455 (2001).
- [113] Y. Gu, E.-S. Kwak, J. L. Lensch, J. E. Allen, T.W. Odom, and L. J. Lauhon, *Appl. Phys. Lett.* **87**, 043111 (2005).
- [114] H. Pettersson, J. Trägårdh, A. I. Persson, L. Landin, D. Hessman, and L. Samuelson, *Nano Lett.* **6**, 229 (2006).
- [115] C. J. Barrelet, A. B. Greytak, and C. M. Lieber, *Nano Lett.* **4**, 1981 (2004).
- [116] F. Qian, S. Gradecak, Y. Li, C.-Y. Wen, and C. Lieber, *Nano Lett.* **5**, 2287 (2005).
- [117] F. Qian, Y. Li, S. Gradecak, H.-G. Park, Y. Dong, Y. Ding, Z. L. Wang, and C. M. Lieber, *Nature Mater.* **7**, 701 (2008).
- [118] B. Hua, J. Motohisa, Y. Kobayashi, S. Hara, and T. Fukui *Nano Lett.* **9**, 112 (2009).
- [119] M. T. Borgström, V. Zwiller, E. Muller, and A. Imamoglu, *Nano Lett.* **5**, 1439 (2005).

- [120] M. T. Björk, B. J. Ohlsson, C. Thelander, A. I. Persson, K. Deppert, L. R. Wallenberg, and L. Samuelson, *Appl. Phys. Lett.* **81**, 4458 (2002).
- [121] C. Thelander, T. Martensson, M. T. Björk, B. J. Ohlsson, M. W. Larsson, L. R. Wallenberg, and L. Samuelson, *Appl. Phys. Lett.* **83**, 2052 (2003).
- [122] M. T. Björk, C. Thelander, A. E. Hansen, L. E. Jensen, M. W. Larsson, L. R. Wallenberg, and L. Samuelson, *Nano Lett.*, **4**, 1621 (2004).
- [123] C. Thelander, H. A. Nilsson, L. E. Jensen and L. Samuelson, *Nano Lett.* **5**, 635 (2005).
- [124] H. A. Nilsson, T. Duty, S. Abay, C. Wilson, J. B. Wagner, C. Thelander, P. Delsing, and L. Samuelson, *Nano Lett.* **8**, 872 (2008).
- [125] H. A. Nilsson, C. Thelander, L. E. Fröberg, J. B. Wagner, and L. Samuelson, *Appl. Phys. Lett.* **89**, 163101 (2006).
- [126] C. Thelander, T. Martensson, M. T. Björk, B. J. Ohlsson, M. W. Larsson, L. R. Wallenberg, and L. Samuelson, *Appl. Phys. Lett.* **83**, 2052 (2003).
- [127] M. T. Björk, C. Thelander, A. E. Hansen, L. E. Jensen, M. W. Larsson, L. R. Wallenberg, and L. Samuelson, *Nano Lett.* **4**, 1621 (2004).
- [128] C. Thelander, H. A. Nilsson, L. E. Jensen, and L. Samuelson, *Nano Lett.* **5**, 635 (2005).
- [130] H. A. Nilsson, C. Thelander, L. E. Fröberg, J. B. Wagner, and L. Samuelson, *Appl. Phys. Lett.* **89**, 163101 (2006).
- [131] X. F. Duan, Y. Huang, R. Agarwal, and C. M. Lieber, *Nature* **421**, 241 (2003).
- [132] E. C. Heeres, E. P. A. M. Bakkers, A. L. Roest, M. Kaiser, T. H. Oosterkamp, and N. de Jonge, *Nano Lett.* **7**, 536 (2007).
- [133] M. T. Bjork, O. Hayden, H. Schmid, H. Riel, and W. Riess, *Appl. Phys. Lett.*, **90**, 142110, (2007).
- [134] C. J. Barrelet, J. Bao, M. Lončar, H.-G. Park, F. Capasso, and C. M. Lieber, *Nano Lett.*, **6**, 11 (2006).
- [135] H.-G. Park, C. J. Barrelet, Y. Wu, B. Tian, F. Qian, and C. M. Lieber, *Nature Photon.*, **2**, 622 (2008).
- [136] N. P. Dasgupta, J. Sun, C. Liu, S. Brittman, S. C. Andrews, J. Lim, H. Gao, R. Yan, and P. Yang. *Advanced Materials*, **26**, 2137 (2014).
- [137] S. M. Sze and K. K. Ng “Physics of semiconductor devices”. Wiley- Interscience, (2007).

- [138] S. Estévez Hernández, M. Akabori, K. Sladek, Ch. Volk, S. Alagha, H. Hardtdegen, M. G. Pala, N. Demarina, D. Grützmacher, and Th. Schäpers. *Physical Review B*, **82**, 235303 (2010).
- [139] C. Thelander. *Solid State Communications*, **131**, 573 (2004).
- [140] Lysov, A., Gutsche, C., Regolin, I., Prost, W., Tegude, F.-J. Privat communication. 2008.
- [141] S. Adachi. *J. Appl. Phys.* **66**, 6030 (1989).
- [142] S. Pal, S D Singh, V. K. Dixit, A. Ingale, P. Tiwari, H. Srivastava, R. Kumar, C. Mukharjee, P. Prakash and S. M. Oak, *Semicond. Sci. Technol.* **28**, 015025 (2013).
- [143] S. Dhara, H. S. Solanki, V. Singh, A. Narayanan, P. Chaudhari, M. Gokhale, A. Bhattacharya and M. M. Deshmukh, *Phys. Rev. B* **79**, 121311 (2009).
- [144] P Brüesch, “Phonons: Theory and Experiments II, Experiments and Interpretation of Experimental Results” Springer-Verlag Berlin Heidelberg (1982).
- [145] W. Hayes and R. Loudon, “Scattering of Light by Crystals” Wiley-Inter science Publication (1930).
- [146] Y. Yu Peter and M. Cardona, “Fundamentals of Semiconductors: Physics and Materials Properties”, 4th edition (2010).
- [147] E. Smith and G. Dent, “Modern Raman Spectroscopy– A Practical Approach” John Wiley and Sons Ltd. (2005).
- [148] C. B. Juang, L. Finzi, and C. J. Bustamante, *Rev. Sci. Instrum.* **59**, 2399 (1988).
- [149] P. J. Goodhew, “Electron microscopy and analysis” John Humphreys and Richard Beanland. 3rd. London: Taylor & Francis (2000).
- [150] P. Buseck, J. Cowley, L. Eyring (Eds) “High Resolution Transmission Electron Microscopy and Associated Techniques” Oxford University Press, New York (1988).
- [151] A. J. Schwartz, M. Kumar, B.L. Adams (Eds.) “Electron Backscatter Diffraction in Materials Science” Kluwer Acad/Plenum Publishers, New York, (2000).
- [152] M. Paladugu et al, *Appl. Phys. Lett.* **91**, 133115 (2007).
- [153] P. Krogstrup, J. Yamasaki, C. B. Sørensen, E. Johnson, J. B. Wagner, M. Aagesen, N. Tanaka, and J. Nygård, *Nano Lett.* **9**, 3689 (2009).
- [154] J. Kim, J.-H. Bahk, J. Hwang, H. Kim, H. Park, and W. Kim, *Phys. Status Solidi RRL* **7**, 767 (2013).
- [155] S. Yazji, I. Zardo, M. Soini, P. Postorino, F. A. I. Morral and G. Abstreiter G, *Nanotechnology* **22**, 325701 (2011) and references therein.

- [156] Y. Jung, S. W. Nam and R. Agarwal R, Nano Lett. **11** 1364 (2011).
- [157] R. Caries, N. Saint-Cricq, J. B. Renucci, M. A. Renucci, and A. Zwick, Phys. Rev. B, **22**, 4804 (1980).
- [158] R. Moriya, H. Kobayashi, K. Shibata, S. Masubuchi, K. Hirakawa, S. Ishida, Y. Arakawa and T. Machida, Appl. Phys. Express **3**, 035001 (2010).
- [159] J. He, P. Chen, W. Lu, N. Dai and D.-M. Zhu, J. Appl. Phys. **111**, 094316 (2012).
- [160] X. X. Xu, K. H. Yu, W. Wei, B. Peng, S. H. Huang, Z. H. Chen and X. S. Shen, Appl. Phys. Lett. **89**, 253117 (2006).
- [161] S. Buchner and E. Burstein, Phys. Rev. Lett. **33**, 908 (1974).
- [162] H. Y. Deng, J. H. Guo, Y. Zhang, R. Cong, G. J. Hu, G. J. Yu, and N. Dai, Appl. Surf. Sci. **288**, 40 (2014).
- [163] G. P. Schwartz, J. E. Griffiths and G. J. Gualtieri, Thin Solid Films **94**, 213 (1982).
- [164] G Hollinger, R Skheyta-Kabbani and M. Gendry, Phys. Rev. B **49**, 11159 (1994).
- [165] G. P. Schwartz, Thin Solid Films **103**, 3 (1983).
- [166] E. J. Flynn, S. A. Solin and G. N. Papatheodorou, Phys. Rev. B **13**, 175 (1976).
- [167] S. Bahfenne, L. Rintoul, J. Langhol and R. L. Frost, J. Raman Spectrosc. **42**, 2119 (2011).
- [168] M. A. Gomez, J.-F. Le Berre, H. Assaoudib and G. P. Demopoulosa, J. Raman Spectrosc. **42**, 62 (2011).
- [169] I. Zardo, S. Conesa-Boj, F. Peiro, J. R. Morante, J. Arbiol, E. Uccelli, G. Abstreiter, A. Fontcuberta i Morral, Phys. Rev. B **80**, 245324 (2009).
- [170] N. G. Hörmann, I. Zardo, S. Hertenberger, S. Funk, S. Bolte, M. Döblinger, G. Koblmüller, G. Abstreiter, Phys. Rev. B **84**, 155301 (2011).
- [171] I. Zardo, S. Yazji, N. Hörmann, S. Hertenberger, S. Funk, S. Mangialardo, S. Morkötter, G. Koblmüller, P. Postorino, G. Abstreiter, Nano Lett. **13**, 3011 (2013).
- [172] J. Johansson, K. A. Dick, P. Caroff, M. E. Messing, J. Bolinsson, K. Deppert, L. Samuelson, J. Phys. Chem. C **114**, 3837 (2010).
- [173] V. Pankoke, P. Kratzer, S. Sakong, Phys. Rev. B **84**, 075455 (2011).
- [174] K. A. Dick, P. Caroff, J. Bolinsson, M. E. Messing, J. Johansson, K. Deppert, L. Reine Wallenberg, L. Samuelson, Semicond. Sci. Technol. **25**, 024009 (2010).

- [175] K. A. Dick, J. Bolinsson, M. E. Messing, S. Lehmann, J. Johansson, P. Caroff, J. Vac. Sci. Technol. B **29**, 04D103 (2011).
- [176] D. Kriegner, C. Panse, B. Mandl, K. A. Dick, M. Keplinger, J. M. Persson, P. Caroff, D. Ercolani, L. Sorba, F. Bechstedt, J. Stangl, G. Bauer, Nano Lett. **11**, 1483 (2011).
- [177] H. Zhou, M. Pozuelo, R. F. Hicks, S. Kodambaka, J. Cryst. Growth **319**, 25 (2011).
- [178] M. Pozuelo, S. V. Prikhodko, R. Grantab, H. Zhou, L. Gao, S. D. Sitzman, V. Gambin, V. B. Shenoy, R. F. Hicks, S. Kodambaka, J. Cryst. Growth **312**, 2305 (2010).
- [179] M. Pozuelo, H. Zhou, S. Lin, S. A. Lipman, M. S. Goorsky, R. F. Hicks, S. Kodambaka, J. Cryst. Growth **329**, 6 (2011).
- [180] Z. Wang et al., Nano Lett. **13**, 5063 (2013).
- [181] A. Belabbes, C. Panse, J. Furthmüller, F. Bechstedt, Phys. Rev. B **86**, 075208 (2012).
- [182] H. Shtrikman, R. Popovitz-Biro, A. Kretinin, L. Houben, M. Heiblum, M. Bukała, M. Galicka, R. Buczko, P. Kacman, Nano Lett. **9**, 1506 (2009).
- [183] J. Wang, F. Demangeot, R. Péchou, C. Bayon, A. Mlayah, B. Daudin, J. Appl. Phys. **114**, 223506 (2013).
- [184] J. Wang, C. Bayon, F. Demangeot, R. Pechou, A. Mlayah, A. Cros, B. Daudin, SPIE Proceedings, 8625 (2013).
- [185] Q. Xiong, J. Wang, O. Reese, L. C. Lew Yan Voon, P. C. Eklund, Nano Lett. **4**, 1991 (2004).
- [186] N. Begum, M. Piccin, F. Jabeen, G. Bais, S. Rubini, F. Martelli, A. S. Bhatti, J. Appl. Phys. **104**, 104311 (2008).
- [187] J. H. Park, PhD. thesis, University of California, LA USA, (2013).
- [188] S. Pal, R. Aggarwal, V. K. Gupta, A. Ingale, Appl. Phys. Lett. **105**, 012110 (2014).
- [189] R. Caries, N. Saint-Cricq, J. B. Renucci, M. A. Renucci, A. Zwick, Phys. Rev. B **22**, 4804 (1980).
- [190] M. Möller, M. M. de Lima Jr., A. Cantarero, Phys. Rev. B **84**, 085318 (2011).
- [191] Z. Zhang, Z.-Y. Lu, H.-Y. Xu, P.-P. Chen, W. Lu, J. Zou, Nano Res. **7**, 1640 (2014).
- [192] L. E. Fröberg, W. Seifert, J. Johansson, Phys. Rev. B **76**, 153401 (2007).
- [193] J. Bubesh Babu, K. Yoh, J. Cryst. Growth **323**, 301 (2011).
- [194] H. J. Joyce, J. Wong-Leung, Q. Gao, H. Hoe Tan, C. Jagadish, Nano Lett. **10**, 908 (2010).

- [195] T. Li, L. Gao, W. Lei, L. Guo, T. Yang, Y. Chen, Z. Wang, *Nanoscale Res. Lett.* **8**, 27 (2013).
- [196] L. Zhang, J.-W. Luo, A. Zunger, N. Akopian, V. Zwiller, J.-C. Harmand, *Nano Lett.* **10**, 4055 (2010).
- [197] F. Zhou et al. *Phys. Rev. B* **83**, 205416 (2011).
- [198] F. Glas, J.-C. Harmand, G. Patriarche, *Phys. Rev. Lett.* **99**, 146101 (2007).
- [199] H. Morkoç, Ü. Özgür, “Zinc Oxide: Fundamentals, Materials and Device Technology”, Wiley-VCH, Weinheim, (2009).
- [200] Y. Chin-Yu, Z. W. Lu, S. Froyen, A. Zunger, *Phys. Rev. B* **46**, 10086 (1992).
- [201] S. Rohmfeld, M. Hundhausen, and L. Ley, *Phys. Rev. B* **58**, 9858 (1998).
- [202] X.-W. Fu, Z.-M. Liao, R. Liu, J. Xu and D. Yu *ACS Nano*, **7**, 8891 (2013).
- [203] P. Bhattacharya, T. K. Sharma, S. Singh, A. Ingale, L. M. Kukreja, *J. Cryst. Growth* **236**, 5 (2002).
- [204] M.-Y. Xie, M. Schubert, J. Lu, P. O. Å. Persson, V. Stanishev, C. L. Hsiao, L. C. Chen, W. J. Schaff, V. Darakchieva, *Phys. Rev. B* **90**, 195306 (2014).
- [205] Y. Kangawa, T. Ito, A. Koukitu, K. Kakimoto, *Jpn. J. Appl. Phys.* **53**, 100202 (2014).
- [206] Lisco, P.M. Kaminski, A. Abbas, K. Bass, J.W. Bowers, G. Claudio, M. Losurdo, J.M. Walls, *Thin Solid Films* **582**, 323 (2015).
- [207] O. Vigil, I. Riech, M. Garcia-Rocha, O. Zelaya-Angel, *J. Vac. Sci. Technol. A* 1997, 15, 2282 and reference there in.
- [208] H. Zhang, X. Ma, D. Yang, *Mater. Lett.* **58**, 5 (2003).
- [209] A. Alka, S.M. Ingale, U. N. Roy, P. Tiwari, L.M. Kukreja, *J. Appl. Phys.* **106**, 084315 (2009) reference there in.
- [210] R. Caries, N. Saint-Cricq, J. Renucci, A. Zwick, M. A. Renucci, *Phys. Rev. B* **22**, 6120 (1980).
- [211] J. K. Panda, A. Roy, *Phys. Rev. B* **92**, 205302 (2015).
- [212] Ilaria Zardo, Ph.D. thesis, Technische Universität Muenchen, (2010).
- [213] C. H. Park, B.-H. Cheong, K.-H. Lee, K. J. Chang, *Phys. Rev. B* **49**, 4485 (1994).
- [214] J. Schneidert, R. D. Kirby, *Phys. Rev. B* **6**, 1290 (1972).

- [215] H. Selke, V. Kirchner, H. Heinke, S. Einfeldt, P. L. Ryder, D. Hommel, *J. Cryst. Growth*, **208**, 57 (2005).
- [216] F. Bechstedt, A. Belabbes, *J. Phys. Condens. Matter*, **25**, 273201 (2013).
- [217] F. Boutaiba, A. Belabbes, M. Ferhat, F. Bechstedt, *Phys. Rev. B* **89**, 245308 (2014).
- [218] F. J. Lopez, U. Givan, J. G. Connell, L. J. Lauhon, *J. ACS nano* **5**, 8958 (2011).
- [219] J. K. Panda, A. Roy, A. Singha, M. Gemmi, D. Ercolani, V. Pellegrini, L. Sorba, *Appl. Phys. Lett.* **103**, 143101 (2014).
- [220] D. Majumdar, A. Basu, G. D. Mukherjee, D. Ercolani, L. Sorba, A. Singha, *Nanotechnology* **25**, 465704 (2014).
- [221] C. Schneider, G. Brink, P. V. Irmer, *Physica B* **256–258**, 625 (1998).
- [222] A. Link, K. Bitzer, W. Limmer, R. Sauer, C. Kirchner, V. Schwegler, M. Kamp, D. G. Ebling, K. W. Benz, *J. Appl. Phys.* **86**, 6256 (1999).
- [223] S. D. Dabhi, P. K. Jha, *J. Phys. Chem. Solid* **83**, 70(2015).
- [224] X.-Y. Xue, S.-R. Xu, Z. Jin-Cheng, L. Z.-Y. Ma, J.-C. L. Zi-Yang, J.-S. Xue, H. Yue, *Chin. Phys. B* **21**, 027803 (2012).
- [225] H. H. Burke, I. P. Herman, *Phys. Rev. B* **48**, 15016 (1993).
- [226] K. Aoki, E. Anastassakis, M. Cardona, *Phys. Rev. B* 1984, **30**, 681.
- [227] N. N. Sirota, L. I. Berger, *Inzh. Fiz. Zhurnal, Akad. Nauk Beloruss., SSR* **2**, 104 (1959).
- [228] Y. A. Burenkov, S. Y. Davydov, S. P. Nikanorov, *Sov. Phys. Solid State*, **17**, 1446 (1975).
- [229] R. Tanta et al. *Nanotechnology* **27**, 305704 (2016).
- [230] M. Yamaguchi, A. Yamamoto, H. Sugiura and C. Uemura, *Thin Solid Films* **92**, 361 (1982).
- [231] R. Tanta, M. H. Madsen, Z. Liao, P. Krogstrup, T. Vosch, J. Nygård, and T. S. Jespersen, *Appl. Phys. Lett.* **107**, 243101 (2015).
- [232] R. Tanta, Ph.D. Thesis, Copenhagen University, Copenhagen (2015).
- [233] G. P. Schwartz, F. A. Thiel, and G. J. Gualtieri, *J. Vac. Sci. & Technol. A* **2**, 1252 (1984).
- [234] Jiayu He, Pingping Chen, Wei Lu, Ning Dai, and Da-Ming Zhu, *Appl. Phys. A*. **115**, 885 (2014) and reference there in.

- [235] T. Ganguli and A. Ingale, Phys. Rev. B. **77**, 033202 (2008).
- [236] ANSYS® Academic Teaching advanced, Release 14.0, Help System “Thermal Analysis Guide” ANSYS, Inc.
- [237] C.S. Krishnamoorthy, “Finite Element Analysis: Theory and Programming, second ed., Tata McGraw-Hill Education”, New Delhi, pp. 514 (1987).
- [238] M. Lax, Appl. Phys. Lett. **33**, 786 (1978).
- [239] Frank P. Incropera, David P. DeWitt, “Fundamental of heat and mass transfer Johan Wiley& Sons” (1978).
- [240] M. Kulik, D. Kołodyńska, J.Zuk, F.F. Komarov and J. Filiks, Chemical Composition of Native Oxide Layers on In+ Implanted and Thermally Annealed GaAs, Acta. Phys. Pol. A, **123**, 943 (2013).
- [241] M, N. O. Sadiku “Numerical techniques in electromagnetics” CRC press (1992).
- [242] R. Bowers, R. W. Ure, J. E. Bauerle, and A. J. Cornish, J. Appl. Phys. **30**, 930 (1959).
- [243] G. Le Guillou and H. J. Albany, Phys. Rev. B **5**, 2301 (1972).
- [244] J. Anaya, A. Torres, A. Martín-Martín, J. Souto J. Jiménez, A. Rodriguez, T. Rodriguez, Appl. Phys. A. **113**, 167 (2013).
- [245] C. J. Glassbrenner and Glen A. Slack, Phys. Rev. **134**, A1058 (1964).
- [246] Robert hull, “Properties of crystalline Silicon” INSPEC London IEE, Series no.20 (1999).
- [247] U. Piesbergen, Journal for Natural Science 18a, **2**, 141 (1963).
- [248] P. Hess, Appl. Surf. Sci. **106**, 429 (1996).
- [249] S. Adachi, “Properties of Group-IV, III–V and II–VI Semiconductors”, United State JOHN WILEY AND SONS (1992).
- [250] F. R. Brotzen, P. J. Loos and D. P. Brady, Thin Solid Films **207**, 197(1992).
- [251] V. K. Gupta, A. A. Ingale, S. Pal, R. Aggarwal and V. Sathe, J. Raman Spectrosc. **48**, 855 (2017).
- [252] D. E. Aspnes and A. A. Studna, Phys. Rev. B **27**, 985 (1983)
- [253] J. A. Goldak., A. Chakravarti & M. J. Bibby “A Double Ellipsoid Finite Element Model for Welding and Heat Sources” IIW Doc-212-603-85(1985).
- [254] C.-L. Chang, V. Shutthanandan, S. C. Singhal, and S. Ramanathan , Appl. Phys. Lett. **90**, 203109 (2007).

- [255] John T. Wolan, Charles K. Mount, and Gar B. Hoflund, *Appl. Phys. Lett.* **72**, 1469 (1998).
- [256] G. P. Schwartz, W. A. Sunder, J. E. Griffiths, and G. J. Gualtieri, *Thin Solid Films* **94**, 205 (1982).
- [257] B. Reifenberger, M. J. Keck, and J. Trivisonno, *J. Appl. Phys.* **40**, 5403 (1969).
- [258] Norman, C. Nicholas, “ed. *Chemistry of arsenic, antimony and bismuth*”, Springer Science & Business Media (1997).
- [259] J. Walia, N. Dhindsa, J. Flannery, I. Khodabadi, J. Forrest, R. LaPierre and S. S. Saini *Nano Lett.* **14**, 5820 (2014).
- [260] J. Walia et al. *Nanotechnology* **27**, 245708 (2016) and references there in.
- [261] A. W. Dey, C. Thelander, E. Lind, K. A. Dick, B. M. Borg, M. Borgström, P. Nilsson, and L.-E. Wernersson, *IEEE Electron Device Letters* **33**, 791 (2012).
- [262] V. K. Gupta, A. A. Ingale, V. Jain, R. Aggarwal and S. Pal, *Journal of Alloys and Compound* **735**, 1331 (2018).
- [263] Erik Mårzell et al. *Nano Lett.* **18**, 907 (2018).
- [264] R. Anufriev, J.-B. Barakat, G. Patriarche, X. Letartre, C. Bru-Chevallier, J.-C. Harmand, M. Gendry and N. Chauvin, *Nanotechnology* **26**, 395701 (2015)
- [265] Q. Xiong, G. Chen, H.R. Gutierrez, P.C. Eklund, *Appl. Phys. A* **85**, 299 (2006).
- [266] V. K. Gupta, R. Aggarwal, A. A. Ingale, and A. Bhattacharya, *AIP Conf. Proc.* **1832** 050121 (2017).
- [267] D. H. Laughlin and C. W. Wilmsen 1980 Thermal oxidation of InAs *Thin Solid Film* **70** 325 (1980).
- [268] H.S. Kim, H.G. Na, J.C. Yang, C. Lee, and H.W. Kim, *ACTA PHYSICA POLONICA A* **119**, 143 (2011).
- [269] R. N. Zitter, “*The Physics of Semi metals and Narrow Gap Semiconductor*” edited by D. L. Carter and R. T. Bate (Pergamon, New York), pp. 285 (1971).
- [270] R. L. Farrow, R. K. Chang, S. Mroczkowski, and F. H. Pollak, *Appl. Phys. Lett.* **31**, 768 (1977).
- [271] G. P. Schwartz, B. Schwartz, D. DiStefano, G. J. Gualtieri, and J. E. Griffiths, *Appl. Phys. Lett.* **34**, 205 (1979).
- [272] J. S. Lannin and B. V. Shanabrook, *Proc. Int. Conf. Phys. 14th Semi. Edinburgh, United Kingdom* (1978).

- [273] B. Liu et al. *Advanced Materials* **27**, 4423(2015).
- [274] J. S. Lannin *Phys. Rev. B* **15**, 3863 (1977).
- [275] R. J. Nemanich, G. Lucovsky, W. Pollard, and J. D. Joannopoulos, *Solid State Commun.* **26**, 137 (1978).
- [276] L. Kou, Y. Ma, X. Tan, T. Frauenheim, A. Du and S. Smith, *J. Phys. Chem. C* **119**, 6918 (2015).
- [277] Zhen Zhu, Jie Guan, and David Tománek, *Phys. Rev. B* **91**, 161404 (2015).
- [278] O. Osters, T. Nilges, F. Bachhuber, F. Pielhofer, R. Wehrich, M. Schoneich, P. Schmidt, *Angew. Chem. Int. Ed.* **51**, 2994 (2012).
- [279] H. Krebs, W. Holz, and K. H. Worms, *Chem. Ber.* **90** 1031 (1957).
- [280] Z. Zhu, Jie Guan, and D. Tománek, arXiv: **1410.6371** (2014).
- [281] J. H. Xu, E. G. Wang, C. S. Ting, and W. P. Su, *Phys. Rev. B* **48**, 17271 (1993).
- [279] C. Kamal and M. Ezawa, *Phys. Rev. B* **91**, 085423 (2015).
- [283] Z. Zhang, J. Xie, D. Yang, Y. Wang, M. Si, and D. Xue, *Appl. Phys. Express* **8**, 055201 (2015).
- [283] Z. Zhang, J. Xie, D. Yang, Y. Wang, M. Si, and D. Xue, *Appl. Phys. Express* **8**, 055201 (2015).

